Numerische Simulationen von bioinspirierten und natürlichen Materialien

Von der Fakultät Energie-, Verfahrens- und Biotechnik der Universität Stuttgart
zur Erlangung der Würde eines Doktors der
Ingenieurwissenschaften (Dr.-Ing.) genehmigte kumulative Abhandlung

Vorgelegt von

Dipl.-Biol. Immanuel Günther Schäfer M. Sc. in Engineering (CUAS)

aus Radolfzell

Hauptberichter: Prof. Dr. rer. nat. Dr. h. c. Siegfried Schmauder

Mitberichter: apl. Prof. Dr. rer. nat. Franz Brümmer

Tag der mündlichen Prüfung: 27.4.2021

Institut für Materialprüfung, Werkstoffkunde und Festigkeitslehre

der Universität Stuttgart

2021

Kurzfassung

Die Arbeit befasst sich mit Finite-Elemente-Simulationen und Modellierungen von natürlichen und bioinspirierten Materialien.

Die bioinspirierten Materialien sind künstliche Materialien, die ein oder mehrere Prinzipien der biologischen Vorbilder erfolgreich umgesetzt haben. Die natürlichen Materialien sind biologischen Ursprungs. Zu Beginn benötigt man immer eine funktionelle Analyse des Systems, um dann die notwendigen Reduzierungen für die Modellierungen herstellen zu können. Wenn das Modell steht, werden Eigenschaften wie zum Beispiel die Dämpfung oder der Widerstand gegen eine lineare Krafteinwirkung in Finite-Elemente-Simulationen analysiert. Die daraus gewonnenen Ergebnisse werden zur Beurteilung des Versagenverhaltens (z. B. des natürlichen Materials) oder zur Erklärung der Eigenschaften des bioinspirierten Materials genutzt. Die vorliegende Arbeit ist in die Analyse und die Diskussion der Ergebnisse verschiedener Materialien in neun Veröffentlichungen unterteilt. Zu Beginn werden die Ergebnisse des ersten bionischen Projektes präsentiert sowie die Lichtaufnahme, Lichtleitung- und Lichtverarbeitungsmöglichkeiten einer sukkulenten Art, der Fensterpflanze diskutiert. Die Perlmuttschale einer Schnecke bzw. ihr bioinspiriertes Produkt ist das Thema der anschließend vorgestellten Arbeiten. Daraus hervor ging auch die Veröffentlichung zu Enzymen und deren Bindungsaffinitäten zu Zinkoxid.

Die Schale der Pomelo, die die kiloschwere Frucht beim Herunterfallen von den ca. 15 m hohen Bäumen vor Beschädigungen schützt, ist das Vorbild für einen Metallschaum im nächsten Beispiel. Als letztes werden die Vorbilder Kokosnuss und Seeigelstachel präsentiert, die im Rahmen eines Transregios (einem von der Deutschen Forschungsgemeinschaft (DFG) geförderten Sonderforschungsbereich, TRR 141) betrachtet wurden. Für den TRR 141 wurde auch eine Ausstellung im Naturkundemuseum Stuttgart organisiert. Im Kapitel 12 wird eine Präsentationsstation beschrieben, die mit NFC(Near-Field-Communication)-Chips gesteuert werden kann. Die Präsentationsstation wurde im Rahmen dieser Arbeit entwickelt und mit dem Museum zusammen gebaut. Mit ihr werden Filme und Präsentationen zu dem Thema des TRR mit Ausstellungsgegenständen (z. B. eine 3D gedruckte Struktur des Seeigelstachels in Vergrößerung) kombiniert. Auf diese Weise zeigt die vorliegende kumulative Dissertation einen Überblick über die gesamten bionischen Arbeiten, die am Institut für Materialprüfung, Werkstoffkunde und Festigkeitslehre bei Herrn Prof. Dr. rer. nat. Dr. h. c. Siegfried Schmauder mit meiner Beteiligung entstanden sind.

Abstract

The work deals with finite element simulations and modelling of natural and bio-inspired materials.

The natural materials are of biological origin, the bioinspired materials are artificial materials that have successfully implemented one or more principles of the biological models. First there is always a functional analysis of the system (the natural material) in order to be able to produce the necessary reductions for the modelings. When the model is ready, it is used to analyse certain properties such as damping or resistance to linear forces in finite element simulations. The results obtained are then used to assess the failure behaviour (e.g.) of the natural material or to explain the properties of the bio-inspired material. The work is divided into the analyzation of different materials, which are treated in nine publications. At the beginning, the results of a first biomimetic project will be presented and the light absorption, light conduction and light processing possibilities of a succulent species, the window plant, will be explained. The mother-of-pearl shell of a snail or its bio-inspired product is the subject of the works presented afterwards. This also led to the publication on enzymes and their binding affinities to zinc oxide.

The shell of the pomelo fruit, which protects the heavy fruit from damage when it falls down from the approximately 15 m high trees, is the rolemodel for a metal foam in the next section. Finally, the rolemodels coconut and sea urchin spines are presented, which were considered within the framework of a Transregio (a special research area funded by the German Research Society (DFG), TRR 141). An exhibition at the Naturkunde Museum Stuttgart was also organised for this TRR 141. The section „Ausstellung im Rosensteinmuseum“ describes a presentation station that can be controlled by NFC (Near-Field-Communication) chips and combines movies and presentations on the topic of the TRR with exhibits (e.g., 3D-printed structure of the sea urchin spine in magnification). The presentation station was developed as part of this work and built together with the museum. The cumulative doctoral thesis is intended to give an overview of the entire biomimetic work done at the Institute for Materials Testing, Materials Science and Strength of Materials at Prof. Dr. rer. nat. Dr. h. c. Siegfried Schmauder with my participation.

Inhaltsverzeichnis

Danksagung

Die vorliegende Arbeit entstand im Rahmen mehrerer Forschungsprojekte an der Universität Stuttgart sowie während der damit einhergehenden Tätigkeit als akademischer Mitarbeiter am Institut für Materialprüfung, Werkstoffkunde und Festigkeitslehre (IMWF). Für die finanzielle Förderung dieser Arbeit an der Universität Stuttgart danke ich der Deutschen Forschungsgemeinschaft (DFG).

Dem gesamtem Team des IMWFs möchte ich für die kollegiale und konstruktive Atmosphäre bedanken, die mich stets motiviert und inspiriert hat. Dankbar bin ich für die fruchtvollen Diskussionen mit meinen Kolleg*innen, für Cthulhu und für Kaffee.

Mein besonderer Dank gilt Herrn Prof. Franz Brümmer für das Interesse an dieser Arbeit als Mitbetreuer und die Übernahme des Mitberichtes.

Großen Dank gilt der Verwaltung, Kerstin Hilscher und Iris Weber, für die Unterstützung nicht nur in organisatorischen und verwaltungstechnischen Angelegenheiten.

Insbesondere möchte ich mich bei Herrn Prof. Siegfried Schmauder für die Möglichkeit bedanken, in das Forschungsteam aufgenommen worden zu sein. Großer Dank gebührt ihm für die Unterstützung bei allen Projekten, Fortbildungsmöglichkeiten, Konferenzen und nicht zuletzt bei dieser Doktorarbeit.

Ich danke auch meiner Familie und meinen Freunden. Zu aller Erst möchte ich meinen Eltern für deren Unterstützung danken. Meinen Geschwistern für die Gastfreundschaft, Diskussionen, Motivation und guten Vorbilder. Ich möchte meiner Frau Anke danken, dass sie mir den Rücken freigehalten hat, wann immer es nötig war und mich immer unterstützt hat. Dann meinen Kindern Pepe und Jana, die auch ihren Teil zur Motivation beigetragen haben und mich jeden Tag aufs Neue begeistern.

Immanuel Schäfer
Juli 2020

Veröffentlichungen

Die in dieser Dissertation besprochenen Beiträge in wissenschaftlichen Zeitschriften und Büchern sind hier aufgelistet. Die Wiederveröffentlichungsrechte wurden eingeholt. Einen Überblick über alle Aufsätze des Autors findet sich am Ende der Dissertation (S. 241, Übersicht aller Veröffentlichungen).

Kapitel 2 Fensterpflanze

I. Schäfer, Immanuel. (2013). Biomimetics in Energy Systems: Light Transmission in the Window Plant *Fenestraria aurantiaca* as Inspiration for New Solutions in the Technical World. Advances in Science and Technology, 84, pp. 51–56.

Kapitel 3 Perlmutt 1

II. Lasko, G., Schäfer, I., Burghard, Ž., Bill, J., Schmauder, S., Weber, U., & Galler, D. (2013). Derivation of the Stress-Strain Behavior of the constituents of Bio-Inspired Layered TiO_2/PE-Nanocomposites by Inverse Modeling Based on FE-Simulations of Nanoindentation Test. Molecular & Celullar Biomechanics, 10(1), pp. 27–42.

Kapitel 4 Perlmutt 2

III. Lasko, G., Burghard, Ž., Bill, J., Schäfer, I., Weber, U., & Schmauder, S. (2013). Simulation of Mechanical Properties of Bio-Inspired TiO_2/PE Nanocomposites. Advanced Engineering Materials, 15(10), pp. 908–920.

Kapitel 5 Proteinbindungseigenschaften an Zinkoxid

IV. Schäfer, I., Lasko, G., Do, T. A., Pleiss, J., Weber, U., & Schmauder, S. (2014). Peptide-zinc oxide interaction: Finite element simulation using cohesive zone models based on molecular dynamics simulation. Computational Materials Science, 95, pp. 320–327.

Kapitel 6 Buch Vorwort und Wiederveröffentlichung

Veröffentlichung Nummer **IV.** wurde in dem Buch

V. Schmauder, S., & Schäfer, I. (Eds.). (2016*). Multiscale materials modeling: approaches to full multiscaling.* Berlin: De Gruyter, ISBN 13: 978-3110412369

dass von Prof. S. Schmauder und mir als Editoren herausgebracht wurde, erneut veröffentlicht:

VI. Schäfer, I., Lasko, G., Do, T. A., Pleiss, J., Weber, U., & Schmauder, S. (2016). Peptide-zinc oxide interaction: Finite element simulation using cohesive zone models based on molecular dynamics simulation. In Multiscale Materials Modeling: Approaches to Full Multiscaling, pp. 303–322.

Dort findet sich das Vorwort, das von Herrn Prof. Schmauder und Immanuel Schäfer zusammen erstellt wurde:

VI.b Schmauder, S., & Schäfer, I. (2016). Multiscale materials modeling: Approaches to full multiscaling. Multiscale Materials Modeling: Approaches to Full Multiscaling - Preface.

Kapitel 7 Pomelo

VII. Schäfer, I., Mlikota, M., Schmauder, S., & Weber, U. (2020). Modelling the damping response of biomimetic foams based on pomelo fruit. Computational Materials Science, 183, pp. 109801.

Kapitel 8 TRR141

VIII. Schmier, S., Lauer, C., Schäfer, I., Klang, K., Bauer, G., Thielen, M., Termin, K., Berthold, C., Schmauder, S., Speck, T., Nickel, K. G. (2016). Developing the Experimental Basis for an Evaluation of Scaling Properties of Brittle and 'Quasi-Brittle' Biological Materials. In *Biomimetic Research for Architecture and Building Construction*, pp. 277–294.

Kapitel 10 Seeigelstachel

IX Schäfer, I., Bräutigam, D., Schmid, P., & Schmauder, S. (2017). Evolution is the better architect: Simulation of cellular solids in sea urchin spines, Conference SMILE 2016, organized by IFP Energies nouvelles (IFPEN), at Rueil-Malmaison, http://www.rs-smile2016.com, *nicht veröffentlicht / Konferenzbeitrag*

1 Einleitung und Motivation

Die Arbeit behandelt die Untersuchung von biologischen und bioinspirierten bzw. bionischen Materialien. Dabei stehen herausstechende Funktionen und Prinzipien der natürlichen Vorbilder im Vordergrund. Das Verständnis der Funktion und deren zugrundeliegenden Prinzipen, aber auch die Umsetzung in die Technik bzw. Materialentwicklung werden besprochen. Dieses Wissen für Studierende und interessierte Erwachsene (u. a.) und die Materie Bionik/Natur/Nachhaltigkeit begreifbar zu machen, ist ein weiteres Thema am Ende der Arbeit.

1.1 Bionik und Simulation

Bionik wird schon seit langer Zeit betrieben; wahrscheinlich seitdem es Menschen gibt. Erste Zeugnisse davon finden sich bei Leonardo da Vinci; schriftliche zum Beispiel bei R. H. Francé, Die Pflanze als Erfinder [1]. In diesem Buch beschreibt der Autor schon 1920 die Suche nach einem perfekten Streugerät für Pulver oder ähnliches. Er findet ein Vorbild in der Mohnsamenkapsel und baut erste Prototypen. Seine Begeisterung über die Nachhaltigkeit der Pflanze drückt er so aus:

> *„Die Pflanzenzelle nutzt alle vier* (…Die Gase: Sauerstoff, Wasserstoff, Stickstoff und Kohlensäure…Einfügung des Autors*) und hat sich dadurch ohne Kosten die billigste Rohstoffquelle der Welt erschlossen“* [1, p. 48].

Er nannte die Wissenschaft damals Biotechnik:

> *„Die Biotechnik ist der Gipfel der Technik überhaupt!“* [1, p. 50]

Im selben Buch beschreibt Francé auch die Schwierigkeit, das Wissen der Natur für alle zugänglich zu machen:

> *„Man wusste von den großen Tatsachen der Biotechnik, aber man benützte sein Wissen nicht, der Biologe hatte dem Techniker nichts zu sagen, und der Ingenieur, der Chemiker, der Architekt fand, dass biologische Kenntnisse nicht zu seinem Fach gehören“* [1, p. 66].

Nachhaltigkeit und Ressourcen hat schon Francé im Zitat oben angesprochen. Auch heute sind die Nachhaltigkeit, die Endlichkeit fast aller Ressourcen und die Kosten unseres Lebensstils für die nachfolgenden Generationen aktueller denn je. Obwohl es von manchen angenommen wird, ist Bionik oder Biomimetik per se nicht nachhaltig:

> *„Sie ist eine Designmethode und als solche frei von Werten. Allerdings – wenn wir schon von der belebten Natur über bessere Zugänge in den Ingenieurwissenschaften lernen, warum sollten wir uns nur auf Muster, Strukturen, Materialien und Prozesse konzentrieren und nicht eine der faszinierendsten Eigenschaften des Lebens mittransferieren – die dem System innewohnende Nachhaltigkeit?“, I. Gebeshuber* [2, p. 61].

Erst die Umsetzung entscheidet über die Nachhaltigkeit des bionischen Prinzips und liegt somit in der Hand des Bionikers. Die im Zitat angesprochen Zugänge aus den Ingenieurwissenschaften sind vielseitig, eine wichtige Methode zur Analyse von Systemen ist die Simulation. Nach Knippers [3] ist die Simulation Bindeglied zwischen Biologie und Anwendung der Prinzipien in der Technik, da es einerseits das Verständnis der biologischen Vorbilder ermöglicht und eine Basis für die Abstraktion der Prinzipien der biologischen Vorbilder liefert und andererseits, das scheint fast wichtiger zu sein, die Kommunikation zwischen den verschiedenen wissenschaftlichen Disziplinen ermöglicht. Die Bedeutung der Simulation wird auch in dem Artikel von Littmark [4] deutlich, in dem er beschreibt, wie sich die Simulation zu dem entwickelt hat, was sie heute ist. Beruhend auf mathematischen Modellen von Newton, Maxwell und vielen anderen wurde es möglich, die zeitliche und räumliche Entwicklung von Modellen unter bestimmten Randbedingungen mithilfe von numerischen Methoden zu beschreiben und vor allem vorherzusagen. Die Simulation ist die Basis zum (besser) verstehen und optimieren. Doch leider gibt es noch viele Bereiche unseres Lebens, die noch nicht für Simulationen zugänglich oder die zumindest Spezialisten vorbehalten sind. Ziel sollte es sein, den Einstieg in Simulationen zu vereinfachen. In dieser Arbeit wird die Simulation als Methode genutzt, um verschiedene biologische Materialien zu analysieren und deren Besonderheiten herauszufinden. Auch bioinspirierte Materialien, also Materialien, die entwickelt worden sind, weil ein biologisches Vorbild dazu inspiriert hat, werden untersucht. Dabei sollen die Prinzipien, die das Material so hervorstechend anders machen, bestimmt und durch Simulationen deren Wirkweise nachgewiesen werden. Dafür werden die zugrundeliegenden Strukturen (es werden in dieser Arbeit struktur-mechanische Simulationen und Prinzipien untersucht) in CAD (compture aided

design) Modelle umgewandelt, die dann vernetzt, mit Randbedingungen versehen und berechnet werden.

Die Verknüpfung der Methoden „Bionik“ und „Simulation“ steht in fast allen der hier dargestellten Veröffentlichungen im Fokus. Durch diese Kombination sind Hypothesen überprüfbar, wie im Beispiel der Perlmuttschale bei den Mineralbrücken des bioinspirierten Materials. Die hohe Festigkeit war zunächst nicht nachvollziehbar, erst mit der Simulation konnte nachgewiesen werden, dass Mineralbrücken an bestimmten Stellen (im Produktionsprozess) entstehen müssen. Sie bestehen aus reinem Titandioxid in der Modifikation Rutil, nur das hat die erforderlichen Materialeigenschaften. Die Details werden im Kapitel 7 erläutert.

Die Arbeit teilt sich in unterschiedliche Veröffentlichungen auf, die verschiedene Materialien und bionische Prinzipien behandeln. Zuerst werden die Ergebnisse meiner Masterarbeit (Fachhochschule Kärnten) vorgestellt. Dort wird mein erstes bionisches Projekt präsentiert und die Lichtaufnahme, Lichtleitungs- und Lichtverarbeitungs-Möglichkeiten einer Sukkulenten Art, der Fensterpflanze vorgestellt. Die Perlmuttschale einer Schnecke bzw. ihr bioinspiriertes Produkt ist das Thema der zwei anschließenden Arbeiten. Daraus hervor ging auch die Veröffentlichung zu den Enzymen und deren Bindungsaffinitäten zu Zinkoxid.

Die Schale der Pomelo, die die kiloschwere Frucht beim Herunterfallen vor Beschädigungen schützt, ist das Vorbild für einen Metallschaum im nächsten Abschnitt. Als letztes werden die Vorbilder Kokosnuss und vor allem Seeigelstachel präsentiert, die im Rahmen eines Transregios (der von der Deutschen Forschungsgesellschaft (DFG) geförderten, überregionalem Sonderforschungsbereich, TRR141) betrachtet wurden. Im Abschluss zeigt eine Diskussion die wichtigsten Aspekte im Zusammenhang auf und ein kurzer Ausflug ins Museum am Ende schließt mit dem Thema Öffentlichkeitsarbeit und Wissensvermittlung mit einer interaktiven Station die Arbeit ab.

1.2 Materialien: Ein Überblick

Zuerst werden Materialien im Allgemeinen und deren Einteilung in Werkstoffklassen und Werkstoffgruppen für einen allgemeinen Überblick vorgestellt. Die in dieser Arbeit untersuchten Materialien werden im Weiteren im Detail besprochen, da diese entweder als biologische Vorbilder, als bioinspiriertes Material oder als Ersatzmaterialien zur Bestimmung bestimmter Formeinflüsse in Simulationen und Experimenten untersucht wurden.

„Werkstoffe sind Materialien, aus denen sich technisch relevante Bauteile herstellen lassen. Ihre Eigenschaften sind dabei von der chemischen Zusammensetzung, dem mikroskopischen Aufbau, dem Herstellungsprozess, der konstruktiven Gestaltung des Werkstoffs und von der Betriebsbeanspruchung des jeweiligen Bauteils abhängig.“ [5]

So lautet die Definition von Weitze und Berger, die die Werkstoffe (blau in Abbildung 1-1) in die folgenden Klassen (rot) bzw. Gruppen (gelb) unterteilen:

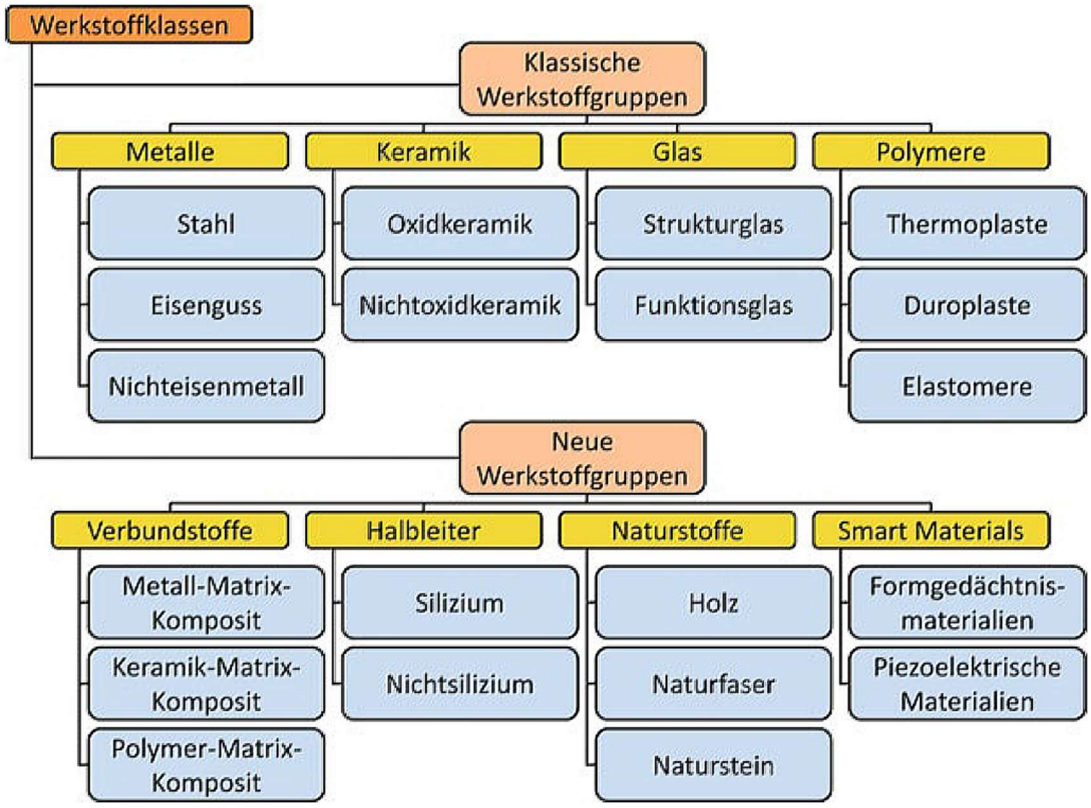

Abbildung 1-1: Werkstoffklassen nach [5]

Polymere und Keramiken ersetzen immer häufiger Metalle in Anwendungen bzw. Werkstoffen. Auch Kompositmaterialien werden verwendet, um die Eigenschaften zweier Materialien zu kombinieren und einen neuartigen Werkstoff zu kreieren. Weiterhin sind viele natürliche Materialien heutzutage immer noch einzigartig, d.h. die Eigenschaften wie z. B. von Holz (ein Verbundwerkstoff) sind mit anderen (künstlichen) Materialien nicht umfassend nachbildbar. Die Doktorarbeit behandelt vor allem Naturstoffe, darunter Perlmutt von Muscheln und Schnecken, das Endokarp (ein Teil der Schale) von Kokosnüssen und die

Fruchtschale der Pomelo, außerdem Seeigelstachel, die hauptsächlich aus Calzit bestehen. Es gibt aber auch einen Ausflug in die Werkstoffgruppe der Polymere bei der Betrachtung von Formeinflüssen auf Zugproben (inspiriert vom Thema Kokosnuss). Weiterhin sind Metalle und Komposite Thema bei der Umsetzung der Mikrostruktur der Pomeloschale und von Perlmutt. Nach Ashby [6] sind die folgenden Einteilungen der Materialien in Eigenschaftskategorien sinnvoll:

Tabelle 1.1: Eigenschaftsklassen von Materialien nach Ashby [7]

Klasse	Eigenschaft
wirtschaftlich	▪ Preis und Verfügbarkeit ▪ Wiederverwertbarkeit ▪ Nachhaltigkeit
Allgemeine physikalisch mechanisch	▪ Dichte ▪ Elastizitätsmodul ▪ Zugfestigkeit und Streckgrenze ▪ Härte ▪ Risszähigkeit ▪ Dauerfestigkeit ▪ Kriechbeständigkeit ▪ Dämpfung
thermisch	▪ Wärmeleitfähigkeit ▪ spezifische Wärmekapazität ▪ Wärmeausdehnungskoeffizient
elektrische und magnetische	▪ spezifischer Widerstand ▪ Dielektrizitätskonstante ▪ magnetische Permeabilität
Wechselwirkung mit der Umwelt	▪ Oxidation ▪ Korrosion ▪ Abrieb
Produktion	▪ Bearbeitbarkeit ▪ Fügbarkeit
ästhetisch	▪ Farbe ▪ Oberflächengestalt ▪ Haptik

Einige der mechanischen bzw. physikalischen Eigenschaften welche in Tabelle 1.1 dargestellt sind, wie Risszähigkeit oder Elastizitätsmodul, werden für die Simulationen und analytischen Berechnung benötigt und werden in den jeweiligen Veröffentlichungen soweit notwendig näher beschrieben.

Die Vorstellung der biologischen Vorbilder und deren Besonderheiten werden im nun folgenden Abschnitt 1.3 behandelt.

1.3 Biologische Vorbilder

Biologische Materialien zeigen besondere Kombinationen von Eigenschaften und sind deshalb oft Gegenstand wissenschaftlicher Untersuchungen. In Biological Materials: "Functional adaptions and bioinspired design" fasst Chen et al. [8] das Thema zusammen,präsentiert die wichtigsten Materialien und stellt gerade die Besonderheiten dieser Materialien in den Vordergrund. Für ein tiefgreifendes Studium wird auf die obige Arbeit verwiesen, hier soll noch einmal betont werden, wie interessant und auch wie unerreicht biologische Materialien in vielen Fällen im Vergleich zu künstlichen sind. Auch wenn schon viel daran geforscht wurde und wird, sind die meisten dieser natürlichen Vorbilder in ihrer Wirkweise noch nicht vollständig verstanden und deren Wirkprinzipien noch nicht in unsere Technik und Anwendungen übertragbar.

1.3.1 Fensterpflanze

Bei der sogenannten Fensterpflanze, der *Fenestraria aurantiaca* ist die Besonderheit in der Lichtverarbeitung der Blätter zu finden. Die Pflanze hat durchsichtige Bereiche (die Fenster) auf ihren keulenartig geformten Blättern, die das Sonnenlicht einfangen. Meist schaut nur die Spitze der Blätter mit dem Fenster aus dem Sand, der Rest der Blätter und der Pflanze ist im Sand versteckt. Dadurch entgeht die Pflanze der Hitze und der UV-Einstrahlung in der namibischen Wüste, wo die Pflanze heimisch ist. Durch die Fenster bekommen die Blätter trotzdem den notwendigen Anteil an Sonnenlicht, um aktive Photosynthese zu betreiben. In Abbildung 1-2 sind einige Details einer Fensterpflanze zu sehen.

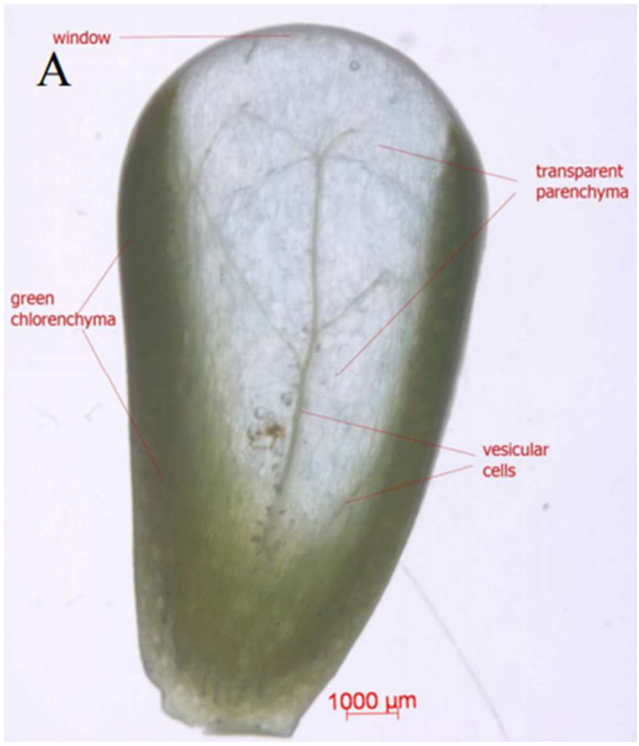

Abbildung 1-2: Schnitt durch eine Fensterpflanze [9]

Die Fenster sind nicht nur einfache Lichtöffnungen, sondern sie filtern das Licht zusätzlich. Der Aufbau der Blätter ermöglicht dann eine gleichmäßige Weiterleitung und Verteilung des Lichts in allen Bereichen des Blattes. Diese Prinzipien werden in der hier vorgestellten Veröffentlichung zuerst definiert, dann analysiert und mögliche Abstraktionen zum Wirkverständnis sowie potenzielle Anwendungsszenarien entwickelt.

1.3.2 Perlmutt

Ein Beispiel, das Steifigkeit, Härte und Bruchzähigkeit in besonderer Weise kombiniert, ist Perlmutt, welches zum Beispiel in den Schalen von Mollusken (das sind Weichtiere wie Schnecken oder Muscheln) zu finden ist. Perlmutt zeigt in Experimenten Werte für Materialeigenschaften wie u. a. Härte und Bruchzähigkeit, die schwer oder nicht von künstlichen (also von Menschen hergestellten) Materialien erreicht werden [10]. Perlmutt besteht hauptsächlich aus Calciumcarbonat ($CaCO_3$) in Aragonitkristallform. Besonders hervorzuheben ist die hohe Bruchzähigkeit der Molluskschalen die 3000 mal höher ist als der Wert von monolithischem $CaCO_3$ [11]. Man weiß von anderen biologischen Materialien wie Knochen und Zähnen, dass diese eine regelmäßige Struktur im Nanometerbereich aus einen harten mineralischen Kristall mit Proteinen als weiche Matrix kombinieren [12,13].

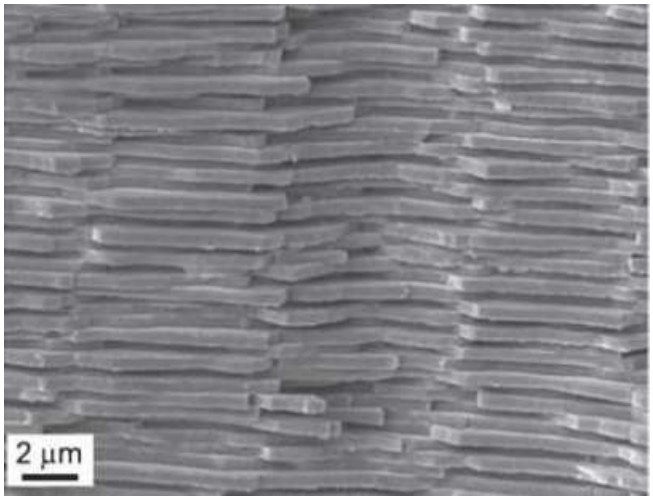

Abbildung 1-3: Die Brick-and-Mortar-Struktur von Perlmutt [14]

Bei Perlmutt findet man dieses (Brick and Mortar, vgl. Abbildung 1-3) Prinzip auch, es wird zusätzlich noch durch sogenannte mineralischen Brücken ergänzt (12,13). Diese Brücken sind ca. 30 nm breit und durchdringen die Proteinschicht in unregelmäßigen Abständen [15]–[17]. Die drei Veröffentlichungen zum Thema Perlmutt (Nummer II, III und IV) widmen sich einem bioinspirierten Material, das in einen gemeinsamen Projekt von den Partnern am Institut für Materialwissenschaft, Stuttgart entwickelt und getestet wurde. Die dort experimentell bestimmten Eigenschaften (z. B. E-Modul) konnten mit den in der vorliegenden Arbeit gezeigten Simulationen der Nanoindentation nachvollzogen werden.

1.3.3 Pomelo

Die Pomelo (*Citrus maxima*) ist eine Zitrusfrucht, die in den 70iger Jahren des letzten Jahrhunderts aus Pampelmuse und Grapefruit gekreuzt wurde. Sie wächst auf ca. 15 m hohen Bäumen und kann bis zu 2 kg schwer werden. Unter der grünen oder gelblichen Schale befindet sich eine weiße Schaumschicht, die das darauffolgende Fruchtfleisch vor Beschädigungen beim Herabfallen schützt. Einen Schnitt durch eine Frucht ist in Abbildung 1-4 gezeigt.

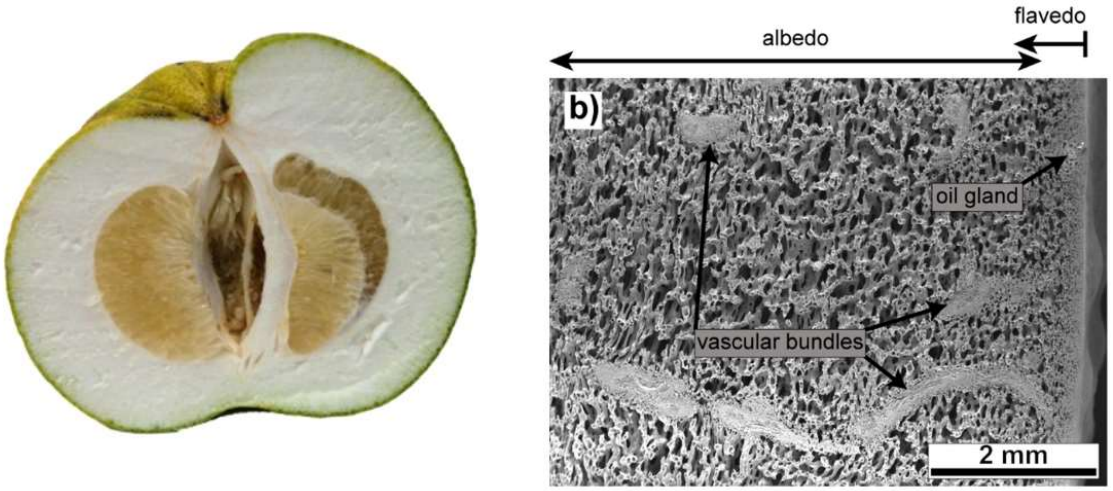

Abbildung 1-4: Links: Schnitt durch eine Pomelo. Grün das Endokarp, die Schale und weiß der weiche Anteil der Schale, Flavedo und Albedo. Gelb ist das Fruchtfleisch. Ausschnitt einer Abbildung aus [18] genau wie Abbildung rechts: SEM-Bild der Albedo Schicht

Genau diese Schutzfunktion, die Dämpfung und Federung sind für die Wissenschaft so interessant, vgl. [18], [19] und ist deswegen Thema in einer der hier vorgestellten Veröffentlichungen (Nummer VII). Der Fokus liegt auf der Art und Weise, wie die Struktur des Schaumes auf die Dämpfungseigenschaften wirkt, und wie Abstraktionen davon, wie zum Beispiel andere Geometrien für die Schwammstege oder Beschichtungen zu Änderungen hierbei führen. Der Schaumstruktur unter der Epidermis (der äußeren Schale) besteht aus Flavedo und Albedo, die beide aus dem Mesokarp hervorgehen. Das Flavedo besteht aus dicht gepackten parenchymatischen Zellen. Im Gegensatz dazu ist das Albedo (vgl. Abbildung 1-4 rechts) aus großen, luftgefüllten Zellen aufgebaut und macht damit den größten Teil der Schale aus. [19]

Projektpartner (Univ. Prof. Dr.-Ing. A. Bührig-Polaczek und Dr.-Ing. S. Fischer vom Gießerei-Institut der RWTH Aachen) haben einen Schaum aus Aluminiumoxid erstellt, der von dem Albedo inspiriert ist. Die Kraft-Verschiebungskurven des Schaums, der Einfluss von Steg-Beschichtungen oder einer Variationen der Stegdicke und der Stegform des Schaumes werden in der Veröffentlichung (Nummer VII) zu dem Thema mit FEM-Simulationen bestimmt und deren Einflüsse diskutiert.

1.3.4 Kokosnuss

Die Frucht der Kokospalme (*Cocos nucifera*) ist eine Steinfrucht und keine Nuss, da ihre Fruchtwand aus drei Schichten besteht und nur die innerste Schicht verholzt ist. Die äußerste Schicht der Kokosnuss ist das ledrige Exokarp, gefolgt vom faserigen Mesokarp und der innersten Schicht, dem harten und festen Endokarp (Abbildung 1-5 links). Interessant ist vor allem das harte Endokarp für die Untersuchungen in Kapitel 7. Das Endokarp besteht zum größten Teil aus sogenannten Steinzellen (vergleiche Abbildung 1-5 rechts), das sind stark verholzte Zellen die dicht gepackt und miteinander verzahnt sind. Die Zellen sind durch mehrere Lagen der sekundären Zellwand verstärkt und stark lignifiziert. Das gibt den Zellen die Festigkeit und Stabilität [20].

Abbildung 1-5: Details der Kokosnuss: Links ein Querschnitt mit dem weiß sichtbaren Nußfleisch, dem darum liegenden harten Endokarp und dem weichen Mesokarp. Daneben der Blick von außen auf das Mesokarp. Rechts ist eine Rasterelektronenmikroskopaufnahme mit den verholzten Wänden der Steinzellen zu sehen. Markiert sind Leitbündel (Verbindungen für Wasseraustausch etc.) zwischen den Zellen. Maßlinie 0,02 mm [21]

Nicht nur das Material, auch die Form der Schale hat einen Einfluss auf die Eigenschaften (z. B. auf die Zähigkeit) des Endokarps. Mit Kerbschlagbiegeversuchen werden Zähigkeitseigenschaften der Materialien bestimmt. Um von den Zähigkeitseigenschaften gekrümmter Proben, die aus den Kokosnussschalen gesägt werden können, auf die Eigenschaften von geraden Proben schließen zu können, wird im Kapitel 9 ein Versuch beschrieben, der noch nicht veröffentlicht ist. Dort werden PVC-Proben mit geraden und gekrümmten Formen hergestellt und im simulierten Kerbschlagbiegetest analysiert. Diese Ergebnisse bekommen

die Partner der Plant Biomechanics Group Freiburg, um sie mit ihren Proben aus Kokosnussendokarp vergleichen zu können. Um die für die FEM-Simulationen notwendigen Inputparameter für die FEM-Simulationen zu erhalten, werden Zugproben des PVC- Materials durchgeführt.

1.3.5 Seeigelstachel

Seeigelstachel sind absolute Leichtbauten: Sie weisen bis zu 60 % Porenvolumen [22] auf und bestehen aus einem absolut spröden Material, Magnesium-Calzit ($[Ca_xMg_{1-x}]CO_3$, mit einem Magnesiumgehalt von bis zu 10 mol %) [23]. Im Falle des hier unter Anderem untersuchten Seeigelstachels der Art *Heterocentrotus mammillatus* (HM) variiert das Volumen des Materialanteils, das offene Poren aufweist, von fast vollständig dicht/fest/geschlossen/nicht porös über 10 vol% im Bereich der Wachstumsringe. Die Porosität kann bis zu 60 vol% im Rest des Stereoms ansteigen. [22] In Abbildung 1-6 sind beispielhaft vier Bereiche aus dem Stereom abgebildet. Dazwischen finden sich immer Bereiche die ehemalige Schalenoberflächen (Kappen) zu sein scheinen, die eine sehr dichte Struktur aufweisen. Bei der zweiten in dem Projekt untersuchten (aber nicht für Simulationen genutzten) Art, *Phylancantus imperalis* (PI) reicht die Porosität von 40 % bis mehr als 65 % im Inneren des Stachels [24].

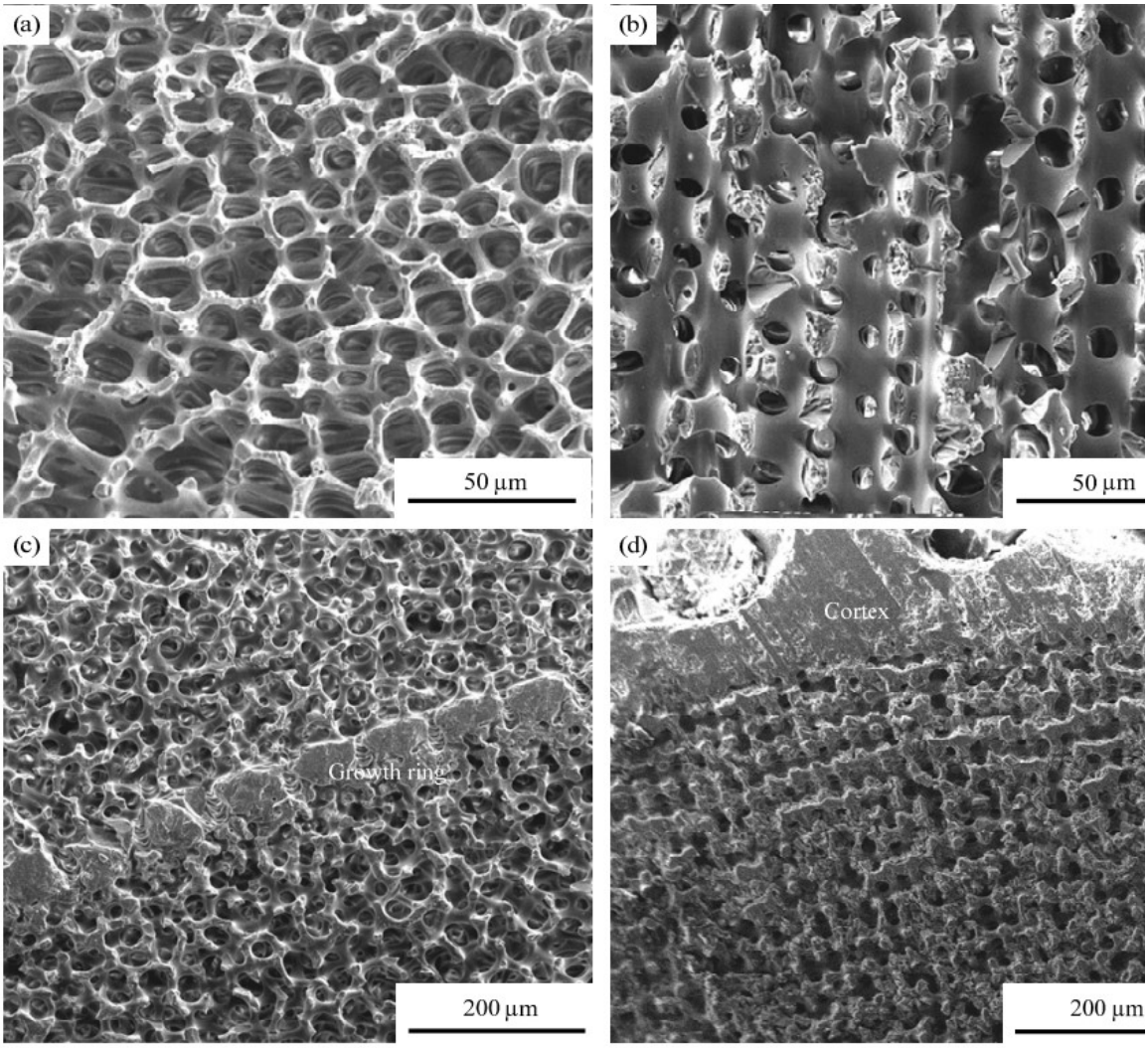

Abbildung 1-6: Vier Bereiche mit unterschiedlich porös ausgebildeten Strukturen des Seeigelstachels (HM): Abbildungen (a) und (b) zeigen typische Stereomstrukturen, in (c) ist ein Waschstumsring abgebildet und (d) zeigt den Kortex, die äußerste Schicht [25]

Interessant ist auch der kristalline Aufbau von dem Grundmaterial $CaCO_2$: Es sind sogenannte Mesokristalle [26] wie Seto et al. herausgefunden haben. Nach Cölfen und Antonietti sind Mesokristalle

„orientierte Überstrukturen aus Nanokristallen mit gemeinsamen äußeren Flächen und bilden einen neuen Typ kolloidaler Kristalle aus nichtspährischen, kristallinen Baueinheiten.“ [27],

also eine Überstruktur aus gegenseitig ausgerichteten Nanokristallen. Oft findet sich eine perfekte Orientierung der Nanokristalle im Mesokristall, weshalb diese gleichzeitig die Ei-

genschaften eines Einkristalls und eines Nanopartikel haben [27]. Mesokristalle in der Natur zeigen, wie wunderbare Strukturen (wie in diesem Beispiel einen extensiven Leichtbau der trotzdem sehr stabil ist und weitere Vorteile aufweist) generiert werden können, was so noch nicht künstlich möglich ist. Der innere Aufbau von Seeigelstacheln unterscheidet sich von Art zu Art (und auch innerhalb derselben Art) stark. Das Stereom, die innere schaumartige Struktur, lässt sich nach verschiedenen Strukturen unterteilen. Einige Beispiele für typische Strukturen sind in Abbildung 1-7 gezeigt.

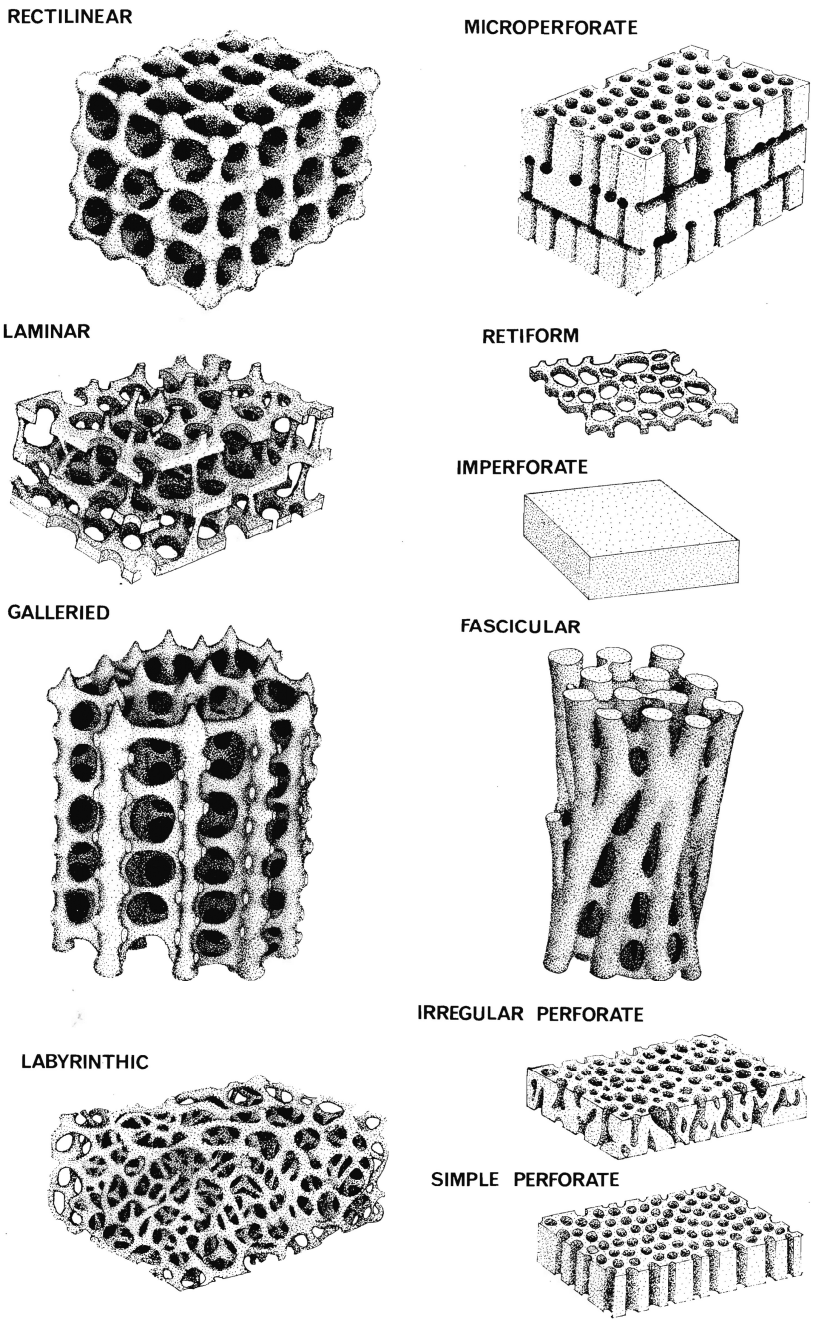

Abbildung 1-7: Typische Seeigelstachel Stereome [28]

Die Zwischenräume der Stereome werden als Stroma bezeichnet und sind im lebendigen Tier mit Flüssigkeit gefüllt. Die Flüssigkeit ist u. a. für den Austausch von Nähr- und Botenstoffen verantwortlich. *Heterocentrotus mammillatus* (HM) zeigt Besonderheiten im inneren Aufbau; seine poröse Struktur ist unterbrochen durch Wachstumsringe oder Kappen (siehe Abbildung 1-8), die wohl ehemals Oberflächen des jungen Seeigelstachels waren.

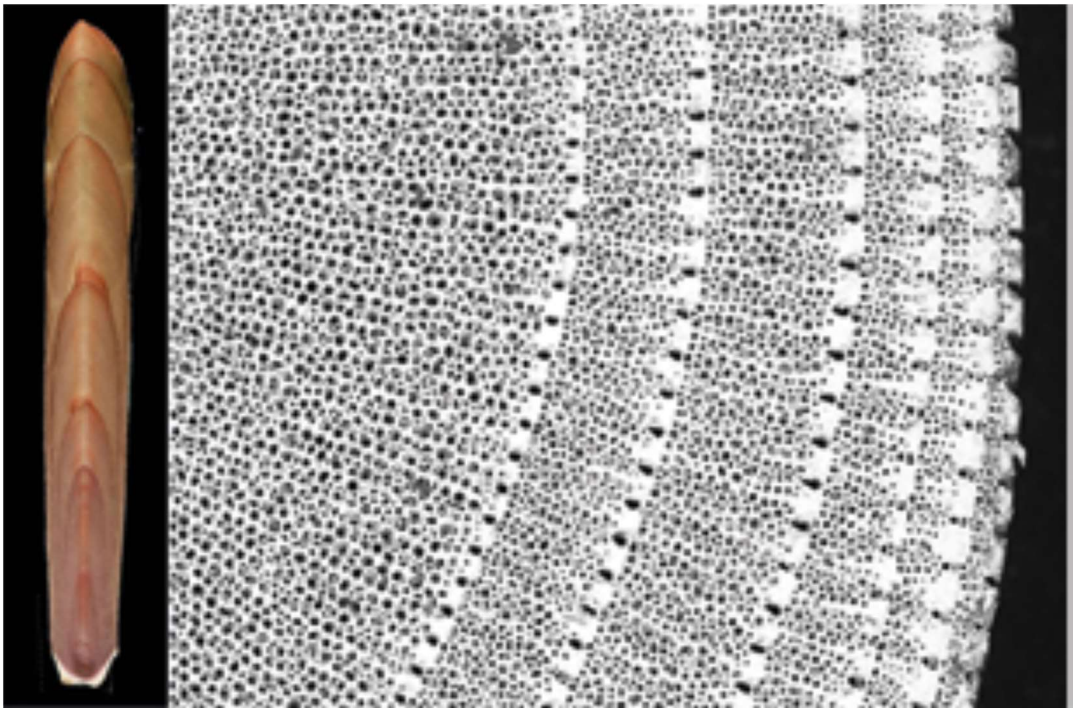

Abbildung 1-8: Kappen bzw. Wachstumsringe der Art Heterocentrotus mammillatus

Die Hierarchieebenen der Mikrostruktur im Seeigelstachel der Art *Heterocentrotus mammillatus* lässt sich auf drei Skalen nach Presser et al. [22], [25] beschreiben:

- Die Nanometerskala, mit den leicht gedrehten Nanodomänen des dichten Kalzits eingebettet in einer dünnen organischen Matrix. Damit zeigt das Material des Seeigelstachels ein mesokristallines Verhalten, nach Presser [22], [25] (wie vorher schon diskutiert kann man es im makroskopischen Sinne als Einzelkristall betrachten).
- Die Mikrometerskala, das Stereom mit seiner offenporigen Struktur. Die Stege, die das poröse Stereom bilden, haben Durchmesser im Bereich von einigen µm und bilden Poren die deutlich unter einem mm im Durchmesser bleiben.
- Die Makroskala im Millimeterbereich, dort finden sich die Wachstumsringe oder Wachstumsschalen.

Einen Eindruck der Skalen gibt Abbildung 1-9.

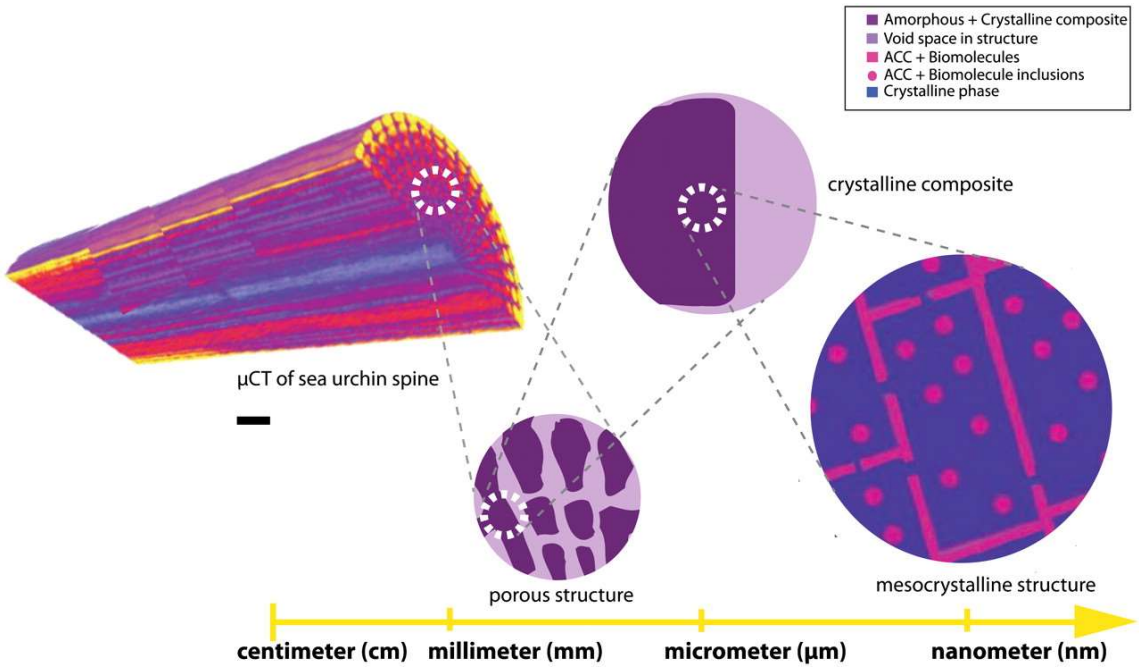

Abbildung 1-9: Multiskaligkeit bei Seeigelstacheln [29]

Diese Skalen und die detaillierte Mikrostruktur stellt die Modellgenerierung vor besondere Aufgaben. Mögliche Ansätze, die Strukturen auf unterschiedlichen Skalen anzugehen und so die Strukturen in FEM-Simulationen einzubringen und in simulierten Druckversuchen zu analysieren, werden im Kapitel 8 über den TRR141 vorgestellt (erste Ergebnisse der Simulationen der Druckversuche sind mit den Projektpartnern der Universität Freiburg (Prof. Speck und Mitarbeiter) und Universität Tübingen (Prof. Nickel und Mitarbeiter) in einer gemeinsamen Veröffentlichung vorgestellt worden) und werden im Kapitel 10 Seeigelstachel im Detail vorgestellt.

1.4 Multiskalensimulationen

Computergestützte Modellierung und Simulation ist nicht nur in der Materialwissenschaft weit verbreitet. Die Simulation ermöglicht eine günstige und vor allem schnelle Herangehensweise zur Lösung von unterschiedlichsten Problemstellungen. Deshalb werden Simulationen in vielen verschiedenen Bereichen, von der Produktentwicklung, über Crashverhalten bei Autos, in der Verhaltensforschung von Mensch und Tier und vielen mehr eingesetzt. Im Falle der Materialwissenschaft spielen die Strukturen und die Eigenschaften des Materials eine besondere Rolle.

In der vorliegenden Dissertation wird im Beispiel der Pomeloschale die Schaumstruktur der Schale simuliert. So lassen sich Analysen der Struktur auf Stabilität und Festigkeit durchführen, Anwendungen oder Versuche virtuell prüfen und das Materialverhalten sowie die Korrelation von Struktur und Eigenschaften bestimmen.

Um eine Simulation zu beginnen, muss zuerst die Skala festgelegt werden, auf der man modellieren will. Es gibt grundsätzlich vier Skalen, die in Abbildung 1-10 mit Beispielen unterlegt sind:

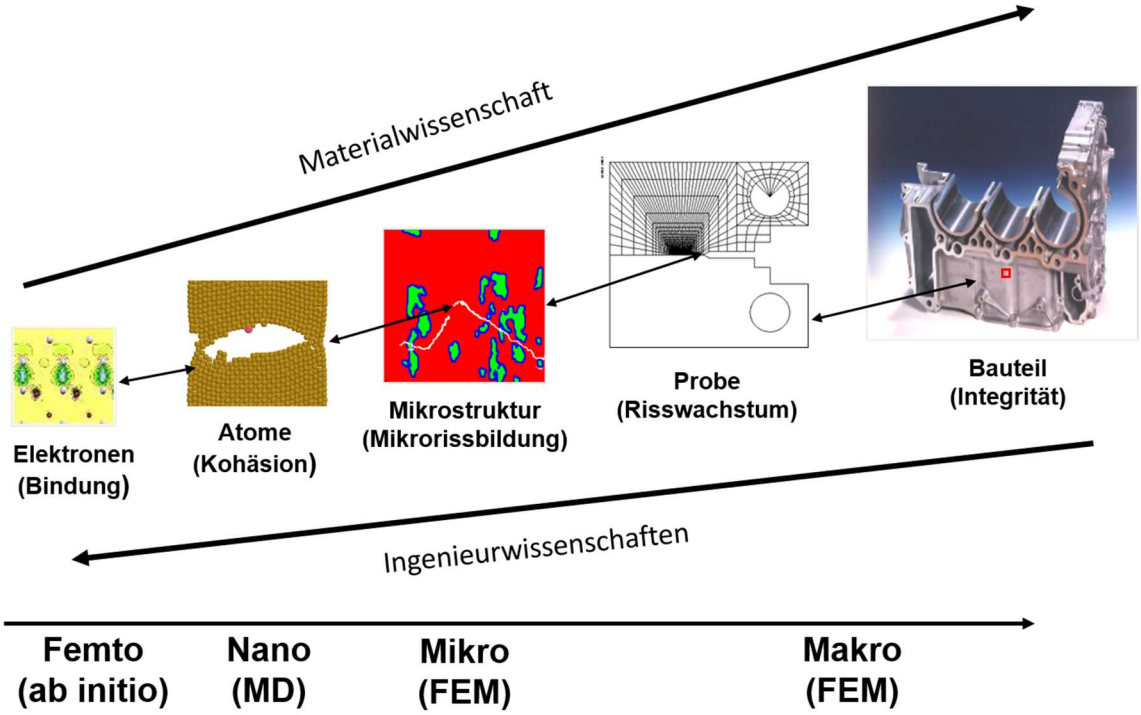

Abbildung 1-10: Multiskaligkeit aus der Sicht des Materialwissenschaft (bottom up approach) und der Sicht der Ingenieurwissenschaften (bottom down approach) nach [30]

1. Femtoskala: Die Bindungen der Elektronen werden hier untersucht. Eine Methode für diese Skala ist z. B. die ab initio Simulation.
2. Nanoskala: Sie behandelt Atome und deren Bindungen bzw. deren Bindungsenergien. Die Molekular-Dynamik(MD)-Simulation ist eine der verwendeten Methoden in diesem Größenbereich. Ein Beispiel wird in Kapitel 5 vorgestellt, dort wird die Konfiguration eines Peptids mit besonders hohen Bindungsaffinitäten zu Zinkoxid mithilfe von MD-Simulationen bestimmt.

3. Mikro(mechanische) Skala: Hier wird z. B. eine Einheitszelle betrachtet, mit hoher Detailtreue (eventuell auch im Nanometerbereich), also ein Materialausschnitt der Struktur, der viele Details (Verbindungen, Oberflächenbeschaffenheit z. B.) abbilden kann aber trotzdem noch gut mit der vorgegebenen Computerinfrastruktur berechnet werden kann. Die Simulationen können z. B. im Rahmen von Finite-Elemente(FE)-Simulationen durchgeführt werden.
4. Makro(mechanische-Skala): Hier ist das Gesamtmaterialverhalten zu betrachten d. h. der Einfluss der Details, die in den beiden kleineren Skalen untersucht wurden, wird im Verhalten des Makromodells sichtbar - aber die Details selbst werden nicht simuliert. [30, Ch. 0 and 1]

Die Bereiche zwischen den vorgestellten Skalen werden auch als Meso(-mechanische) Skala bezeichnet. Diese finden sich zwischen Nano- und Mikro- und zwischen Mikro- und Makroskala. Bei letzterer werden zum Beispiel Abschnitte mit Abmessungen mehrerer Einheitszellen simuliert. Der betrachtete Ausschnitt ist größer im Vergleich zur Mikroskala, erreicht aber nicht die Makroskala. Hier ist die Größe des strukturellen Elements im Fokus. Das heißt, es sind sogenannte verschmierte Eigenschaften zu verwenden, um das Verhalten des Schaumes abzubilden (lokale Eigenschaften oder Effekte werden lediglich im Mittel berücksichtigt). Zusätzlich sind die Randbedingungen teilweise kompliziert und umfangreich einzustellen, da sich im Gesamt-Zell-Verbund (d.h. im realen Vorbild mit sehr vielen Einzelzellen) andere Randbedingungen ergeben als im Mehrzellmodel (Mesoskala). [30, Ch. 0 and 1]

In der Materialwissenschaft, insbesondere für Metalle, werden seit kurzem Multiskalensimulationen eingesetzt, um die Ergebnisse der Molekulardynamik (MD) als Eingangsdaten für andere Simulationswerkzeuge wie die Finite-Elemente-Methode (FEM) oder die Phasenfeldmodellierung zu nutzen. Molnar et al. berichteten über Multiskalensimulationen zur Vergröberung von Cu-reichen Ausscheidungen in α-Fe mittels kinetischer Monte-Carlo-, Molekulardynamik- und Phasenfeldsimulationen [31]. Ähnliche Multiskalensimulationen wurden auch an Metall/Keramik-Materialien durchgeführt, bei denen der Bruch an der Metall/Keramik-Grenzfläche analysiert wurde [32]. In der vorliegenden Arbeit in Kapitel 5 wird eine Methode präsentiert, wie MD-Simulationen der Peptidbindung an eine keramische Oberfläche mit FEM-Simulationen kombinierbar sind. Die Kopplung von Molekulardynamiksimulationen an FE-Simulationen ist wichtig, um die Ergebnisse im Nano-

skalenbereich in die Simulation auf der Mikro- bzw. Makroskala zu überführen. MD-Simulationen wurden in der Vergangenheit erfolgreich eingesetzt, um atomistische Effekte im Nanobereich biologischer Moleküle zu untersuchen [33], [34], obwohl sie in der Regel auf Mikrosekunden-Zeitskalensimulationen für typische Systeme (10^5-10^6 Atome) beschränkt sind [35], während FEM-Simulationen im Rahmen der konventionellen Kontinuumsmechanik für das mikro- und makroskopische Materialverhalten verwendet werden [36]. Eine Kombination der beiden Simulationsmethoden und durch den Einbezug von Ergebnissen aus Nanoindentationsexperimenten und Rasterkraftmikroskop ermöglicht es, die mechanischen Eigenschaften von organisch-anorganischen Nanokompositen über mehrere Skalen vorherzusagen, wie in [37] gezeigt.

1.5 Simulation von zellulären Materialien / Schaum

Zellulare Materialien sind durch ihre geringe Dichte und ihrer Mikrostruktur charakterisiert. Deshalb beruht ihr Verhalten auch auf dem Verhalten der Stege oder Zellwände und natürlich dem Material, aus denen diese aufgebaut sind. Eine Simulation der mikromechanischen Eigenschaften lässt unter anderem Rückschlüsse auf die elastischen Eigenschaften des Materials zu. Durch verschiedene Belastungsfälle lassen sich an einem mikromechanischem Modell die unbekannten elastischen Konstanten wie den E-Modul oder die Poisson-Zahl bestimmen.

Um die effektiven Eigenschaften der zellulären Materialien auf der Makroebene beschreiben zu können, kann u. a. das Verhalten in der Mikroskala (also das Verhalten einzelner Stege z. B.) homogenisiert werden. Damit kann ein homogenisiertes Ersatzmaterial erstellt werden. Mit diesem Prozess des Homogenisierens wird die Anzahl der Freiheitsgrade des Models reduziert und damit die benötigte Rechenleistung deutlich verringert.

Weiterhin lassen sich somit auch Fließen und Knicken von Stegen im Schaum untersuchen. Dabei müssen für das makroskopische Verhalten bestimmte Materialmodelle benutzt werden, zum Beispiel das von Deshpande und Fleck [38] für Metalle. Dieses zeichnet sich dadurch aus, dass es eine Formänderung der Dehnungsoberfläche durch Differentialhärtung entlang der hydrostatischen und deviatorischen Achsen ermöglicht. Zur Generierung des Modells lassen sich auch CT-Bilder (oder auch Schnittbilder von Materialien) heranziehen. Damit lassen sich sehr detailgetreue Modelle erzeugen, welche aber hohe Rechenkapazitäten erfordern. Um die Anforderung an die Rechenleistung zu reduzieren, werden

Voxelmodelle herangezogen. Da diese Voxelmodelle die Strukturen immer noch verhältnismäßig gut erhalten (z. B. werden Kurven durch Geraden nur angenähert, aber die Porositäten bleiben vergleichbar), sind Berechnungen des E-Moduls von unterschiedlichen porösen Ausschnitten des Seeigelstereoms möglich (siehe Kapitel Seeigelstachel).

Einer der wichtigsten Schritte bei der Entwicklung einer von biologischen Materialien inspirierten Mikrostruktur ist die Analyse der Mikrostruktur des Vorbilds. Ein weiterer wichtiger Aspekt ist, dass die Simulation Einblicke in Struktur-Material-Beziehungen liefert, die über die Grenzen klassischer Experimente hinausgehen. So ist z. B. der Einfluss der unterschiedlichen Porengrößen oder der Mesostruktur wie die Kappen (vgl. Abbildung 1-8) nicht leicht von den Bulkmaterial- / Gefügeeigenschaften zu unterscheiden. Computertomographie(CT)-Bilder bilden die Grundlage für drei Arten von Modellerstellungstechniken. Da die Daten aus den CT-Scans enorm groß sind (pro Bild 4-5 MB, bei einem Stacheldurchmesser von ca. 2 cm bei ca. 1000 Bildern pro cm Höhe), ist ein Konzept für einen effizienten Umgang mit den Daten erforderlich. Die Eigenschaften der Zellwerkstoffe werden durch die sehr geringe Dichte und die poröse Mikrostrukturmorphologie definiert. Daher haben die die Poren definierenden Streben den größten Einfluss auf die Eigenschaften des gesamten Schaums. Wie in der Arbeit von Daxner (33) beschrieben, sind die Standardverfahren zur Analyse von Schaummikrostrukturen die folgenden:

Zuerst beschreibt er mehrzellige Modelle (eine Zelle umschließt eine Pore) einer kleinen Probe. Dies sind Modelle,

> *"die mit der verfügbaren Hard- und Software eine echte Schaumprobe möglichst genau darstellen. Ziel dieses Ansatzes ist es, das Verhalten einer tatsächlichen Schaumprobe unter realistischen Belastungsbedingungen vorherzusagen, die in den meisten Fällen einer einachsigen Verdichtung entsprechen" (33).*

Der Ansatz, der im ersten Abschnitte des Kapitel 10 über den Seeigelstachel genutzt wird, basiert auf hochauflösenden CT-Bildern, um hochdetaillierte Modelle ausgewählter Zellen bzw. Poren des Schaums zu erstellen und zu analysieren. Dies wird als direkter Modellierungsansatz bezeichnet. Damit kann ein Verständnis für die Einflüsse der Strukturelemente wie der Streben und der Porengröße erzeugt werden. Dies ist der direkteste Ansatz zur Erstellung eines Modells, aber auch der rechenintensivste. Die Analysemöglichkeit ist jedoch aufgrund der benötigten Rechenleistung begrenzt, da mit dieser Methode aufgrund

des enormen Rechenaufwands nur sehr kleine Ausschnitte der Struktur simuliert werden können.

Um diese Einschränkungen zu überwinden, wird in der zweiten Veröffentlichung zu dem Thema (Nummer IX) in Kapitel 10 ein Voxel-basiertes Modell verwendet. Dieser Ansatz basiert ebenfalls auf CT-Bildern, reduziert aber die zu verarbeitende Datenmenge erheblich. Die genaue Funktionsweise wird in Kapitel 10 beschrieben, grob gesagt wird eine Kurve mit Geraden nachgeführt und dadurch die Genauigkeit zwar reduziert, aber die Struktur (in diesem Fall die Porosität) bleibt erhalten.

Zweitens beschreibt Daxner die Verwendung von Einheitszellmodellen, die sich periodisch wiederholen. Mit solchen Modellen kann eine Studie über die Variationen der geometrischen Parameter durchgeführt werden. Auch der parametrisierte Ansatz wird in Veröffentlichung IX im letzten Kapitel verwendet, der mit der zweiten Methode von Daxner et al. [39] vergleichbar ist, bei der stark idealisierte Strukturen berücksichtigt und analysiert werden.

2 Fensterpflanze

Der folgende Aufsatz wurde aus den Ergebnissen meiner Masterthesis an der Fachhochschule Kärnten erstellt. Die Veröffentlichung entstand im Zusammenhang mit einem Konferenzbesuch im Rahmen meiner Anstellung als akademischer Mitarbeiter am IMWF und ist deshalb Teil dieser Dissertation.

Der Titel lautet:

I. Schäfer, Immanuel. (2013). Biomimetics in Energy Systems: Light Transmission in the Window Plant *Fenestraria aurantiaca* as Inspiration for New Solutions in the Technical World. Advances in Science and Technology, 84, pp. 51–56.

Die Veröffentlichung ist einem peer-reviewed Journal veröffentlicht worden und wurde von mir komplett selbständig erstellt.

Betreuer der Masterarbeit an der Fachhochschule Kärnten in Villach, Österreich waren Herr D.ID. Mag. Peter Piccottini und Herr Prof. Dr. rer. nat. Helmut Tributsch.

Biomimetics in energy systems: Light transmission in the window plant *Fenestraria aurantiaca* as inspiration for new solutions in the technical world

Immanuel Schäfer

IMWF, University of Stuttgart, Pfaffenwaldring 32, 70569 Stuttgart, Germany

ImmanuelSchaefer@gmx.de

Keywords: *biomimetics in energy systems; biomimicry; bionik; Fenestraria aurantiaca; window plant; energy; cooling; distribution; light transmission; photovoltaic; solar cells; transparent; mobile devices; displays; non-imaging optics; Winston collector*

Abstract

Fenestraria aurantiaca (also known as window plant) is a succulent with specialized adaptations to deal with heat, light and aridity. *Fenestraria aurantiaca* (F. a.) grows with most of its body under the sand. Just the top, with a light transparent surface – the window – on it, protrudes from the surface hence giving explanation to the plants name. Experiments with light, and detailed microscopy studies show the physical, biological and chemical capabilities of F. a. It was found that the window works as a lens, light from a 90 ° angle is directed into the plant. Thereby the window filters the light. Up to 90 % of the visible light is blocked; with rising wavelength the window gets more transparent until the near infrared light (1000 nm) where the transparency declines rapidly. But the parenchyma is up to 90 % transparent. Based on those results the principles of the plant were defined, which are used for abstractions. Generally F. a. has four principles: light handling, surface cleaning, heat avoidance and water storing. Improvements founded on the inspiration of the window plant seem to be possible in photovoltaic systems, which have problems with overheating and also light concentration. An example solution called “buried solar cells” is presented. Another working field is the screen of mobile devices, where the clarity and readability suffers from direct sunlight. With the help from the methods displayed by F .a., there is an energy saving solution explained.

2.1 Introduction

Fenestraria aurantiaca is a succulent from the Namib-Desert (Africa). The climate is very arid; with rainfall less than 100 mm per year combined with the heat that is generated by the sun. This makes the plant an ideal object for biomimetic studies; life in extreme environments commonly demonstrates special features that are interesting for abstractions in technology. F. a. grows with most of its round shaped, four centimeters long and one centimeter thick body under the sand. Just the top, with a light transparent surface – the window – on it, protrudes from the surface. This has many advantages: the surface which could collect heat is reduced; the sand around the plant cools it down, works as buffer and also helps against feeding damage. But a plant needs light to grow: F. a. is able to collect, filter and distribute the light to the photosynthetically active cells on the side of the walls of its body. The light collection feature of the plant works like a Winston collector or a non-imaging optic. The features of the plant were examined in the authors master thesis (written at the Carinthia University of Applied Sciences, AT), this paper introduces the reader the most important results.

2.2 Experimental Methods

Different methods were used to examine the features of F. a. A spectral analyzer (Nicolet evolution 100, Thermo Fisher Scientific Inc., Waltham, MA 02454 USA) was used for transparent measurements and wavelengths from 300 µm to 1000 µm were analyzed. For the laser experiments, a red laser pointer (LASERPOINTER "SCHLÜSSELANHÄNGER", ROT, Co. Conrad electronic SE, Hirschau, Germany) was used. The images where then recorded via the light microscope or a digital camera (Digital IXUS 80 IS, Canon Inc, Tokio, Japan). Methyl blue dyeing was made with

0.2 g methyl blue in 7000 µl 100 %Ethanol added 10000 µl H2O. The probes where then colored for 5 min. in the methyl blue dilution and then cleaned with ethanol as well as water.

2.3 Results and Discussion

Selected results from the master thesis are presented here.

Methyl Blue Dyeing: Methyl blue colors cell walls; the transparent tissue inside the leaf is then more visible because of the higher contrast. Figure 1 A shows a vertical cross-section

of a leaf where the chlorenchyma on the sides and the transparent window on the top are visible. The inner part of the leaf is nearly transparent and the stained cell walls are visible.

Experiments with Laser

These experiments involved a standard laser pointer. In Figure 1 B a part of a leaf is put into the opening of the laser pointer, the light illuminates the leaf from beyond and the whole parenchyma gets illuminated in red light. Transparent openings on the outer side of the leaf are also existent (not shown), most likely stomata. In Figure 1 C a vertically cut of a leaf was illuminated with the laser on the window with a nearly 90° degree angle. The leaf is capable to direct the light to the base.

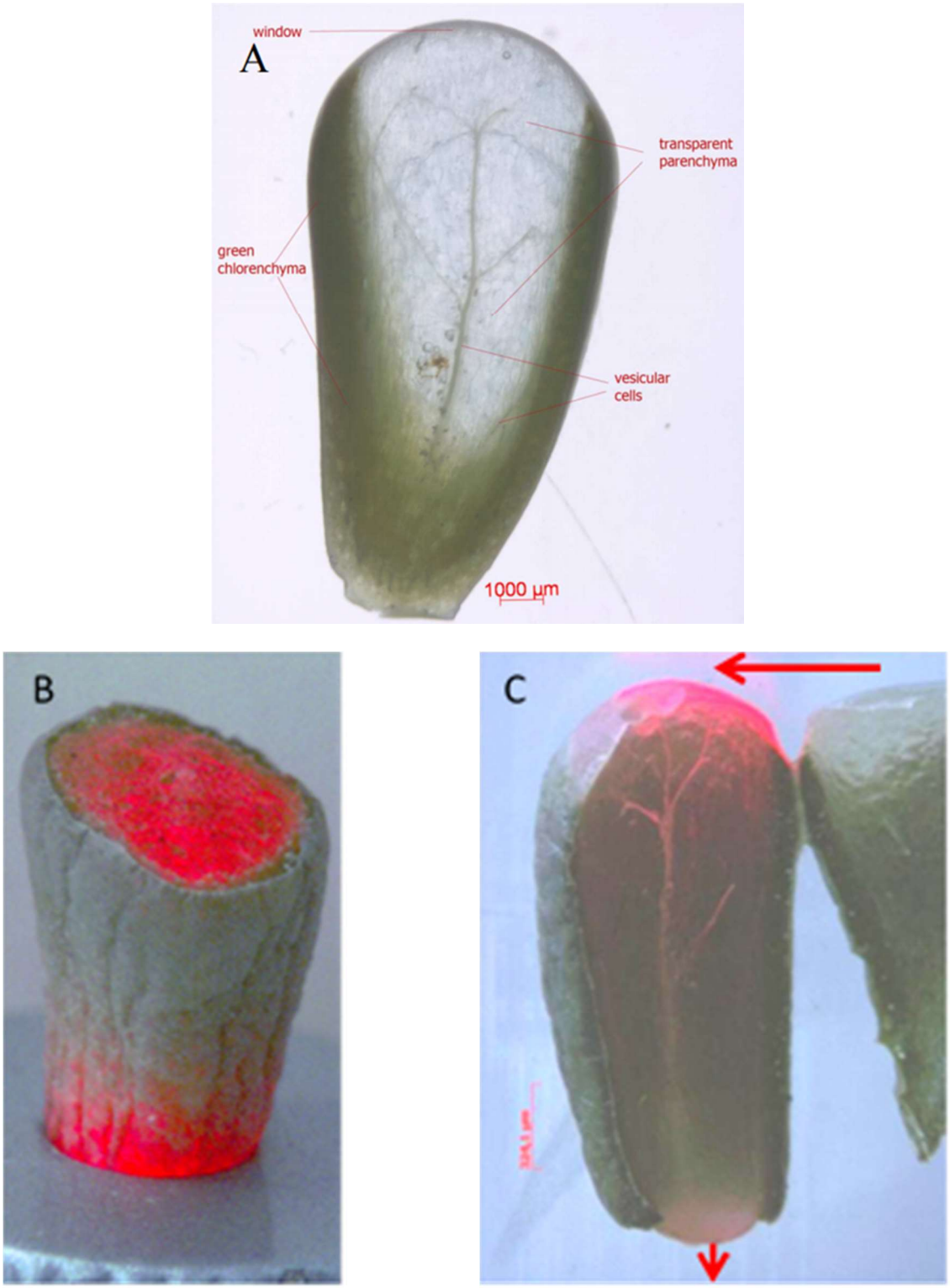

Figure 2-1: Methyl blue dyeing and laser experiments results

Vertical cross-section of a leaf, methyl blue dyed (A). The parenchyma on the sides and the window on the top are visible. The leaf is nearly transparent inside. The sample was ca. 0.8 cm long. B shows a leaf that was horizontally cut and illuminated with the laser beam from

beyond. The laser beam illuminates the whole parenchyma. In C a leaf was vertically cut and then illuminated by the laser from a 90 ° degree angle on the window. The light gets directed to the base (see arrows).

2.3.1 Results of the Spectrometer Analysis

One leaf was cut in 2-3 mm thick slices and measured in the spectrometer (see Fig. 2). The window strongly filters the light and the following 4 mm to 8 mm are far more transparent. It seems that there are preferred wavelengths and that with higher wavelengths, the intensity gets higher. The first four parts are showing a transparency up to 85 % at 950 nm wavelength. The window only has a transparency of up to 20 %. The parts after part four are as transparent as the window.

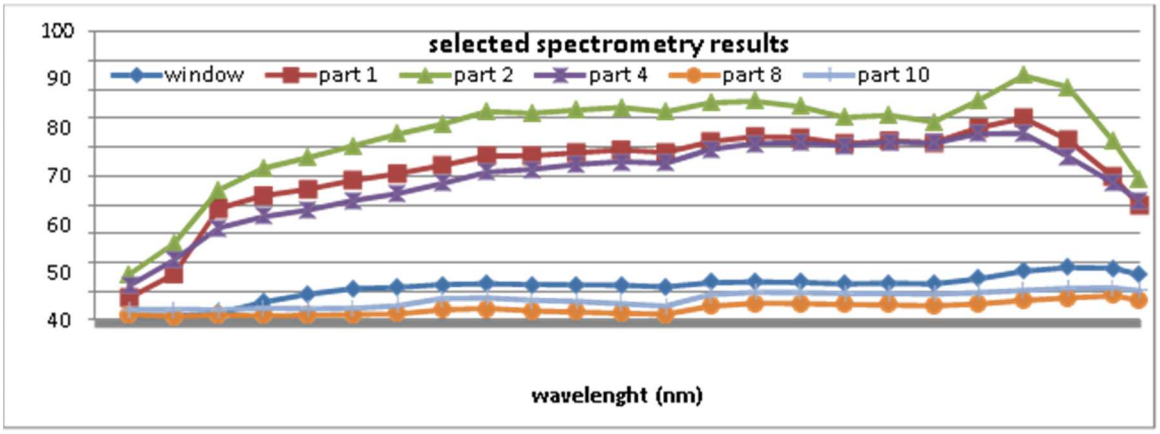

Figure 2-2: Selected spectrometry results

13 parts of a long leaf were measured in the spectrometer (not all results shown here for better readability). The first four parts are showing a transparency up to 85 % at 950 nm wavelength. The window has only a transparency of up to 20 %. The parts after part four are as transparent as the window. The cuts were between 2-3 mm thick.

2.3.2 Principles of *Fenestraria aurantiaca*

The following principles were defined based on the results of the experiments.

Table 2.1: Principles of light processing

principles	function	part	abstraction
collection	light gets collected from a big angle	window	lens
filter	filters intensity and special wavelengths	window parenchyma	filter system
guide	transportation of the light into the leaf	parenchyma	optical fiber
distribution	light gets scattered and distributed	parenchyma and cell walls	scattering system

Table 2.2: Principles of heat processing

principles	function	part	abstraction
thermal conductive	soil absorb heat	whole outer surface	heat exchanger
filter	filters infrared light	window and parenchyma	infrared filter system
small surface	reduced attack area	window/leaf	minimize contact area

2.3.3 Possible Biomimetic Applications

Many products that process light have problems with generated heat or with filtering of specific wavelengths. Also the distribution of light is a difficult working field. For these problems, the plant is an inspiration and the principles and combinations thereof can help to improve existing solutions or to generate new systems of (solar-) light handling.

Improvements of Solar Cell Systems

Concentrators on solar cells are not standard, but there exist prototypes. It is shown in a work of Pelosi [1] concentrators can maximize the output and that it is much cheaper to produce lenses for surface than to create bigger solar cells. One example of a solar cell with concentrator optics, the SolFocus 1100S Systems, uses non-imaging optics like the window

plant [2] and it only needs 1/1000th of solar cell material compared to traditional photovoltaic cell systems. Problems exist with overheating, because PV-cells loose much of their efficiency if they overheat (a temperature increase of 1 K leads to a decrease of the open circuit voltage by 0.3-0.4 % [3, 4], which lowers the conversion output. To combine all principles of the window plant (see Table 1 & 2) together in one solar-ray collecting and converting system, the concept of buried solar-cells is developed (Fig. 3). Two standard sized photovoltaic (PV) cells (100-160 cm × 100 cm) are laid on the outer walls of a V-shaped channel. On top of this, a lens-like light collecting system will concentrate the light and scattering material beyond it will distribute the light evenly to the solar cells. The basic concept is shown in Figure 3 (V.1). The angle of the V is defined through the lens or the scattering material and needs to be adapted to the optical properties of the material. A good compromise would be 45° that would leave enough space between the PV-cells for optical systems but would save space compared to a flat solar panel. The lens system has to fulfill the following functions: focus, filter and concentrate the light, remain clean and stable (physically and chemically) and whilst still being affordable.

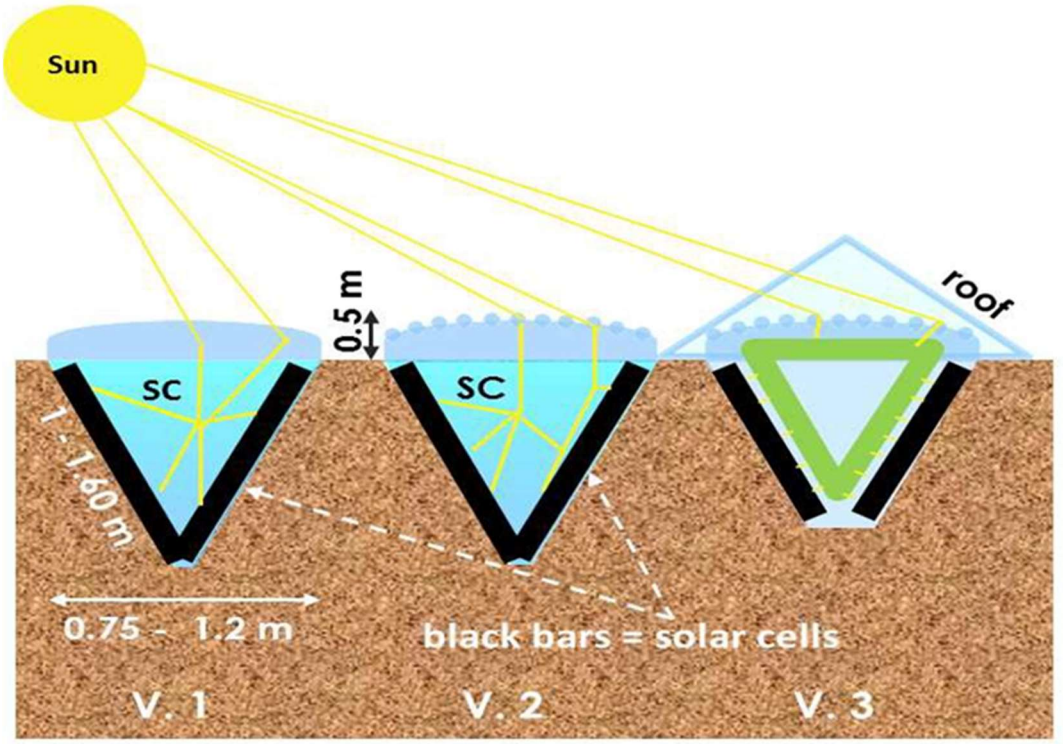

Figure 2-3: Three versions of the buried solar cell system

The first one (V.1) has a big lens that concentrates the light. The light will then be scattered inside the V-shaped space. Scattering systems (SC) could consist of water or prisms. Version 2 has many small lenses instead of the big lens, the micro optic system. The light gets collected and concentrated and then coupled into the scattering system or a wave guide (the upper horizontal part of the green triangle in V.3). The waveguide consists of a lens array and slab waveguide. At the focus of each lens, 120° mirrored prisms couple light into the waveguide. To distribute the light onto the solar cells, the light gets than directed into a system of optical lightning film and extraction foil (the V-part of the green triangle). V.3 has also a transparent roof on top, to improve maintenance and setup. To avoid problems through pollution and to reinforce abrasion resistance of the lens-system, a surface-structure like the sandfish or the lotus plant has (depending on the geographic location of the system) is applied. This should solve the problem of cleaning them on a daily basis. An optimization of the concept of the single big lens (version 1) in Figure 3 is version 2 (and version 3 which has a wave channel and a roof on top) with many small lenses instead of only one. These small lenses could be like the one described in the article "A micro-optics solar concentrator" [5] where an array of micro lenses focuses onto localized mirrors. These are arranged to reflect light at angles that exceed the critical angle for total internal reflection and couple the now homogenized light into the scattering system (version 2) or in the waveguide like in version 3. Karp and Ford could show in simulations that with this system light can reach the solar cells with 89 % (on the basis of an optimized system). Compared to Fresnel-lens concentrators this is an enhancement of up to 11 %. A prototype showed an optical efficiency of 32.43 %. If the lens system is arranged in a dome-like shape, it could collect sun light passively all day and all season long. This shape has also the advantage that on the top exist higher wind velocities which helps to remove dirt particles. This is most probably also the function of the club-shaped leaf of F. a. The scattering system could consist of prisms, capillary systems or even water with metal particles inside. Water would also filter the light, (discussed in the literature [6], these systems reached a noticeable improvement in the photovoltaic parameters of the module with it) it would then provide the filtering and scattering of the light. If water is not usable as scattering system, foils called optical lightning film, from 3M [7] could be used because they have perfect properties for light distribution: the structure reflects light (coefficient of reflection of 98 %), but allows transmission if the angle of incoming light is higher than 27.6 degrees.

Illumination Systems for Displays

Other application possibilities of the principles (see Table 1 & 2) of the window plant exist in illumination systems of displays. Modern televisions, mobile phones and cameras have displays that are illuminated from behind with electrical light. If the light intensity is not sufficient, e.g. during the day, glaring on the displays occurs. This is mostly annoying with mobile devices which are often used outside. One solution is to get higher light intensity with the help of electricity, which leads to higher energy demand. A better answer would be not to fight the sun, but to take the power and use it for our profit. A small lens-stripe (or a single lens or Winston cones) around the display could collect the light and reinforce the brightness when needed (see Fig. 4). A few lenses or Winston cones should be enough to illuminate a relatively big touchscreen display (3.5 inch) because of the high concentration properties Fresnel lenses can have. (Concentration ratios of up to 500 × with Fresnel lenses [8] and up to 650 × with Winston cones [2] can be achieved. The collected light from the sun has to be coupled into optical fibers which then transfer the light to the backlight foil (additional to the LEDs). In comparison to solutions like the iMoD-display (which uses the sunlight directly to produce colors like the structure on butterfly-wings, [9]) the concept presented here is complementing the existing technology which does not change the production of the display itself. If not all sun light is needed to illuminate the display, the light that is left over could be used to generate electrical energy.

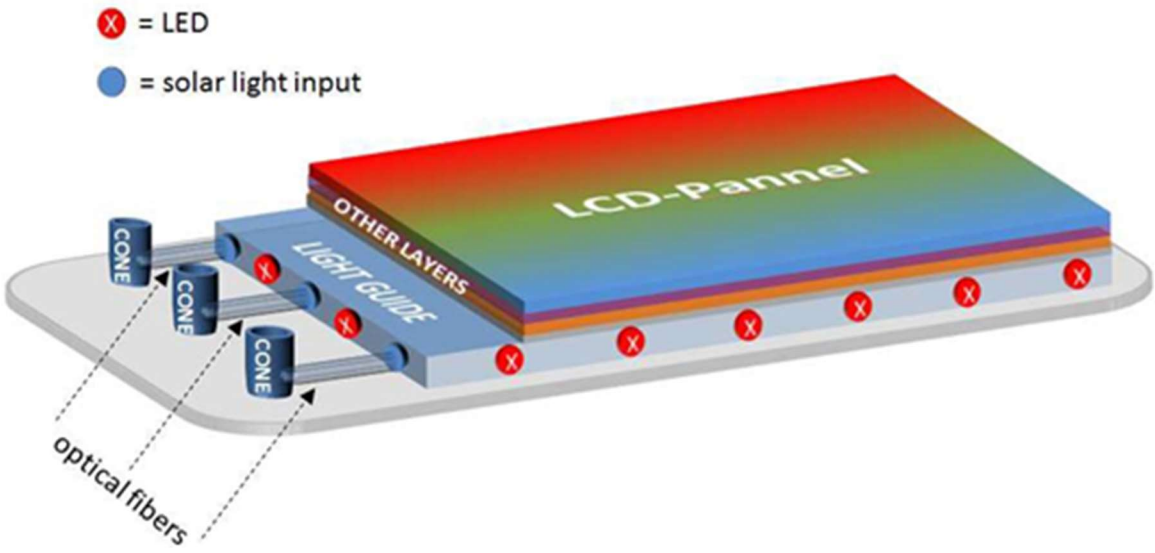

Figure 2-4: Light collecting system for displays

The blue cones or lenses are situated in the monitor bezel (not shown) of the display and collect the light, which then gets guided through the optical fibers into the light guide. Without surrounding light, only the LED-illumination is used.

2.4 Summary

Fenestraria aurantiaca proved to have astonishing capabilities and the principles which assist these features may well be used in state-of-the-art technology. The light microscopy images delivered new insights of the plant structure. The spectrometer experiments exposed the filter capabilities of the window and the parenchyma. The window is a strong filter (up to 90 % of the visible light gets blocked) that helps the plant to survive in its hard environment. In addition it works as a lens; a good supply with light during the day is assured. The water rich cells in the parenchyma filter the light but are much more transparent (up to 90 %) and distribute it. The parenchyma has then three main functions: store water, distribute light and filter infrared rays (with the help of water). The plant stays clean, because the shape prevents sand particles from staying on the surface. With these results, four main principles the plant uses could be defined: light handling, surface cleaning, heat avoidance and water storing. On these principles, three abstractions were made. Improvements founded on the inspiration of the window plant seem to be possible in photovoltaic systems, which have problems with overheating and also light concentration. The buried solar cells implement all principles of the window plant and can avoid most of the problems that conventional PV-cells have to deal with. The principle of light collecting and transferring combined with mobile displays lead to the idea to illuminate the display indirect with solar light but without conversion into electrical energy. Displays are then better readable in sunlight without stressing the batteries. The next steps are now to transfer these abstractions into real biomimetic prototypes. This would reveal the usability of the presented materials and solutions. Future work should concentrate on the chemical structure of the window and the parenchyma as this could lead to new information about the scattering system of the plant. The distribution to the chlorenchyma is one of the most interesting questions. Simulation with the physical values of cell walls, cells and organelles could help to investigate the physics behind.

2.5 References

[1] C. Pelosi, “Light concentration increases solar-cell efficiency and reduces cost,” SPIE Newsroom, 2007.

[2] SolFocus Inc., “SolFocus Technology,” 2011. [Online]. Available: http://www.solfocus.com/en/technology. [Accessed: 09-Aug-2011].

[3] P. Würfel, Physics of solar cells. Wiley - VCH Verlag GmbH &Co. KGaA, 2005.

[4] T. Bührke and R. Wengenmayr, Erneuerbare Energie: Alternative Energiekonzepte für die Zukunft, 2. ed. Wiley-VCH Verlag GmbH & Co. KGaA, 2009.

[5] J. Karp and J. E. Ford, “A micro-optic solar concentrator,” SPIE Newsroom, vol. 17, no. 5, pp. 320-326, Aug. 2010.

[6] E. Custodio, L. Acosta, P. . Sebastian, and J. Campos, “A better solar module performance obtained by employing an infrared water filter,” Solar Energy Materials and Solar Cells, vol. 70, no. 3, pp. 395-399, Dec. 2001.

[7] 3M Innovation, “3M Optical Lighting Film Typ 2301.” [Online]. Available: http://www.starlight-sl.de/mb/3M_Lighting_Films/OLF2301_neu.pdf. [Accessed: 31-Aug- 2011].

[8] Green Rhino Energy Ltd., “Concentrating Photovoltaics (CPV),” 2010. [Online]. Available: http://www.greenrhinoenergy.com/solar/technologies/pv_concentration.php. [Accessed: 01- Sep-2011].

[9] QUALCOMM MEMS Technologies, “iMoDTM Technology - a revolution in displays,” 2006. [Online]. Available: http://www.qualcomm.cn/common/documents/white_papers/iMoD_Display_Overview.pdf. [Accessed: 15-Aug-2011].

3 Perlmutt 1

In den ersten Veröffentlichungen, die aus dem Perlmutt-Projekt entstanden sind, steht die Analyse der Nanoindentationsergebnisse des Komposit-Materials im Vordergrund. Das Kompositmaterial wurde von den Partnern im Projekt hergestellt.

Zuerst folgt die Veröffentlichung:

II. Lasko, G., Schäfer, I., Burghard, Ž., Bill, J., Schmauder, S., Weber, U., & Galler, D. (2013). Derivation of the Stress-Strain Behavior of the constituents of Bio-Inspired Layered TiO_2/PE-Nanocomposites by Inverse Modeling Based on FE-Simulations of Nanoindentation Test. Molecular & Celullar Biomechanics, 10(1), pp. 27–42.

Der Anteil meiner Arbeit an der Veröffentlichung umfasst:

- Konzeptualisierung, Erstellung des Manuskripts, mit Frau Dr. G. Lasko (Anteil meiner Arbeit 75 %)
- Erstellung der Diagramme und Abbildungen (Anteil meiner Arbeit 100 %)
- Erstellung und Durchführung der Simulation der Nanoindentation mit unterschiedlichen Parametern. Formale Analyse, Untersuchung, Datenkuration, Validierung. (Anteil meiner Arbeit 100 %)
- Diskussion der Ergebnisse und Optimierung der Simulation in Zusammenarbeit mit den Mitautoren (Anteil meiner Arbeit 60 %)

Derivation of the stress-strain behavior of bio-inspired layered TiO_2/PE-nanocomposites by inverse modeling based on FE-simulations of nanoindentation test

G. Lasko[1], I. Schäfer[1], Z. Burghard[2], J. Bill[2], S. Schmauder[1], U. Weber[1]

[1]Institute for Materials Testing, Materials Science and Strength of Materials, University of Stuttgart, Pfaffenwaldring 32, D 70569, Stuttgart, Germany

E-mail: galina.lasko@imwf.uni-stuttgart.de

[2]Institute of Materials Science, University of Stuttgart, Heisenbergstrasse 3, D 70569 Stuttgart, Germany

Abstract

Owing to the apparent simple morphology and peculiar properties, nacre, an iridescent-layer, coating of the inner part of mollusk shells, has attracted considerable attention of biologists, material scientists and engineers. The basic structural motif in nacre is the assembly of oriented plate-like aragonite crystals with a 'brick' ($CaCO_3$ crystals) and 'mortar' (macromolecular components like proteins) organization. Many scientific researchers recognize that such structures are associated with the excellent mechanical properties of nacre and biomimetic strategies have been proposed to produce new layered nanocomposites. During the past years, increasing efforts have been devoted towards exploiting nacre's structural design principle in the synthesis of novel nanocomposites. However, the direct transfer of nacre's architecture to an artificial inorganic material has not been achieved yet. In the present contribution we report on laminated architecture, composed of the inorganic oxide (TiO_2) and organic polyelectrolyte (PE) layers which fulfill this task.

To get a better insight and understanding concerning the mechanical behaviour of bio-inspired layered materials consisting of oxide ceramics and organic layers, the elastic-plastic properties of titanium dioxide and organic polyelectrolyte phase are determined via FE-modeling of the nanoindentation process. With the use of inverse modeling and based on numerical models which are applied on the microscopic scale, the material properties of the constituents are derived.

Keywords: *Nanoindentation, stress-strain constitutive law, inverse modeling, biomimetics*

3.1 Introduction

Biomaterials are perfect models for specialized materials that can reveal amazing combinations of mechanical properties. Some of their properties such as stiffness, hardness and fracture toughness are hardly attained by artificial materials (1). Nacre, which is the inner layer of mollusk shells, shows a high performance. Also it is build out of relatively weak components. Based on this prototype, new materials can be developed which are stiff but also have high fracture toughness. One example of the bio-inspired synthesis route to inorganic layers is the chemical bath deposition technique (CBM) (2). Combined with the layer-by-layer technique it was possible to create Titandioxid (TiO_2) / Polyelectrolyte (PE) multilayered films with a nacre-like architecture (3). The chemical bath deposition method operates at low temperatures (30–100°C), similar to the biomineralization process that occurs in natural organic–inorganic nanocomposites. One of the main problems is that the constitutive properties of the components of the nanocomposite are almost unknown. For the macroscopic objects there exists the possibility of verification of the constitutive behavior of the constituents by comparison of the stress-strain curves obtained by inverse modeling with the experimentally obtained ones. When performing an analysis of the thin coatings, the performance of experimental tests is difficult or even impossible and here a simple and easy method to define the mechanical properties is the nanoindentation technique. Nanoindentation testing was carried out with a scanning nanoindenter including a depth-sensing force transducer (Hysitron TriboScope), combined with a commercial scanning probe microscope (NanoScope III Multimode, Digital Instruments). Indentations were made with a cube corner diamond indenter with a nominal tip radius of ~40 nm. In all experiments, a maximum force of 80 μN was applied, which yields a penetration depth of about 100 nm. In the present work, we report on the computer simulation of mechanical properties of the components of this nanocomposite film, composed of alternating layers of TiO_2 as inorganic component and PE as the organic component. The stress-strain behavior of separate phases of the nanostructured layered TiO_2/PE nanocomposite are analyzed, and have been inversely obtained by numerical modeling with the finite element (FE) Method of nanoindentation test of separate phases of the TiO_2/PE nanocomposite. For the first time, the stress-strain curves of the constituents of the bio-inspired TiO_2/PE layered nanocomposite have been determined by coupling the results of the experiments with the FE simulations of nanoindentation.

3.2 Definition of Young's modulus from nanoindentation tests

Based on the indentation load-displacement data, mechanical properties such as hardness and Young's modulus of the solid-supported film can be determined. In experiments (2, 3) a cube corner indenter has been used instead of the usually used Berkovich indenter. Moreover, the cube corner indenter is sufficiently sharp (tip radius ~40 nm) to allow scanning of the surface in order to identify positions that are flat enough for indentation (Figure 1a). In addition, it enables creating plastic deformation within small indentation depths, which ensures remaining within the plastic and elastic field of the film, and minimizing the impact of the substrate which is crucial for investigating very thin films. In all experiments, initially a standard calibration of the tip was carried out on fused quartz within the penetration depth range of 3 to 100 nm. This procedure yielded for the hardness H = 9.3 GPa ± 0.3 and the Young's modulus E = 69.5 ± 1.67 GPa. In general, nanoindentation data obtained at shallow penetration depths are affected by the surface roughness of the sample, and the substrate has a noticeable influence for indentation depths larger than 20 % of the total film thickness (4). Thus, in order to take these limitations into account, the nanoindentation data were evaluated in the contact depth range between 10 % and 20 % of the total film thickness. The obtained data were evaluated using the method described by Oliver and Pharr (4).

The indentation force was varied during subsequent load/partial unload-cycles over 25 steps, with automatic recording of the indentation depth after each step. For each specimen, the results were averaged over fifteen indentations made at different locations.

According to Oliver and Pharr (4), the hardness H of the tested material is given as the maximal applied load Pmax (read from the load-displacement curve) divided by the projected contact area of the indentation at this load Ac:

$$H = \frac{P_{\max}}{A_c}. \qquad [1]$$

The contact area A_c is considered as an area function of the contact depth h_c:

$$A_c = F(h_c) = C_0 h_c^{\,2} + C_1 h_c + C_2 h_c^{\,1/2} + C_3 h_c^{\,1/4} + C_4 h_c^{\,1/8} + C_5 h_c^{\,1/16}, \qquad [2]$$

where C_0 is 2.598 for a cube corner probe, C_i (i = 1-5) are positive coefficients, F is the force and the contact depth h_c is given by the equation:

$$h_c = h_{\max} - \varepsilon \cdot \frac{P_{\max}}{S}. \qquad [3]$$

The latter term describes the deflection of the surface at the contact parameter. The geometric constant ε is founded on the geometry of the indenter tip ($\varepsilon = 0.75$) and the initial unloading contact stiffness S. S is the slope of the upper portion of the unloading curve during the initial stage of unloading and is defined as following equation:

$$S = \frac{dP}{dh}. \qquad [4]$$

The reduced elastic modulus E_r can be calculated from the contact area A_c and the unloading contact stiffness S as follows:

$$E_r = \frac{\sqrt{\pi}}{2\sqrt{A_c}} \cdot S \cdot \qquad [5]$$

The reduced elastic modulus E_r is defined by the Young's modulus of the sample E_s:

$$\frac{1}{E_r} = \frac{\left(1-\upsilon_i^2\right)}{E_i} + \frac{\left(1-\upsilon_s^2\right)}{E_s}. \qquad [6]$$

The symbols ν and E denote the Poisson's ratio and Young's modulus for the sample with subscript s and the indenter material with subscript i. In the experiments, the nanoindenter consists out of diamond with E_i = 1141 GPa and ν_I = 0.07.

According to the procedure described above the Young's modulus of pure titanium dioxide and polyelectrolyte have been obtained from nanoindentation. The averaged Young's modulus of over 50 indents in cross sections as well as the surface for the different indentation depth have been obtained and are equal to 27 GPa for TiO_2, and 5 GPa for PE.

3.3 Finite element modeling of nanoindentation

Limited studies are available to obtain the plastic properties with the nanoindentation technique. Therefore, the indentation loading process is simulated with the Finite Element Method (FEM) and the software ABAQUS/CAE (Version 6.11-1, Dassault Systemes Simulia Corp., Providence, RI, USA), assuming finite deformation characteristics. Instrumented indentation using a conical indenter (shown in Fig. 1a) has been simulated assuming axisymmetric and frictionless contact. For the simulation of deformation response of

the pure titanium dioxide layer and the pure PE layer 80000 four-node axisymmetrical elements (CAX4) were used.

The model of the indenter used in the present simulations has a conical shape with a tip-radius of 40 nm and a semi vertical angle of 40.3° which gives the same area to depth function as that of a cube-corner indenter, used in the experiment. Since large deformation takes place near the indenter tip, mesh refinement was accomplished near the contact zone. The conical indenter was modeled by the use of an analytical rigid surface. Symmetry boundary conditions were applied to the cut faces of the quadrant while the remaining edges were unconstrained in the modeling of indentation by a conical indenter. In the case of indentation of the conical indenter the nodes along the axis of rotation were free to move only along the Y-axis (Fig. 1b).

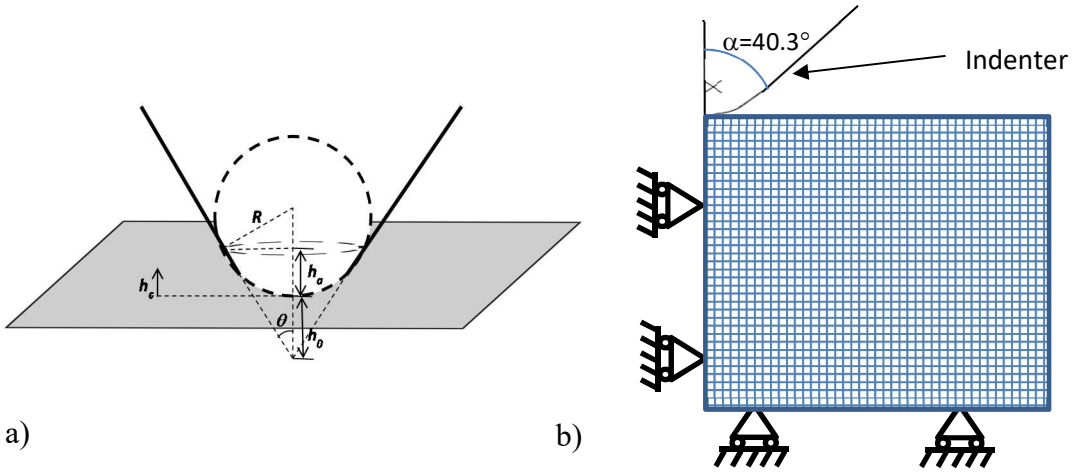

Figure 3-1: a) The sketch of the tip radius geometry of the used intender in the FE-simulation; b) model with boundary conditions

By applying a downward displacement to the rigid body reference node of the indenter the indentation process was simulated. The indentation depth was measured from the displacement of the node, situated directly under the indenter tip, i. e. at the point of first contact and the indentation load for the conical indenter was the reaction force of the reference node of the rigid indenter.

The friction between the material and indenter does not require special consideration and can be omitted in the inverse analysis (5).

For the definition of the plastic properties of the constituent phases (TiO_2 and PE) the method of inverse modeling has been applied in two steps:

At first, the stress-strain curve for pure titanium dioxide has been obtained by comparing the P-h curve obtained from the FE-calculations with the experimentally obtained one for pure titanium dioxide. The second step was to follow the same procedure for the stress-strain curve of polyelectrolyte.

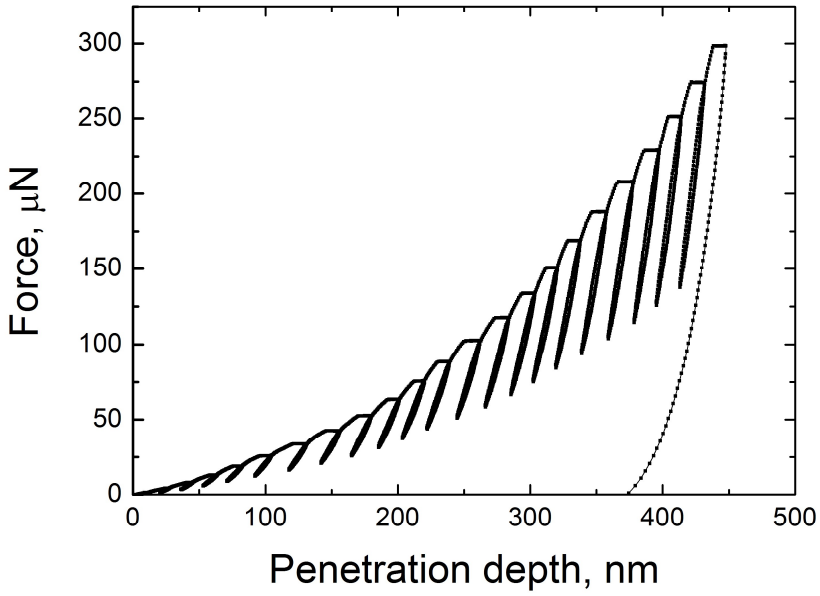

Figure 3-2: The experimentally obtained force-penetration depth-curve for TiO_2-from nanoindentation

Shown in Fig. 2 is the force-penetration curve that has been obtained in the experiment. Nanoindentation tests have been performed till the penetration depth being equal to 120 nm following the procedure loading-unloading, the maximum force attained in the experiment was around 80 μN and the penetration depth around 120 nm. The material is supposed to be homogeneous, isotropic and elasto-plastic using the classical plasticity model with von Mises criterion.

3.4 Basic constitutive laws used for definition of stress-strain behaviour of material via inverse modeling

There exist several models used in inverse modeling of the constitutive behavior: Hollomon's model (6), Ramberg-Osgood (7) and bilinear material models (8).

The Hollomon's model defines the power law relationship between the stress of the material and the value of plastic strain:

$$\sigma = \sigma_y + K * \varepsilon_p^n. \quad [7]$$

where σ_y is the flow stress, K is the hardening coefficient, ε_p is the plastic strain and n is the strain hardening exponent.

The advantage of using the simple Hollomon relationship (6) is the necessity of determining two unknown parameters, what is essential for keeping the costs of computational testing of the proposed inverse methods low.

The Ramsberg-Osgood model (7): it describes the non-linear relationship between strain and stress, which is normally defined by a stress-strain curve resulting from an experiment. The following equation defines the strain:

$$\varepsilon = \frac{\sigma}{E} + \alpha\left(\frac{\sigma}{\sigma_0}\right)^{n-1}\frac{\sigma}{E} \quad [8]$$

where ε is the strain, σ_0 is the yield stress, α and n are fitting parameters.

The last model used here is the bilinear model (8). A bilinear constitutive law (relationship between the true stress and the true strain) is defined by the elastic modulus E, the yield stress σ_y and the work hardening rate β.

The model is expressed by the following equations for the stress σ_i:

$$\sigma_i = E\varepsilon_i \;\; if \;\; \sigma_i \geq \sigma_y \quad [9]$$

$$\sigma_i = \sigma_y + \beta\left(E\varepsilon_i - \sigma_y\right) if \;\; \sigma_i < \sigma_y \quad [10]$$

with $0 \leq \beta \leq 1$; $\beta = 1$ for ideal elastic materials, $\beta = 0$ for ideal plastic materials.

3.5 Modeling the titanium dioxide elasto-plastic behavior

Shown in Fig. 3 are the contour plots of von Mises stress at different instances of indenter penetration into the pure titanium dioxide layer. Fig. 3c matches the penetration depth being equal to 50 nm, and Fig. 3e shows the stress state after withdrawal of the indenter from the material. After withdrawal of the indenter the material did not return to the initial shape of the specimen, but the indenter leaves an imprint on the surface of the specimen, indicating that plastic deformation occurs during testing, as confirmed by experimental observations.

The indentation depth was limited to 50 nm which represents 10 % of the size of the model. After 10 % indentation depth the substrate will influence the results.

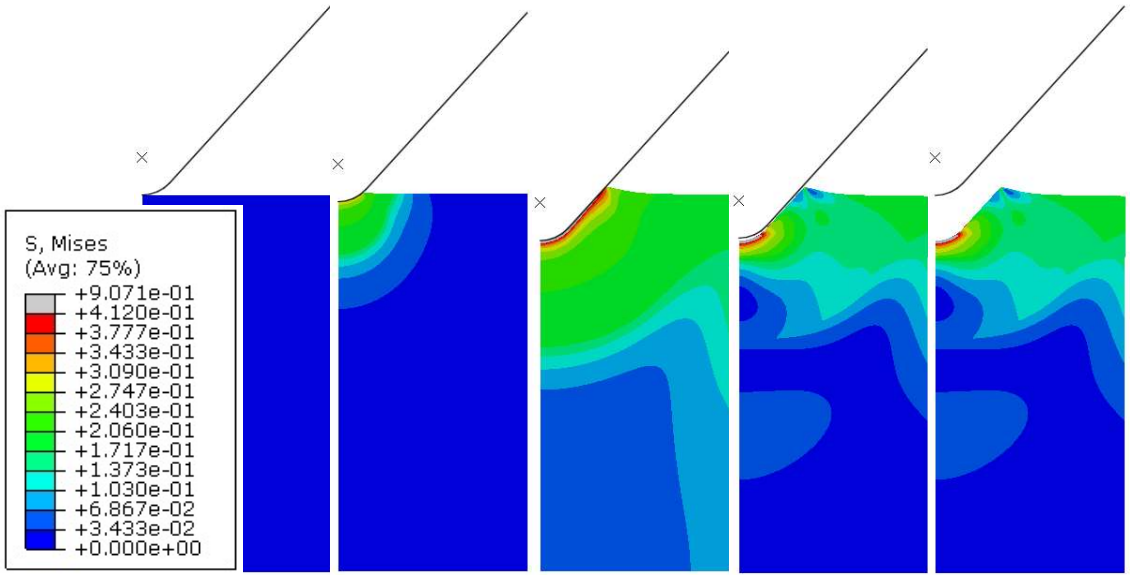

Figure 3-3: Contour plots of von Mises stress obtained as a result of the FE-simulations of the nanoindentation test of a TiO_2 single layer at different instants of the penetration depth: a) beginning of the nanoindentation test (0 nm); b) 25 nm; c) 50 nm; d) 25 nm; e) 0 nm

For the definition of the stress-strain curve of titanium dioxide three different models have been applied, Hollomon, Ramberg-Osgood and bilinear material model.

The stress-strain curves to be taken as an input for the FE-simulations of the nanoindentation tests which match the Hollomon constitutive behavior are represented in Fig. 4. The corresponding load-displacement curves, obtained as output from the FE-nanoindentaton simulations with these stress-strain curves as input and an experimentally defined load-displacement curve are depicted in Fig. 4b.

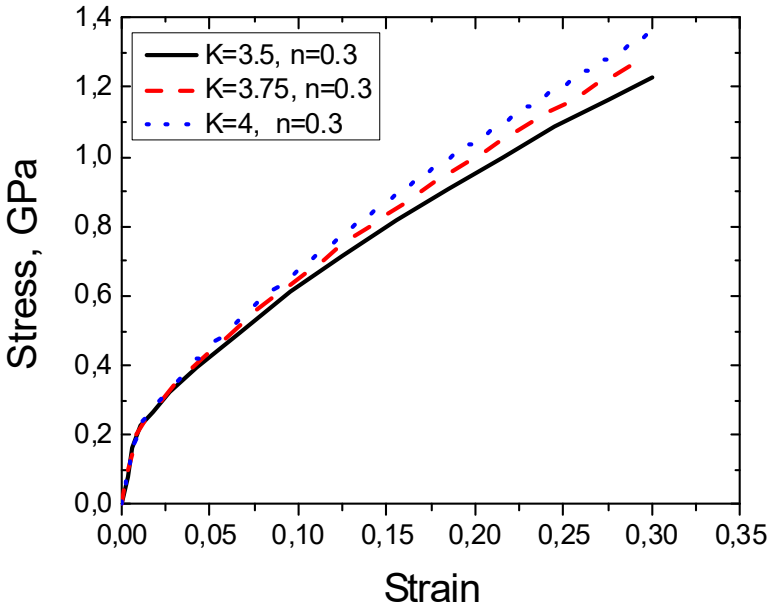

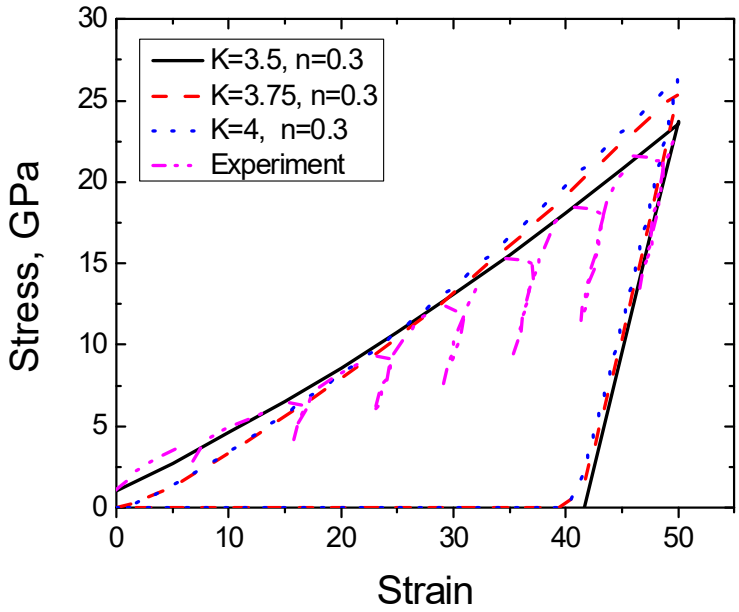

Figure 3-4: a) Variation of input stress-strain curves for TiO_2 with fixed parameters: Young's modulus $E = 27$ GPa and Yield stress $\sigma_y = 0.2$ GPa and a variation of Hollomon's constitutive law coefficients: $K = 3.5$; 3.75; 4, ($n = 0.3$ GPa); b) Comparison of the force-penetration curves, obtained from experiments on nanoindentation (dash-dot-dot-curve) and from the FE-simulations for different parameters of Hollomon's constitutive law. The best fit to the experimental force-penetration curve gives the curve obtained from the FE-simulation of the nanoindentation test with a constitutive behavior following Hollomons constitutive law with the parameters $K = 4$ and $n = 0.3$

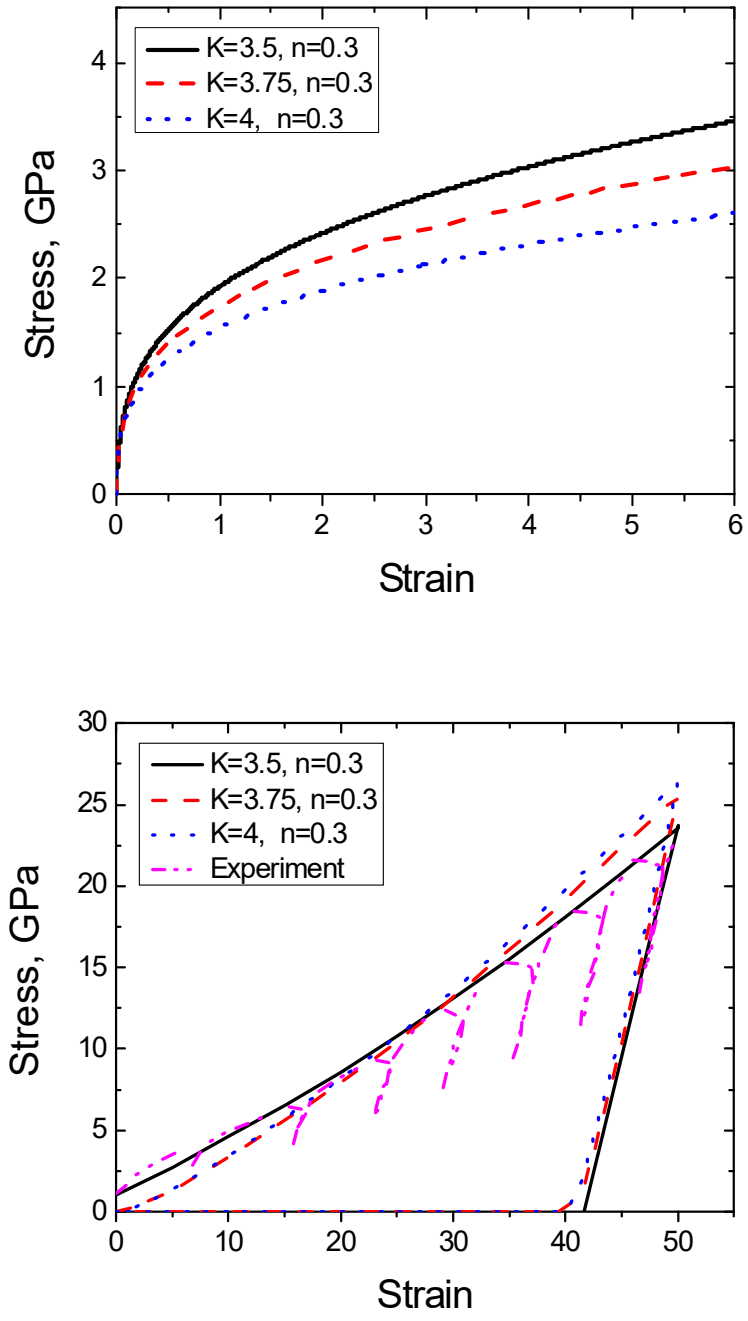

Figure 3-5: a) Variation of the input stress-strain curves for TiO_2 with fixed parameters: Young's modulus E = 27 GPa and yield stress σ_y = 0.2 GPa and a variation of the Ramberg-Osgood constitutive law coefficients: n = 3.15; 3.3; 3.5, (α = 0.1 GPa); b) The comparison of the force-penetration curves, obtained from the experiments on nanoindentation (dash-dot-dot-curve) and from the FE-simulations for different parameters of the Ramberg-Osgood constitutive law

The input stress-strain curves for the Ramberg-Osgood constitutive law are depicted in Fig. 5a and the corresponding force-penetration curves obtained from the FE-simulations of nanoindentation tests are depicted in Fig. 5b. As the Young's modulus for TiO_2 is known from experiments, the parameters σ_y, α and n are determined using inverse analysis. The bilinear constitutive law has been applied to the TiO_2 material while its elastic modulus has been determined experimentally.

Fig. 6b shows the indentation force-penetration curves for pure titanium dioxide for different input stress-strain curves with a maximum indentation depth of 50 nm. Fig. 6a represents the input stress-strain curves for titanium dioxide with different work-hardening coefficient. The comparison of the resulting force-penetration curves for pure titanium dioxide obtained from the FE simulations with the one, obtained in the experiment is represented in Fig. 6b.

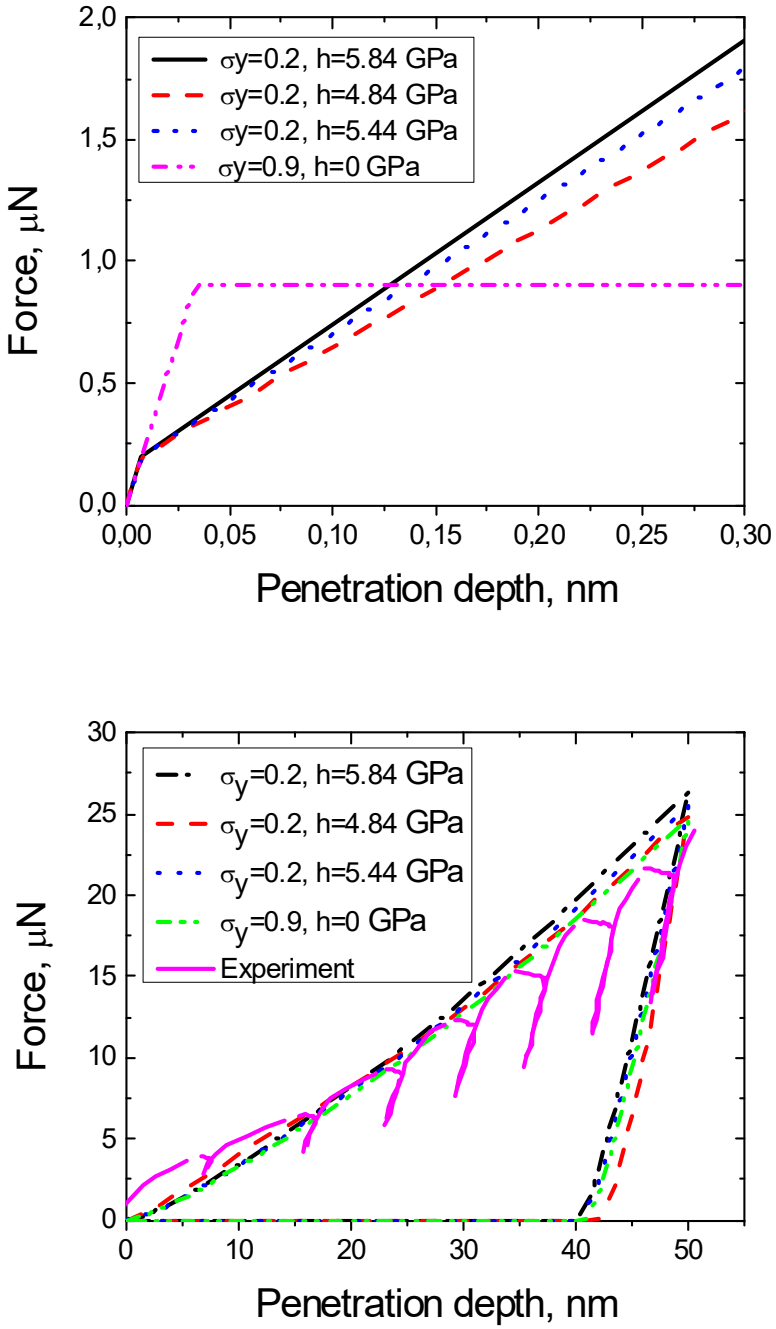

Figure 3-6: a) Variation of input stress-strain curves for TiO_2 with fixed parameters: Young's modulus E = 27 GPa and yield stress σ_y = 0.2 GPa and variation of work-hardening coefficient: h = 5.84, 4.84 and 5.44 GPa (according to eq. 7); b) The comparison of force-penetration curves, obtained from nanoindentation experiments (continuous line) and from FE-simulations with a variation of parameters like in Fig. 6a

It can be seen from Fig. 6b that the dash-dot-dot-curve (σ_y = 0.9 GPa and h = 0) and the dash-dot-dash-curve (σ_y = 0.2 GPa and h = 5.44) represent the best fit for the experimentally obtained force-penetration curve (dash-dot-dot-curve and dash-dot-dash-curve) in Fig. 6a.

The best fit of the force-penetration curves, obtained via inverse modeling following different constitutive laws to the experimentally obtained one are represented in Fig. 7:

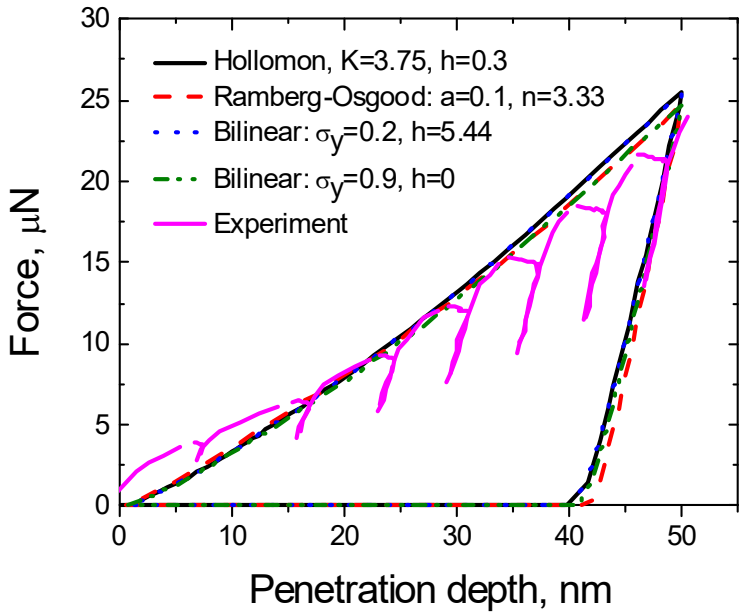

Figure 3-7: Best fitted force-penetration curves, obtained from the FE-simulations of nanoindentation tests obtained from the stress-strain curves according to different constitutive laws

It can be observed that among the most fitting curves the best fit to the experimentally defined force-penetration curve is the elastic-perfectly plastic constitutive law with a Young's modulus being equal to 27 GPa and a yield stress of σ_y = 0.9 GPa (dash-dot-dot-curve).

3.6 Modeling the PE elastic-plastic behavior

Having defined the stress-strain curve for the TiO_2 phase, the same procedure has been used to define the stress-strain behavior of the PE-phase. The experiments on nanoindentation of single layer of polyelectrolyte have been performed. Cube corner indenter penetrates the PE-layer with 500 nm thickness till the penetration depth of 477 nm. The experimentally obtained Force-penetration curve is represented in Fig. 8.

In order to exclude the influence of the silicone substrate, the force-displacement curve obtained in the experiment should be compared, at a penetration depth not exceeding 10-20 % of the film thickness (around 50-70 nm). Inverse modeling of the stress-strain behavior of PE with the Hollomon constitutive law (Fig. 9a) gives the load-displacement curves represented in Fig. 9b.

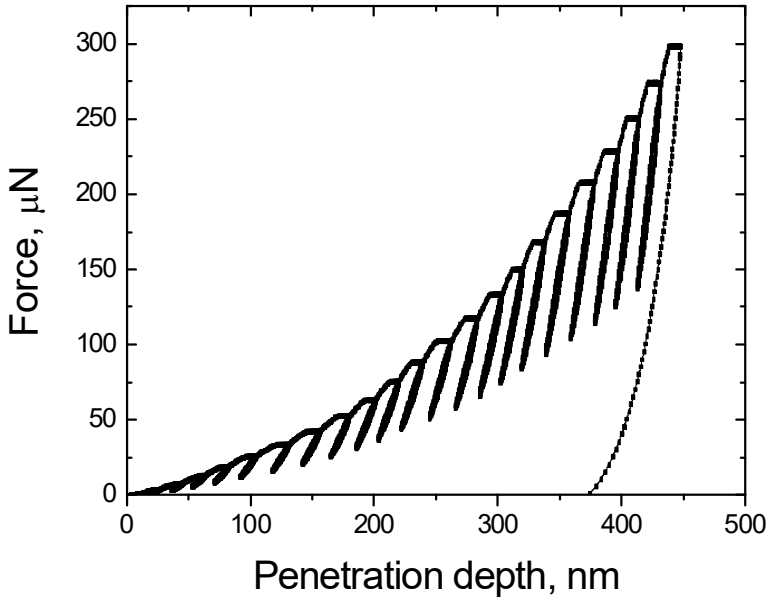

Figure 3-8: The experimentally obtained force-penetration depth curve from nanoindentation

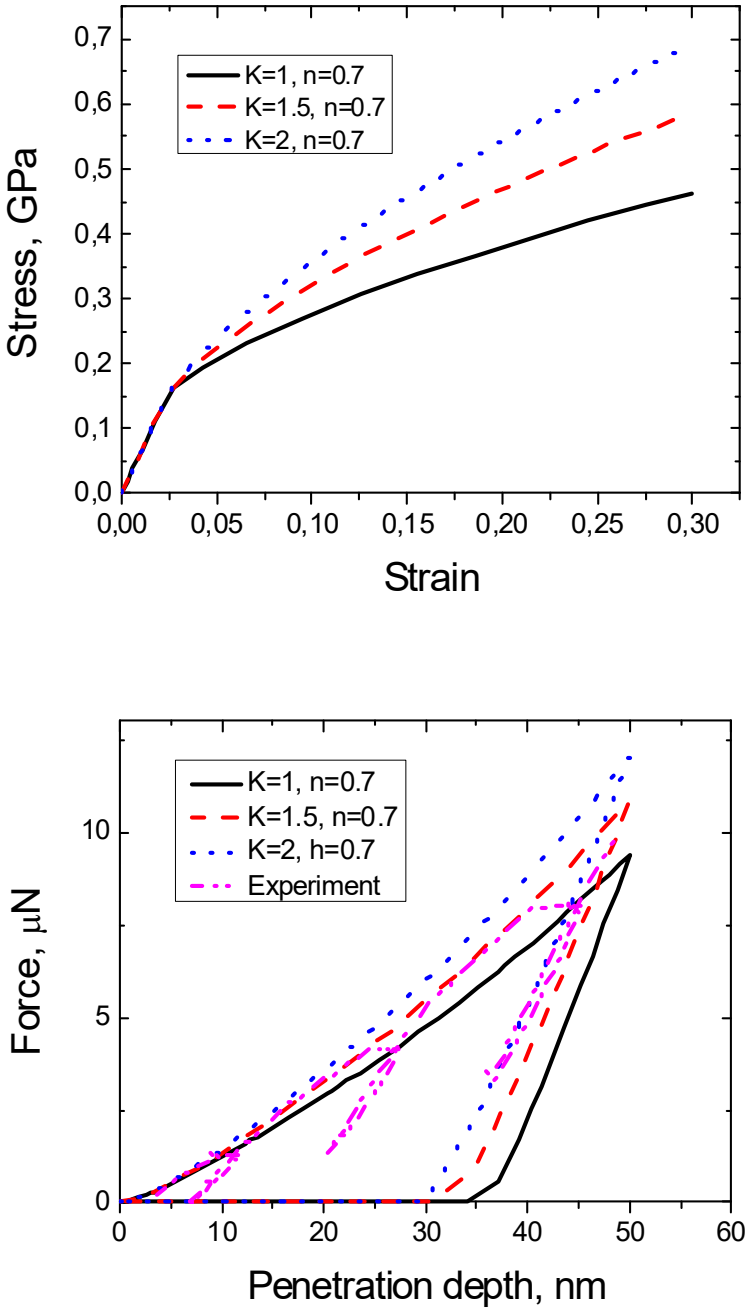

Figure 3-9: a) Variation of the input stress-strain curves for PE following the Ludwig-Hollomon constitutive law with a variation of the following parameters: $K = 1$, $n = 0.7$; $K = 1.5$, $n = 0.7$; $K = 2$, $n = 0.7$; b) Comparison of the force-penetration curves, obtained from experiments on nanoindentation (dash-dot-dot-curve) and from FE-simulations with Hollomon's constitutive law with different parameters

One can see in Fig. 9 that the best fit of the Force-Penetration curve obtained from FEM-simulations of the nanoindentation test among all input stress-strain curves following Hollomon's constitutive behavior gives the curve with the parameters: $K = 1$, $n = 0.7$.

For the simulations of nanoindentation of PE-phase, the input stress-strain curve of the polyelectrolyte is also approximated with the Ramberg-Osgood equation [8]. A number of iterations have been performed with adjustments of the parameters σ_0, α and n respectively (Fig. 10a). The corresponding force-penetration curves are depicted in Fig. 10b. The best fit to the experimental curve is achieved with the Ramberg-Osgood constitutive law with the following parameters: $\alpha = 0.1$, $n = 3.2$.

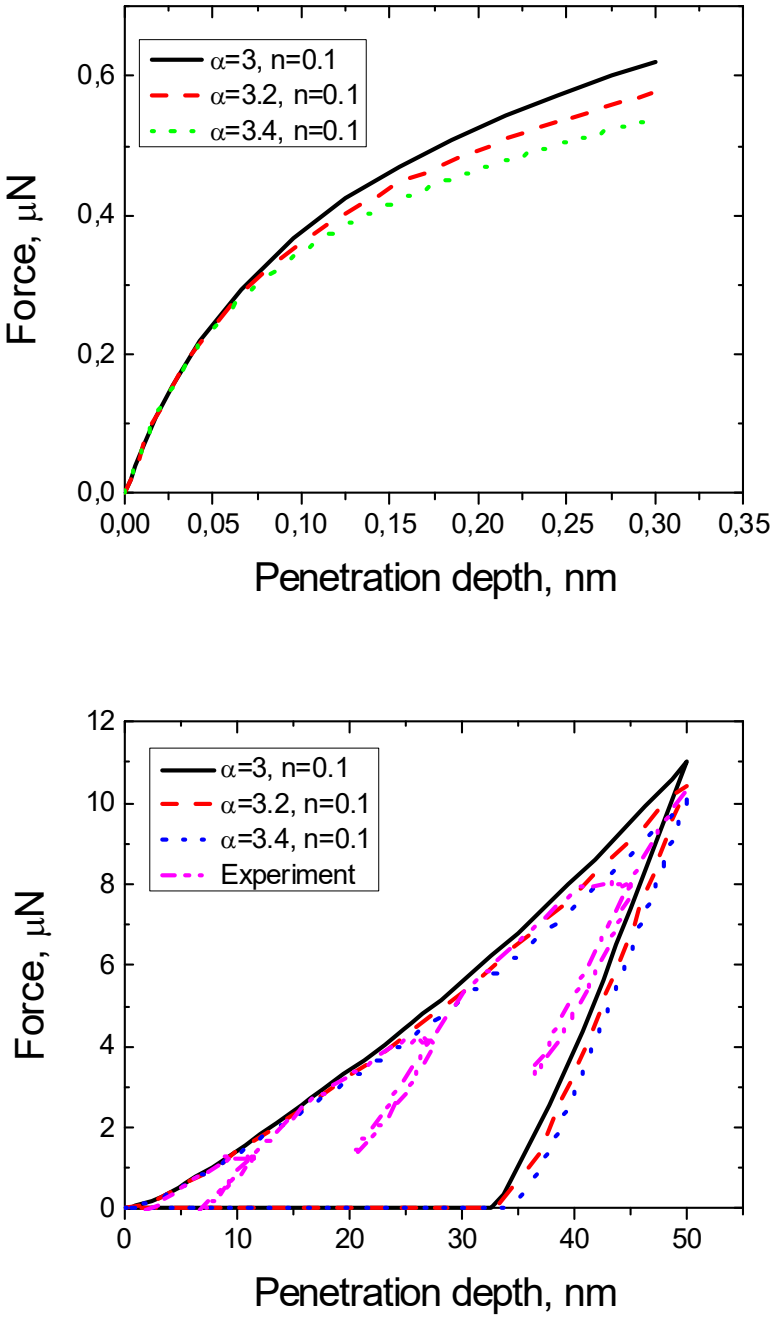

Figure 3-10: a) Stress-strain curves, obtained according to the Ramberg-Osgood equation with different parameters; b) Force-penetration curves, obtained as a result of the FE-simulations of nanoindentation test with the input stress-strain curves from Fig. 10a as input

The nanoindentation simulations of the PE film have been also performed with the bilinear constitutive law. The Young's modulus has been taken from the experiment and the yield stress and work-hardening have been varied till the force-penetration curve obtained from

the FE-simulations achieves the closest fit to the experimentally obtained one. As can be seen from Fig. 11a, two stress-strain bilinear constitutive stress-strain curves σ_y = 0.1 GPa, h = 3.98 GPa and σ_y = 0.2 GPa, h = 2.91 GPa give the same force-penetration curve in Fig. 11b. The elastic perfectly plastic stress-strain curve gives the best fit to the experimentally obtained one among all other curves of the bilinear constitutive behavior.

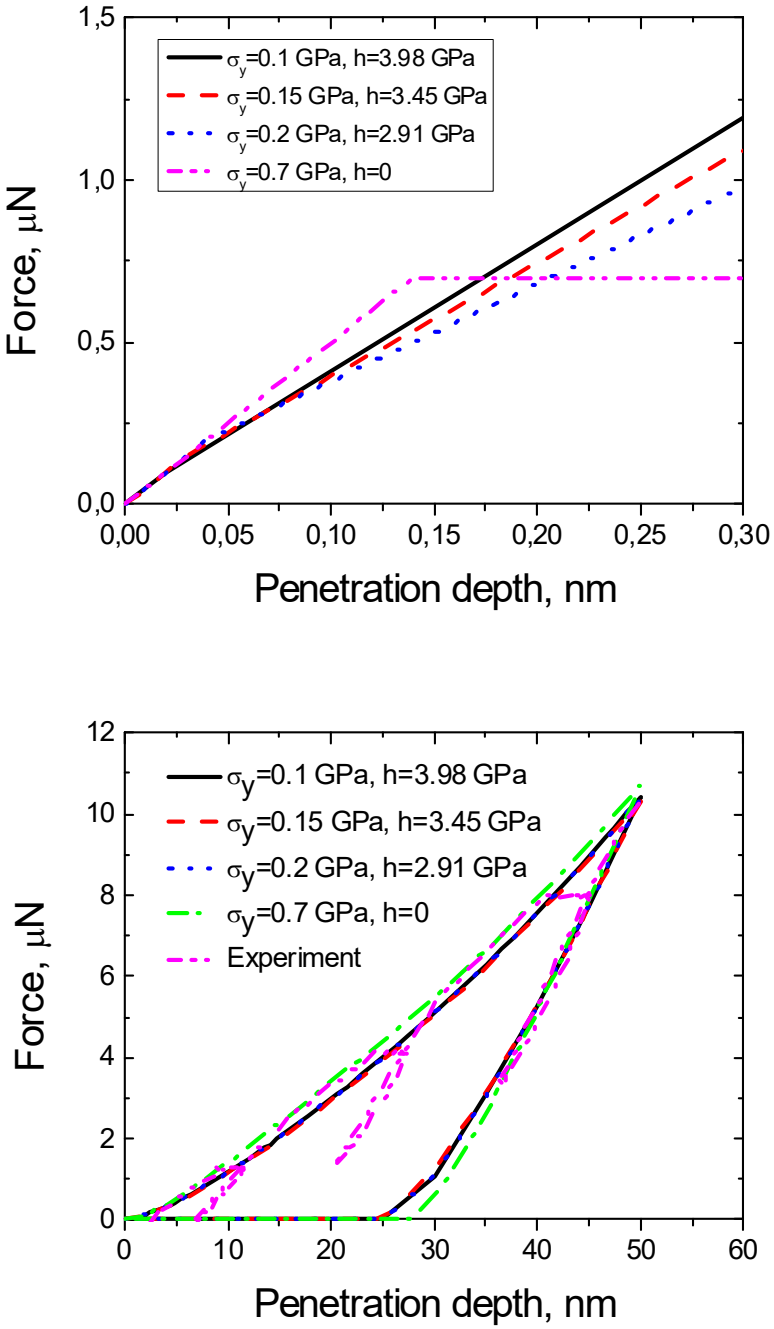

Figure 3-11: a) Variation of the input stress-strain curves for PE with Young's modulus $E = 5$ GPa and variation of the yield stress and the work-hardening coefficient: $\sigma_y = 0.1$ GPa, $h = 3.98$ GPa; $\sigma_y = 0.15$ GPa, $h = 3.45$ GP; $\sigma_y = 0.2$ GPa, $h = 2.91$ GPa; $\sigma_y = 0.7$ GPa, $h = 0$ GPa; b) Comparison of the force-penetration curves, obtained from the FE-simulations with the stress-strain curves of Fig. 11a as input, with the one obtained from experiments on nanoindentation (dash-dot-dot-curve)

The best fit of the force-penetration curves for PE, obtained via inverse modeling following different constitutive laws to the experimentally obtained one, are represented in Fig. 12:

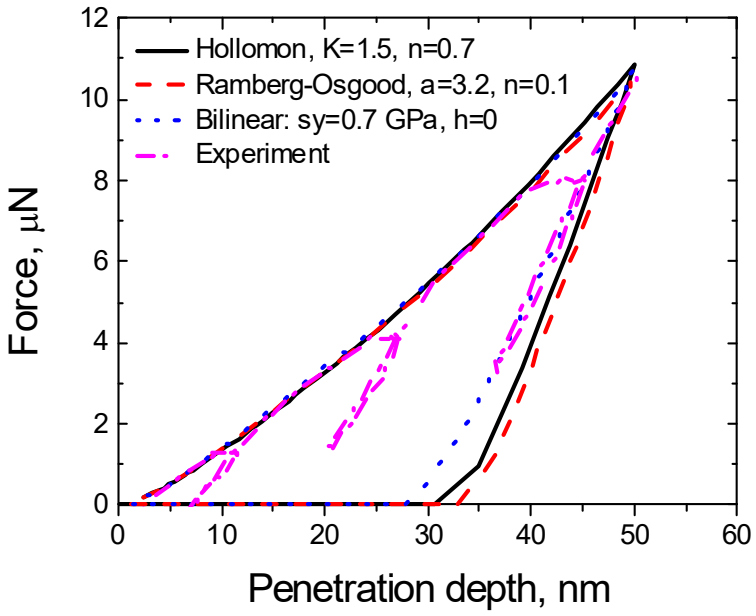

Figure 3-12: Best fit force-penetration curves, obtained from FE-simulations of nanoindentation tests obtained from stress-strain curves according to different constitutive laws. Young's modulus was taken from the experiment (5 GPa)

The Young's modulus being equal to 5 GPa has been taken from the experiment and following the equation 8, the work–hardening parameter has been adjusted till the experimental curve fits the computed one (Fig. 6b). The stress-strain curve with σ_y = 0.7 GPa and with perfect plasticity has been determined as the constitutive law for the polyelectrolyte film.

3.7 Conclusions

In the present work, finite element modeling was successfully utilized to simulate the nanoindentation of the films obtained by chemical bath deposition technique (TiO_2) and layer by layer technique (PE) to obtain the mechanical properties (elastic and plastic properties) of inorganic (TiO_2) and organic (PE) thin films.

The output force-penetration curves, obtained from the FE-simulations of nanoindentation tests of thin TiO_2 and PE films based on inverse modeling with taking into account the

input stress-strain curves following different constitutive laws have been compared with force-penetration curves, obtained from the experiment.

For the TiO_2 film, the force-penetration curves, obtained from the FE–simulations of nanoindentation tests is obtained being identical to the experimental one either with lower yield σ_y = 0.2 GPa and work-hardening (h = 5.44), or with perfect plasticity and higher yield stress (σ_y = 0.9 GPa). For the polyelectrolyte film the force-penetration curve, obtained from the FE–simulations of nanoindentation tests, is obtained being identical to the experimental one with perfect plasticity and stress (σ_y = 0.9 GPa).

The work-hardening behaviour and higher yield stress of ceramics (TiO_2) and organic (PE) are not typical for materials produced by chemical bath deposition technique (TiO_2) and layer-by-layer deposition technique (PE). For amorphous or non-metallic materials, the work-hardening is assumed to be very low (9). Both effects could be explained by the manifestation of the influence of the more rigid substrate. In the present work we did not take into account the influence of the substrate, assuming that at the shallow penetration of 10 % there is no influence of the substrate. The ambiguity of bilinear stress-stain constitutive law with work-hardening and without it (with perfect plasticity) will be the topic of our further investigations.

3.8 Acknowledgements

The authors acknowledge funding by the German Research Foundation (Deutsche Forschungsgemeinschaft, DFG) (project number Schm 746/88-1).

3.9 References

[1] Barthelat F (2007) Biomimetics for next generation materials. Philosophical transactions Series A, Mathematical, physical, and engineering sciences 365:2907–19.

[2] Burghard Z et al. (2007) Nanomechanical Properties of Bioinspired Organic–Inorganic Composite Films. Advanced Materials 19:970–974.

[3] Burghard Z et al. (2009) Toughening through nature-adapted nanoscale design. Nano letters 9:4103–8.

[4] Oliver W, Pharr G (1992) An improved technique for determining hardness and elastic modulus using load and displacement sensing indentation experiments. Journal of Materials Research 7 (6):1564–1583.

[5] Kopernik M, Szeliga D (2007) Modelling of nanomaterials-sensitivity analysis with respect to the material parameters. Computer Methods in Materials Science 7:255–261.

[6] Hollomon J (1945) Tensile deformation. Transactions of the American Institute of Mining, Metallurgical and Petroleum Engineers 162:268–290.

[7] Ramberg W, Osgood W (1943) Description of stress-strain curves by three parameters. National Advisory Committee for Aeronautics, Washington, DC, Technical Note No 902 07.

[8] Kopernik M, Pietrzyk M (2007) 2D numerical simulation of elasto-plastic deformation of thin hard coating systems in deep nanoindentation test with sharp indenter. Archives of Metallurgy and Materials 52:299–310.

[9] Knapp J a., Follstaedt DM, Myers SM, Barbour JC, Friedmann T a. (1999) Finite-element modeling of nanoindentation. Journal of Applied Physics 85:1460.

4 Perlmutt 2

Die folgende Veröffentlichung beschreibt die Simulation der Nanoindentationsexperimente in Bezug auf spezielle Strukturen, den Nanobrücken. Ergänzend wird auch ein analytischer Ansatz präsentiert, der die Simulationsergebnisse unterstützt:

III. Lasko, G., Burghard, Ž., Bill, J., Schäfer, I., Weber, U., & Schmauder, S. (2013). Simulation of Mechanical Properties of Bio-Inspired TiO_2/PE Nanocomposites. Advanced Engineering Materials, 15(10), pp. 908–920.

Der Anteil meiner Arbeit in der Veröffentlichung umfasst:

- Konzeptualisierung, Erstellung des Manuskripts mit Frau Dr. G. Lasko (Anteil meiner Arbeit 70 %)
- Erstellung der Diagramme und Abbildungen (Anteil meiner Arbeit 100 %)
- Erstellung und Durchführung der Simulation der Nanoindentation mit unterschiedlichen Parametern. Formale Analyse, Untersuchung, Datenkuration, Validierung (Anteil meiner Arbeit 100 %)
- Einführung der Mineralbrücken in die Simulation und Definition des E-Moduls derselben (Anteil meiner Arbeit 100 %)
- Analytischer Nachweis (Anteil meiner Arbeit 100 %)
- Diskussion der Ergebnisse und Optimierung der Simulation in Zusammenarbeit mit den Mitautoren (Anteil meiner Arbeit 60 %)

Simulation of mechanical properties of bio-inspired TiO_2/PE nanocomposites**

By G. Lasko*, Z. Burghard, J. Bill, I. Schäfer, U. Weber, S. Schmauder

[*] Dr. G. Lasko, I. Schäfer, Dr. U. Weber, Prof. S. Schmauder,
Institut für Materialprüfung, Werkstoffkunde und Festigkeitslehre (IMWF),
Pfaffenwaldring 32,
70569 Stuttgart, Germany
E-mail: galina.lasko@imwf.uni-stuttgart.de
Dr. Z. Burghard, Prof. J. Bill
Institute of Materials Science,
Heisenbergstrasse 3,
70569 Stuttgart, Germany

[**] The authors acknowledge funding by the German Research Foundation (Deutsche Forschungsgemeinschaft, DFG) project number Schm 746/88-1 and BI 469 15-1 within the scope of the project "Biologische Erzeugung von Oxidkeramiken" (PAK 410).

Abstract

The extraordinary combination of strength and toughness attained by nature's highly sophisticated structural design in nacre has inspired the synthesis of novel layered nanomaterials. In the present work, numerical and analytical models are applied on the nanometer scale to attain a better insight and understanding concerning the mechanical behavior of bio-inspired layered materials. The material is composed of the oxide TiO_2 and organic polyelectrolyte (PE) layers. The efforts focus on applying continuum mechanics in nanoscale numerical models to the layered TiO_2/PE system, obtained by a chemical bath deposition (CBD) procedure at low temperatures.

Based on previous experimental investigations, Finite-Element-(FE)-simulations of the mechanical behavior of the layered ceramic and organic phases (TiO_2-PE) are performed. The elastic-plastic properties of titania and organic polyelectrolyte phases are determined

via FE-modeling of the nanoindentation process. Based on experimental observations the influence of mineral bridges has been taken into account in calculations of Young's modulus of the layered nanocomposite as a function of the thickness ratio of the constituents. The mineral bridges have been considered to possess a high Young's modulus (achieving the Young's modulus of bulk rutile TiO_2 = 282 GPa). Taking the experimental dependence of the Young's modulus on the thickness ratio of the constituents into account, a method is elaborated to define the volume fractions of the mineral bridges. Numerical and analytical models with the as above defined volume fractions of mineral bridges generate results which match the ones of the experiment. By application of this approach the mechanical properties of artificially produced materials, mimicking nacre structure, can be predicted.

Keywords: *biomimetics, bio-inspired, TiO_2/PE nanocomposites, nanoindentation, FEM.*

4.1 Introduction

Over many million years nature developed optimized and highly specialized materials with outstanding features. Biomaterials reveal remarkable combinations of mechanical properties such as stiffness, hardness and fracture toughness which are hardly attained by artificial materials.[1] Mollusk shells are an excellent example of such high performance natural materials, they consist mainly of $CaCO_3$ in its aragonite form. The impressive feature of shells is their high work of fracture: in a work of Jackson et al. the authors state that the work of fracture is 3000 times higher than that of monolithic $CaCO_3$.[2] The underlying principles and features of nacre are summarized in the work of Gao where the correlations between size, hierarchy, material properties and fracture behavior are described.[3] Other strong biomaterials like bones and teeth show a comparable concept in their construction: A nanometer sized hard mineral crystal is arranged in a parallel staggered pattern in a soft matrix which consists of proteins - it is known to be a general principle in nature to reinforce materials.[4][5] The special properties of biomaterials inspired the development of a large class of biomimetic materials and organic/inorganic composites[6]–[8] and especially the properties of nacre are of interest for scientific researchers. It was found that aragonite layers consist of hexagonal platelets which are interconnected by so called mineral bridges. Both structures are important for the reinforcement of nacre.[6][9] In this paper the mineral bridges and their role for the mechanical properties of the bio-inspired nanocomposite will be of main interest. Mineral bridges are described as a number of small mineral structures

with a diameter about 30 nm, randomly distributed in the protein layer that pervade through the organic layer and interconnect the hexagonal platelets.[10] Their existence and first models for their function are described by Schäffer et al. and even in more detail by Song et al.[11][12]

In the past decade a number of nacre-like nanostructures have been artificially manufactured in the laboratory by different methods like clay/electrolyte layered material and ice-templated alumina with infiltrated aluminum (alumina–Al-Si composites wit 45/55 vol %).[7][13]–[15] The salient feature of the latter one is the formation of ceramic bridges between lamellae like the natural prototype with its mineral bridges. One of the bio-inspired synthesis routes to obtain inorganic layers is the chemical bath deposition method (CBM) which enables the use of proteins as component because of the low processing temperature procedure.[8] The CBM operates at low temperatures, similar to the biomineralization process in nature for the production of natural organic/inorganic layered nanocomposites. Burghard et al. took advantage of the negatively charged oxide surface to alternate Titandioxide (TiO_2) with positively charged polyelectrolytes (PE). Combined with the layer-by-layer technique (where thin layers in the order of a few nanometers are achievable) it was possible to prepare TiO_2/PE polymer multilayered films with a nacre-like architecture, including mineral bridges, which interconnect the TiO_2-layers.[8] The layered structure consists of different thicknesses of the polyelectrolyte layer (PE): 5 nm, 10 nm, 15 nm and 20 nm respectively, the thickness of the TiO_2 layer is always 100 nm. Compared to real nacre, the thickness of the PE layer is in the same range than the thickness of the organic biopolymer in nacre (about 5-20 nm) as shown in the work of Li and co-workers.[16] It was found that the nacreous platelets in nacre consist of nanograins, which results in a special microstructure and mechanisms (e.g. rotation of nanograins).[17][18] The microstructure of TiO_2/PE nanocomposite reveals a similar grain structure as the nacreous platelets. Phenomena like the nanograin rotation could be observed in this material too, but it was not investigated within the scope of the present paper.

The layered composite was then tested for its effective mechanical properties by nanoindentation.[8] Traditional mechanical testing methods for bulk materials are not easily applicable on small-scale structures and also nanoindentation is a very delicate method. An alternative for testing newly created nano-materials are computer simulations, for example FE-software. With the help of simulation, the needed layer thicknesses and number of mineral bridges for a layered material with certain required material properties can be

estimated. Moreover, the stress-strain behavior of the constituents can be varied and defined by inversely adjusting them to the experimentally derived bulk properties. This reduces the costs of building and testing prototypes. In a number of numerical works nanoindentation tests of nanocoatings have been performed numerically.[19][20] One example is the work of Tang et al. where different coatings and the effect of microstructural heterogeneity on the deformation fields have been investigated.[13] Also, the indentation behavior of metal/ceramic multilayers at the nanoscale has been simulated.[13] It was shown that numerical models featuring explicitly the multilayers and homogenized multilayer composites on the other hand show very different responses in hardness and elastic modulus.[20] Investigations of the mechanical properties by nanoindentation of nacre and their simulations by using FE-software have been reported as well.[21]–[23] For instance in the work of Barthelat and Espinosa the authors analyzed the Young's modulus of the protein- and the calcium layer of nacre by nanoindentation simulations.[23] They compared the results of FE-simulations with the results of a model which consists of a Voigt composite in compression (two different materials are loaded in series, which represents the compression across the tablets in nacre). With this arrangement they solved an inverse problem about the properties of the platelets and interfaces of nacre and stated that with these (more accurate material properties) results better computational models of nacre can be made.

A 3-D FE-modeling of the mechanical response of nacre-based hybrid nanocomposites has been performed using the material parameters obtained from nanoindentation techniques.[21] The non-linear response of the nanocomposite at higher loads was simulated under the assumption that nonlinearity in nacre results entirely from the elasto-plastic response of the organic layer. In their model, the inorganic component is modeled as an elastic solid. Simulated tensile tests under identical loading conditions indicated that a very high (400 MPa) yield stress of the organic phase is necessary to generate the experimentally obtained stress-strain behavior and yield stress of nacre. This value of the yield stress is higher than that observed for a real protein and even higher than that found in biological hard tissue. In a work of Katti and Katti simulations are used to explain the functions of the platelets which play a significant role on deformation of nacre and the organic matrix and its molecular interactions at the organic–inorganic interface.[22]

In spite of the fact that there exists a large number of works devoted to the simulation of the mechanical behavior of bio-inspired materials, there is a lack of work devoted to the

simulation and mathematical modeling of layered bio-inspired nanocomposites and composites with a serial arrangement of layers obtained by CBD technique combined with the layer-by-layer technique.

In the present work, computer simulations and mathematical modeling of the mechanical properties of nanocomposite films, composed of alternating layers of TiO_2 as inorganic component and polyelectrolytes (PE) as the organic component, are reported.

For the first time FE-simulations have been applied to simulate the mechanical response without unrealistic assumptions with respect to each property of the components of bio-inspired laminated organic/inorganic nanocomposites obtained by CBD. The effective Young's modulus of the layered TiO_2/PE-nanocomposite, which has been obtained from analytical and numerical modeling, is compared with experimentally based definitions of Young's moduli from nanoindentation experiments (using the unloading portion of the load-displacement curve). The qualitative match of the experimentally-obtained dependence of Young's modulus on the thickness ratio of the constituent layers has been reached with a combination of the numerically obtained dependences. The analytical model of Young's modulus of a nanolaminate has been elaborated by taking into account mineral bridges with a high value of Young's modulus close to the Young's modulus of crystalline bulk rutile TiO_2 and the influence of the thickness ratio between organic and inorganic phases. The maximum number of bridges per volume fraction of the composite was defined as less than 9 % by an analytical model and the result was then used in FE-simulations of nanoindentation tests at different thickness ratios of TiO_2/PE-constituents in order to define the Young's modulus of the composite.

4.2 Definition of Young's modulus from nanoindentation test

4.2.1 Nanoindentation test

In recent years considerable progress has been made in the investigation of different mechanical properties of thin films on a substrate[24]–[26] mainly due to new methodologies such as nanoindentation in micromechanics.[27]

Nanoindentation is a useful tool that allows the direct measurement of hardness and Young's modulus of various types of solid-supported films, while the mechanical properties of thin films cannot be determined using conventional tensile test experiments.

Based on the indentation Force-Penetration data, the Young's modulus of the solid-supported film can be determined, according to the method introduced by Oliver and Pharr.[28] The performance of nanoindentation tests allows the determination of hardness and elastic modulus of thin films of a thickness of several tens of nanometers till several 100 of nanometers. From contact mechanics it is known that the reduced Young's modulus E_r is calculated from the contact area A_c and the unloading contact stiffness S as follows:[29]

$$E_r = \beta \frac{\sqrt{\pi}}{2\sqrt{A_c}} * S \,. \qquad [1]$$

where S is the initial unloading contact stiffness, which is the slope of the upper portion of the unloading segment of load-displacement curve during the initial stage of unloading and is defined from the Force-Penetration curve by the following equation:

$$S = \frac{dP}{dh}. \qquad [2]$$

where dP is the portion of decreasing value of the force at the initial stage of unloading and dh is the portion of decreasing of the penetration depth of indentation.

The contact area Ac is considered as an area function of the contact depth h_c:

$$A_c = F(h_c) = C_0 h_c^{\,2} + C_1 h_c + C_2 h_c^{\,1/2} + C_3 h_c^{\,1/4} + C_4 h_c^{\,1/8} + C_5 h_c^{\,1/16}, \qquad [3]$$

where C_0 is 2.598 for a cube corner probe, C_i (i = 1-5) are coefficients and the contact depth h_c is given by the equation:

$$h_c = h_{\max} - \varepsilon * \frac{P_{\max}}{S}. \qquad [4]$$

where P_{max} is the maximum load and hmax is the maximum depth of indenter penetration in the specimen

The latter term accounts for the deflection of the specimen surface from the maximum penetration depth of the indenter after its withdrawal. The geometric constant ε is based on the geometry of the indenter tip (in experiment with cube cone indenter: ε = 0.75).

The reduced elastic modulus E_r of the system is related to the Young's modulus of the sample E_s:

$$\frac{1}{E_r} = \frac{\left(1-\nu_i^2\right)}{E_i} + \frac{\left(1-\nu_s^2\right)}{E_s}. \qquad [5]$$

The symbols ν and E denote Poisson's ratio and Young's modulus for the sample with subscript *s* and the indenter material with subscript *i*. For the applied nanoindenter in the experiment, the material of the indenter probe is diamond with E_i = 1141 GPa and ν_i = 0.07.

The above–mentioned method of extracting properties from the measured Force-Penetration data were developed for monolithic materials.[28] The same methods are often applied to film/substrate systems for determining film properties without explicit consideration of how the substrate influences the measurements. In order to measure 'film-only' properties, a commonly used rule is to limit the indentation depth to less than 10 % to 20 % of the film thickness.[28]

Nanoindentation testing was carried out with a scanning nanoindenter comprising a depth-sensing force transducer (Hysitron TriboScope), combined with a commercial scanning probe microscope (NanoScope III Multimode, Digital Instruments). Indentations were made with a cube corner diamond indenter with a nominal tip radius of ~40 nm. In all experiments, a maximum force of 80 µN was applied, which yielded a penetration depth of about 120 nm.

4.2.2 FE model of the nanoindentation test

For the definition of Young's modulus of the layered TiO_2/PE-nanocomposite, FE-simulations of nanoindentation testing have been performed and the Young's modulus of the nanocomposite has been defined from the initial segment of the unloading Force-Penetration curves.

An axisymmetric FE-model is applied in the present paper. The models of the nanoindentation tests have been developed in ABAQUS CAE. The representation of the geometry and boundary conditions of the FE-model is shown in Figure 1.

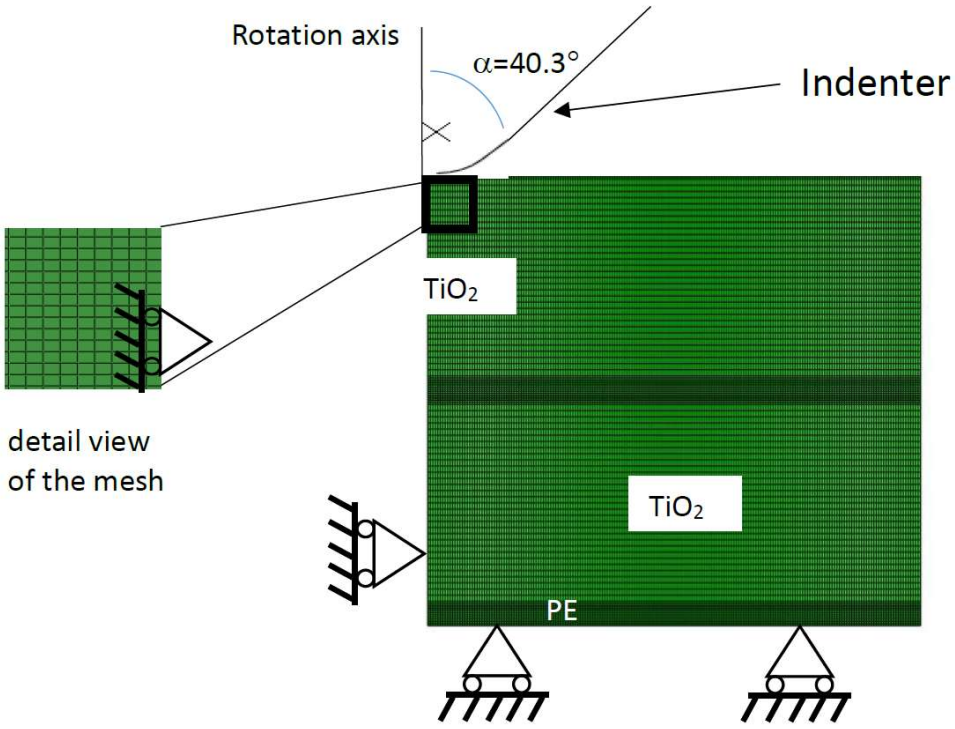

Figure 4-1: Finite-element mesh and boundary conditions of the axisymmetric model (only two layers shown here) for the nanoindentation test

The model of the indenter used in the present simulations possesses a conical shape with a tip-radius of 40 nm and a semi vertical angle of 40.3° which gives the same area to depth function as that of a cube-corner indenter, used in the experiment.

For the definition of the Young's modulus of the nanocomposite from the FE-simulations, the same formulae (1, 2, 4, 5) were used, except of equation 3 for the definition of the area function. Depending on the depth of the indenter penetration one of the following equations (Equation 6) should be applied. Here, a spherical-conical fitting based on the second equation is used:[30]

$$A_c = A_{spherical} = \pi h_c (2R - h_c), \text{for} h_c \le h_a ,$$
$$A_c = A_{conical} = \pi \tan^2 \vartheta (h_c + h_o)^2, \text{for} h_c \ge h_a , \quad [6]$$

where R is the tip radius of the indenter and h_c is the indentation depth. The transition from $A_{\text{spherical}}$ to A_{conical} occurs at $h_a = R - R\sin\vartheta$ and h_0 is the distance between the apex of the indenter tip and the apex point of the equivalent conical indenter $h_0 = R / R\sin\theta - R$ (Fig. 2)

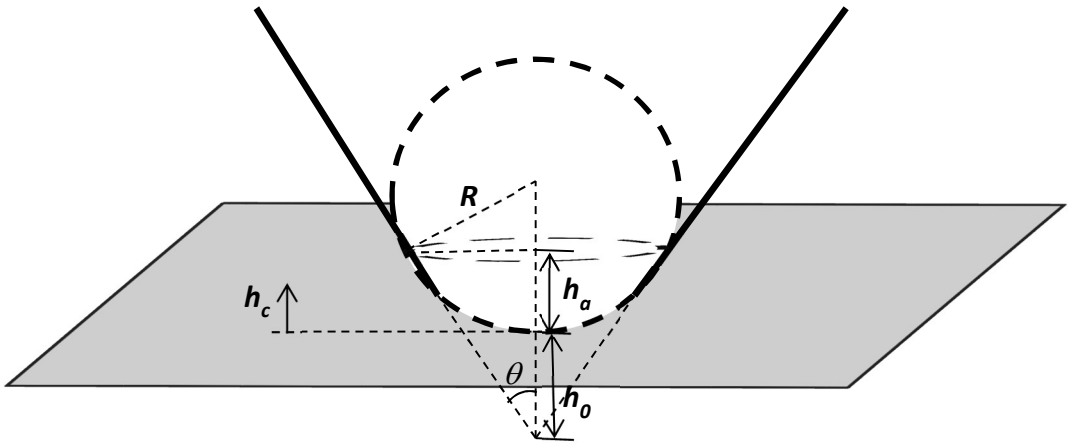

Figure 4-2: Sketch of the tip radius geometry of the intender used in the FE-simulations

4.3 Determination of the stress-strain behavior of the constituent phases of the TiO_2/PE-nanocomposite

4.3.1 Modeling of the plastic behavior of a titania film

The modeling of the material behavior of composites is generally based on a model for the behavior of each constituent or phase of the composite. For the calculation of the nanoindentation behavior of a layered TiO_2/PE structure the stress-strain curves of both phases (TiO_2 and PE layer) are required. For the definition of the stress-strain behavior of the constituents the developed methodology involving the combination of nanoindentation technique and Finite Element Method to characterize the mechanical (elastic and plastic) behavior of the titanium oxide thin film is applied.

The elastic-plastic properties of TiO_2 are calculated by solving the inverse problem via axisymmetric Finite Element analysis. For this purpose, a stress-strain curve is first assumed as a constitutive law for the TiO_2 thin film and based on this law the Force-Penetration curve is then determined by FE-modeling. The computed Force-Penetration curve is then compared with the experimental one and further on iteratively modified until close agreement is reached between the computed and the experimental Force-Penetration curves. The stress-strain curve that leads to such an agreement can be considered to represent the constitutive behavior of a thin film. In Figure 3 the experimentally obtained Force-Penetration curve of TiO_2 is shown.

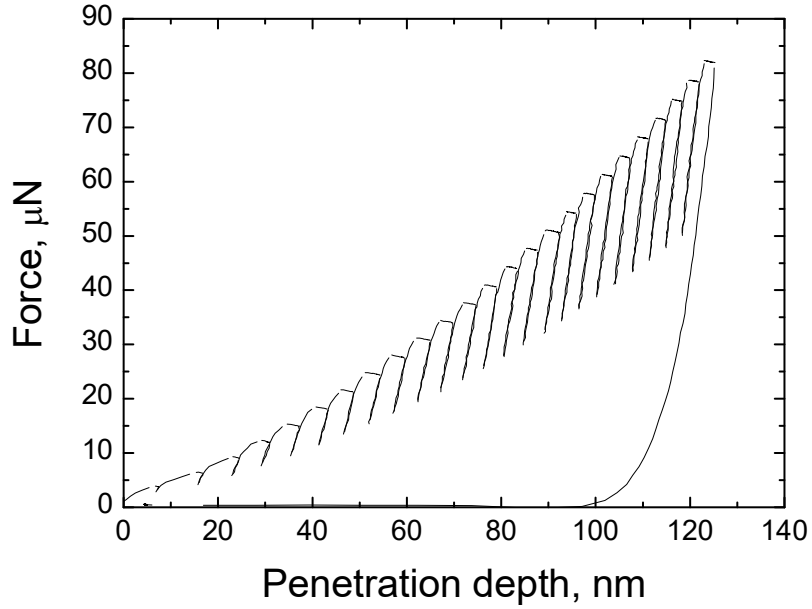

Figure 4-3: Experimentally obtained Force-Penetration depth-curve for TiO_2 from nanoindentation

Nanoindentation tests have been performed till a penetration depth equal to 120 nm following the loading-unloading procedure, where a maximum force of 80 μN was attained in the experiment.

Before deriving a stress-strain curve obtained for titania, the β parameter in equation 1 is defined by equating the known Young's modulus (determined experimentally with equations 1 and 5) to the one derived from FE-simulations of Force-Penetration curves of nanoindentation tests. In this way a value of $\beta = 1.178$ has been determined which was used in all subsequent analyses.

There exist several models used in inverse modeling: Hollomon's model, Ramberg-Osgood and bilinear material models for homogeneous isotropic elasto-plastic material.[31][32] In the present work we used the bilinear material model.

To match the simulated curve with the experimental one, the yield stress σ_y and the work-hardening coefficient h are varied for the titania film, although the Young's modulus E is taken to be equal to one, as determined experimentally. The model is expressed by the following equations:

$$\begin{aligned} \sigma &= E * \varepsilon \quad if \quad \sigma \le \sigma_y , \\ \sigma &= \sigma_y + h\left(E \cdot \varepsilon - \sigma_y\right) \quad if \quad \sigma \ge \sigma_y , \end{aligned} \qquad [7]$$

where σ is the axial stress, ε is axial strain, E is Young's modulus, σ_y is the yield stress and h is the hardening coefficient ($0 \le h \le 1$): $h = 1$ for ideal elastic materials, $h = 0$ for ideal plastic materials. As the Young's modulus for titania is known from experiments, the parameters σ_Y (yield stress) and h (work-hardening coefficient) are determined by using an inverse analysis.

In Figure 4 the contour plots of von Mises stresses at different instances of indentation of indenter penetration into a pure titania layer are shown. In Figure 4a the curve demonstrates the penetration depth being equal to 50 nm (10% of the titania film thickness), and Figure 4b shows the stress state after releasing the indenter from the material. After withdrawal of the indenter the material did not follow the initial shape of the specimen, but the indenter leaves an imprint on the surface of the specimen, testifying to the fact that plastic deformation occurs, as is confirmed by experimental observations.[33]

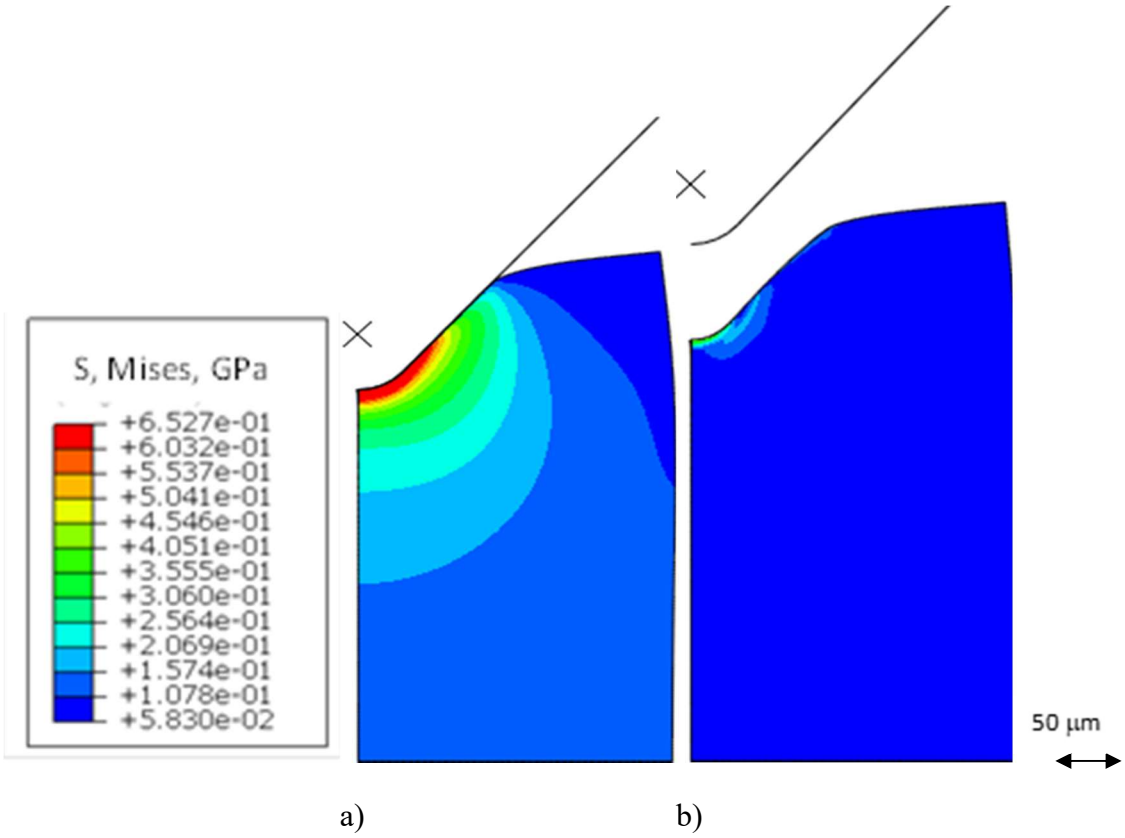

Figure 4-4: Contour plots of von Mises stress obtained as a result of FE-simulations of a nanoindentation test of a TiO_2 bulk material during (a) and after indentation (b)

Figure 5 represents the input stress-strain curves for titania with different work-hardening coefficient and the corresponding Force-Penetration curves obtained by FE-simulations (ABAQUS, General purpose finite element program, Version 6.7, Hibbit Karlson and Sorensen Inc., Pawtucket, RI, 20). For the simulation a yield stress of $\sigma_y = 0.2$ GPa was used, which was applied as defined by inverse modeling.

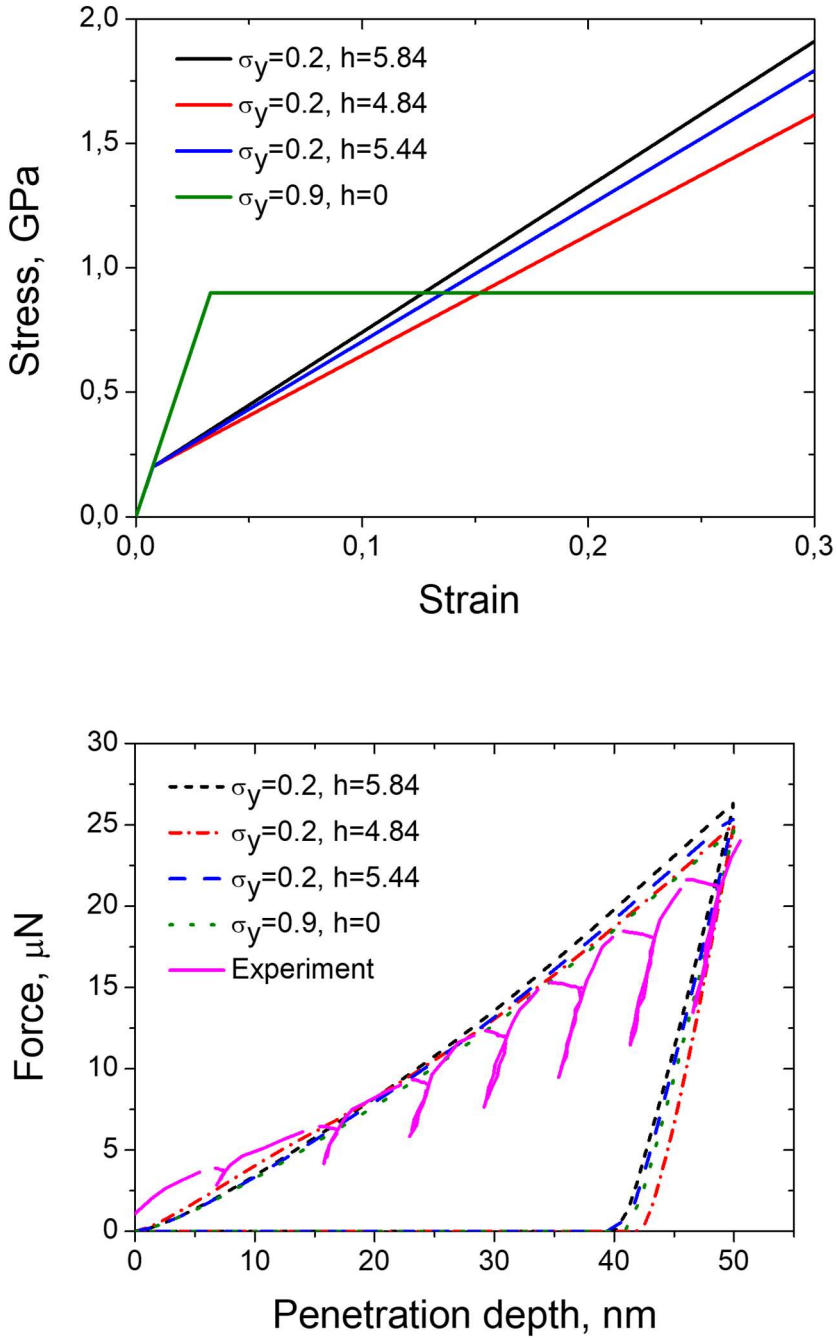

Figure 4-5: Figure 5: a) Variation of input stress-strain curves for TiO_2 with fixed parameters: Young's modulus E = 27 GPa and yield stress σ_y = 0.2 GPa and variation of work-hardening coefficient: h = 5.84, 4.84 and 5.44 GPa (according to eq. 7); b) The comparison of Force-Penetration curves, obtained from nanoindentation experiments (continuous line) and from FE-simulations with a variation of parameters like in Fig. 5a

These values have been defined from inverse modeling by fitting the Force-Penetration curve obtained from FE-simulations with the one obtained experimentally. A comparison

of the resulting Force-Penetration curves for pure titania obtained from the FE-simulations with the one obtained in the experiment is shown in Figure 5b. There exists a difference between the experimental test and the one derived numerically. In the experiment, partial unloading (Figure 3 and Figure 5b) is made while in the simulation a complete unload of the specimen is modelled. The stress-strain curves with $\sigma_y = 0.2$ GPa and $h = 5.44$ GPa and $\sigma_y = 0.9$ and $h = 0$ provide the best fit of the Force-Penetration curve obtained from FE-simulations of the nanoindentation test and the ones derived from experiment (Figure 5b).

4.3.2 Modeling of the plastic behavior of polyelectrolyte

Having defined the stress-strain curve for the TiO_2 phase, the same procedure for defining the stress-strain behavior of polyelectrolyte is used. Nanoindentation experiments of single layers of polyelectrolyte have been performed. A cube-corner indenter is used to penetrate the PE-layer and the experimentally obtained Force-Penetration curve is represented in Figure 6.

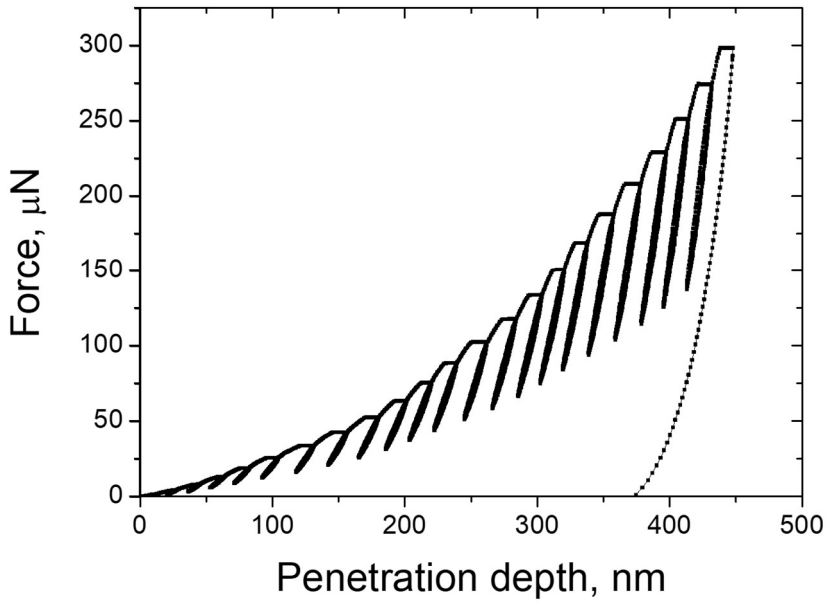

Figure 4-6: The experimentally obtained Force-Penetration depth-curve for PE from nanoindentation

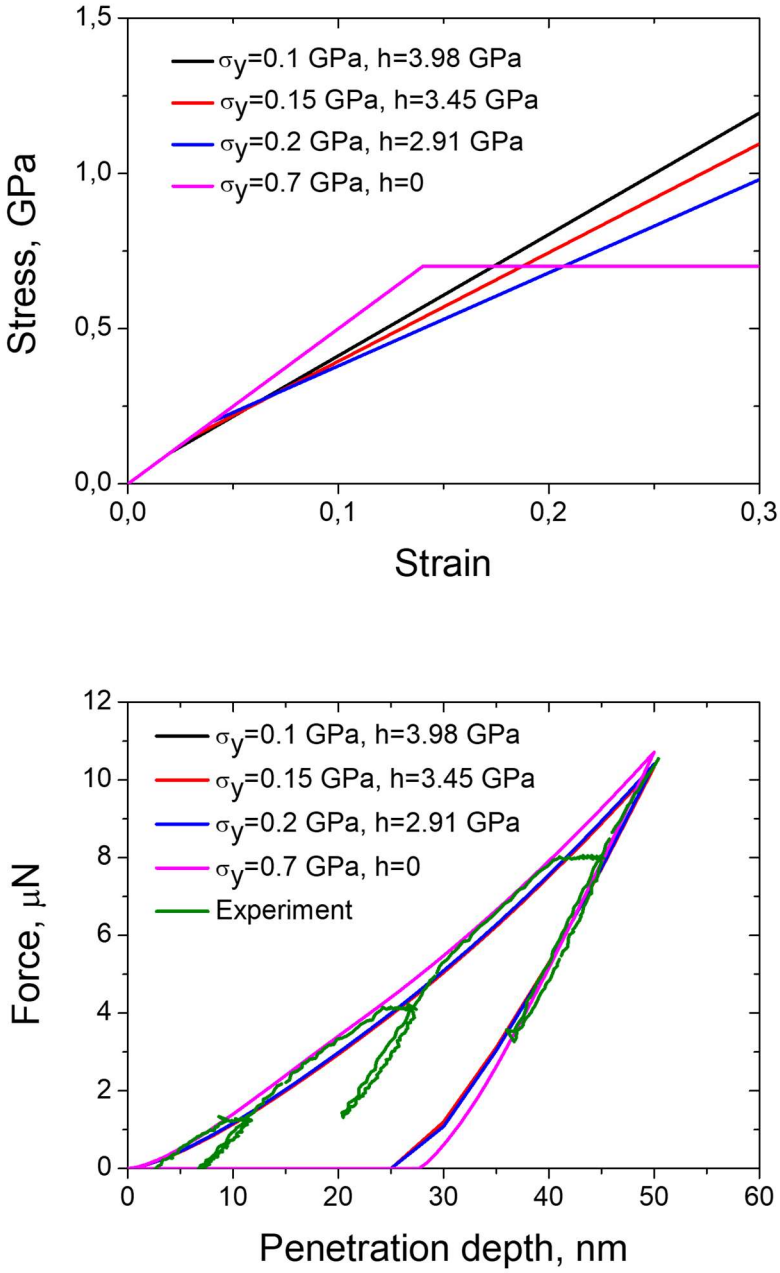

Figure 4-7: a) Variation of the input stress-strain curves for PE with Young's modulus E =5 GPa and variation of the yield stress and the work-hardening coefficient: σ_y=0.1 GPa, h=3.98 GPa; σ_y=0.15 GPa, h=3.45 GP; σ_y=0.2 GPa, h=2.91 GPa; σ_y=0.7 GPa, h=0 GPa; b) Comparison of the Force-Penetration curves, obtained from the FE-simulations with the stress-strain curves of Fig. 7a as input, with the one obtained from experiments on nanoindentation (black curve)

As can be seen, the slope of the initial unloading segment on the Force-Penetration curve changes much more than in the case of TiO_2 with increasing penetration depth of the indenter.

For the simulation of the stress-strain curve the same bilinear law as for pure titania has been used in the inverse modeling of nanoindentation. The Young's modulus being equal to 5 GPa has been taken from experiment and work-hardening has been adjusted till the experimental Force-Penetration curve fits with the calculated one (Figure 7b). A stress-strain curve with σ_y = 0.150 GPa and h = 3.6 GPa has been determined as the constitutive law for the polyelectrolyte film.

4.4 Determination of Young's modulus of bio-inspired TiO_2/PE nanocomposites

4.4.1 Determination of Young's modulus with FE-simulations of nanoindentation test

In order to define the Young's modulus of a layered TiO_2/PE structure and to analyse the effect of the thickness ratio of the constituent phases on the Young's modulus of the nanocomposite, FE-simulations of indentation tests of the layered nanostructures have been performed. The input Young's moduli and stress-strain curves for TiO_2 and PE were those obtained from inverse modeling of the constituents. Taking the stress-strain curve of the constituents (compare Figure 5a and 7a) into account, nanoindentation tests have been calculated using finite elements and the Young's modulus has been defined from the initial segment of the unloading curve following the procedure of Oliver and Pharr, as explained in section 2.1. Numerical nanoindentation test experiments with the TiO_2/PE nanocomposite have been performed with variation of the thickness of the PE-layers (5 nm, 10 nm, 15 nm and 20 nm). The indenter was typically pushed into the top layer TiO_2 with a thickness of 100 nm. The whole layered structure consists of 5 TiO_2 layers with a thickness of 100 nm each and 5 PE-layers. In each case, the total film thicknesses were 525 nm, 550 nm, 575 nm and 600 nm respectively. The achieved penetration depth in the FE-simulations was limited to 120 nm (ca. 20 % of the total thickness of the film), to avoid an influence of the substrate). Shown in Figure 8 are the contour plots of von Mises stress at different instances of time during the indenter penetration.

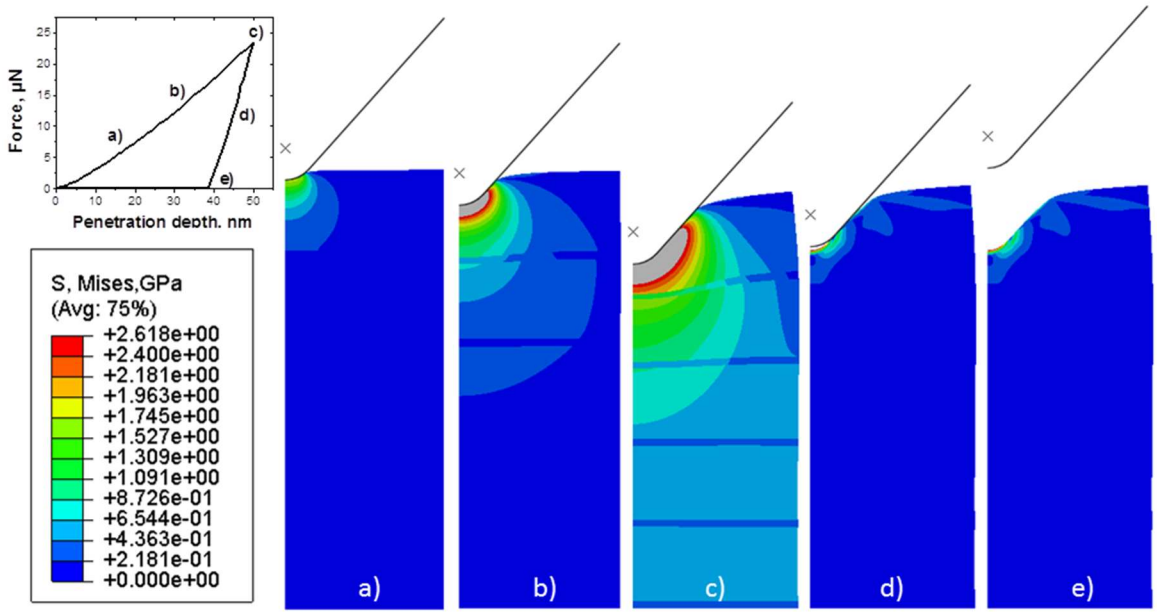

Figure 4-8: Contour plots of von Mises stresses at different stages of simulations of a nanoindentation test of a five-fold layered TiO_2/PE-nanocomposite, the layer thickness of TiO_2 is 100 nm and the layer thickness of PE is 5 nm. a) and b) show two stages of the beginning of the indention process, c) shows the maximum depth of the indenter and d) and e) show two stages of relaxation during unloading of the material. The stress is distributed up to the base of the model. The figure in the left upper corner shows the stages a) to e) on the Force-Penetration curve

As can be seen from Figure 8, as the indenter penetrates the specimen the contact area increases and the regions of stress perturbation expand (green colour in Figure 8c, the level of von Misses-stress also increases, which is depicted with lighter blue colour in Figure 8b and c. As the indenter is uplifted from the material the average stress level decreases (Figure 8d and 8e).

The comparison of the experimentally obtained Force-Penetration curve of the layered nanocomposite (with a PE-layer of thickness of TiO_2 being equal to 10 nm) with the one, derived from FE- simulations of the nanoindentation test of a layered nanocomposite is shown in Figure 9.

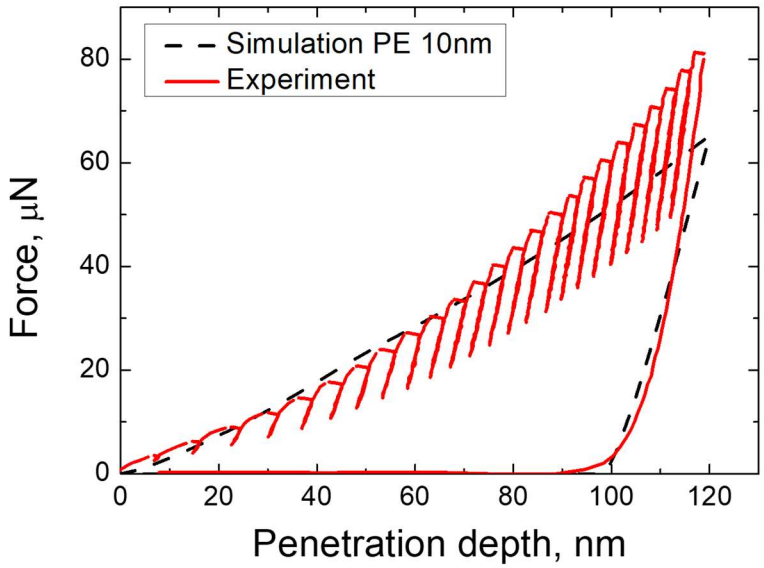

Figure 4-9: Comparison of the Force-Penetration depth curves of the layered TiO_2/PE-nanocomposite (thickness of TiO_2-layer is 100 nm and the thickness of PE is 10 nm), obtained from FE-simulation of the nanoindentation test and from experiment. The curve of the nanoindentation results possesses a monotonic character (dashed curve) and underestimates the results of the experiment

It is seen that the slope of the initial part of the unloading curve (after achieving 120 nm), obtained by simulation is smaller than the slope of the experimentally obtained curve. This means that the produced layered structure of the nanocomposite possesses higher strength properties than one expected from the rule of mixture from the constituents.

Figure 10a shows the Force-Penetration curves of multi-layered nanocomposites, obtained from nanoindentation simulations for different thicknesses of PE (5 nm, 10 nm, 15 nm and 20 nm), the thickness of the TiO_2 layer was equal to 100 nm in all cases. The experimentally measured Young's modulus of the layered structure is higher by a maximum of approximately 22 % (Fig. 10b) than the one derived from finite element simulations of nanoindentation tests. The reason of the higher Young's modulus of the layered structure with a peak value at a thickness ratio of 10 could be the formation of mineral bridges with a very high Young's modulus as is discussed in the following chapter.

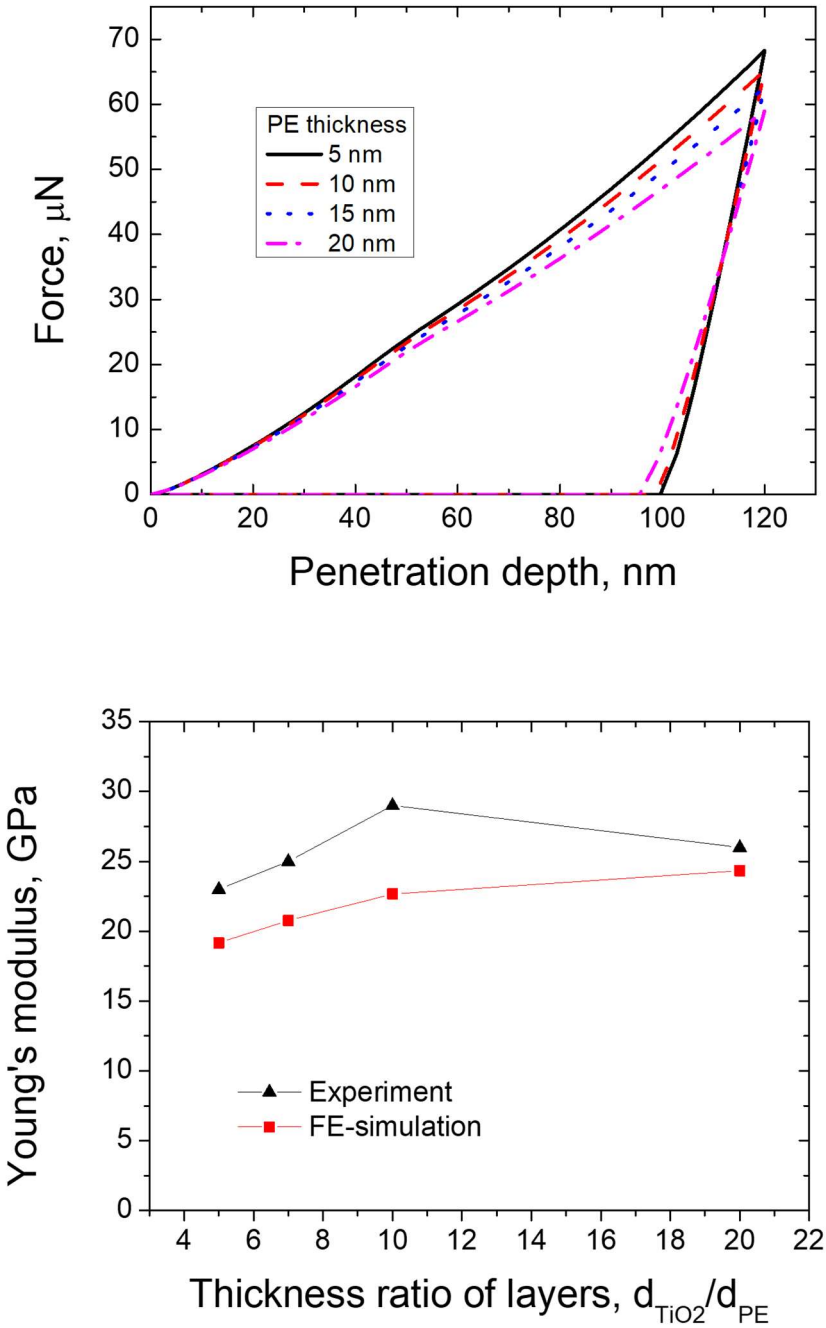

Figure 4-10: a) Force-Penetration curves of multi-layered nanocomposites, obtained from nanoindentation simulations for different thicknesses of PE (5 nm, 10 nm, 15 nm and 20 nm), the thickness of the TiO_2 layer was the same (100 nm) in all cases; b) The dependence of Young's modulus of the layered TiO_2/PE-nanocomposite on the thickness ratio of the constituents

4.4.2 The influence of mineral bridges

In a number of publications on biological and bio-inspired materials a lot of attention is paid to the effect of mineral bridges in the soft phase with respect to an enhancement of the resulting mechanical properties of the composite.[6][13][34] In the work of Song et al. a direct observation of a microstructure in the organic matrix layers of nacre was obtained with a transmission electron microscope.[9] The existence of mineral bridges in nacre was confirmed and it was shown that the microarchitecture of nacre should be described as a "brick-bridge-mortar" arrangement rather than a traditional "brick and mortar" one. This is supported through experimental work of Schaffner et al. where the authors describe statistically (and supplemented by AFM, SEM, and TEM images) the growth of nacre with the help of mineral bridges.[12] In a work of Meyers et al. the function of the soft protein layer (the soft phase or the mortar) of nacre is described as to provide small holes with a diameter of 50 nm. These holes enable the formation of mineral bridges between the hard layer of nacre.[35] It is remarkable, that mineral bridges are observed in artificially made TiO_2/PE-nanocomposites, where the mineral bridges are clearly pronounced at a definite thickness ratio of TiO_2 and PE layers and the resulting Young's modulus of the composite is found to be higher than that of its components.[36] In Figure 11 a cross-sectional transmission electron microscopy image of an artificially produced TiO_2/PE film is shown. The organic layers appear as bright regions with a thickness of 5 nm (Figure 11a), 10 nm (Figure 11b) and 20 nm (Figure 11c). We assume that the artificial mineral bridges consist out of TiO_2, but not in its amorphous phase. TiO_2 changes from the amorphous state to a crystal state (rutile). TEM images from a nanocomposite like the one analysed here showed possible signatures of TiO_2 nanocrystals.[8] In a work of Ismagilov et al. it was shown that the preparation of TiO_2 nanoparticles is influenced by the pore size of the gel used in preparation.[37] With smaller pore size, the TiO_2 particles change from the anatase crystal system to the rutile crystal system.[37] Also the likelihood that rutile crystals grow gets higher with a higher acid preparing solution.[38] The CBM used to generate the thin TiO_2 films also contained a low PH-value.[8] Based on these considerations, it seems very likely that rutile crystals are formed and even more likely that they exist as part of the connecting bridges (because of the small pores generated by the PE-layer). The Young's modulus for these TiO_2-bridges is then that of rutile TiO_2 (E = 282.67 GPa). [39][40]

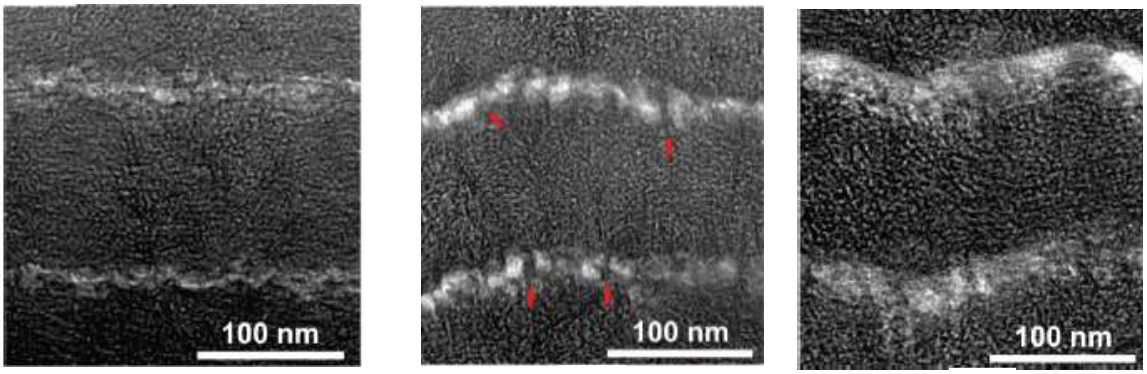

Figure 4-11: Cross-section of PE/TiO_2 composite film with a TiO_2 layer of 100 nm thickness and a PE layer of nominal thickness of a) 5 nm, b) 10 nm with the marked mineral bridges and c) 20 nm.[25] Reprint with permission from Burghard, Z.; Zini, L.; Srot, V.; Bellina, P.; van Aken, P.A.; Bill J., Toughening through nature-adapted nanoscale design, Nano letters 2009 American Chemical Society, 9(12), 4103 8. Copyright 2009 American Chemical Society

The experimentally observed dependence of Young's modulus of layered TiO_2/PE-nanocomposites on the thickness ratio of its constituents is shown in Figure 12, where the maximum value of Young's modulus, which matches the thickness ratio being equal to 10, is clearly pronounced.

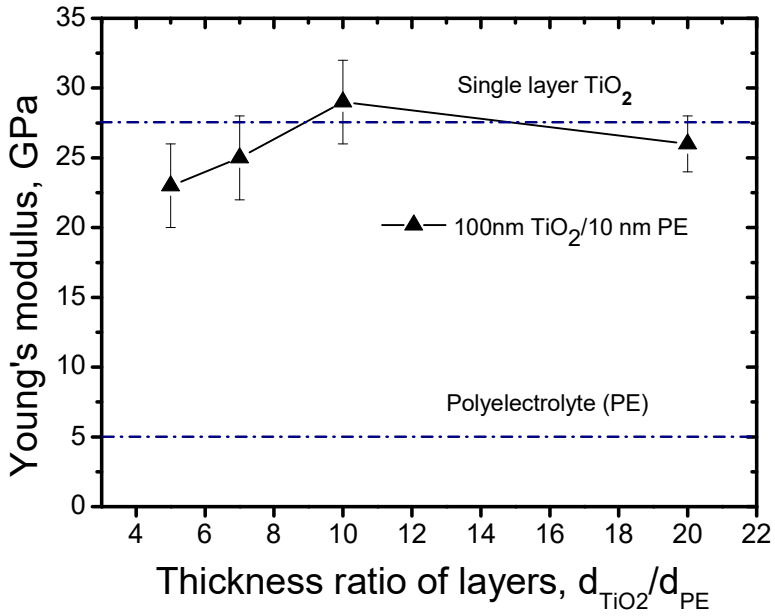

Figure 4-12: Experimentally obtained dependence of Young's modulus on different thickness ratios of oxide and polyelectrolyte layers.[25] Reprint with permission from Burghard, Z.; Zini, L.; Srot, V.; Bellina, P.; van Aken, P.A.; Bill J., Toughening through nature-adapted nanoscale design, Nano letters 2009 American Chemical Society, 9(12), 4103 8. Copyright 2009 American Chemical Society

For thicker and thinner PE-layers, interpenetration of the PE-layer through TiO_2-bridges is less pronounced, although still some connections between the inorganic layers exist in the form of isolated TiO_2 bridges. The width of the bridges amounts up to 10 nm and is somewhat smaller as compared to the typical width of 50 nm documented for mineral bridges in natural nacre. In spite of the fact that mineral bridges in nacre have been investigated experimentally, investigations on simulations of mineral bridges in nacre and artificial nacre are lacking in literature. In the following section the modeling of layered structure with mineral bridges is first performed with an analytical model.

4.4.3 Analytical model of Young's modulus of layered structures with mineral bridges

As can be seen from the comparison of the experimentally obtained dependence of the Young's modulus of layered TiO_2/PE-nanocomposites on the layer thickness of its constituents and the one obtained from FE-simulations of the nanoindentation tests (Figure 10b), there exists a quantitative and qualitative difference between this two curves. From the experimental investigations of the microstructure of the TiO_2 nanocomposite (Figure 11) it

is known that mineral bridges are clearly pronounced at a thickness ratio of the constituents being equal to 10 and they are less pronounced at the thickness ratios of the constituents of 5, 7 and 20 as well.

To analyse and explain the difference in the Young's moduli, the influence of the mineral bridges with a high Young's modulus is taken into account with an analytical model.

A rule-of-mixture-type formula for the Young's modulus of the composite (E_c) has been derived by Voigt assuming that the average strain of each phase is equal to the applied strain (parallel model):[41]

$$E_C = f_A E_A + (1 - f_A) E_B \,, \qquad [8]$$

where f_A and f_B are the volume fractions of phases A and B of the composite, respectively, while E_A and E_B are the Young's moduli of the respective constituents.

Reuss proposed the so-called "reciprocal rule of mixture" to determine the elastic moduli by averaging strains, expressed in terms of stresses, assuming stress uniformity (serial model):[42]

$$1/E_C = f_A / E_A + (1 - f_A) / E_B \,. \qquad [9]$$

In Zahl et al. a new model is developed based on averaging two building blocks following the rule of mixture.[43] By considering different arrangements of the composite components (parallel to the loading direction or perpendicular to the loading direction), the resulting composite stiffness is given by a modified uniform strain model and a modified uniform stress model, respectively. Equal weighting of the models of Voigt and Reuss has been taken as an average input for these two models (parallel to the loading direction or perpendicular to the loading direction).

In the following this approach is applied to the present case of the layered TiO_2/PE-nanocomposites for taking the mineral bridges into account (Figure 13). As the calculational cell in Figure 13b is symmetric, only one-half of the cell (compare Figure 13c) has to be considered.

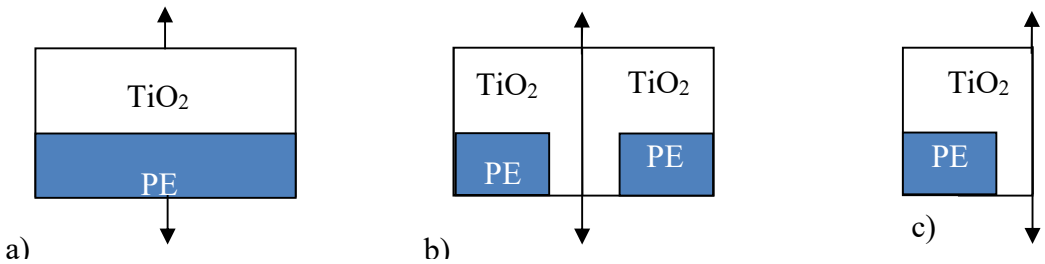

Figure 4-13: Schematic representations of calculational cells of a layered nanocomposite: a) without mineral bridges; b) in the presence of mineral bridge; c) unit cell (part of cell in Fig. 13b) that is considered in the calculations

The composite consists of inorganic layers, which are connected through mineral bridges in the organic layers. The bridges are arranged parallel to the loading direction. The Young's modulus of this calculational cell of the composite could be considered in two ways. For convenience the letter A was assigned to the TiO_2-phase and the letter B was assigned to the PE-phase (Figure 14).

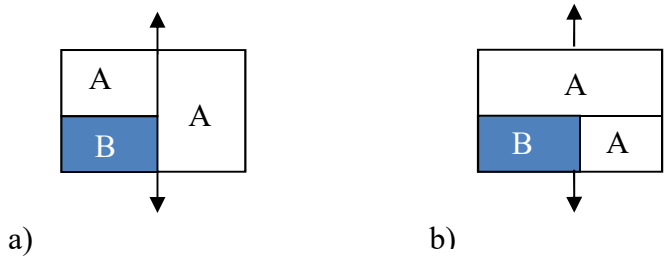

Figure 4-14: Schematic representation of the sequence of calculation of Young's modulus: a) left hand side of the unit cell is calculated according to the formula by Reuss and Young's modulus of the whole cell with Voigt's formula; b) First the lower part of the composite is calculated with Voigt's formula and then the Young's modulus of the specimen is calculated with the formula by Reuss

At first for the components A and B the formula by Reuss has been applied to the left-hand side of the calculational cell (Figure 14a). The resulting Young's modulus according to Voigt's formula has been derived.

For the case a) the following formula is valid:[43]

$$E_{C1} = \frac{f_{AB}}{\frac{f_{A/AB}}{E_A} + \frac{1 - f_{A/AB}}{E_B}} + (1 - f_{AB})E_A \ , \qquad [10]$$

where $f_{A/AB}$ is the volume fraction of the phase A in the left-hand side part of the A/B composite (Figure 14a), fAB is the volume fraction of the left-hand side of the composite in Figure 14a.

For the second case b) (see Figure 14b) the Voigt formula has been applied to the components A and B at the lower part of the calculational cell and the resulting Young's modulus was calculated according to the formula of Reuss.

Thus, for the case b) the following formula is derived:[43]

$$\frac{1}{E_{C2}} = \frac{f_{AB}}{f_{A/AB}E_A + (1 - f_{A/AB})E_B} + \frac{(1 - f_{AB})}{E_B} \ , \qquad [11]$$

where f_{AB} is the volume fraction of phase A and B at the left-hand side of the unit cell, $f_{A/AB}$ is the volume fraction of phase A of the subcell AB (left hand side volume of the unit cell) of the unit cell and E_A and E_B are the Young's moduli of phases A and B, respectively.

Following the reasoning mentioned in Zahl et al., the Young's modulus of the composite could be calculated as average value of the formulae 10 and 11:[43]

$$E_C = \frac{1}{2}(E_{C1} + E_{C2}) \ . \qquad [12]$$

The analysis of the influence of the volume fraction of mineral bridges on the Young's modulus of the nanocomposite at different thickness ratios of the constituents has been performed with the Zahl et al. unit cell model and the monotonic dependence of Young's modulus on the thickness ratio of the constituent phases for the different volume fraction of mineral bridges (1 %, 2 % and 4 %) has been obtained accordingly (Figure 15).

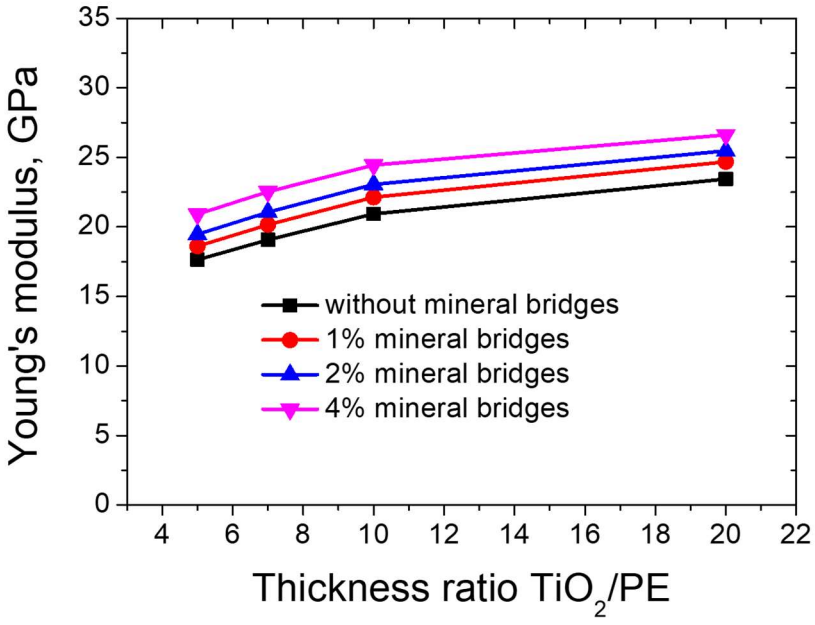

Figure 4-15: Comparison of the dependencies of the Young's moduli of the layered nano-composites on the thickness ratio of non-organic and organic phases for different volume fractions of mineral bridges

In order to define the Young's modulus for the different thickness ratio of the constituents (20, 10, 7 and 5), the Zahl et al. formulae have been applied and the volume fraction of mineral bridges has been determined for each thickness ratio of the constituents, taking into account that the maximum volume fraction of mineral bridges should not exceed 9 % (9 % represents a 10 nm thick PE layer fully filled with TiO_2; calculated with the help of an analytical model which is based on the model shown in the appendix) at a thickness ratio being equal to 10 (see Fig. 16). For comparison, the Zahl et. al. model with a constant volume fraction ratio (4 %) of bridges for all thickness ratios of the constituents is shown.

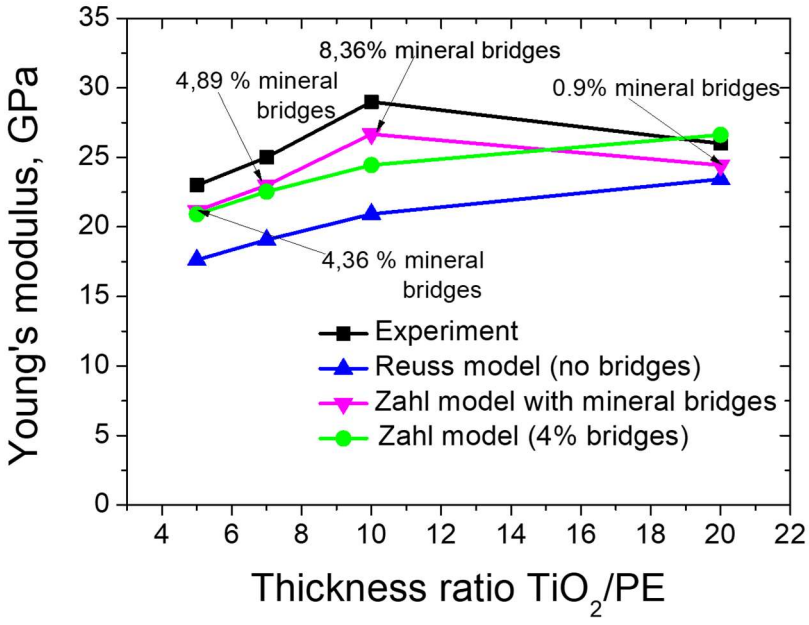

Figure 4-16: The dependence of the Young's modulus of the layered TiO_2/PE-nanocomposite on the thickness ratio of the constituents with the Reuss model without bridges and with the Zahl et al. model with variable volume fraction of mineral bridges (inversed triangle) and with constant volume fraction of mineral bridges (4 %) at different thickness ratios of the constituents (circle symbols) [43]

The volume fraction of the mineral bridges has been defined for each thickness ratio of the constituents TiO_2- and PE-phases (see Fig.16). With increasing thickness ratio of the constituents the volume fraction of the mineral bridges increases from 4.36 %, achieving its maximum (8.36 %) at a thickness ratio of 10 and then decreases (0.9 %) for the thickness ratio of the constituents being equal to 20.

Moreover, there exists still a quantitative difference between the experimentally defined curve and the analytically defined Young's modulus with the Zahl et al. model.[43] The reason is that one should take into account the higher value of the Young's modulus of the mineral bridges, as these nanoscale bridges have by virtue of their dimensions (10 nm in diameter) a Young's modulus that reaches the value of bulk rutile TiO_2.

In order to take this higher value of the Young's modulus of the mineral bridges of ca. 282 GPa into account, the Zahl et al. formula has been modified by taking into account the higher Young's modulus of the mineral bridges.[43] The volume fraction of the mineral

bridges has been defined which match the Young's modulus for different thickness ratios as obtained in the experiments of nanoindentation. The results are shown in Figure 17.

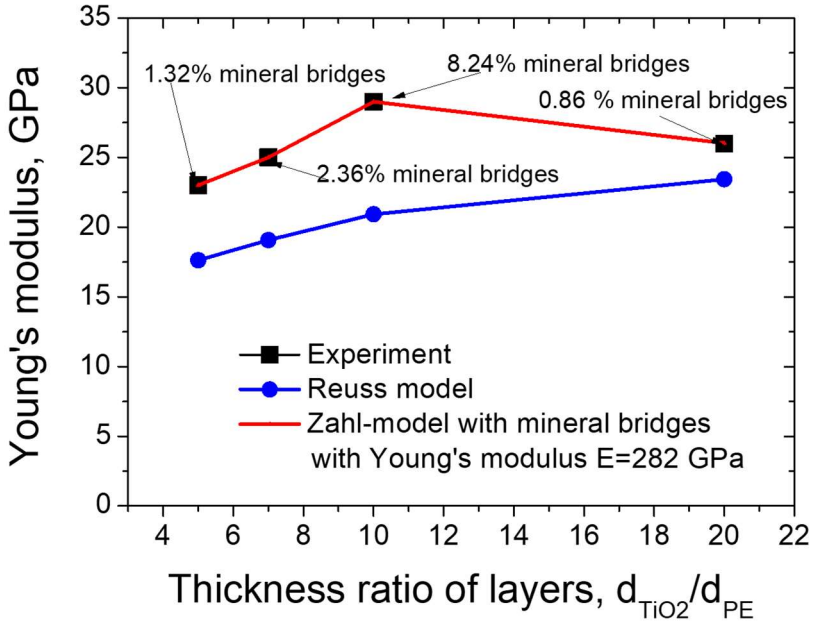

Figure 4-17: The dependence of the Young's modulus of the layered TiO_2/PE-nanocomposite on the thickness ratio of the constituents. Only with taking into account a very high Young's modulus for the bridges, the results of the experiment can be reached with the Zahl et al. model (experimental curve and the curve calculated with the Zahl et al. model are overlapping)

4.4.4 FE-simulations of nanoindentation of layered structures with mineral bridges

The influence of mineral bridges on the dependence of Young's modulus of bio-inspired layered TiO_2/PE-nanocomposites has also been studied in FE-simulations of nanoindentation tests. Approximately the same volume fractions of mineral bridges for each thickness ratios of the nanostructured nanocomposites as in the analytical model have been considered. Taking into account that the width of each mineral bridge in the TiO_2/PE nanocomposite is about 10 nm, the total volume fraction of the mineral bridges, defined from the analytical model has been spread among the bridges with the width of 10 nm (Figure 18). FE-simulations of the nanoindentation tests have been performed till a penetration depth of 120 nm.

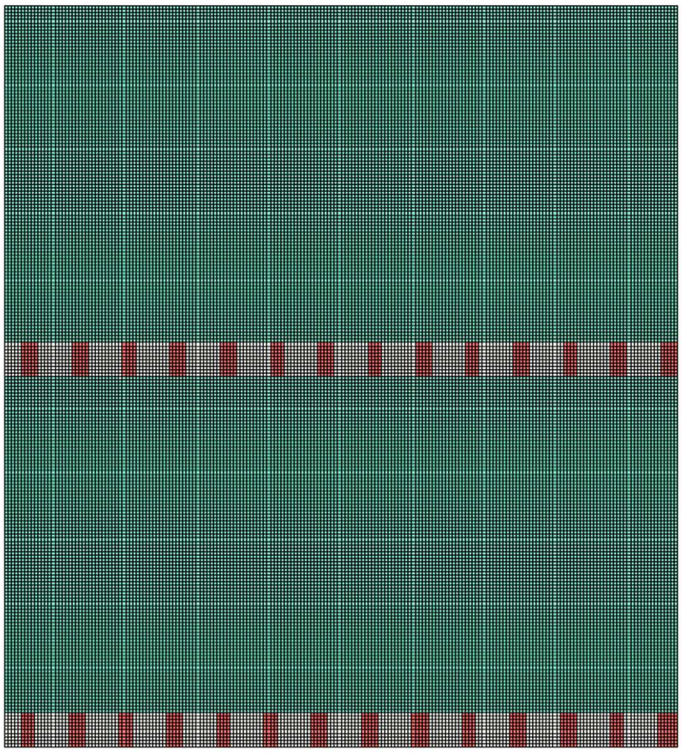

Figure 4-18: Finite element mesh of two layers of the nanostructured TiO_2/PE-nanocomposite, showing mineral bridges as a phase with different mechanical properties

The results of the simulations are presented in Figure 19. At all volume fraction ratios of the layers the results show good qualitative agreement with the experimentally gained results but underestimate the Young's modulus as obtained in the experiments and from the analytical model with taking into account the same volume fraction of mineral bridges. This can be attributed to the complex state of stress during indentation and the anisotropic nature of the layered material. For the verification of the results obtained from FE-simulations of the nanoindentation tests, the tensile test experiments have been simulated with the same volume fraction of mineral bridges.

As can be seen from the Figure 19 the best fit to experimental curves gives the analytical model with taking into account a variable volume fraction of mineral bridges.

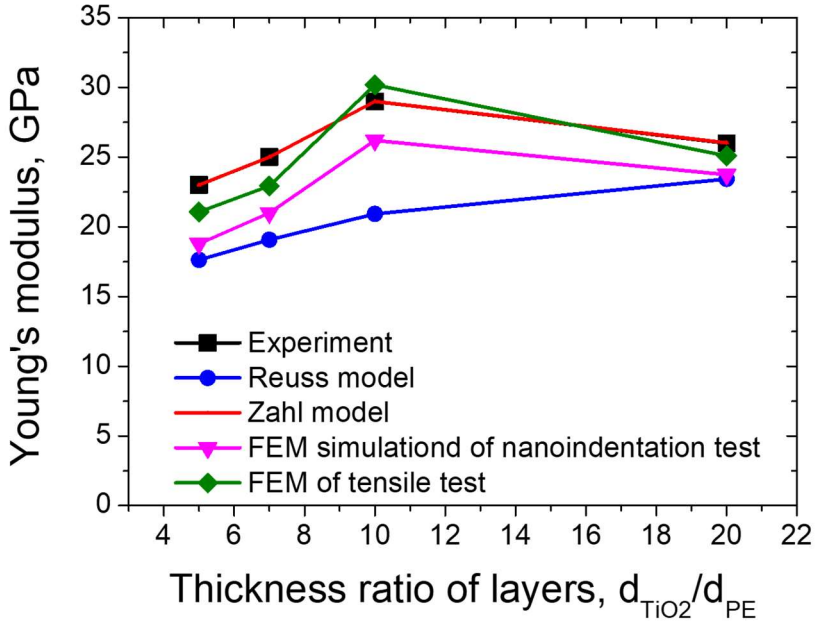

Figure 4-19: The dependence of the Young's modulus of the layered TiO_2/PE-nanocomposite on the thickness ratio of the constituents. The comparison of the experimentally defined Young's modulus with the one derived from FE-simulations of nanoindentation test. All models include mineral bridges with a very high Young's modulus of 282 GPa (experimental curve and the curve calculated with the Zahl et al. model are overlapping)

4.5 Conclusions

Inspired by the mechanical performance of nacre, a number of artificially-made materials, mimicking its structural design have been studied during the last decade. The subjects of this study are the mechanical properties of bio-inspired TiO_2/PE-layered nanocomposite, obtained by low-temperature chemical bath deposition and layer-by-layer technique. The influence of different thickness ratios of the constituents (organic (PE) and inorganic (TiO_2) phases) and the influence of mineral bridges on the Young's modulus of the nanocomposite has been investigated with analytical and numerical methods. The elasto-plastic stress-strain behavior of TiO_2- and PE-phases of the layered nanocomposites have been defined by inverse modeling based on FE-simulations of nanoindentation tests of the individual phases in comparison with experimental results of nanoindentation testing. The simulations of indentation tests with a 2D-axisymmetric model have been performed till penetration depths of 120 nm. It was found that due to the structural design of the layered structure the Young's modulus of the composite cannot be obtained by simply following the rule of

mixture of its constituents. The high Young's modulus is assumed to be achieved through the formation of mineral bridges. The considered bio-inspired material (TiO_2/PE) shows similar reinforcements through mineral bridges like nature shows in nacre. Only with the presence of different volume fractions of mineral bridges at each thickness ratios of constituents and a very high Young's modulus of these mineral bridges, the computer simulations and analytical calculations show results comparable to the results of the experiment. These bridges interconnect the hard layers like in nacre shells and reinforce the material. Additionally these bridges are small enough to be considered as a crystal. The bridges then possess different material properties compared to the amorphous TiO_2; their Young's modulus reaches the value of rutile TiO_2 which is ca. 282 GPa. With this theory the resulting Young's moduli of the experiment can be reproduced by the analytical and numerical models. By application of the here presented approach one can predict mechanical properties of artificially produced materials, mimicking geometry and reinforcement levels of the structure of nacre.

4.6 References

[1] H. Gao, B. Ji, I.L. Jäger, E. Arzt, P. Fratzl, Proceedings of the National Academy of Sciences U.S.A. 2003, 100, 5597.

[2] A.P. Jackson, J.F. V. Vincent, R.M. Turner, Proceedings of the Royal Society of London. Series B, Biological Sciences. 1988, 234, 415.

[3] H. Gao, International Journal of Fracture 2006, 138, 101.

[4] Jäger, P. Fratzl, Biophysical Journal 2000, 79, 1737.

[5] Biomimetic and Bioinspired Nanomaterials (Nanomaterials for Life Sciences (VCH)), Wiley-VCH2010.

[6] F. Barthelat, D. Zhu, Journal of Materials Research 2011, 26, 1203.

[7] S. Deville, E. Saiz, R.K. Nalla, A.P. Tomsia, Science (New York, N.Y.) 2006, 311, 515.

[8] Ž. Burghard, A. Tucic, L.P.H. Jeurgens, R.C. Hoffmann, J. Bill, F. Aldinger, Advanced Materials 2007, 19, 970.

[9] F. Song, A.K. Soh, Y.L. Bai, Biomaterials 2003, 24, 3623.

[10] D.R. Katti, S. Pradhan, K. Katti, Reviews on Advanced Materials Sciences 2004, 6, 162.

[11] F. Song, X.H. Zhang, Y.L. Bai, Journal of Materials Research 2011, 17, 1567.

[12] T. Schäffer, C. Ionescu-Zanetti, Chemistry of Materials 1997, 4756, 1731.

[13] Z. Tang, N.A. Kotov, S. Magonov, B. Ozturk, Nature Materials 2003, 2, 413.

[14] T. Liu, B. Chen, J.R.G. Evans, Bioinspiration & Biomimetics 2008, 3, 016005.

[15] Sellinger, P. Weiss, A. Nguyen, Y. Lu, Nature 1998, 394, 256.

[16] X. Li, W.-C. Chang, Y.J. Chao, R. Wang, M. Chang, Nano Letters 2004, 4, 613.

[17] X. Li, Z.-H. Xu, R. Wang, Nano Letters 2006, 6, 2301.

[18] X. Li, Z. Huang, Physical Review Letters 2009, 102, 075502.

[19] M. Kopernik, M. Pietrzyk, Archives of Metallurgy and Materials 2007, 52, 299.

[20] G. Tang, Y.-L. Shen, D.R.P. Singh, N. Chawla, International Journal of Mechanics and Materials in Design 2008, 4, 391.

[21] D.R. Katti, K. Katti, J. Sopp, M. Sarikaya, Computational and Theoretical Polymer Science 2001, 11, 397.

[22] K.S. Katti, D.R. Katti, Materials Science and Engineering: C 2006, 26, 1317.
[23] F. Barthelat, H.D. Espinosa, MRS Proceedings 2011, 844, 1.
[24] Bhattacharya, W. Nix, International Journal of Solids and Structures 1988, 24, 1287.
[25] J. Breuils, H. Pelletier, J. Krier, V. Vignal, Surface and Coatings Technology 2010, 204, 2068.
[26] R. King, International Journal of Solids and Structures 1987, 23, 1657.
[27] S. Bec, A. Tonck, J. Georges, J.-L. Loubet, Philosophical Magazine 1996, 74, 1061.
[28] W. Oliver, G. Pharr, Journal of Materials Research 1992, 7 (6), 1564.
[29] Sneddon, International Journal of Engineering Science 1965, 3, 47.
[30] Eds: A.F. McClintock, A.S. Argon, Mechanical Behavior of Materials, Addison-Wesley 1966.
[31] J. Hollomon, Transactions of the American Institute of Mining, Metallurgical and Petroleum Engineers 1945, 162, 268.
[32] W. Ramberg, W. Osgood, National Advisory Committee for Aeronautics, Washington, D.C., Technical Note No. 902 1943, 07.
[33] Y. Gaillard, V.J. Rico, E. Jimenez-Pique, A.R. González-Elipe, Journal of Physics D: Applied Physics 2009, 42, 145305.
[34] F. Barthelat, Philosophical Transactions. Series A, Mathematical, Physical, and Engineering Sciences 2007, 365, 2907.
[35] M.A. Meyers, A.Y.-M. Lin, P.-Y. Chen, J. Muyco, Journal of the Mechanical Behavior of Biomedical Materials 2008, 1, 76.
[36] Ž. Burghard, L. Zini, V. Srot, P. Bellina, P. a Van Aken, J. Bill, Nano Letters 2009, 9, 4103.
[37] Z.R. Ismagilov, L.T. Tsikoza, N. V Shikina, V.F. Zarytova, V. V Zinoviev, S.N. Zagrebelnyi, Russian Chemical Reviews 2009, 78, 873.
[38] S. Watson, D. Beydoun, J. Scott, R. Amal, Journal of Nanoparticle Research 2004, 1, 193.
[39] J. Shackelford, W. Alexander, CRC Materials Science and Engineering Handbook, CRC Press Inc., Page 5102000.
[40] Z. Jian-Zhi, W. Guang-Tao, L. Yong-Cheng, Chinese Physics Letters 2008, 25, 4356.
[41] W. Voigt, Annalen Der Physik 1889, 274, 573.
[42] Reuss, ZAMM - Journal of Applied Mathematics and Mechanics / Zeitschrift Für Angewandte Mathematik Und Mechanik 1929, 9, 49.
[43] D. Zahl, S. Schmauder, R.M. McMeeking, Zeitschrift Für Metallkunde 1993, 84.11, 803.

Appendix A

In Figure A 1a the unit cell of the composite with four mineral bridges is shown. The unit cell can be represented as a cell with accumulated thickness of a single mineral bridge (Fig. A 1b). The geometry of the cell is represented in the following figure:

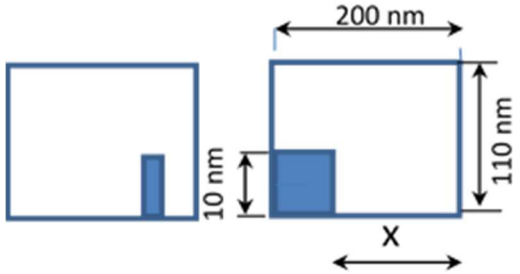

Figure 4-A1: Schematic representation of a simulation cell for calculating Young's modulus with four equidistant identical mineral bridges: left: the cell with mineral bridges is shown explicitly; right: another representation of a calculational cell with identical overall properties accummulated thickness of mineral bridges-x

As mentioned in the paper (Chapter The influence of mineral bridges4.4.2), the calculations of the Young's modulus of the nanocomposite with mineral bridges have been performed according to Zahl et al.'s formula as averaged value from two calculational cells Fig. A 2a and A 2b:[43]

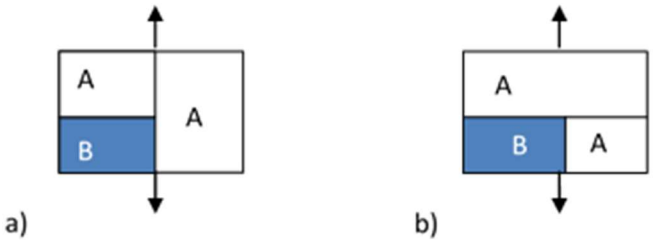

Figure 4-A2: Schematic representation of the consequence of calculation of Young's modulus. a) First the left part of the cell is calculated according to the formula by Reuss and after that the whole cell is calculated with the Voigt's formula; b) First the lower part of the composite is calculated with the Voigt's formula and then the Young's modulus of the specimen is calculated with the formula by Reuss [43]

According to these schemes two formulas have been derived:

$$E_{C1} = \frac{f_{AB}}{\frac{f_{A/AB}}{E_A} + \frac{1 - f_{A/AB}}{E_B}} + (1 - f_{AB})E_A \quad , \qquad [13]$$

which matches the case in Fig. A 2a, and

$$\frac{1}{E_{C2}} = \frac{f_{AB}}{f_{A/AB}E_A + (1-f_{A/AB})E_B} + \frac{(1-f_{AB})}{E_B}\ , \qquad [14]$$

which matches the case represented in Fig. A 2b.

The Young's modulus of the composite with mineral bridges could be calculated according to the following formula [43]:

$$E_C = \frac{1}{2}(E_{C1} + E_{C2})\ . \qquad [15]$$

By equating E_c obtained from the last equation to the experimentally observed one the accumulated thickness of mineral bridges can be obtained. Following the first scheme, one should calculate first the Young's modulus of the left-hand side of the composite in Fig. A 1a, (as defined by Reuss formula beeing equal to 26.49), while the Young's modulus of the calculational cell in Fig. A 2a can be written as follows:

$$E_{C1} = (200-x)*E_{AB}/200 + x*E_A/200, \qquad [16]$$

with E_{AB} = 26.49 GPa, and E_A = 38.43 GPa.

Young's modulus of the TiO_2-phase was taken to be 38.43 GPa, which matches the Young's modulus of the composite obtained from FE-simulations of the nanoindentation test from experiment being equal to 26.49 GPa. Young's modulus of TiO_2 was calculated from the analytical (Reuss) formula:

$$1/E_C = f_A/E_A + (1-f_A/E_B)\ . \qquad [17]$$

For the calculational cell in Fig. A 2b) for the lower part of the composite we apply the (Voigt) formula:

$$E_{AB} = (200-x)*E_{B/AB}/200 + x*E_{A/AB}/200, \qquad [18]$$

and the Young's modulus of the unit cell in Fig. A 2b is defined by (Reuss) formula:

$$1/E_{c2} = 100/110*E_A + 10/110*E_{AB}\ . \qquad [19]$$

By substituting the experimentally obtained value Ec = 29 GPa and the Young's modulus of the nanocomposite obtained with both calculational cells Ec1 and Ec2 into the formula:

$$E_C = \frac{1}{2}\left(E_{C1} + E_{C2}\right) , \qquad [20]$$

The accumulated width of the mineral bridges has been obtained from the specific calculational cell geometry (length is equal to 200 nm) and the accumulated width is equal to 42 nm. Taking into account that the width of each mineral bridge is about 10 nm, we could define that in the calculational cell with the width of 200 nm, about 5 bridges are observed and the volume fraction of mineral bridges is equal to 1.9 %.

5 Proteinbindungseigenschaften an Zinkoxid

Die nächste Veröffentlichung beschreibt einen virtuellen keramischen Verbundwerkstoff, der aus Zinkoxid (ZnO) und Peptiden mit hoher Bindungsaffinität für ZnO besteht. Der molekulare Bindungsmechanismus von Peptiden an ZnO wurde durch MD-Simulationen untersucht und die Bindungsaffinitäten bewertet. Diese werden durch Zugversuche mit unterschiedlichen Geschwindigkeiten in der MD-Simulation bestimmt. Aus den Ergebnissen einer MD-Simulation wurden die notwendigen Parameter für FEM-Simulationen generiert, eine sogenannte Multiskalensimulation. Die Rissausbreitung an der Grenzfläche zwischen ZnO und einer Peptidschicht werden untersucht, unter der Annahme, dass sich der Riss nicht primär innerhalb der Peptidschicht ausbreitet. Die Rissausbreitung in der Peptidschicht könnte durch Vernetzung der Peptide oder durch die Verwendung längerer Polypeptide statt kurzer Peptide wie im hier vorgestellten Modell verhindert werden:

IV. Schäfer, I., Lasko, G., Do, T. A., Pleiss, J., Weber, U., & Schmauder, S. (2014). Peptide-zinc oxide interaction: Finite element simulation using cohesive zone models based on molecular dynamics simulation. Computational Materials Science, 95, pp. 320–327.

Der Anteil meiner Arbeit in der Veröffentlichung umfasst:

- Erstellung des Manuskripts, der Diagramme und der Bilder (Anteil meiner Arbeit 100 % außer der Abschnitte und Bilder, die die Molekular-Dynamik-Simulationen betreffen, diese wurden von Do, T. A. erstellt)
- FEM-Simulationen, Aufstellung, Durchführung, Analyse, Diskussion (Anteil meiner Arbeit 100 %)
- Diskussion der Ergebnisse und Optimierung der Simulation in Zusammenarbeit mit den Mitautoren (Anteil meiner Arbeit 60 %)

Peptide - zinc oxide interaction: finite element simulation using cohesive zone models based on molecular dynamics simulation**

I. Schäfer[1], G. Lasko[1], T. A. Do [2], J. Pleiss[2], U. Weber[1], S. Schmauder[1]

[1]Institute for Materials Testing, Materials Science and Strength of Materials (IMWF), Pfaffenwaldring 32, D-70569 Stuttgart

Corresponding Author: Immanuel Schäfer,

Immanuel.Schaefer@imwf.uni-stuttgart.de

Tel: +49 711 685 62734

[2]Institute of Technical Biochemistry, Allmandring 31, D-70569 Stuttgart

[**] The authors acknowledge funding by the German Research Foundation (Deutsche Forschungsgemeinschaft, DFG) project number Schm 746/88-1 and PL 145/8-1

Abstract

In this study, a multiscale simulation approach of coupling molecular dynamics (MD) and finite element method (FEM) simulations was established to investigate the mechanical properties of a ZnO-peptide material. MD simulations of a single 6-mer peptide adsorbed on the polar ZnO(0001)-O surface were performed to calculate the adsorbed peptide conformations and their adsorption force parameters, which were used to estimate mechanical properties of the ZnO-peptide composite material in three point bending tests using FEM simulations. The results from the multiscale simulations revealed that the influence of the Elastic modulus of the peptide on the material properties of the composite differs depending on the elastic properties of the cohesive zone. For developing a nanocomposite based on ZnO and a peptide, this dependency should be carefully considered and used to create stronger nanocomposites. Based on these simulation results, a set of binding affinities of the peptide and mechanical properties like the crack opening displacement of ZnO-peptide material could be predicted.

Keywords: *biomimetic, bio-inspired, zinc oxide (ZnO), peptide, nano composite, MD simulation, FEM simulation, multiscale, COD.*

5.1 Introduction

In material science, especially for metals, multiscale simulations have been recently applied to use the results of molecular dynamics (MD) simulations as input data for other simulation tools like finite element method (FEM) simulation or phase field simulations. Molnar et al. reported on multiscale simulations on the coarsening of Cu-rich precipitates in α-Fe using kinetic Monte Carlo, molecular dynamics and phase-field simulations [1]. Similar multiscale simulations were also performed on metal/ceramic materials where fracture on the metal/ceramic interface was analyzed [2]. In the present work, a method is developed to combine MD simulations of peptide binding to a ceramic surface with FEM simulations. Coupling molecular dynamics simulations to FE simulations is important for bridging the gap between nanoscale and micro- or macroscale. MD simulations have been successfully applied to study atomistic effects in nanoscale of biological molecules [3,4], although they are usually limited to microsecond timescale simulations for typical systems (106-105 atoms) [5], while FEM simulations in the framework of conventional continuum mechanics are used for macroscale material behavior [6]. A combination of the two simulation methods is able to predict mechanical properties of organic-inorganic nanocomposites as shown in [7].

A virtual ceramic composite material which consists of zinc oxide (ZnO) and peptides with a high binding affinity for ZnO was examined for its mechanical properties. The molecular binding mechanism of peptides to ZnO was studied by MD simulations and the binding affinities were evaluated.

The material properties of layered structures of peptides and zinc oxide are of high interest for the industry. The use of ZnO is based on its favorable properties making it well suited for many applications [8], which leads to the need to understand the mechanical properties of peptides adsorbed on the ZnO surface material. The use of ZnO includes construction of solar cells, luminescent materials and acoustic devices [8–11]. Within the last decade, many attempts have been made to study the adsorption of peptides to the ZnO surface to prepare nanostructured hybrid materials [12–17]. It was also demonstrated that ZnO-binding peptides could be used as bioactive layers for surface functionalization and modification [18] and that nano-sized structures of ZnO have unique material properties and a remarkable performance in electronics, optics, and photonics [19]. One major disadvantage of ZnO is that it is a relatively soft material [20]. A reinforcement of the mechanical properties of

these nanomaterials could lead to longer life spans and an improved usability of these systems in environments where resistance against mechanical stress is essential [21]. An exciting hybrid material with superior mechanical properties can be found in nature: nacre, the inner layer of mollusk shells. Nacre contains a relatively brittle mineral phase that is combined with an organic microstructure resulting in an increase of toughness of the composite compared to the mineral phase alone which is reinforced through microstructures

Nacre is hierarchically structured, it consist of a layered brick (95 % aragonite – platelets) and mortar structure (5 % organic components like proteins) [22]. Viewed in more detail, nano-mineral-bridges between the platelets get visible. Artificial nacre with material properties that are optimized for the respective application would be highly appreciated in engineering [23,24]. Based on a mechanical model derived from multiscale simulations, optimal peptides can be designed as a basis of future ZnO-peptide hybrid materials with optimized mechanical stabilities.

ZnO-binding peptides (6- to 12-mer) are usually selected through biopanning techniques of phage display [13,16] or bacterial surface display [25–27] peptide libraries. In a previous study [16], the adsorbed conformations and the adsorption free energy of peptide 31 (amino acid sequence HHGHSPTSPQVR) was investigated using MD simulations. Peptide 31 was previously identified by phage display [17]. It was found that the peptide preferred the negatively charged ZnO(0001)-O surface. To investigate peptide binding to this surface, peptide 31-6 with amino acid sequence HHGHSR was designed which was derived from peptide 31. In a first step, the adsorption properties of peptide 31-6 were studied by MD simulations to obtain mechanical properties on the atomic level. In a second step, the thus obtained nanoscopic mechanical properties were used for a three point bending test of a ZnO-peptide composite to characterize the macroscopic mechanical properties, thus bridging the gap between MD simulations and FEM simulations as within a multiscale approach.

The necessary parameters for FEM simulations were generated from the results of the MD simulations. Because the Elastic modulus (EM) of the peptide is not exactly known, a sensitivity analysis with different elastic moduli for the peptides layer was made for the peptide conformation.

In our study, crack propagation at the interface between ZnO and a peptide layer was studied, assuming that the crack will not primarily propagate within the peptide layer. Crack

propagation in the peptide layer could be prevented by crosslinking the peptides or by using longer polypeptides rather than short peptides as in the model presented here.

5.2 Material and Methods

5.2.1 Using MD simulations to estimate the adsorption affinity of the peptide

The adsorption force of peptide 31-6 on the ZnO surface were determined from the MD simulations of a single peptide adsorbed and desorbed on the negative polar ZnO(0001)-O surface. The MD simulation procedure involves three stages: first, the peptide was pulled slowly towards the surface using steered MD simulations. Second, the pulling force was removed after the peptide contacted the surface, and the peptide was equilibrated on the ZnO surface. Third, the peptide was pulled away from the surface in the desorption process using steered MD simulations, as described previously [16]. All MD simulations were performed in explicit water at constant temperature (300 K) and pressure (1 bar) using Berendsen's thermostat implemented in the simulation package GROMACS 4.5.3 [28]. Further details of the simulation can be found in the appendix.

To obtain different binding conformations of the peptide, three independent steered MD simulations were performed where peptide 31-6 was pulled towards the ZnO(0001)-O slab model and equilibrated at the surface. The last snapshot of each equilibrium simulation was chosen as the adsorbed conformation of the peptide.

To calculate the adsorption force, peptide 31-6 was pulled away from the ZnO surface in the desorption process using steered MD simulation. The external force applied in the steered MD simulation was monitored to measure the adsorption force. Three different conformations of the adsorbed peptide were used as starting conformations for the steered MD simulations. In order to evaluate the dependence of the potential of mean force (PMF) on different pulling velocities, the peptide was pulled with 4 different velocities (0.25, 0.5, 1.0, and 1.5 nm/ns). Each simulation was repeated 10 times with different initial velocities.

5.2.1.1 MD simulation details

All MD simulations were performed using the standard AMBER force field [29,30] for the peptide and TIP3P model for water [29]. Histidines and arginines were simulated in their protonated state, while the N-terminus and the C-terminus were simulated in their protonated and deprotonated state, respectively. The ZnO slab was modeled based on a wurtzite crystal structure with lattice parameters of a = 0.3249 nm and c = 0.5207 nm [16,31]. The

force field parameters for ZnO were used based on initial computations by Raymand [32] using atomic partial charge values of 1.026e and -1.026e for Zn and O atoms, respectively. To reduce the dipole moment of the polar ZnO(0001) surface, 25 % of the negatively charged oxygen atoms on the O-terminated side and 25 % of the positively charged Zinc atoms on the Zn-terminated side were removed, as described by Kornherr [33]. The negative surface charge of the O-terminated side is in agreement with the experimentally determined zeta potential at neutral pH [17]. In aqueous environment, water adsorbed to the negatively charged ZnO(0001)-O surface forming ordered water layers.

After equilibration of peptide 31-6 in explicit water for 5 ns at a distance of 6 nm from the ZnO surface, the adsorption was simulated by pulling the center of mass of the peptide along the z-axis towards the ZnO surface in a steered MD simulation of 20 ns, in which a spring constant of 3000 kJ mol-1 nm-1 and a decrease in pulling velocity from 0.5 to 0.1 nm ns-1 were used. When the peptide contacted the ZnO surface within a center of mass distance of 1.1 nm, the peptide was simulated for 5 ns without external forces to reach an equilibrium state for the system. The peptide conformation at the end of this equilibration time was used as an adsorbed conformation for the next MD simulations in the adsorption process. The adsorption force (f) during a steered MD simulation is monitored and can be represented at time t by the following equation:

$$f(t) = k[(Z_{peptide}(0) + vt) - Z_{peptide}(t)], \quad [1]$$

where k is the spring constant, v is the pulling velocity, and $Z_{peptide}$ (t) and $Z_{peptide}(0)$ are the z coordinates of the center of mass of peptide 31-6 at time t and initial time 0, respectively. The rupture event during the desorption process is recognized when an anchor residue is detached from the ZnO surface meanwhile the force reaches a peak in the adsorption force profile.

5.2.2 FEM simulations

FEM simulations of a three point bending test of a ZnO/peptide composite were conducted. The peptide was simulated as one averaged peptide, which was calculated from the results obtained from three adsorbed conformations of the MD simulations. In a real bulk material, which would consist out of the three or even more peptide confirmations, the material properties of all peptide conformations would influence the results of the composite material and so an averaged peptide conformation will be used in the FEM simulations (compare

Table 3). FEM simulation was made with ABAQUS 6.11. To model the adhesive like bonding between ZnO and peptide, so called “cohesive elements” were used. The nature of the mechanical constitutive response or damage is based on the traction-separation law of the interface [34].

5.2.2.1 Variations of material properties

The material properties of the two components of the composite have to be defined. The properties of ZnO are described in Table 1. However, the Young`s modulus and the Poisson ratio of the peptide are not exactly defined. Therefore, a parameter study was performed to analyze the influence of these parameters. The isothermal compressibility (β_T) of the peptide, which is reciprocal to the factor *K* (bulk modulus), has the value of 0.04-0.116 GPa based on the MD simulation. Because only a specific loading geometry is considered here (normal to the ZnO surface) not the word Young`s modulus is used but Elastic modulus.

The Elastic modulus is defined through the following formula [35]:

$$E=3K^{*}(1-2V), \qquad [2]$$

where *V* is the Poisson ratio and *K* the bulk modulus.

The Poisson ratio normally has a value in between 0 and 0.5. A typical value for the Poisson ratio of amorphous materials is 0.3 [36] and does not vary widely for different amorphous polymers [37]. The value of an amorphous polymer like polystyrene, which has value of 0.3 [38] can therefore be used as a value for the Possion ratio of the protein. A sensitivity study including *K* and *E* was performed (Table 2) to study the influence of Poisson ration, isothermal compressibility and Elastic modulus, which might influence the results of the simulation as described previously [39].

Table 5.1: Young´s modulus and Poisson ratio for ZnO used for FEM simulations

Material	Poisson ratio	Young`s modulus [GPa]	Source
ZnO	0.356	35	[40], [41]

Table 5.2: Calculated values for Elastic modulus of the peptides based on isothermal compressibility

Poisson ratio	Isothermal compressibility (1/K) [GPa]	Elastic modulus [GPa]	
0.01	0.04	73.5	used in simulation
0.01	0.116	25.35	
0.2	0.04	45	
0.2	0.116	15.52	
0.25	0.04	37.5	used in simulation
0.25	0.078	19.23	used in simulation
0.25	0.116	12.93	used in simulation
0.3	0.04	30	used in simulation
0.3	0.078	15.38	used in simulation
0.3	0.116	10.35	used in simulation
0.39	0.04	16.5	
0.39	0.078	8.46	used in simulation
0.39	0.116	5.69	used in simulation
0,44	0.12	3,10	used in simulation
0.49	0.04	1.5	used in simulation
0.49	0.116	0.52	used in simulation

5.2.2.2 Determination of cohesive element values for the peptide conformations

Based on the results of the MD simulations the input values for the FEM simulation have been determined. The adsorption force curves were visualized as stress/displacement curves, which represent the binding capabilities of the peptide. One example for these curves is shown in Figure 1. The curve exhibits several maxima, which are characterized by the loss of a connection between single amino acids and the ZnO-surface. From these curves, the required values for the FEM-analyses were extracted (see next chapter) as well as the correct geometric properties of the analyzed specimen (see Table 4, which shows the contact area used in the MD simulations).

The resulting stress/displacement curve (Figure 1) from the MD simulations was recalculated to start at zero (A). The first maximum describes the first detachment of one of three anchor amino acids (B). The last maximum describes the moment when the peptide is fully detached (C). These values were used to determine the required input values for cohesive traction separation simulation in ABAQUS. The results are presented in Table 3.

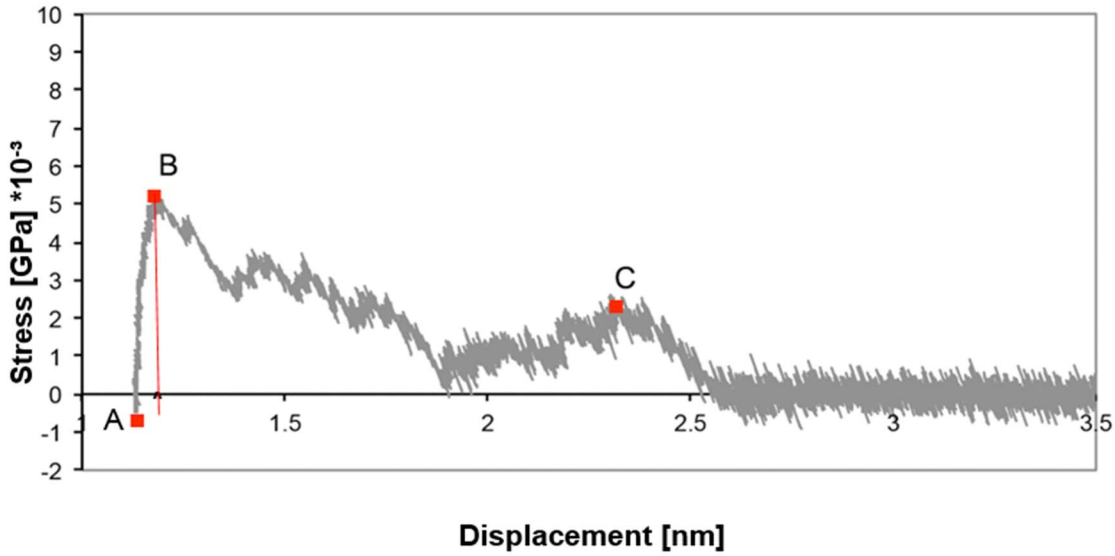

Figure 5-1: The three points on the load/displacement curve obtained from the adsorption stress profile of the conformation 1 at the pulling velocity of 0.25 nm/ns. Important events for the cohesive element calculation are marked with square symbols: A - offset value, B - first maximum (initiation point), and C - last maximum

Table 5.3: Input parameters for the cohesive element function of ABAQUS for the three different conformations. The sketch shows the responding points on a traction-separation curve

	Conformation 1	Conformation 2	Conformation 3	Averaged
δ_{init}, [nm] (x-value of point B in Fig. 1)	0.040868	0.189105	0.319635	0.183203
N_{max}, [GPa] (y- value of point B in Fig. 1, red line)	0.0051486	0.0056713	0.0054042	0.005408
EM (N_{max}/δ_{init}) [GPa/nm]	0.125982	0.02999	0.016907	0.02952
δ_C (Maximal displacement at failure) [nm] (x-value of point C in Fig. 1)	1.170144	0.994595	1.172075	1.112271

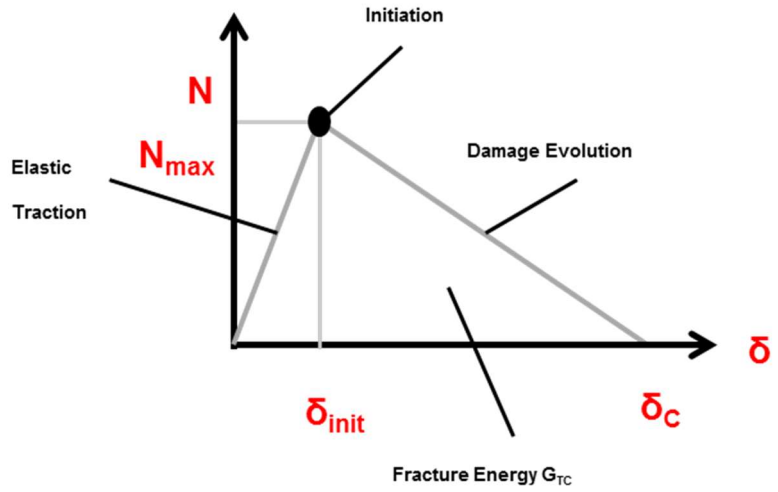

5.2.2.3 Three point bending probe simulations

The results of the MD simulations are used to simulate a FEM model of layered material later on. The model consists of a soft part containing many peptides and bulk ZnO. The specimen was investigated in a three point bending test and the results of the three different peptide conformations with different Elastic moduli (EM) were compared. It was shown in literature [42], that the traction separation law which is used in ABAQUS to describe the detachment and crack propagation, is independent of the geometry of the specimen. Based

on this work, the calculated values for traction separation in Chapter 3.2 can be used for specimen in different sizes, going from the nanoscale to the macroscale to test specimen in a practical size. First the averaged conformation was tested with different EM of the peptide. Comparisons are shown in the next part.

A three point bending specimen that consists of bulk ZnO bonded to bulk peptide was bended. The cohesive elements are found in-between the two materials (compare Figure 5, which also shows the stress distribution in the model), because the authors are mainly interested in the connection between ZnO and peptides. The model is a 2D model and consists out of two element types: 23 elements of quadratic cohesive elements for the cohesive zone and 2053 quadratic plane strain elements for the ZnO and peptide areas.

5.3 Results and Discussion

5.3.1 MD-Simulations

MD simulations were performed to characterize the molecular mechanism of the adsorption of a peptide to the ZnO surface.

5.3.1.1 Adsorbed conformations of the peptide on the ZnO surface

Three independent steered MD simulations were performed to obtain different conformations of peptide 31-6 bound to the ZnO(0001)-O surface. The adsorbed conformations differed in anchor amino acid residues and the backbone structure. Their snapshot structures (Figure 2) and their different shape and volume (Table 4) indicated that a single peptide could adsorb in different conformations onto the ZnO surface.

Table 5.4: Contact area of the three peptide conformations

	Conformation 1	Conformation 2	Conformation 3
Area A(contact) (nm^2)	1.68	1.47	1.88

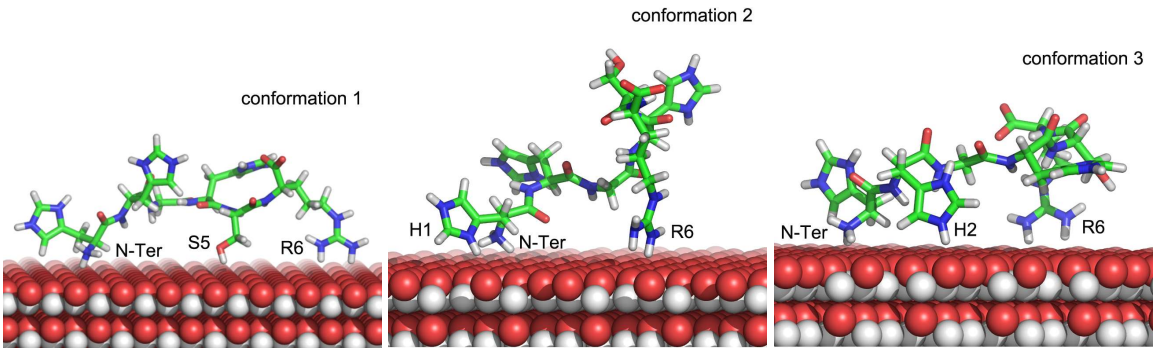

Figure 5-2: Three adsorbed conformations of peptides 31-6 (stick models) on ZnO(0001)-O surface (sphere models) showing anchor residues corresponding to their minimum distance to the ZnO(0001) O surface less than or equal to 0.3 nm. The snapshot was taken from the initial conformation of the desorption simulations. The ZnO surfaces were reoriented for a better visualization of each adsorbed peptide

The contact area Acontact of ZnO and the adsorbed peptide in three conformations was calculated from Apeptide, Azno, and Atotal (the solvent accessible surface area of the peptide, the ZnO slab and the ZnO-peptide complex, respectively) by

$$A_{\text{contact}} = ((A_{\text{peptide}} + A_{\text{zno}}) - A_{\text{total}}))/2, \quad [3]$$

A_{peptide}, A_{zno}, and A_{total} were determined by averaging over 11 simulation snapshots of the peptide from the first 100 ps of the MD simulation of the adsorbed peptide using the GROMACS tool g_sas.

For the three conformations, the contact areas were 1.68 nm² 1.47 nm², and 1.88 nm². Despite their different conformation, the contact area was similar (1.5 nm2) and deviated by only 15 %.

5.3.1.2 Adsorption force

Steered MD simulations of the desorption process were performed to determine the adsorption force of peptide 31-6 on the ZnO(0001)-O surface. It has been observed previously that different pulling velocities in steered MD simulations lead to different rupture forces [43–45]. Therefore, four different pulling velocities of 0.25, 0.5, 1.0, and 1.5 nm/ns were performed in 40 different steered MD simulations (Figure S1, Appendix). Although the adsorption force curves obtained from the desorption simulations shared a similar shape, high pulling velocities results in higher peaks of the adsorption force curve. A linear fitting

of four average maximum forces revealed an extrapolated rupture force for the pulling velocity approaching zero (Figure S2, Appendix). The detachment of anchor residues (Figure 2) from the surface gave the rupture events that suggest a critical role of these residues in the desorption process of peptide 31-6 from the ZnO(0001)-O surface.

The adsorption force profile also showed three distinct phases for all three peptide conformations (Figure S1, Appendix). In the first phase, the force increased rapidly to a maximum peak, where the rupture event happened at a center of mass distance of 1.2 1.5 nm from the ZnO surface, slightly depending on the adsorbed conformation and the pulling velocity. The force then decreases to lower peaks or plateaus in the second phase, before reducing to a constant value near zero in the third phase. In the first phase, the adsorption force increased until it was large enough to detach the first anchor residue from the ZnO surface. In the second phase, further anchor residues were detached subsequently from the surface. The force, therefore, showed smaller peaks or remained constant in this phase. The second phase ended with the detachment of the last anchor residue. In the third phase, the peptide was not in contact with the ZnO surface. The maximum force needed for the first detachment of anchor residues and the maximum displacement before complete detachment of the peptide varied by only 10-20 % for the three conformations.

5.3.2 Multiscale simulations

5.3.2.1 Three point bending probe simulations

The three point bending test was chosen to analyze the influence of the Elastic moduli of the peptide on the crack opening displacement (COD). In Figure 3 the von-Mises stress distribution in the middle of the simulation is shown.

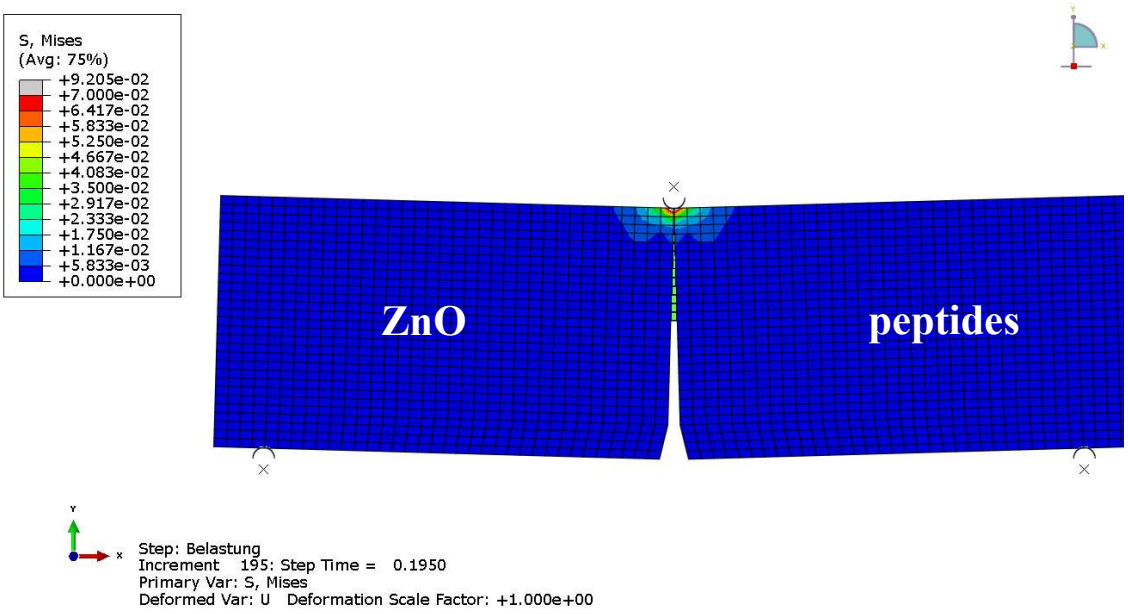

Figure 5-3: The three point bending test model with colored materials and (von-Mises-) Stress-distribution with half-opened crack (Peptide COD = 2.7 nm). On the right side of the crack are peptides found, on the left side bulk ZnO and green (the bright colored elements in the middle) represents the cohesive elements

Two different approaches were chosen to analyze the influence of the Elastic modulus of the peptide: “peptide COD” and “full COD”. First the horizontal movement of the marked node on the peptide material (compare Figure 4) relative to the baseline is measured and compared in Figure 6 in a load/displacement diagram to analyze the influence of the elastic modulus of the peptide (“peptide COD”). Second the “full COD” is analyzed (see Figure 5) which is defined through the change in distance between the marked node on the peptide material and the marked node on the ZnO material. The influence of the different Elastic moduli of the peptide on the “full COD” is then compared in Figure 7.

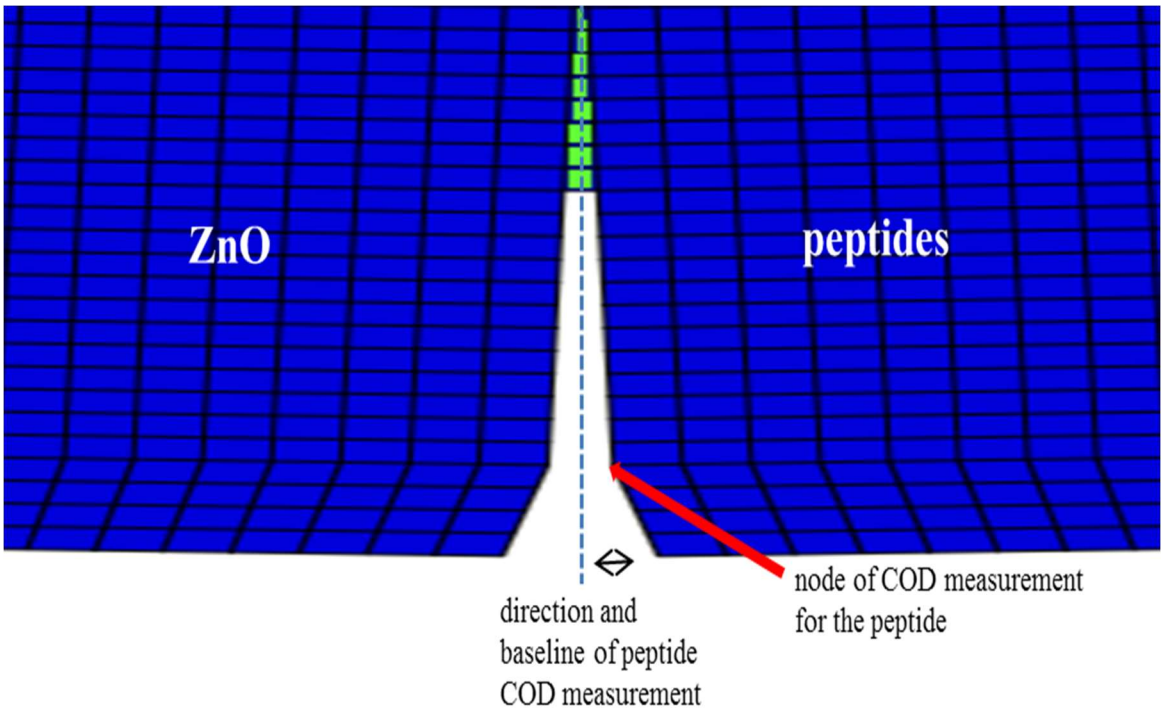

Figure 5-4: Peptide COD: Description of the measurement method of the COD measurement of the COD of the peptides. The dotted line represents the ground line to which the distance of the marked node is measured

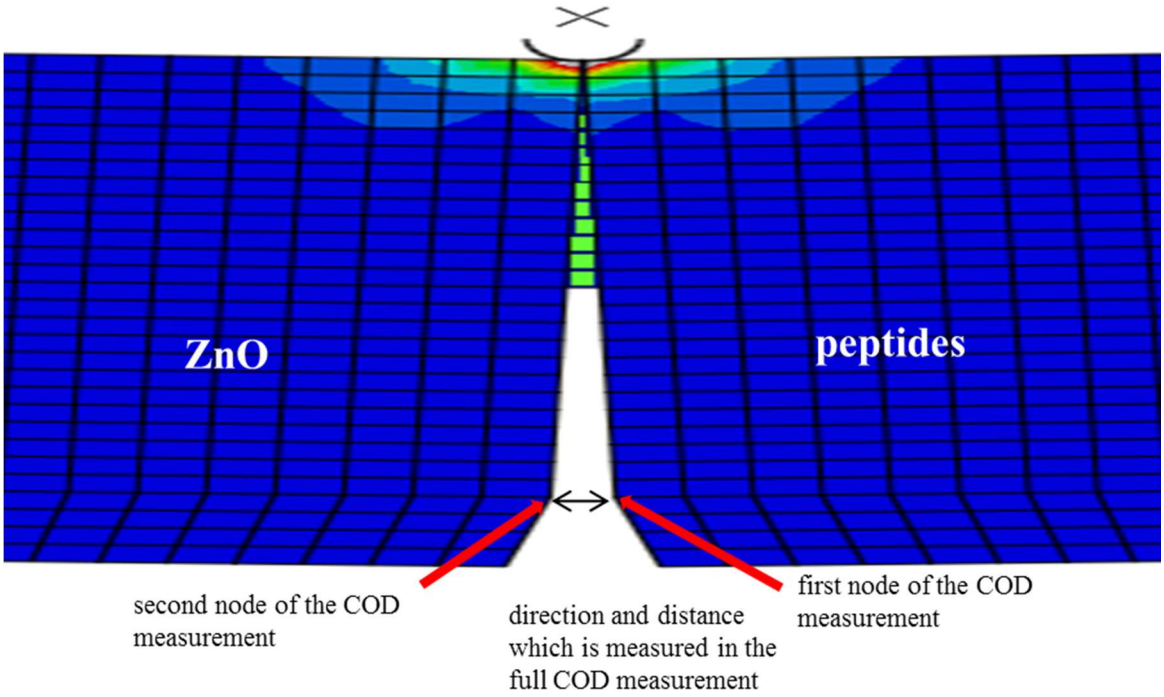

Figure 5-5: Full COD: Description of the measurement method of the full COD measurement where the distance between the marked nodes of both materials is used in the investigation

The comparison of the results shows that the influence of the Elastic modulus (EM) is linear (see Figures 6 and 7). The materials used in the simulations were considered to be fully elastic. With a higher EM, a higher load is required to bend the specimen as far as with a peptide with a lower Elastic modulus. Also, the curves show first an elastic behavior, then the cohesive elements get bended, then the crack occurs (the first cohesive element loses its connection, see marked area in Figures 6 and 7) and then the curve experiences an exponential softening. The differences in the EM of the peptide did not result in a big change of the force/COD curve for values of the EM above 6 GPa.

An Elastic Modulus below 6 GPa results in a different material behavior. This is particularly visible in the comparisons of the results of the peptide COD analysis. For example the curve of the peptide with an EM of 0.52 GPa shows the following different result: first the curve shows an elastic behavior until it depicts negative displacements. Here the influence of the ZnO deformation gets visible, which results in the negative displacement of the peptide node. In that case, no crack formation occurs, because the simulation cannot run to the end because of the very high and unrealistic Possion ratio of 0.49 and the very low EM of 0.52 GPa (compare Figure 6).

The peptide COD curve with 1.5 GPa displays a comparable behavior: first the curve shows an elastic behavior until it depicts negative displacements based on the same reasons as mentioned before with the low EM of 0.52 GPa. The energy first gets dissipated during the deformation of the peptides, but then the behavior of the ZnO elements starts to influence the results through their elastic deformation. The cohesive elements open up at a force of 0.08 GPa. But in comparison to the results of the peptide with 0.52 GPa a crack occurs (with forces around 0.9 GPa). With higher EM the curves converge more and more to each other and finally again to zero (the crack is then fully opened).

The full COD curve shows that all values of the Elastic modulus of the peptide result in comparable force/COD curves without any negative displacement. Differences exist also with values of the Elastic modulus below 6 GPa. Here, the maximal forces differ by 0.64 GPa (from 0.52 to 5.69 GPa), whereas the differences of the maximal forces of the different curves above 6 GPa account only for 0.008 GPa.

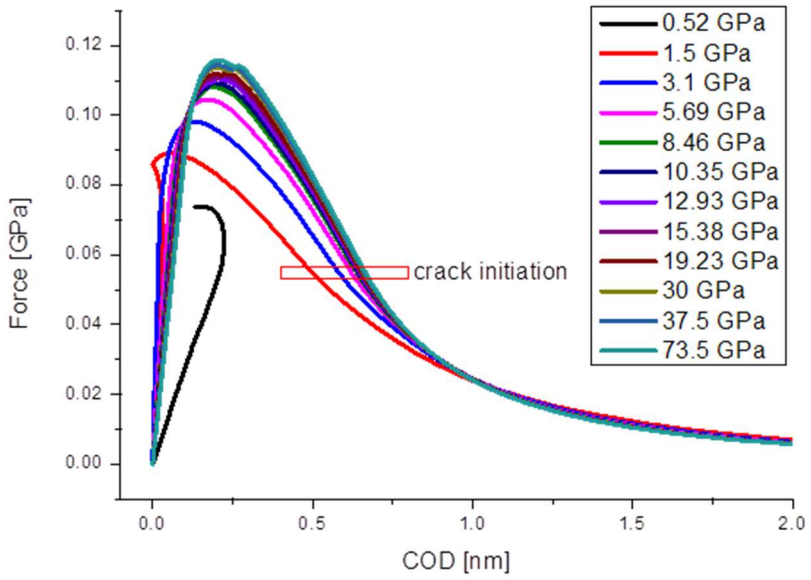

Figure 5-6: Peptide COD: Influence of the EM of the peptide with averaged conformation on the force/COD behavior

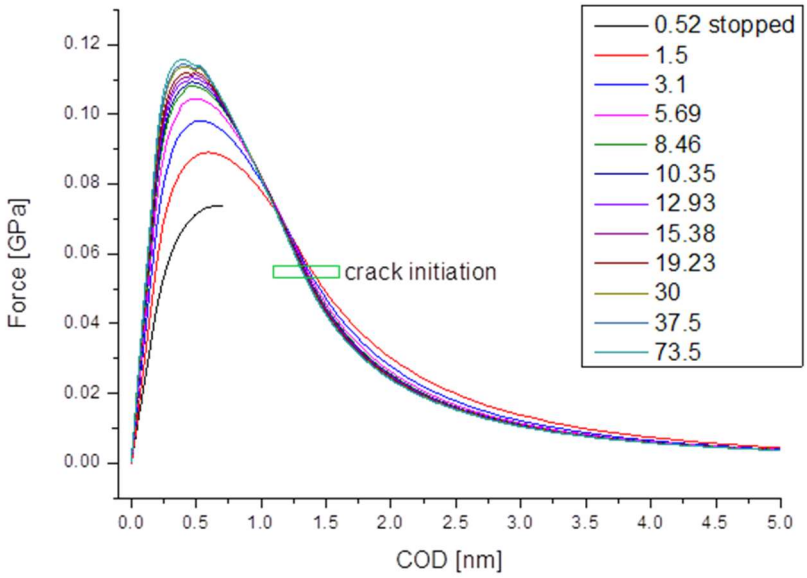

Figure 5-7: Full COD: Influence of the EM of the peptide with averaged conformation on the force/COD behavior

5.3.2.2 Distribution of the crack extension

The development of the crack opening can be represented by plotting the force and the crack front (delta a). The Figure 8 represents the results of selected EM of the peptide. The

influence on the curves of the EM of the peptide is low but exists. With a lower EM, a higher force is needed to start the crack but to the end of the curve the results are converging.

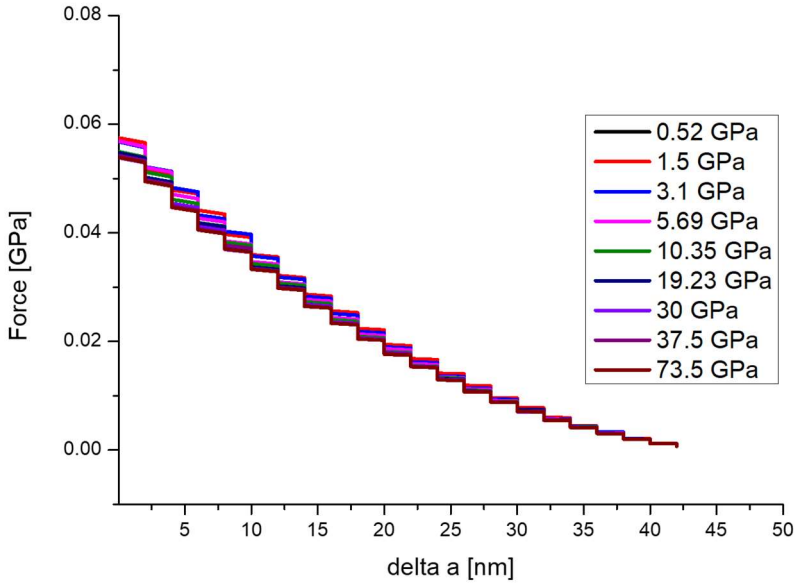

Figure 5-8: Development of the crack opening of the averaged conformation

5.3.2.3 Influence of the stiffness of the damage zone

The influence of the peptide Elastic modulus will increase if the stiffness of the damage zone (SDZ) change. With more than one peptide (e.g. a layer of peptides) the Elastic modulus of the SDZ likely will increase. This results in a different situation, the EM of the other components perhaps will influence the simulation differently. A FEM simulation with an EM value of 10 GPa and an EM of the peptides of 15.38 GPa and other examples are presented in the following figures:

a)

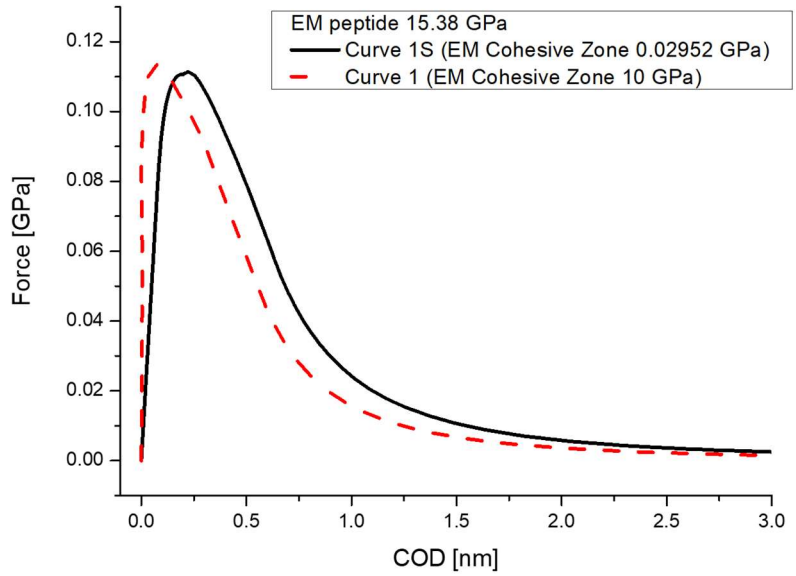

b)

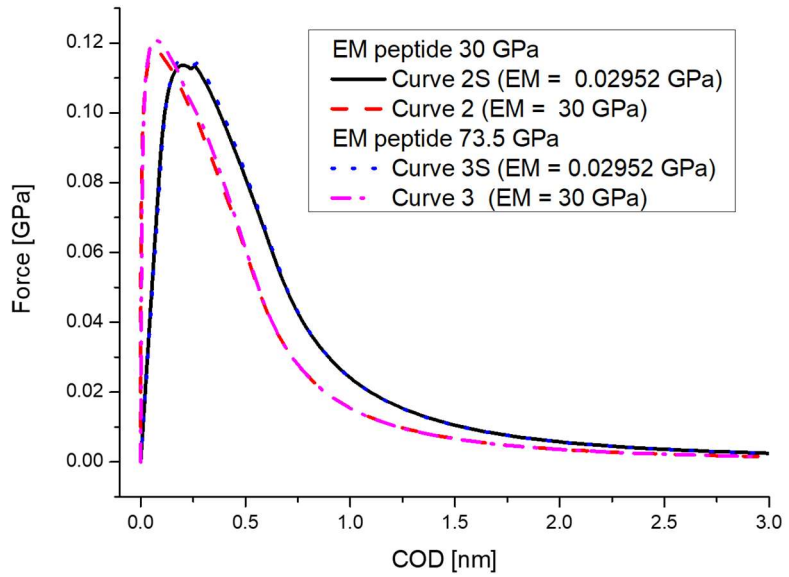

Figure 5-9: Peptide COD: a) Comparison between different values (0.2952 GPa and 10 GPa) for the SDZ for an EM of the peptide of 15.38 GPa. b) Comparison between different values for the SDZ (30 GPa and 0.2952 GPa) for an EM of the peptide of 30 GPa and 73.5 GPa

a)

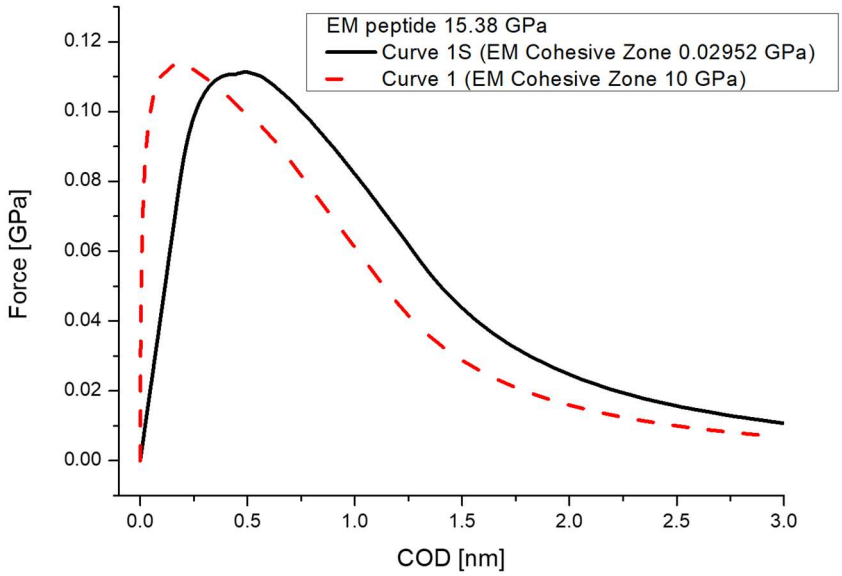

b)

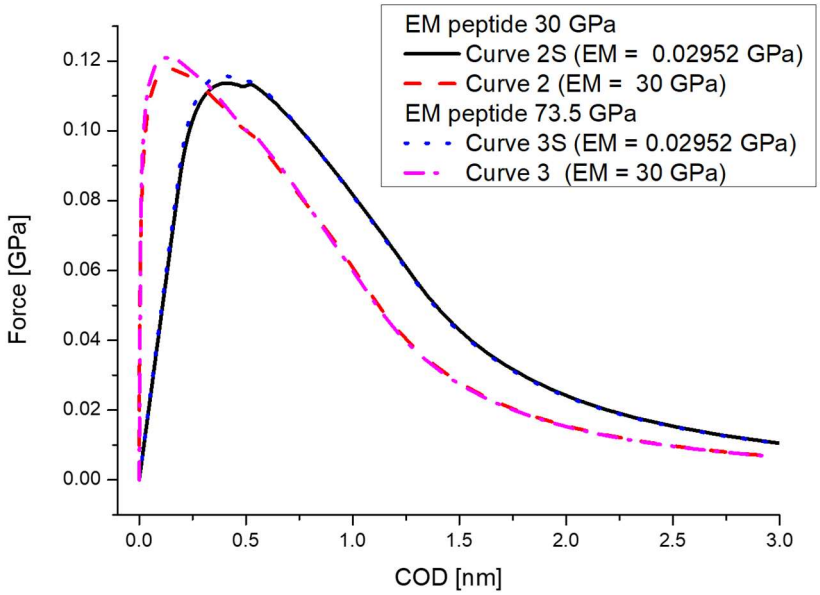

Figure 5-10: Full COD: a) Comparison between different values (0.2952 GPa and 10 GPa) for the SDZ for an EM of the peptide of 15.38 GPa. b) Comparison between different values for the SDZ (30 GPa and 0.2952 GPa) for an EM of the peptide of 30 GPa and 73.5 GPa

The standard value for the SDZ (EM value) is 0.2952 GPa for the averaged configuration (a capital S behind the curve name marks the standard cohesive zone value for the EM).

The Figure 9 a) peptide COD) and 10 a) (full COD) display the peptide conformation with an EM of the protein of 15.38 GPa (Curve 1S) which shows a lower maximum and a flat slope than the same conformation with a EM value of 10 GPa (Curve 1). This accounts also for the comparisons between two peptide conformations with an EM of the peptide of 30 GPa (Curves 2S and 2) and 73.5 GPa (Curves 3S and 3) which are presented in 9 b) and 10 b). With a higher value for the SDZ, the slope of the curve gets steeper and a higher maximum value of force is reached. E.g. the maximum of the force for the peptide with an EM of the peptide of 73.5 GPa and a EM value of 30 GPa has the maximum of 0.121 GPa (Curve 3) which is about 0.005 GPa higher than the value of Curve 3S with a EM value of 0.116 GPa in the comparison of the Peptide COD. The differences in the maxima of the forces between the different curves (1S and 1, 2S and 2, 3S and 3) account for less than 5 % in the peptide COD. For the full COD comparisons the results are comparable, with a higher value for the SDZ, the slope of the curve gets steeper and a higher maximum value of force is reached.

5.4 Conclusions

Steered MD simulations were applied to model the adsorption force and the binding affinity of a model peptide adsorbed to the ZnO(0001)-O surface. Parameters such as contact area, maximum force, displacement at maximum force and maximum displacement at failure were extracted from the simulation and used as parameters for subsequent FEM simulations. The cohesive element analysis and the traction separation law showed a good consistency. Despite the fact that the force curves generated by the MD simulations were approximated by the FEM simulations and that the peptide was bound in different conformations, the results were robust and deviated by less than 20% (not shown here). In the future, a more realistic simulation of a whole layer of peptide is promising to account for peptide-peptide interactions.

The three point bending test with the sensitivity analysis of the material with different Elastic moduli revealed that influence of the Elastic modulus of the peptide on the simulation results exists. The use of the averaged results of the MD simulations mirrors the real situation in a bulk peptide material: Even with only one pre-defined crystal orientation of the ZnO material, the peptides will be absorbed in a large number of different conformations. All three different conformations will influence the material behavior differently. With the here presented approach three different conformations and their binding energies averaged

and then used as one averaged peptide conformation in the FEM simulations to show the general idea. Ideally one should consider even more configurations, which would involve high computational costs and manpower which was not able to provide in this project.

The results showed a great influence of the used Elastic modulus of the peptide layer.

With lower EM higher forces are needed to introduce a crack as shown in chapter 3.2.3. Also the unrealistic low values of 0.52 GPa and 1.5 GPa as shown in Figure 4 are influencing the simulation so that the behavior of the composites differs greatly from the composites with higher values for the EM of the peptide.

With a thicker layer of peptides, the influence of stiffness of the damage zone, as shown in the last chapter also needs to be considered wisely, while planning and designing a composite like the one presented here.

In future works, the different peptide conformations will be simulated with a crack simulation procedure like XFEM and again for comparison with cohesive elements, to generate materials with the highest crack resistance possible while using ZnO and peptides as components. Therefore, the plasticity information of the material needs to be researched on and the possible range of the values of the Elastic moduli of the peptide will be estimated. Especially for a layer of peptides the stiffness of the damage zone will be interesting, as shown in the last chapter. Also more complicated structures will be analyzed, like a so called brick and mortar structure which can be found in natural nacre and other promising arrangements. This can lead to development of crack resistance ceramics out of ZnO and peptides, which do not exist until now.

5.5 References

[1] D. Molnar, R. Mukherjee, A. Choudhury, A. Mora, P. Binkele, M. Selzer, et al., Multiscale simulations on the coarsening of Cu-rich precipitates in α-Fe using kinetic Monte Carlo, molecular dynamics and phase-field simulations, Acta Materialia. 60 (2012) 6961–6971.

[2] Siddiq, S. Schmauder, Interface fracture analyses of a bicrystal niobium/alumina specimen using a cohesive modelling approach, Modelling and Simulation in Materials Science and Engineering. 14 (2006) 1015–1030.

[3] M. Karplus, G. Petsko, Molecular dynamics simulations in biology, Nature. 347 (1990) 631–639.

[4] M. Karplus, J.A. McCammon, Molecular dynamics simulations of biomolecules, Nature Structural Biology. 9 (2002) 646–652.

[5] M.C. Zwier, L.T. Chong, Reaching biological timescales with all-atom molecular dynamics simulations, Current Opinion in Pharmacology. 10 (2010) 745–752.

[6] B. Ji, H. Gao, Mechanical properties of nanostructure of biological materials, Journal of the Mechanics and Physics of Solids. 52 (2004) 1963–1990.

[7] D. Sikdar, S.M. Pradhan, D.R. Katti, K.S. Katti, B. Mohanty, Altered phase model for polymer clay nanocomposites, Langmuir : the ACS Journal of Surfaces and Colloids. 24 (2008) 5599–5607.

[8] U. Özgür, Y.I. Alivov, C. Liu, a. Teke, M. a. Reshchikov, S. Doğan, et al., A comprehensive review of ZnO materials and devices, Journal of Applied Physics. 98 (2005) 041301.

[9] Z.L. Wang, Zinc oxide nanostructures: growth, properties and applications, Journal of Physics: Condensed Matter. 16 (2004) 829–858.

[10] X. Fang, Y. Bando, U.K. Gautam, C. Ye, D. Golberg, Inorganic semiconductor nanostructures and their field-emission applications, Journal of Materials Chemistry. 18 (2008) 509–522.

[11] R.A. Jensen, H. Van Ryswyk, C. She, J.M. Szarko, L.X. Chen, J.T. Hupp, Dye-sensitized solar cells: sensitizer-dependent injection into ZnO nanotube electrodes, Langmuir: The ACS Journal of Surfaces and Colloids. 26 (2010) 1401–1404.

[12] P. Gerstel, R.C. Hoffmann, P. Lipowsky, L.P.H. Jeurgens, J. Bill, F. Aldinger, Mineralization from Aqueous Solutions of Zinc Salts Directed by Amino Acids and Peptides, Chemistry of Materials. 18 (2006) 179–186.

[13] M. Umetsu, M. Mizuta, K. Tsumoto, S. Ohara, S. Takami, H. Watanabe, et al., Bioassisted Room-Temperature Immobilization and Mineralization of Zinc Oxide - The Structural Ordering of ZnO Nanoparticles into a Flower-Type Morphology, Advanced Materials. 17 (2005) 2571–2575.

[14] M. Okochi, T. Sugita, S. Furusawa, M. Umetsu, T. Adschiri, H. Honda, Peptide array-based characterization and design of ZnO-high affinity peptides, Biotechnology and Bioengineering. 106 (2010) 845–851.

[15] T. Togashi, N. Yokoo, M. Umetsu, S. Ohara, T. Naka, S. Takami, et al., Material-binding peptide application--ZnO crystal structure control by means of a ZnO-binding peptide, Journal of Bioscience and Bioengineering. 111 (2011) 140–145.

[16] J. Baier, T. Naumburg, N.J. Blumenstein, L.P.H. Jeurgens, U. Welzel, T. A. Do et al., Bio-inspired mineralization of zinc oxide in presence of ZnO-binding peptides, Biointerface Research in Applied Chemistry. 2 (2012) 380–391.

[17] D. Rothenstein, B. Claasen, B. Omiecienski, P.Lammel, J. Bill, Isolation of ZnO-Binding 12-mer Peptides and Determination of Their Binding Epitopes by NMR Spectroscopy, Journal of the American Chemical Society. 134 (2012) 12547–12556.

[18] M.M. Tomczak, M.K. Gupta, L.F. Drummy, S.M. Rozenzhak, R.R. Naik, Morphological control and assembly of zinc oxide using a biotemplate, Acta Biomaterialia. 5 (2009) 876–882.

[19] Y. Zhang, M.K. Ram, E.K. Stefanakos, D.Y. Goswami, Synthesis, Characterization, and Applications of ZnO Nanowires, Journal of Nanomaterials. 2012 (2012) 1–22.

[20] B. Bhushan, X. Li, Nanomechanical characterisation of solid surfaces and thin films, International Materials Reviews. 48 (2003) 40.

[21] J.E. Bradby, S.O. Kucheyev, J.S. Williams, C. Jagadish, M. V. Swain, P. Munroe, et al., Contact-induced defect propagation in ZnO, Applied Physics Letters. 80 (2002) 4537.

[22] M. Sarikaya, An introduction to biomimetics: a structural viewpoint, Microscopy Research and Technique. 27 (1994) 360–375.

[23] S.M. Waraich, B. Hering, Ž. Burghard, J. Bill, P. Behrens, H. Menzel, Fabrication and characterization of biocompatible nacre-like structures from α-zirconium hydrogen phosphate hydrate and chitosan, Journal of Colloid and Interface Science. 367 (2012) 74–82.

[24] F. Barthelat, D. Zhu, A novel biomimetic material duplicating the structure and mechanics of natural nacre, Journal of Materials Research. 26 (2011) 1203–1215.

[25] K. Kjaergaard, J.K. Sørensen, M.A. Schembri, P. Klemm, Sequestration of zinc oxide by fimbrial designer chelators, Applied and Environmental Microbiology. 66 (2000) 10–14.

[26] K. Kjaergaard, M.A. Schembri, P. Klemm, Novel Zn(2+)-chelating peptides selected from a fimbria-displayed random peptide library, Applied and Environmental Microbiology. 67 (2001) 5467–5473.

[27] C. Thai, H. Dai, M. Sastry, Identification and characterization of Cu2O and ZnO binding polypeptides by Escherichia coli cell surface display: toward an understanding of metal oxide binding, Biotechnology and Bioengineering. 87 (2004) 129–137.

[28] D. Van Der Spoel, E. Lindahl, B. Hess, G. Groenhof, A.E. Mark, H.J.C. Berendsen, GROMACS: fast, flexible, and free, Journal of Computational Chemistry. 26 (2005) 1701–1718.

[29] S.J. Weiner, P.A. Kollman, D.A. Case, U.C. Singh, C. Ghio, G. Alagona, et al., A new force field for molecular mechanical simulation of nucleic acids and proteins, Journal of the American Chemical Society. 106 (1984) 765–784.

[30] Y. Duan, C. Wu, S. Chowdhury, M.C. Lee, G. Xiong, W. Zhang, et al., A point-charge force field for molecular mechanics simulations of proteins based on condensed-phase quantum mechanical calculations, Journal of Computational Chemistry. 24 (2003) 1999–2012.

[31] Y.-N. Xu, W. Ching, Electronic, optical, and structural properties of some wurtzite crystals, Physical Review B. 48 (1993) 4335–4351.

[32] D. Raymand, A.C.T. van Duin, M. Baudin, K. Hermansson, A reactive force field (ReaxFF) for zinc oxide, Surface Science. 602 (2008) 1020–1031.

[33] Kornherr, S. French, A. Sokol, Interaction of adsorbed organosilanes with polar zinc oxide surfaces: a molecular dynamics study comparing two models for the metal oxide surface, Chemical Physical Letters. 393 (2004) 107–111.

[34] SIMULIA, Abaqus Analysis User's Manual, Dassault Systèmes Simulia Corp., Providence, RI, USA., 2011.

[35] M. Sadd, Elasticity: theory, applications, and numerics, Elsevier Butterworth–Heinemann, 2009.

[36] J. Pérez-Rigueiro, C. Viney, Mechanical properties of silkworm silk in liquid media, Polymer. 41 (2000) 8433–8439.

[37] J. Brydson, Plastics materials, 7th ed., Butterworth-Heinemann, 1999.

[38] J.M.G. Cowie, Polymers: Chemistry and Physics of Modern Materials, Second Edition, CRC Press Inc, 1991.

[39] B. Liu, L. Zhang, H. Gao, Poisson ratio can play a crucial role in mechanical properties of biocomposites, Mechanics of Materials. 38 (2006) 1128–1142.

[40] L. Martin, D. Dadon, M. Rosen, Evaluation of Ultrasonically Determined Elasticity Porosity Relations in Zinc Oxide, Journal of the American Ceramic Society. 79 (2005) 1281–1289.

[41] P. Lipowsky, Ž. Burghard, L.P.H. Jeurgens, J. Bill, F. Aldinger, Laminates of zinc oxide and poly(amino acid) layers with enhanced mechanical performance, Nanotechnology. 18 (2007) 345707–345712.

[42] O. Mintchev, S. Schmauder, U. Weber, Finite Element Simulation of Crack Initiation and Growth Based on a Critical Traction Criterion : - Some Examples -, Proceedings of an International Workshop on Nonlocal Modelling of Failure of Materials. (2007) 73–82.

[43] J. Krüger, G. Fels, Potential of mean force of ion permeation through alphS6 nAChR ion channel, Proceedings of IWPLS. 4 (2009) 1–7.

[44] J.A. Lemkul, D.R. Bevan, Assessing the stability of Alzheimer's amyloid protofibrils using molecular dynamics, The Journal of Physical Chemistry. B. 114 (2010) 1652–1660.

[45] S.-W. Hung, P.-Y. Hsiao, C.-C. Chieng, Dynamic information for cardiotoxin protein desorption from a methyl-terminated self-assembled monolayer using steered molecular dynamics simulation. The Journal of Chemical Physics. 134 (2011) 194705.

6 Buch: Multiscale materials modeling

Die zuletzt besprochene Veröffentlichung in dieser Dissertation ist auch in dem Buch „Multiscale materials modeling: approaches to full multiscaling“ erneut mit Erlaubnis des Verlags (Computational Materials Science) veröffentlicht worden.

Dieses Buch (Figure 6-1):

V. Schmauder, S., & Schäfer, I. (Eds.). (2016*). Multiscale materials modeling: approaches to full multiscaling.* Berlin: De Gruyter, ISBN 13: 978-3110412369

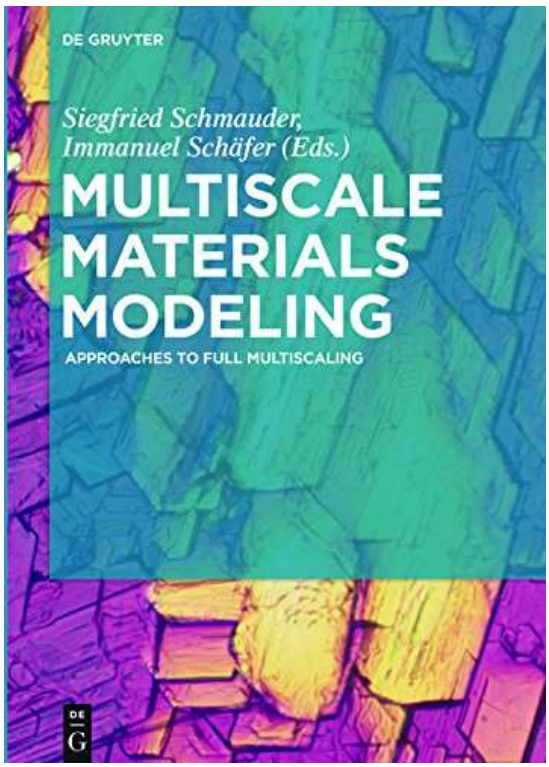

Figure 6-1: Front Cover des Buches

ist von Prof. S. Schmauder und I. Schäfer als Editoren herausgebracht worden. Das Vorwort dazu stammt von den Editoren. Das komplette Zitat der Veröffentlichung lautet:

VI. Schäfer, I., Lasko, G., Do, T. A., Pleiss, J., Weber, U., & Schmauder, S. (2016). Peptide-zinc oxide interaction: Finite element simulation using cohesive zone models based on molecular dynamics simulation. In Multiscale Materials Modeling: Approaches to Full Multiscaling. https://doi.org/10.1515/9783110412451_018, [43]

Da die Veröffentlichung eine Wiederveröffentlichung ist, von der, die in Kapitel 5 gezeigt wurde, wird auf jenes Kapitel verwiesen.

7 Pomelo

In der Fortsetzung des DFG Schwerpunktprogramms (Priority Program) SPP1420, Impact resistant hierarchically structured materials based on fruit walls and nut shells, oblag dem IMWF die Aufgabe verschiedene Varianten von Schaummodellen (u. a. Einflüsse von Geometrie- und Materialvariationen) zu modellieren und numerisch zu analysieren. Die Modelle beruhen auf der Struktur der Schale der Pomelo. Diese Zitrusfrucht ist aufgrund ihrer außerordentlichen Größe und der Schalenstärke ein besonders interessantes Vorbild in der Bionik, zum Beispiel als Ideengeber für Crashsysteme und ähnliches. Einige der Ergebnisse wurden in der folgenden Arbeit veröffentlicht:

VII. Schäfer, I., Mlikota, M., Schmauder, S., & Weber, U. (2020). Modelling the damping response of biomimetic foams based on pomelo fruit. Computational Materials Science, 183, pp. 109801.

Der Anteil meiner Arbeit in der Veröffentlichung umfasst:

- Erstellung des Manuskripts mit M. Mlikota (Anteil meiner Arbeit 50 %)
- FEM-Simulationen der Beschichtungen der unterschiedlichen Stegformen, Erstellung der Bilder und der Diagramme, Analyse und Diskussion zu diesem Teil des Projektes (Anteil meiner Arbeit 100 %)
- Die Simulationen der Kelvinzellen und der Stegporositäten bzw. der Gipspartikel sind von Dr.-Ing. U. Weber durchgeführt worden
- Diskussion der Ergebnisse, Optimierung der Simulation und die Optimierung des Manuskripts in Zusammenarbeit mit den Mitautoren (Anteil meiner Arbeit 50 %)

Modelling the damping response of biomimetic foams based on pomelo fruit

I. Schäfer[1]*, M. Mlikota[1], S. Schmauder[1], U. Weber[2]

[1)] Institute for Materials Testing, Materials Science and Strength of Materials (IMWF), University of Stuttgart, Stuttgart, Germany

[2)] Materials Testing Institute (MPA), University of Stuttgart, Stuttgart, Germany

* Corresponding author (immanuel.schaefer@imwf.uni-stuttgart.de)

Abstract

Some sorts of fruits, like pomelo (*Citrus maxima* or *Citrus grandis*), also spelled pummelo, are of special interest for researchers and engineers during the development of impact resistant structures. It is assumed that the interaction of structural features on different length-scales of such fruits enables the dissipation of large amounts of energy during their impact against a hard surface. Accordingly, the aim of this paper is to perform an analysis by using a numerical model at different hierarchical levels by means of Finite Element Methods (FEM) in order to identify different structural features that contribute to the damping performance of the pomelo fruit. The considered numerical model was created on the basis of homogeneous aluminum (AlSi7Mg0.3) foam structure, inspired by the pomelo fruit shell structure. In the present approach, the Si- or Fe-rich intermetallic particles on the struts of AlSi7Mg0.3 foam are considered additionally, this enabled more detailed investigations on the structural behavior of the foam during different loading conditions. Comparison of the results from simulation and experimental compression tests showed promising results with respect to the deformation behavior, which are offering support to the design of biomimetic metallic foams. Understanding the principles of combining the structure and material inspired by biological systems enables constructing new lightweight bio-inspired materials of high impact and puncture resistance with a combination of high-energy dissipation, high damping properties and a significant recovery from large deformations.

7.1 Introduction

Plants represent almost 99.9% of the biomass of our planet. This means that virtually every environment that can be colonized by life has been explored and populated by plants. To achieve such amazing results while being unable to move from the site of seed germination, plants have evolved an arsenal of solutions that make them suitable for life in the most

demanding and extreme conditions. In addition, it is well established that plants and their fruits are able to show considerable plasticity in their morphology and physiology in response to variability within their environment and to survive extremely diverse environmental conditions and stresses [1]. Thus, the morphology of their structures and their mechanical properties represent a goldmine of solutions that, with appropriate investigation, may be used to obtain new design rules for advanced bio-inspired systems and materials in countless applications. [2]

Accordingly, one of the major boosts in materials science nowadays is given by inspiration from nature. The inspiration by natural solutions allows the development of new materials with enhanced structural properties, applicable in several fields (including consumer products, automotive, and architecture) and with sensing and actuation capability. The interesting aspect of natural materials is related to the numerous functionalities that they can exploit (e.g., stability, stiffness, toughness, self-healing, etc.), even if they are based on a limited number of basic components (i.e., cellulose, hemicellulose, lignin, and pectin). This variety of properties is mainly due to the hierarchical organization of such components. Extraction of the principles underlying these properties is one of the key approaches in developing bio-inspired materials. [3]

The most famous example of technology inspired by plants commonly used in many different fields and applications is the Velcro invention. Velcro resulted in 1948 from a Swiss engineer, Georgede Mestral, noticing how the hooks of the plant burrs (*Arctium lappa*) stuck in the fur of his dog. From this observation, Georgede Mestral derived the idea of a novel type of zip fastener [4]. From a structural point of view, another interesting example is obtained from the pomelo fruit, which shows characteristics of a peculiar damping system, allowing the fruit to resist to a drop from heights of up to 15 m. In this case the fruit wall, thanks to a complex hierarchical structure (see Figure 1) consisting of interconnected porous coatings combined with branched fiber networks, is able to dissipate more than 90% of the impact energy thus preventing pulp damage [5][6]. The principles of this natural product have been exploited in the development of new materials for enhanced crash absorbers, based on metal foams [7][8][9][10][3].

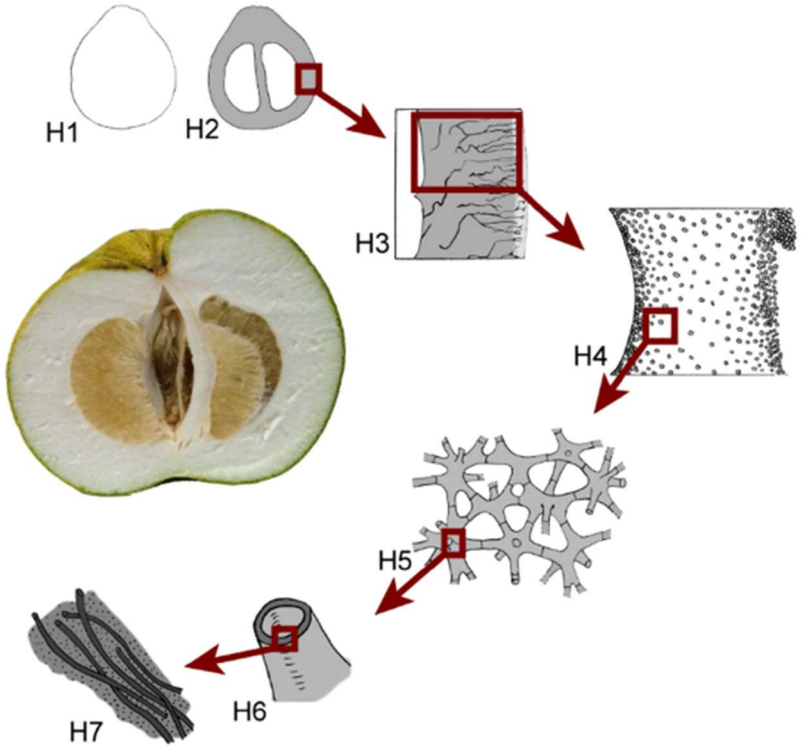

Figure 7-1: Schematic representation of the hierarchical levels of the pomelo peel H1–H7 [9]

The transfer of advantageous aspects from biology to technology is mainly achieved through the abstraction of basic principles of biological systems on artificial systems and by deriving a set of indicators and according weighting based on corresponding transposed rules [11]. Scientists regularly use abstractions with the aim to describe and understand the reality they are examining.

Computational modelling is the process of representing real world problems in mathematical terms in an attempt to find solutions to their associated complex systems. A formal model is an abstraction of the real-world onto a mathematical/computational domain that highlights some key features while ignoring others that are assumed to be secondary. A numerical model should not be considered as representation of the truth, but instead as a statement of the current knowledge of the phenomenon under research. One of the main objectives of any model is to provide a predictive capability, that is, the possibility to make guesses in terms of plausible hypotheses related to the behavior of the observed phenomenon in different scenarios that are of interest to experts [12]. With high speed calculators and the development of computational methods (e.g., FEM), simulation has become the

favorite design tool, allowing optimization of the investigated system. With mere experiments, it is nearly impossible to investigate the whole design space for understanding still unexplained mechanisms in order to mimic nature and make steps towards enhanced application of these mechanisms [13]. In the work of Lasko et al. [14], Schäfer et al. [15] or in the paper of Schmier et al. [16] examples are given were simulation and biomimetic are combined to reveal the principles of nature's role models.

The pomelo fruit is of special interest from a modelling point of view since it provides a good basis for the development of impact resistant structures. It is assumed that the interaction of structural features on different length-scales enables the dissipation of large amounts of energy during impact of the fruit against a hard surface. The aim of this study is, therefore, to perform a numerical analysis on a model – based on the pomelo fruit – at different hierarchical levels (H1- H7, Figure 1), aiming at the identification of structural features or levels that are most important for its mechanical behavior. Ultimately, the acquired knowledge provides support to the design of biomimetic metal foams.

The paper is structured as follows. First, the homogenized modelling of the bio-inspired material is defined. The second part of the paper is devoted to detailed modelling of the same material, by taking into account its microstructure (the pores inside the struts). Besides of that, case studies under different loading conditions are presented in this section. Finally, some conclusions are drawn.

7.2 Modelling of the pomelo-inspired material

As shown in Figure 1, the hierarchically organized fruit walls of the biological role model (*Citrus maxima*) compose a highly damping spongy gradient structure. These structural elements are transferred in the work of Bührig-Polaczek et al. [9] into hierarchically organized technical materials (Al7Si0.3Mg foam) consisting of a solid structure in combination with a particle-reinforced coating ensuring high toughness and high energy dissipation.

Furthermore, Bührig-Polaczek et al. [9] developed and adapted characterization methods allowing for multi-scale mechanical testing and structural analysis applicable as well to the role model as to the bio-inspired foams (Al7Si0.3Mg foam). The focus of the following chapter is the numerical analysis of the elastic-plastic response of the Al7Si0.3Mg foam obtained experimentally, as depicted in Figure 2.

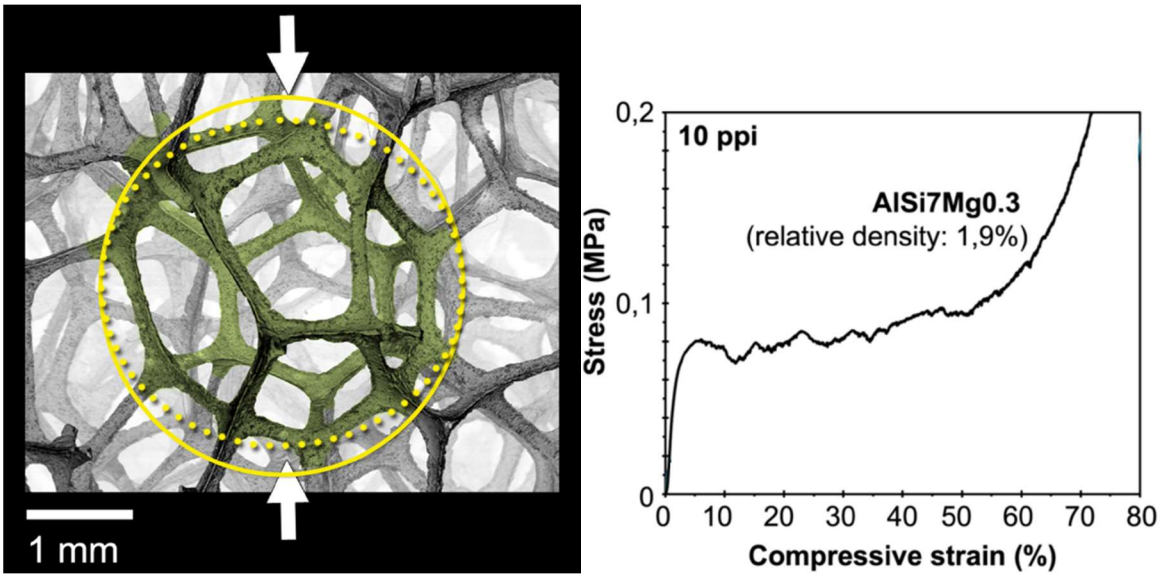

Figure 7-2: Left- Individual struts of a representative Al7Si0.3Mg foam sample; Right - Typical stress–compression diagrams of a 10 ppi (pores per inch) Al7Si0.3Mg foam [9]

7.2.1 Homogenized modelling

Reconstructing the structure and behavior of biological systems is of fundamental importance to the field of biomimetics. In general, biological systems exhibit complex nonlinear dynamic behavior. A common approach to constructing a model of an observed biological system is to decompose the modelling process in two tasks [17]. The first task, referred to as structure identification and often solved by a modelling expert, is to specify the model structure. The second task of determining appropriate values for/from the model, based on observations and measurements, is referred to as parameter estimation and performance measurement. [18]

The model of interest for this study was created on the basis of imaging data given in Figure 2, as obtained in an experimental study [9]. The representative model in this case has the form of a Kelvin cell with near-circular cross section, as shown in Figure 3. The strut length (B in Figure 3) is equal to 2.59 mm and the diameter is 0.2391 mm, what dimensionally corresponds to the values that can be extracted from Figure 2 - Left.

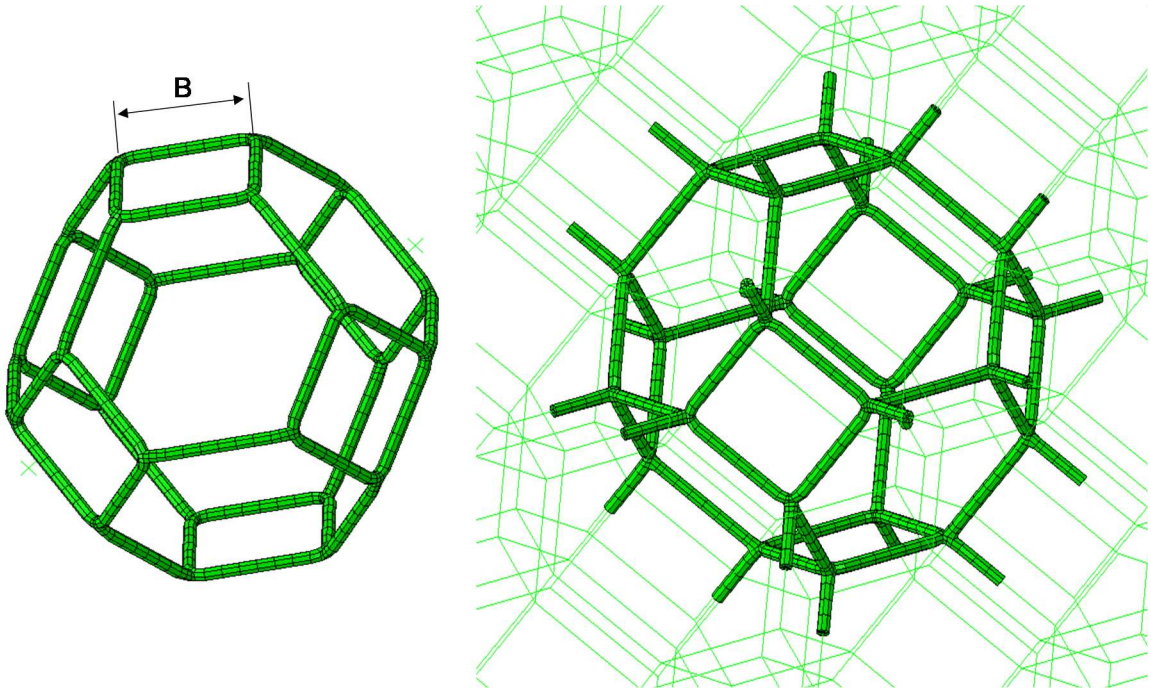

Figure 7-3: Kelvin cell with strut length of B = 2.59 mm and cross-sectional diameter of D = 239.1 µm

Concerning the model parameters, pure isotropic elasticity is adopted in the structural model, with the AlSi7Mg0.3 characteristic values for the yield strength, σy = 80 MPa, Young's modulus, E = 70 GPa and Poisson's ratio, ν = 0.3 (Ref.)

The model of the aluminum (AlSi7Mg0.3) foam structure, modelled by using Kelvin cells, has been compressed in controlled conditions, similar as in the experimental study of Bührig-Polaczek et al. [9]. The cell was embedded in the bulk model in a following step. This was done in two ways to find a computationally efficient way. In the first variant of the model, which in both cases consists of 3 x 3 x 3 units, all cell units were modelled by using solid finite elements (Figure 4 – Left). In the other variant, just the central cell was modeled as solid with C3D20 elements while the remaining cell units were modelled by using beam elements (Figure 4 – Right). Solid C3D20 elements are excellent elements for linear elastic calculations. The use of this element type (C3D20) is based on the more accurate simulation results for the material part compared to other element types like hexahedral ones. Aside of that, stress concentrations at the surface of an investigated structure can be well captured, what is an important aspect when analyzing foam structures.

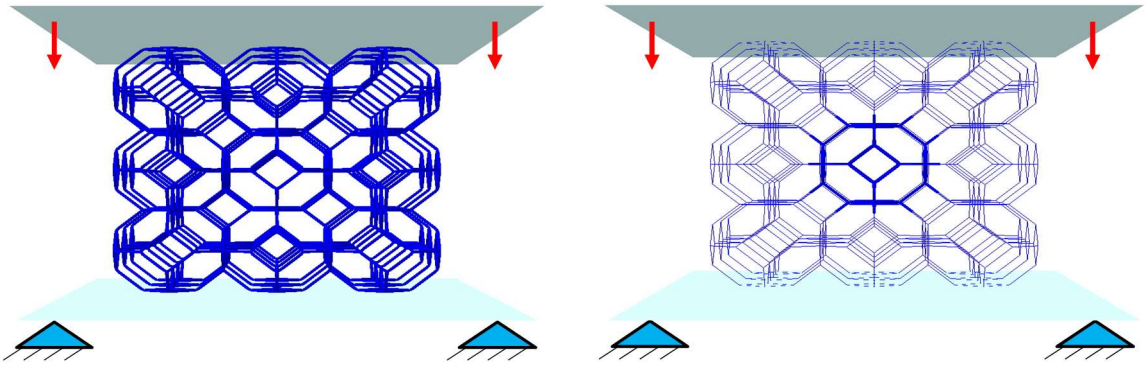

Figure 7-4: Left - Complete structure made out of solid cells; Right - Central solid Kelvin cell embedded into bulk beam model

Both models were compressed using displacement-controlled boundary conditions (Figure 4) and the results are presented in Figure 5, respectively. It is visible from Figure 5 that the completely solid cell structure deforms in a different manner than the model with just one solid cell located centrally in the bulk beam model. Namely, the solid structure deforms first in the coatings that are in contact with compressing surfaces (Figure 5 – Left), while the solid-beam structure deforms first in the middle coating of cells containing the solid kelvin cell (Figure 5 – Right).

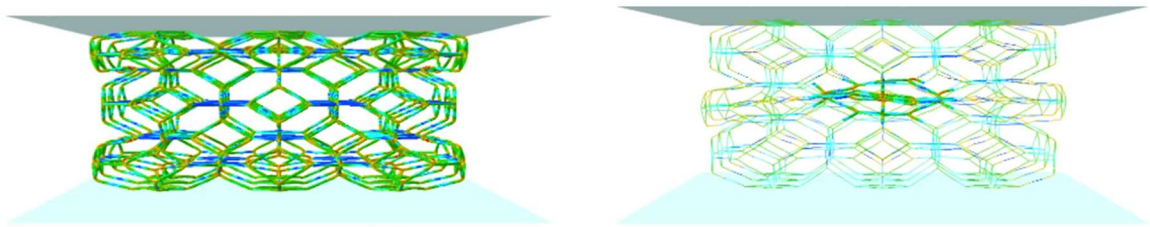

Figure 7-5: Left - Deformed models under compression: Left – Fully solid model; Right – Beam model with centrally positioned solid cell

Comparison between the models in the compressed state is shown in Figure 6, too, where the correlation between the reaction force and the displacements is given. What can be concluded from the reaction curves is that the completely solid model shows highest compressibility and by that the highest damping response. The beam (bulk) model with the centrally located solid cell and complete beam (bulk) model show very similar results, which can be eventually interpreted as poor damping ability. The two curves are not complete calculated because of instabilities, so a comparison with the solid structure curve is not possible. Worth noting is that the model completely made out of solid cells took 42

hours of computing time on a standard desktop computer, while the simplified model with just the central solid cell took considerably less time, “just” 4 hours.

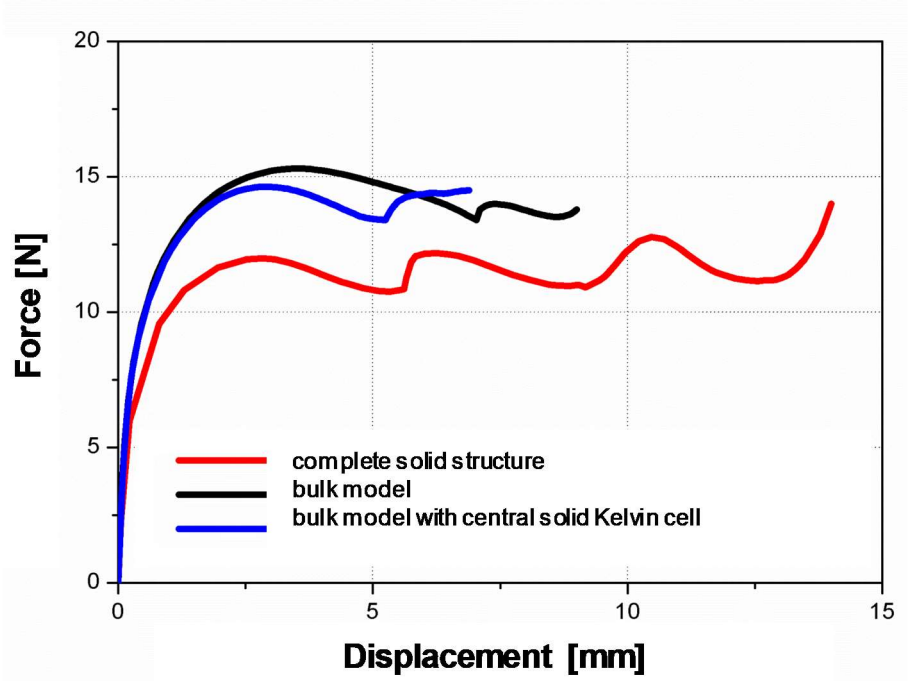

Figure 7-6: Comparison between the fully solid model, the bulk model and the bulk model with centrally positioned Kelvin cell

The complex solid cell model has been used in further studies in order to draw a comparison with the experimental results from the study of Bührig-Polaczek et al. [9]. Qualitative comparison can be drawn from Figure 7 and Figure 8. As mentioned earlier in the text, the first deformation in the numerical model is observed in the top coating of the solid cells, which is followed by the deformation in the bottom region. The middle region deforms last as visible from Figure 7 – Right. A similar behavior has been noticed in the experimental study [9], as shown in Figure 8. Blue regions in the images of Figure 8 represent highest surface strains at defined stages of the compression test performed on the AlSi7Mg0.3 foam, as calculated by digital image correlation (DIC) of light micrographs in [9]. Namely, Figure 7 – Left corresponds to the Figure 8 – a-d, where the first deformation in the struts are observed in the top coating of both the numerical model and the AlSi7Mg0.3 foam. Figure 7 – Middle corresponds to the state shown in Figure 8 – e-f, where the bottom coating starts deforming. The similarity between Figure 7 – Right and Figure 8 – g-h is evident as both structures are highly deformed.

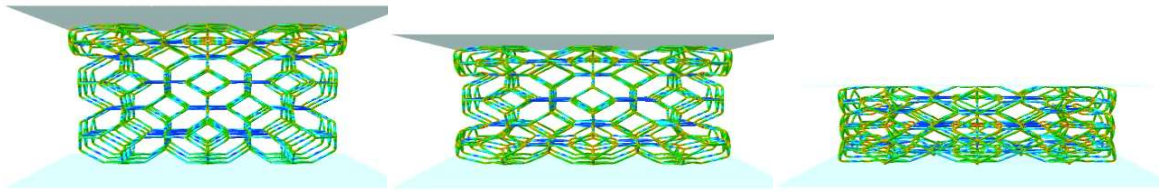

Figure 7-7: Left – Deformation in the top cell coating of the fully solid model; Middle – Deformation of the bottom coating of Kelvin cells; Right – Concluding deformation in the middle coating

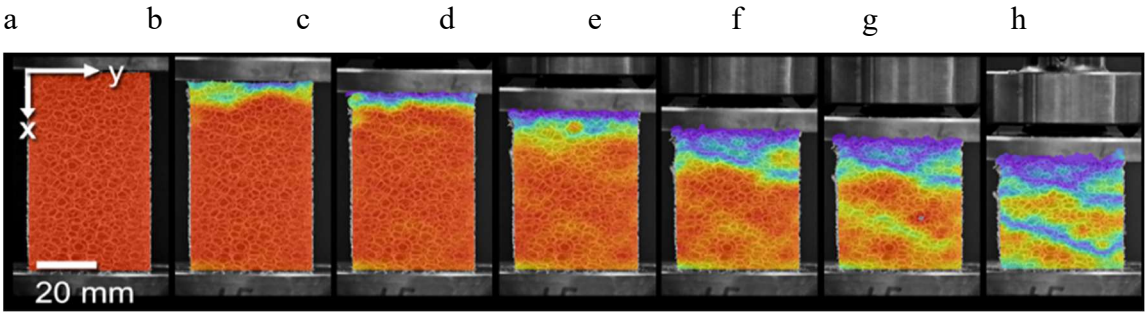

Figure 7-8: Surface strain maps at defined stages of the compression test performed on the AlSi7Mg0.3 foam, as calculated by digital image correlation (DIC) of light micrographs (blue colour = high surface strains) [9]

7.2.2 Strut shapes and influence of coatings

The next step involved a 50 µm coating of the struts and different shapes of the struts, which were analyzed in parameter studies. The idea is to reinforce the struts and improve the behavior of the foam. For this, the Kelvin cells were covered with a coating (thickness of 50 µm) of a different material, in Figure 9 an example is shown of a nickel coating. The idea is that the coating should improve the damping behavior of the foam, so that it can withstand more compression force.

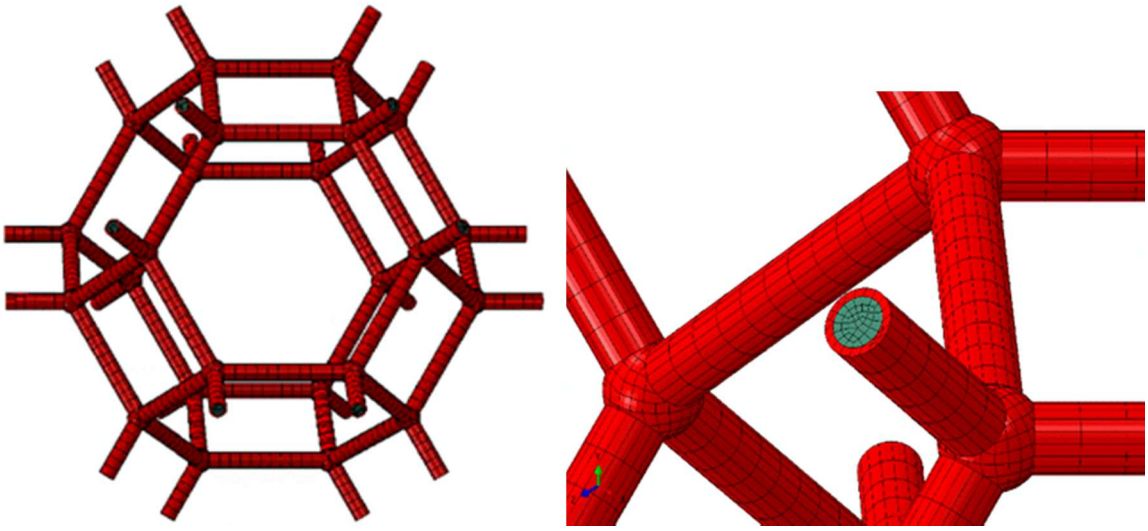

Figure 7-9: left: Kelvin cell with Ni coating, right: magnification with nickel coating (50 µm) in red (elastic) and in green the base material (AlSi7Mg0.3)

The models are then analyzed in a pressure test simulation. One example of the boundary conditions is shown in Figure 10, where blue arrows represent the direction of movement and the yellow dots represent the struts which were fixed.

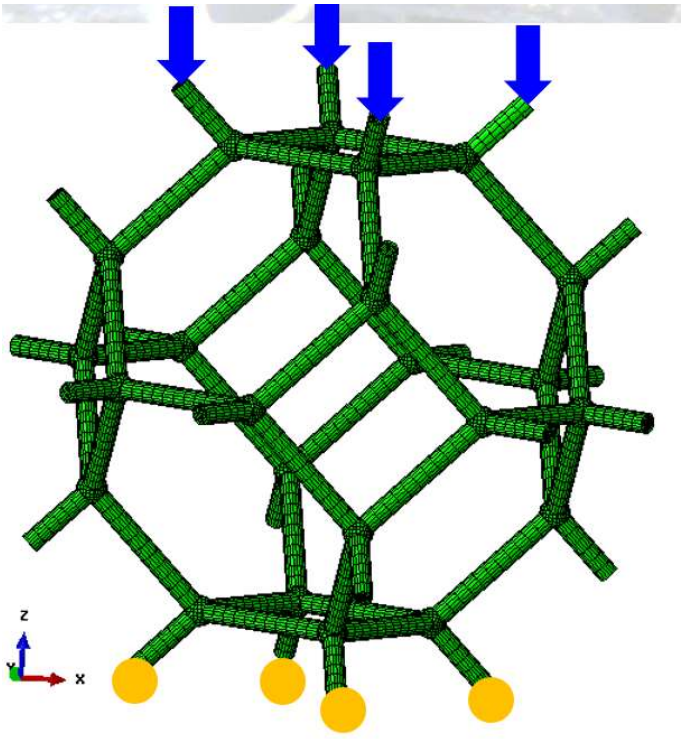

Figure 7-10: Boundary conditions of the simulation with coatings on the Kelvin cell

The result is shown in Figure 11, with an Al coating (Young's modulus of 70 GPa, left) and a Ni coating (Young's modulus of 200 GPa, right). The influence of the different materials becomes apparent when the deformation is related to the load steps. To compare the deformation at the same load level in the right picture (Ni coating) 27 steps more are necessary than in the left picture, which shows the model with Al coating.

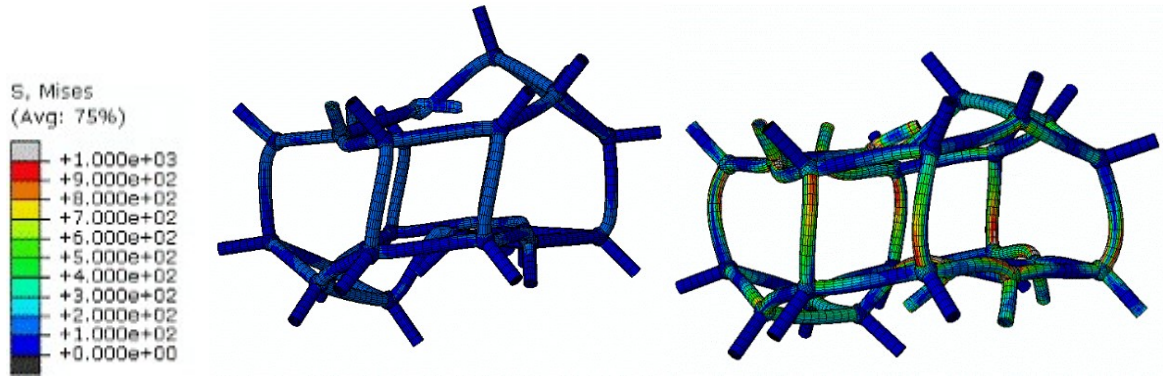

Figure 7-11: left: Al coating (50 µm), 95 load steps, right: Ni coating (50 µm), 122 load steps

This behavior can also be seen in the diagram (Figure 12). The compression of the Ni-coated structure requires a force of 8 N for a compression of 1 mm compared to the Al-coated version, which has a maximum force of 5 N.

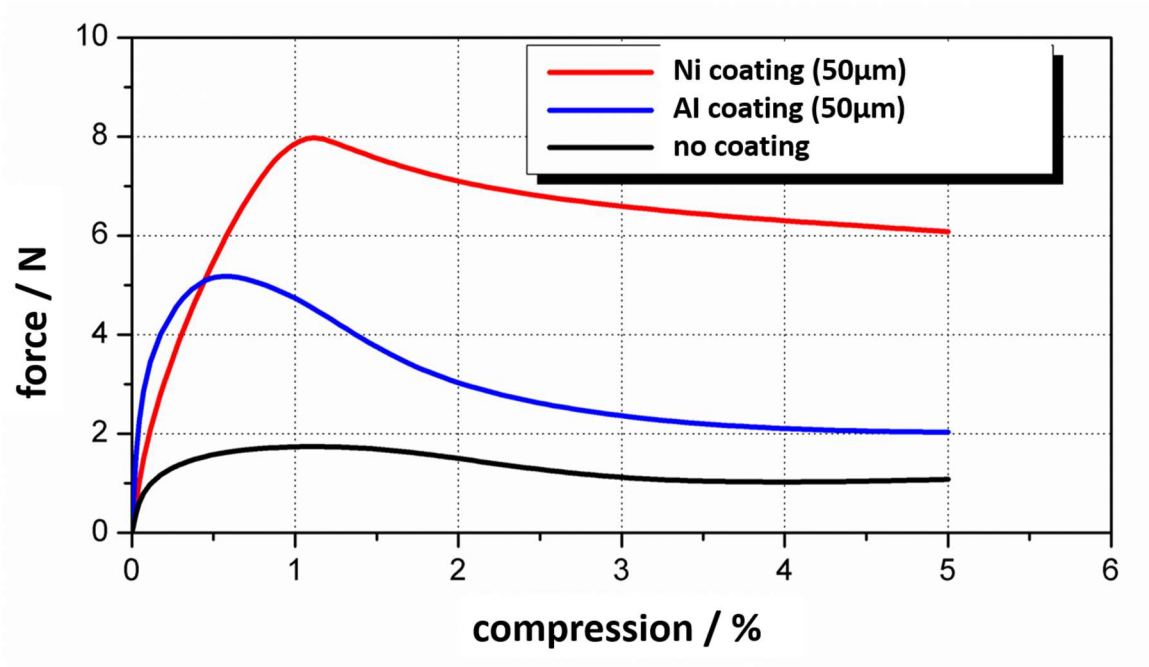

Figure 7-12: Force/compression curve for different coatings (Al, Ni and no coating)

The numerical analyses of the loads on the foam structure carried out show clear influences due to the coating with additional materials. The influence of different profiles of the struts will be shown in the next section. Three different cross-sections such as triangle, equal area square and equal area circle, Figure 13, with and without coatings were analyzed.

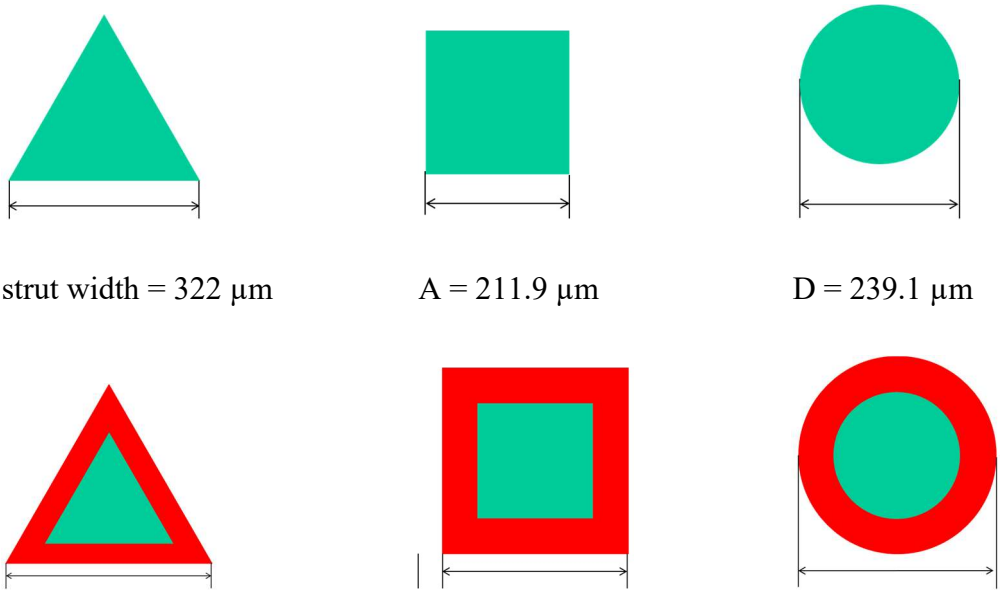

Figure 7-13: Above: Different shapes of the struts, adapted to cover the same area: Triangle, square and circle with base material (green) and on the bottom with coating (red)

The pressure test showed clear differences in the force compression curve without coating: The triangular and the circular shape show a stronger gradient, whereas the square shape has a longer maximum (see Figure 14). Also the curve of the circular shape shows a long maximum, which is getting lower to the end of the curve, a behavior the curve of the square shape is not showing. Figure 14 – bottom also shows comparisons between coated and uncoated shapes, where the Ni-coating shows the highest maximum without going down again, but the Al-coating has a clear maximum around 10% compression and then shows a local minimum, perhaps followed by a next maximum after 30%.

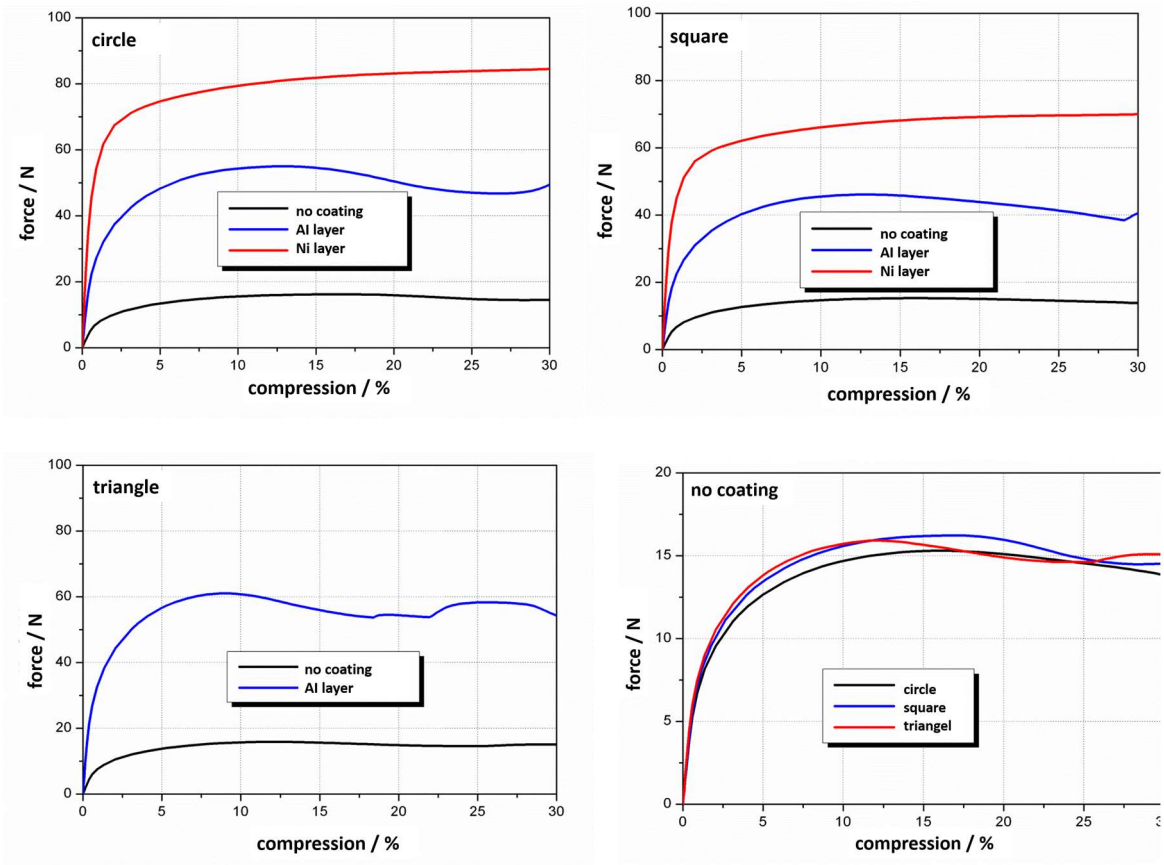

Figure 7-14: Influence of the selected cross-sections on the force compression curves, top circle (without and with Al and Ni coatings),second image square (without and with Al and Ni coatings), third image triangle with and without Al coating (Ni-coating simulation was unstable) and bottom right comparing the three shapes without coating

The comparison in the case of triangular strut profile was done only between the non-coated strut and the strut with Al-coating. Numerical calculations on the strut with Ni-coating was unstable and eventually would fail. A probable reason for this could be that the triangular profile introduces too high stress spikes in the calculation, which then results in an error in the simulation.

In order to analyze the influence of different geometry definitions, a comparison between the profile "Circle" with coating and "Circle" and "Pipe" was simulated with Abaqus. For "Circle" and "Pipe" the coating is realized by the profile "Pipe", which simplifies the modelling process (instead of creating the shape by hand the usage of profiles which are inbuilt into the software is much faster). Figure 15 shows the result, where the curves show a large agreement, so the constellation "Circle" and "Pipe" could be used for the following simulations of coated circular profiles (variations of the modulus of elasticity).

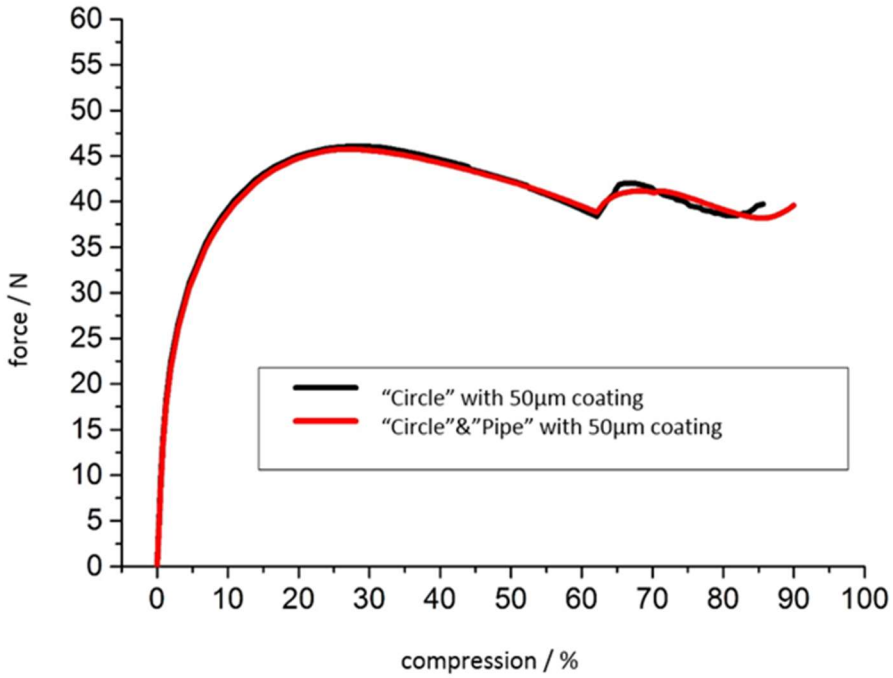

Figure 7-15: Comparison "Circle" and "Circle" + "Pipe" each with additional 50 µm coating

The following simulation results show the effect of variations of the E-modulus of the coating and their influence on the force compression curves. Figure 16 gives an impression of a comparison between Kelvin cells with coatings and with different moduli of elasticity. The coating with a low modulus of elasticity (20000 MPa) leads to a slightly lower maximum force and even at the end of the curve no increase can be seen as with the other moduli of elasticity (50000, 71000 and 100000 MPa). The differences between the curves with moduli of elasticity of 50000 to 100000 MPa are significantly smaller compared to the curve with modulus of elasticity of 20000 MPa.

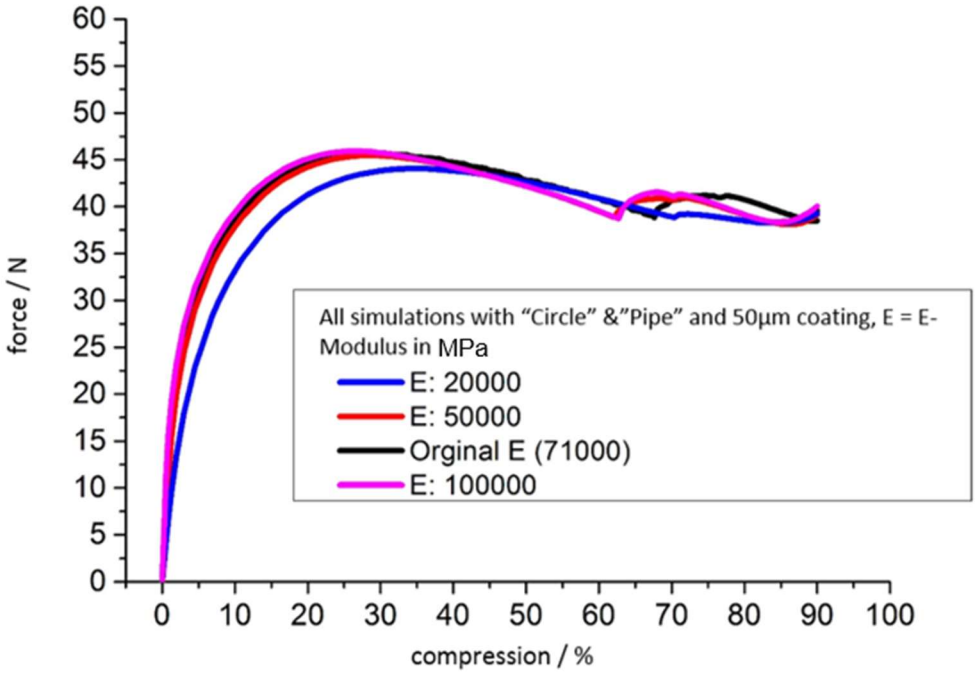

Figure 7-16: Comparison "Circle" + "Pipe" each with different moduli of elasticity of 20000 Pa, over 50000 Pa, 71000 (original) to 100000 Pa

In Figure 17 is the influence of the coating thickness with the same modulus of elasticity shown. The differences in the gradients and maxima are almost linear to the coating thickness. The second maximum at the end of the curve is particularly noticeable with the highest coating thickness of 100 µm. The other curves show this behavior much less pronounced.

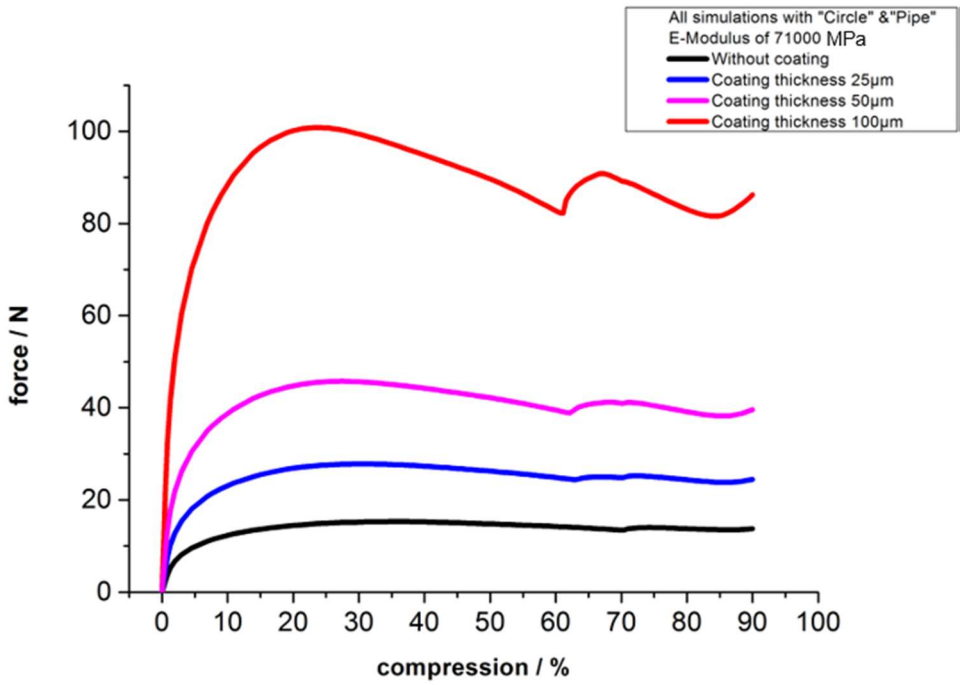

Figure 7-17: Comparison "Circle" + "Pipe" each with different coating thicknesses (25, 50,100 µm)

The next variation involved the change of the moduli of elasticity of the beams middle part (red part in Figure 18 – Right). Here, only the outer green sections of the beams were varied in different moduli of elasticity and the coating thickness was not varied.

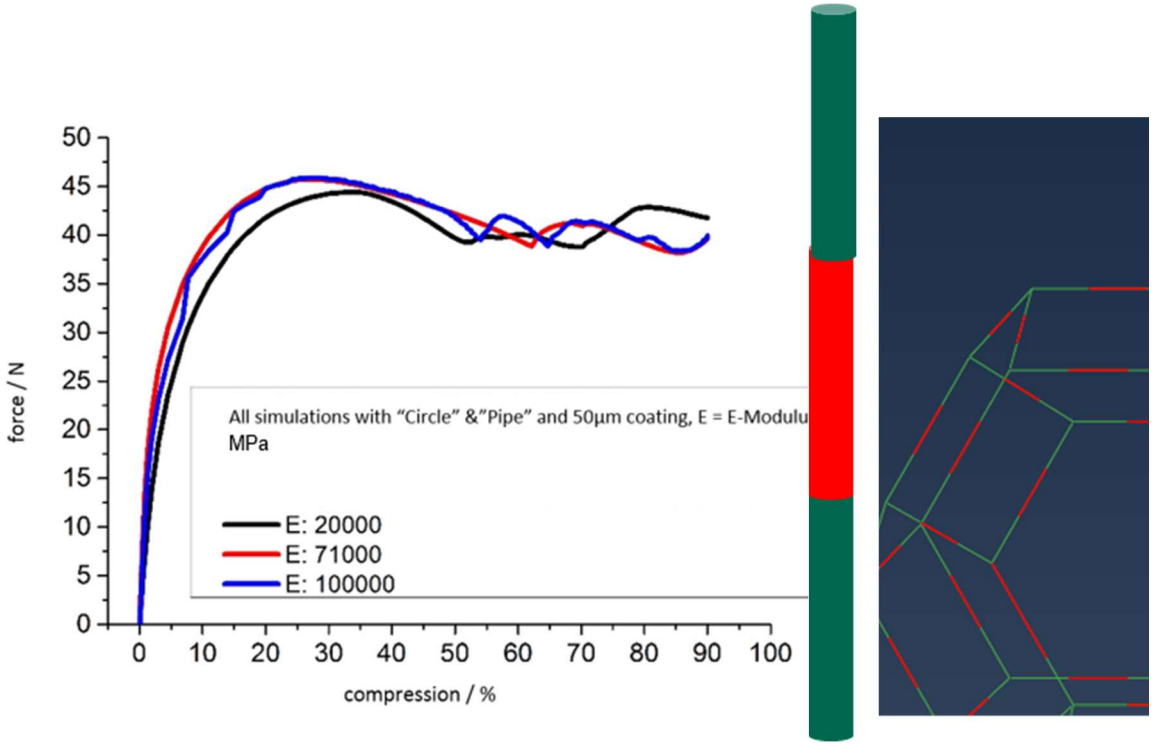

Figure 7-18: left: Comparison "Circle" + "Pipe" each with different gradients in the modulus of elasticity of the coating on the outside (green part of the bar) but the same thickness of the coating, on the right: representation of the struts in the model

7.3 Detailed hierarchical modelling of the bio-inspired metallic foams

Due to the highly nonlinear behavior and the limited measurability, detailed modelling including the microstructure of bio-inspired materials is challenging and computationally expensive. Most detailed models are multi-modal, i.e., they have many local maxima and/or minima that require particular attention [18]. Furthermore, the models are often high-dimensional, making the simulation task computationally complex. Despite those challenges, this substudy is focused on the influence of Si- or Fe-rich intermetallic particles within the struts of AlSi7Mg0.3 foams or instead of the particles, on the influence of pores.

7.3.1 Porous struts

Porosity inside the struts is one way to reduce the material use in foams. With that step, the next level or hierarchy is involved because pores can be found inside the foam and also inside the struts which are building the foam. In Figure 19 the sketch of the porous strut idea is shown. The meeting point of four struts with pores inside is depicted as well. One way to idealize the structure for the use in simulations is a so called self-consistent matricity

model or self-consistent cell model (SCECM). Such a model is used to describe and analyze the mechanical behavior of composites with two randomly distributed phases of interpenetrating microstructure. More information about the model can be found in the paper of Leßle, Dong and Schmauder, Self-consistent matricity model to simulate the mechanical behavior of interpenetrating microstructures [19].

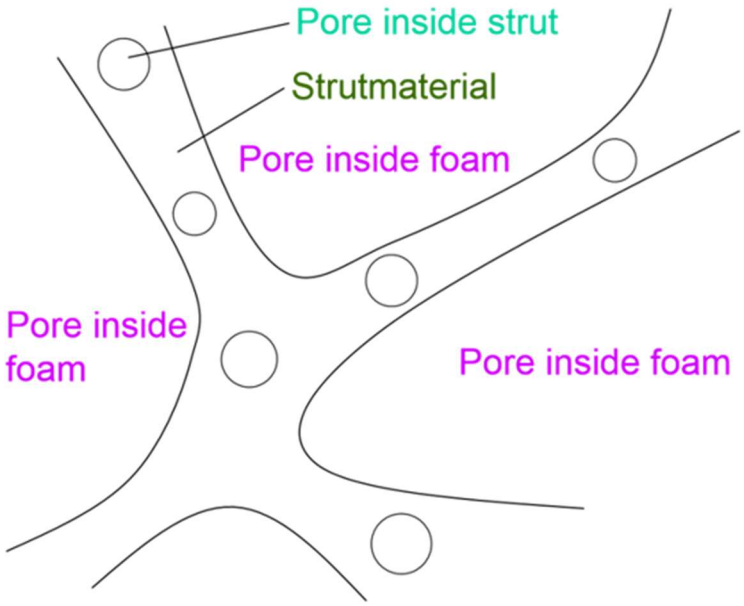

Figure 7-19: Schematic of the porosity inside the strut.

The simulation results of tensile tests are shown in Figure 20. For the simulations, four different porosities inside the struts from 0%, 5%, 10% to 20% were analyzed. The curves are showing a comparable behavior, a maximum is reached with a little more than 2% strain. The result were then compared with a 3D simulation, with 10% porosity in the Figure 21.

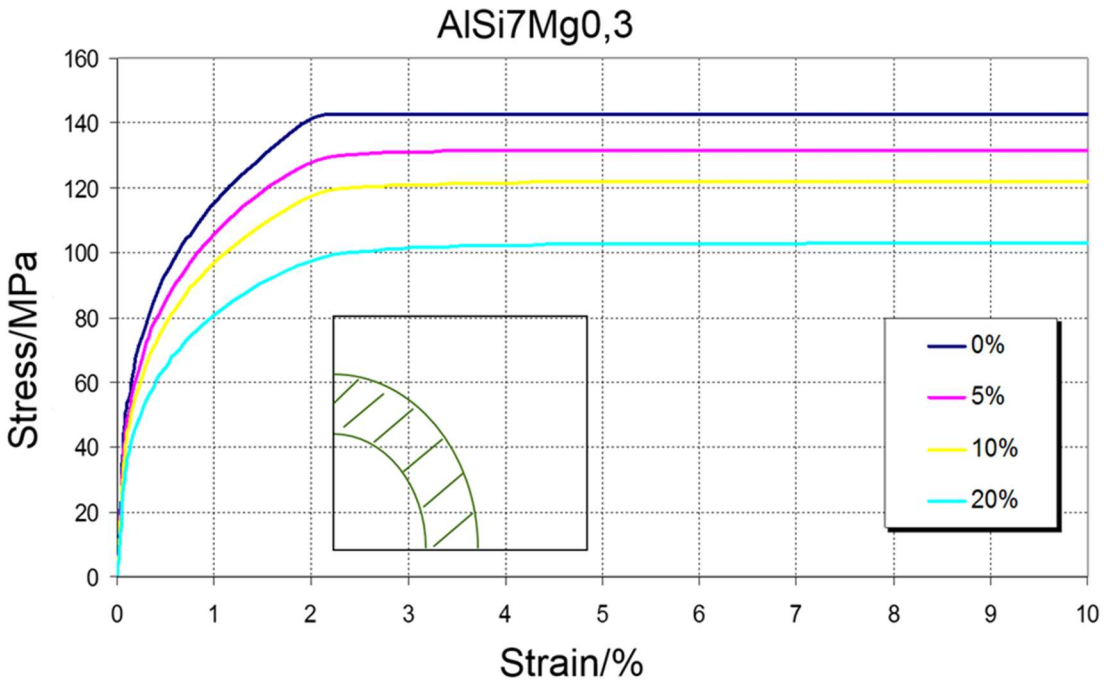

Figure 7-20: The results of the tensile simulations of four different porosities inside the struts from a SCECM

The SCECM represents a statistically distributed porosity. The comparison in the next figure shows that there are not many differences in the three curves. So the influence of big pores or small pores in the SCECM simulation is nearly equal as expected form continuum mechanical analyses and in good agreement with the 2D simulation of 10 % from Figure 21.

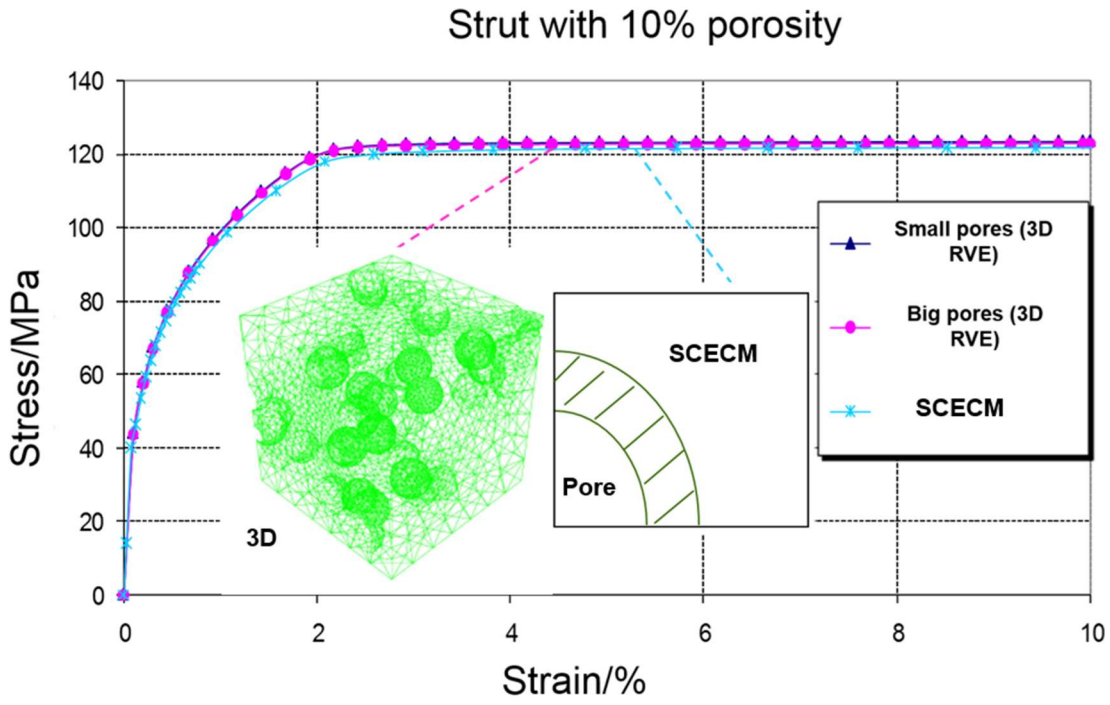

Figure 7-21: Simulation of small and big pores inside the struts in comparison

With that information, also the different porosities like in the 2D SCECM model were analyzed in simulations of the 3D SCECM foam. But this time, the simulations cover the whole foam, not only the struts. The porosity is included through the usage of the before mentioned SCECM. Also, a direct correlation between porosity and strength was found (see Figure 22).The influence of the porosity inside the struts is generally linear. With more pores, the less the strength the struts can withstand. Interestingly, the maxima of stress (found in Figure 21) are reached for every variation between two and three percent strain. In the case of 3D simulations, where the porosity inside the struts is around 10%, shows that good agreement between the 3D and the SCECM simulation can be found. The part of the curve, short before the maximum stress is reached, differs slightly and is a little bit smaller than the curve of the 3D simulations. But generally, with such a good agreement the use of 2D simulations to achieve faster calculations seems to be legit. The differences between the big pores and small pores are found to be small, because the most influence on the result is due to the removal of material, not because of the size of the pores.

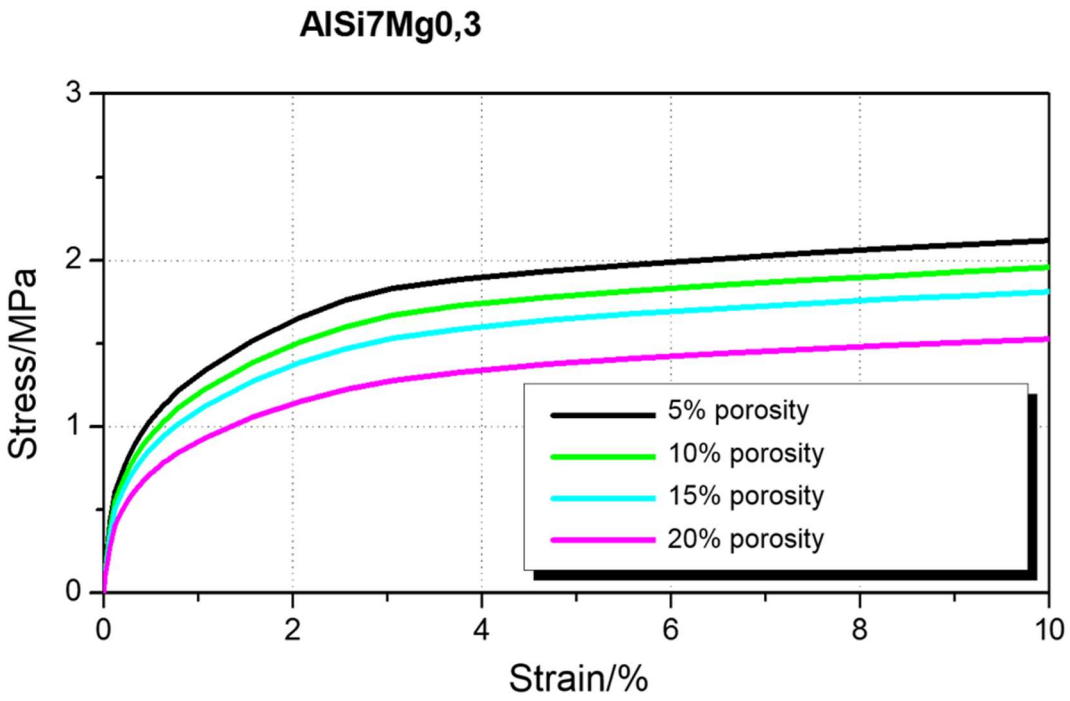

Figure 7-22: Foam with porous struts - results of the simulation

7.3.2 Particles within the struts

Analyzation of the influence of Si- or Fe-rich intermetallic particles within the struts of AlSi7Mg0.3 foams follows. Additionally, the study aims to find the effects of different loading conditions on the model thereby providing the best support to the experimental observations [9]. Examples of these efforts in the particular case of the AlSi7Mg0.3 foam are given below. As observed in [9], the Si- or Fe-rich intermetallic particles within the struts of the AlSi7Mg0.3 foam reduce the strut ductility as they promote the formation and growth of micro-cracks. The light bodies detected by using the scanning electron micro-graphs and which are shown in Figure 23 demonstrate the presence of the brittle particles in the microstructure of the foam.

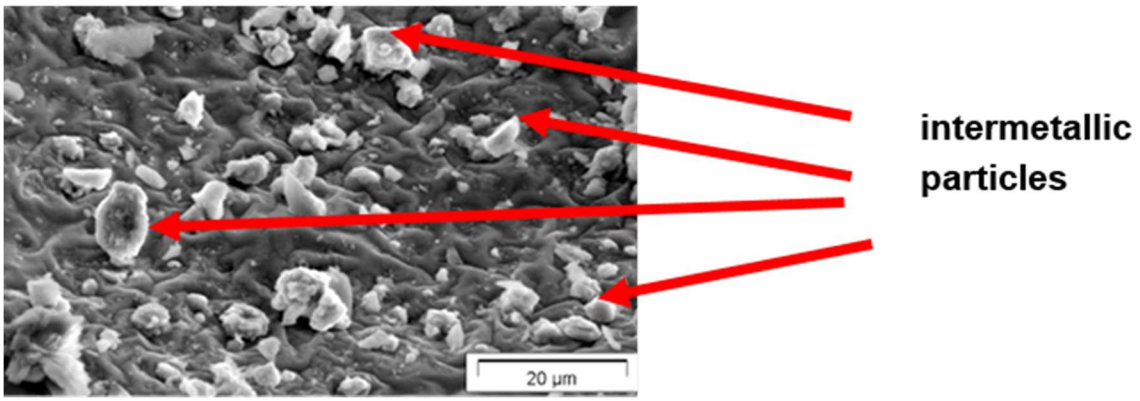

Figure 7-23: AlSi7Mg0.3 containing intermetallic particles (light color)

Figure 24 shows the investigated case where the intermetallic (plaster) particles have been homogenized with another SCECM together with the base material (AlSi7Mg0.3) and applied to the foam struts as coating. The coating containing the homogenized material is shown in Figure 24. The volume of 1.8% for the plaster content results from the use of a thickness of 3 µm of the coating.

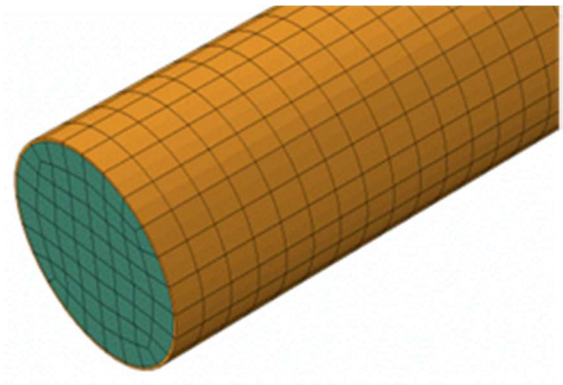

Figure 7-24: Strut (green) with homogenized plaster particles coating (Volume 1.8% (brown))

A comparison between strut made of pure base material and the struts with different homogenized coatings is given in Figure 25 – Left. Homogenized coatings vary depending on the volume contribution of the intermetallic particles, i.e. 9%, 16% and 36% particle-based coated struts have been considered. For that fully bulk models were used.

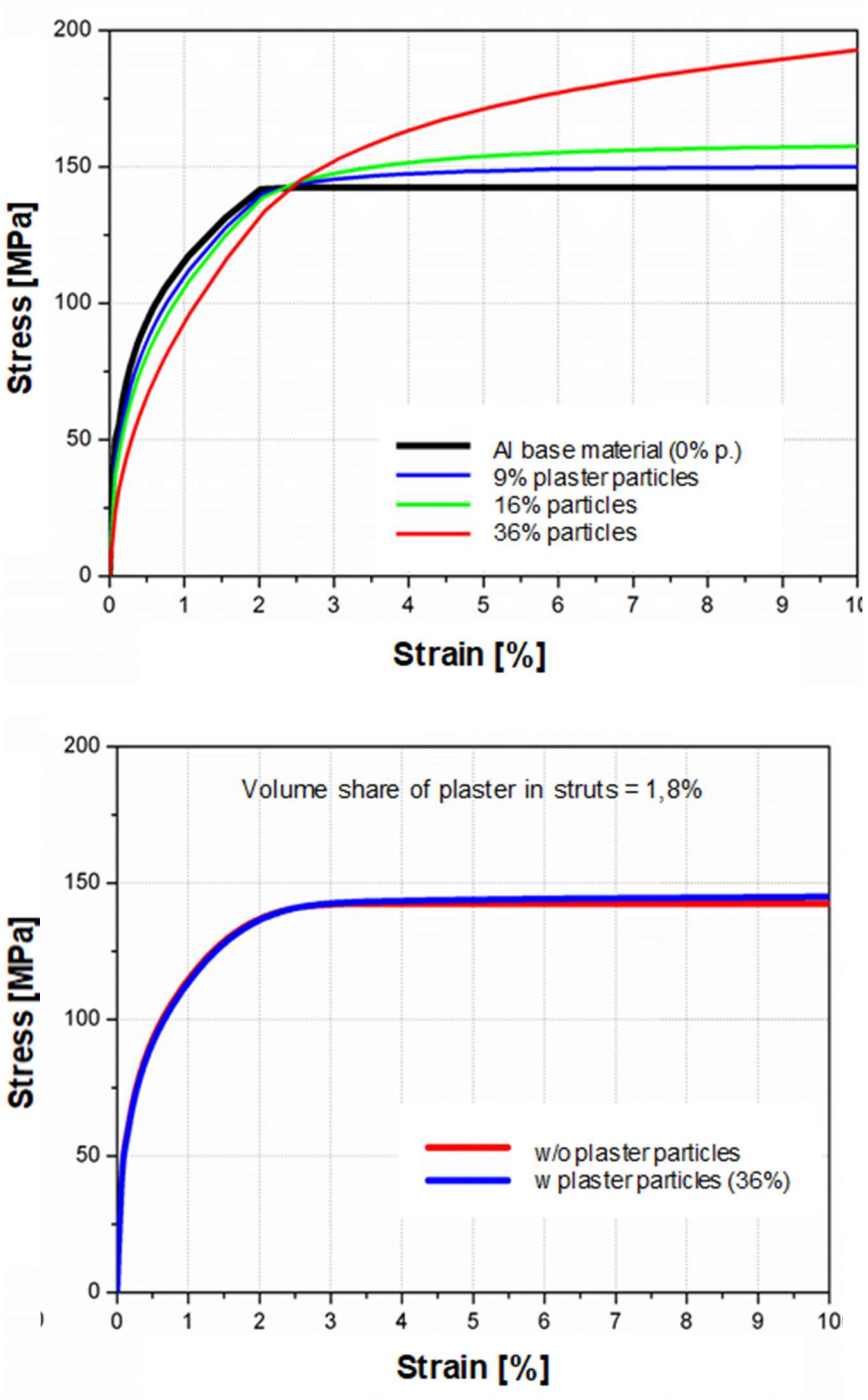

Figure 7-25: Left – Homogenization of the coating; Right – Homogenization of the complete strut

The particles in the outer homogenized coating of the foam struts play an important role, as shown in Figure 25 – Left. More precisely, the higher the volume fraction of the particles, the higher the strain energy, i.e. toughness, of the material system. Interestingly the curve with 36% particles shows even after 2% strain a high rising behavior, but this behavior was

also shown in Literature [19,20]. In another case where the complete strut has been modelled by applying the homogenized material and eventually compared to the model with the base material the difference in the mechanical response, especially in terms of stiffness, was minimal, Figure 25 – Right. The reason for this is likely the small amount of plaster particles in the struts (1.8 %).

In the following case study, a cutout of the strut (light green Kelvin cell in the bottom right of Figure 26) has been substituted with a representative volume element (RVE) of the strut (top right), using the submodelling technique. The SCECM contains the base material, AlSi7Mg0.3, (dark green), a homogenized coating, AlSi7Mg0.3 + 36% plaster particles (red) and finally 36 (6 x 6) cuboidal plaster particles (3 x 3 x 3 µm3) that have been embedded into the base material.

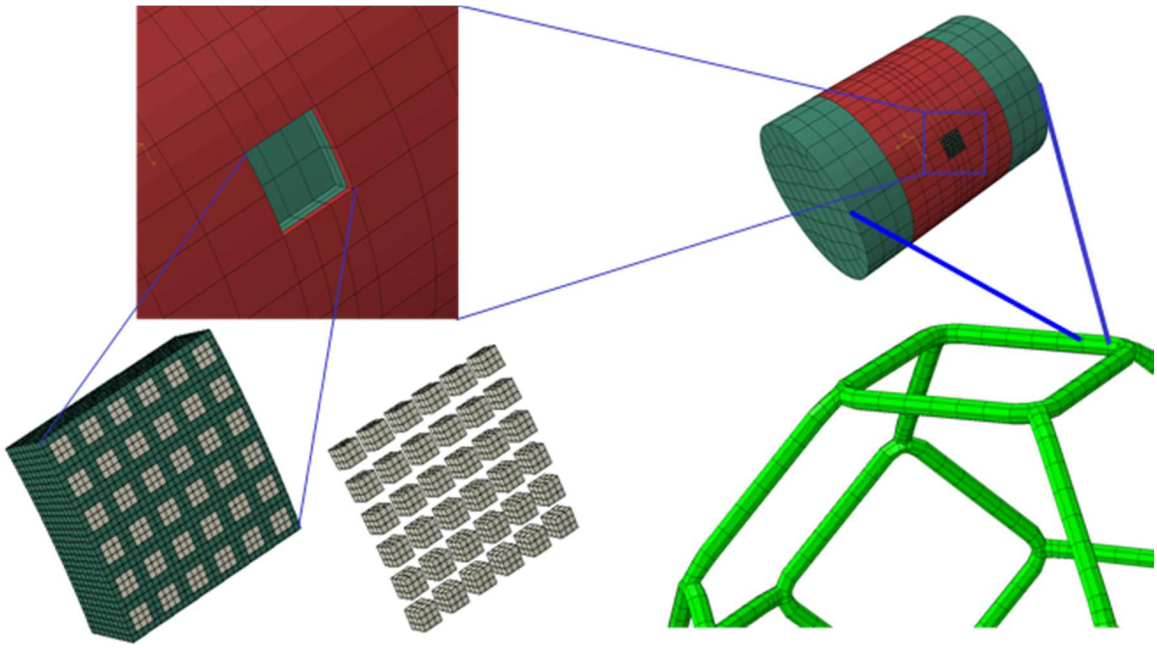

Figure 7-26: Substitution of a cutout of the strut (light green) with a SCECM of the strut (top right), using the submodelling technique. The SCECM of the strut contains the base material (AlSi7Mg0.3, dark green), homogenized (AlSi7Mg0.3 + 36% plaster particles) coating and finally 36 (6 x 6) cuboidal plaster particles (3 x 3 x 3 µm3) that are embedded into the base material

As reported in [9], the individual struts are mainly loaded in bending or torsion and failure is characterized by plastic buckling or fracture. Accordingly, a section (containing the aforementioned cutout) of the Kelvin cell strut has been modelled and analyzed under loading conditions, which are present in reality, i.e. under separate and combined bending and torsion. The results of these studies are shown in Figure 27 and Figure 28.

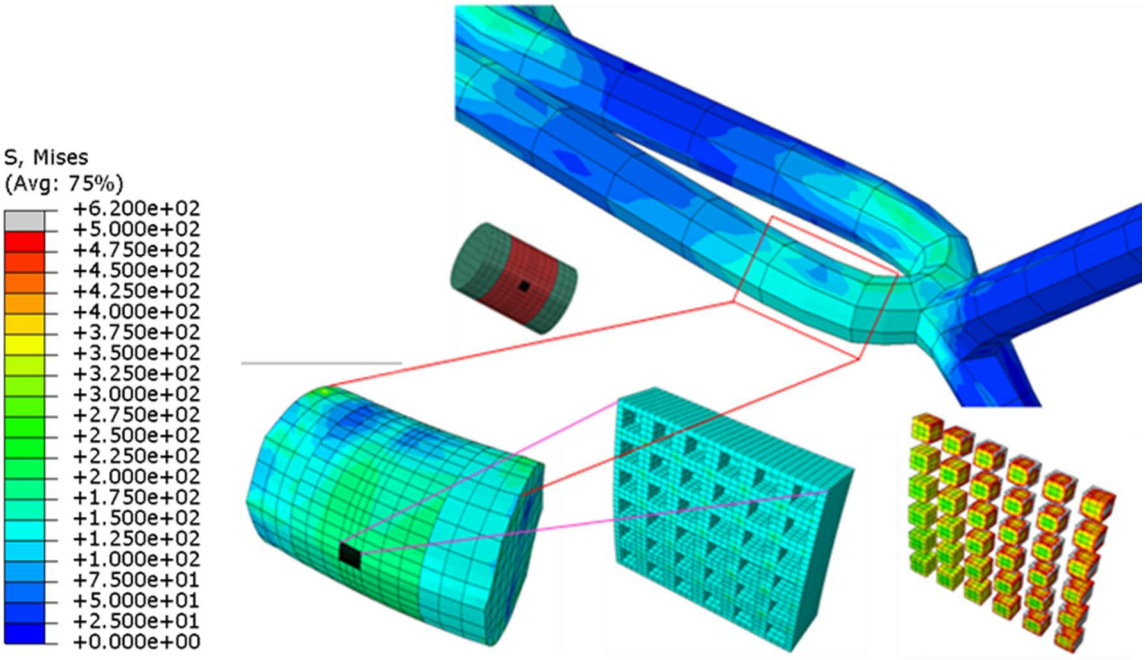

Figure 7-27: Relatively high disturbances in the stress response of particels under application of the RVE

Figure 27 depicts negligible disturbances in the global stress response of the foam strut under realistic loading conditions when using the RVEs. On the other hand, the intermetallic particles in the SCECM are exposed to increased stresses, which may result in breaking off of the particles under application of appropriate damage criterions (Figure 28).

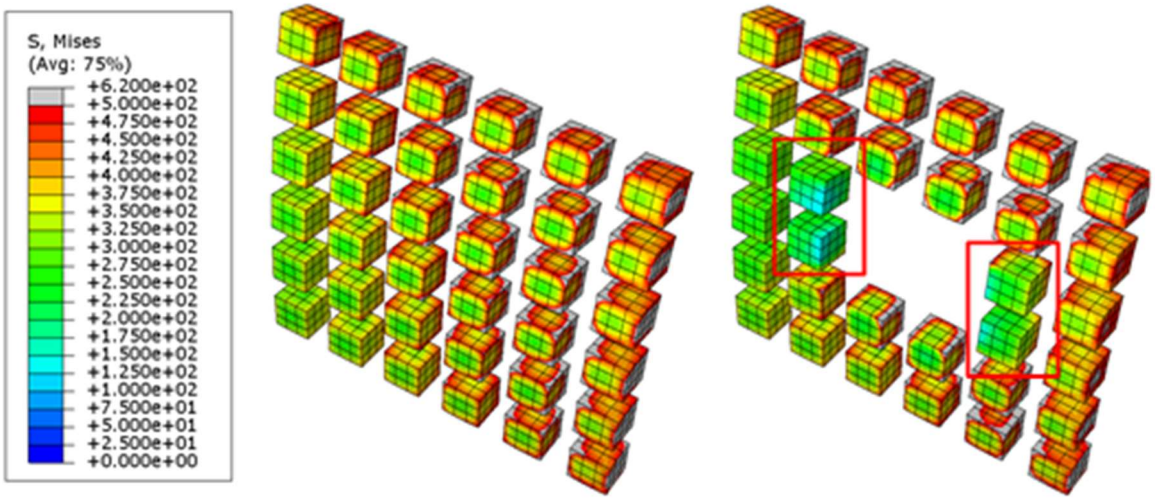

Figure 7-28: A removal of intermetallic particles leads to stress relaxation in the neighboring particles

By removing certain particles from the model, the stress relaxations in the neighboring particles are achieved, as visible from Figure 28 – Right. No specific relaxation technique, like e.g. heat treatment, was applied to relieve the stresses around the particles shown in Figure 28 – Right. The relaxation of the particles is simply a byproduct of removing certain number of neighboring particles, which normally act as stress intensifiers. With variations in size, number and material of the particles it is possible to adapt and modify the strut to certain loading situations. E.g. the higher the volume fraction of the particles, the higher the strain energy, i.e. toughness, of the material system as seen in the example of the strut with 36% particles. Interestingly, the size shows substantial influences on the behavior of the coating for particles larger than 3 μm. A combination of these effects could result in a significant improvement of the toughness and the deformation behavior of the coating.

7.4 Conclusions

The study and the extraction of biological key principles have been widely adopted nowadays [3]. Furthermore, their translation into design guidelines for a new generation of materials and technological solutions is a driving force in many research fields. The paper presents a modelling approach to analyze structures that are based on biological role models adopted from nature. The analysis includes both the homogeneous and the detailed study; the latter by taking into account different components of the by the pomelo fruit bio-inspired aluminum-based AlSi7Mg0.3 metallic foam. Due to its special mechanical property and a wide range of engineering applicability (e.g. protection systems), this metallic foam has aroused intense interests in the field of materials science (e.g. in [7][8][9]). Simulation results of mechanical response of the bio-inspired system are provided to illustrate the effectiveness and feasibility of the proposed modelling approach. Here are some general findings that can be drawn from the study on the bio-inspired metallic foam:

The simulation show a good agreement with the experimental results.

- Material: The softer Ni-coating shows a higher force in compressions test (a higher damping behavior) in comparison to the AI coating;
- Shape: The shape of the struts has an influence on the force/compression behavior, a circular shape showed a little less maximum force in compression test in comparison to the triangle and square shapes but all in all the influence is very low;

- Coating thickness: With a coating thickness of 100µm the hill at the end of the force/compression curve is much more pronounced compared to the other coating thicknesses;
- 2D and 3D simulation: of porous struts show a good agreement, the pores inside the struts reduce the maximal stress the foam can withstand;
- Particles:
    - Influence of Si- and Fe-rich intermetallic (plaster) particles on the deformation behavior of the outer coating is significant for particles larger than 3 µm;
    - The toughening aspect of the particles is clearly visible with 36 % particles;
    - Removal of plaster particles (which show high stresses) leads to stress relaxation in the neighboring particles;

Conclusion: The method of hierarchical modelling on three levels gives access to different optimization options for the resulting foam, like the shape and coating of the struts, particles inside the struts and the resulting macrostructure - the foam itself.

7.5 Acknowledgments

The authors wish to thank Claudia Fleck, Andreas Bührig-Polaczek, Thomas Speck, Paul Schüler, Sebastian Fischer and Mark Thielen for the provided data. We also want to thank Dubravka Mijuca for her support on creating the RVEs. Funding was provided by the German Research Foundation (DFG) within the priority program SPP1420 ‘Biomimetic Materials Research: Functionality by Hierarchical Structuring of Materials’.

7.6 Data availability

The raw/processed data required to reproduce these findings cannot be shared at this time due to technical or time limitations.

7.7 References

[1] Fujita, M.; Fujita, Y.; Noutoshi, Y.; Takahashi, F.; Narusaka, Y.; Yamaguchi-Shinozaki, K. & Shinozaki, K. (2006), 'Crosstalk between abiotic and biotic stress responses: a current view from the points of convergence in the stress signaling networks', Current Opinion in Plant Biology 9(4), 436-442.

[2] Mazzolai, B. & Mancuso, S. (2013), 'Smart solutions from the plant kingdom', Bioinspiration & Biomimetics 8(2), 020301.

[3] Mazzolai, B.; Beccai, L. & Mattoli, V. (2014), 'Plants as model in biomimetics and biorobotics: New perspectives', Frontiers in Bioengineering and Biotechnology 2(2), 1-5.

[4] Velcro, S. S. (1955), 'Velvet type fabric and method of producing same' (Patent No. 721 338).

[5] Martone, P. T.; Boller, M.; Burgert, I.; Dumais, J.; Edwards, J.; Mach, K.; Rowe, N.; Rueggeberg, M.; Seidel, R. & Speck, T. (2010), 'Mechanics without muscle: Biomechanical inspiration from the plant world', Integrative and Comparative Biology 50(5), 888-907.

[6] Thielen, M.; Schmitt, C. N. Z.; Eckert, S.; Speck, T. & Seidel, R. (2013), 'Structure-function relationship of the foam-like pomelo peel (Citrus maxima) - an inspiration for the development of biomimetic damping materials with high energy dissipation', Bioinspiration & Biomimetics 8(2), 025001.

[7] Fischer, S. F.; Thielen, M.; Loprang, R. R.; Seidel, R.; Fleck, C.; Speck, T. & Bührig-Polaczek, A. (2010), 'Pummelos as concept generators for biomimetically inspired low weight structures with excellent damping properties', Advanced Engineering Materials 12(12), B658-B663.

[8] Seidel, R.; Thielen, M.; Schmitt, C.; Bührig-Polaczek, A.; Fleck, C. & Speck, T. (2013), 'Fruit walls and nut shells as an inspiration for the design of bio-inspired impact-resistant hierarchically structured materials', International Journal of Design & Nature and Ecodynamics 8(2), 172-179.

[9] Bührig-Polaczek, A.; Fleck, C.; Speck, T.; Schüler, P.; Fischer, S. F.; Caliaro, M. & Thielen, M. (2016), 'Biomimetic cellular metals–using hierarchical structuring for energy absorption', Bioinspiration & Biomimetics 11(4), 045002.

[10] Speck, T.; Thielen, M. & Speck, O. (2018), 'What can be learnt from ageing in biology and damage-tolerant biological structures for long-lasting biomimetic materials?', in The Ageing of Materials and Structures, ed. van Breugel, K.; Koleva, D. & Beek, T. v., Springer International Publishing, Cham, pp. 27-38.

[11] Horn, R.; Dahy, H.; Gantner, J.; Speck, O. & Leistner, P. (2018), 'Bio-inspired sustainability assessment for building product development–Concept and case study', Sustainability 10(1), 130.

[12] Perez-Jimenez, M. J. (2014), 'A bioinspired computing approach to model complex systems', in Membrane Computing, ed. Gheorghe, M.; Rozenberg, G.; Salomaa, A.; Sosik, P. & Zandron, C., Springer International Publishing, Cham, pp. 20-34.

[13] Signetti, S. & Pugno, N. M. (2015), 'Frontiers in modeling and design of bio-inspired armors', Frontiers in Materials 2(17), 1.

[14] Lasko, G.; Burghard, Z.; Bill, J.; Schäfer, I.; Weber, U. & Schmauder, S. (2013), 'Simulation of mechanical properties of bio-inspired TiO_2/PE nanocomposites', Advanced Engineering Materials 15(10), 908-920.

[15] Schäfer, I.; Lasko, G.; Do, T.; Pleiss, J.; Weber, U. & Schmauder, S. (2014), 'Peptide-zinc oxide interaction: Finite element simulation using cohesive zone models based on molecular dynamics simulation', Computational Materials Science 95, 320-327.

[16] Schmier, S.; Bauer, G.; Buck, G.; Klang, K.; Lauer, C.; Toader, N.; Gericke, O.; Haase, W.; Schäfer, I.; Schmauder, S.; Sobek, W.; Nickel, K. G. & Speck, T. (2017), Baubionik, eds. Jan Knippers; Ulrich Schmid & Thomas Speck, Stuttgarter Beiträge zur Naturkunde, Stuttgart, 41-61.

[17] Chou, I.-C. & Voit, E. O. (2009), 'Recent developments in parameter estimation and structure identification of biochemical and genomic systems', Mathematical Biosciences 219(2), 57-83.

[18] Lin, J. H.; Chou, C. W.; Yang, C. H.; Tsai, H. L. & Lee, I. H. (2012), 'A bio-inspired optimization algorithm for modeling the dynamics of biological systems', in 2012 Third International Conference on Innovations in Bio-Inspired Computing and Applications, pp. 206-211.

[19] Leßle, P.; Dong, M. & Schmauder, S. (1999), 'Self-consistent matricity model to simulate the mechanical behaviour of interpenetrating microstructures', Computational Materials Science 15(4), 455 - 465.

[20] Schmauder, S.; Weber, U. (2001), 'Modelling of functionally graded materials by numerical homogenization', Archive of applied mechanics, 71, 182-192.

8 TRR141: Teilprojekt B01

In dem nun folgenden Abschnitt werden Ergebnisse vorgestellt, die in einem Teilprojekt des Transregios 141 (DFG gefördert) gewonnen wurden.

Die vollständige Bezeichnung des TRRs und des Teilprojektes B01 lauten:

TRR141: Biological Design and Integrative Structures

Analysis, Simulation and Implementation in Architecture

B01: Scaling of Properties of Highly Porous Biological and Biomimetic Constructions

Im Teilprojekt B01 sind u. a. die Kokosnuss und der Seeigelstachel Vorbilder für die Architektur. Eine Vorstellung der beiden Themen und deren Besonderheiten, Analysemethoden und Simulationsansätze folgt in der Veröffentlichung:

VIII. Schmier, S., Lauer, C., Schäfer, I., Klang, K., Bauer, G., Thielen, M., Termin, K., Berthold, C., Schmauder, S., Speck, T., Nickel, K. G. (2016). Developing the Experimental Basis for an Evaluation of Scaling Properties of Brittle and 'Quasi-Brittle' Biological Materials. In *Biomimetic Research for Architecture and Building Construction*, pp. 277–294.

Der Anteil meiner Arbeit in der Veröffentlichung umfasst Kapitel 8.5, (100 %); das gesamte Manuskript wurde von allen Autoren zusammen erstellt.

Danach folgt ein ergänzendes Kapitel (Kokosnuss: Simulation Kerbschlagbiegeversuch) zu der genannten Veröffentlichung, worin unveröffentlichte Details zur Kokosnussschale diskutiert werden (Anteil meiner Arbeit 100 %).

Developing the Experimental Basis for an Evaluation of Scaling Properties of Brittle and 'Quasi-Brittle' Biological Materials

Stefanie Schmier, Christoph Lauer, Immanuel Schäfer, Katharina Klang, Georg Bauer, Marc Thielen, Kathrin Termin, Christoph Berthold, Siegfried Schmauder, Thomas Speck, and Klaus G. Nickel

S. Schmier • G. Bauer • T. Speck

Plant Biomechanics Group, Botanic Garden, Faculty of Biology, University of Freiburg, Schänzlestraße 1, D-79104 Freiburg, Germany

Freiburg Centre for Interactive Materials and Bioinspired Technologies (FIT), University of Freiburg, Georges-Köhler-Allee 105, D-79110 Freiburg, Germany

e-mail: stefanie.schmier@biologie.uni-freiburg.de

C. Lauer • K. Klang • K. Termin • C. Berthold • K.G. Nickel

Applied Mineralogy (AMIN), University of Tübingen, Wilhelmstraße 56, 72074 Tübingen, Germany

I. Schäfer • S. Schmauder

Institute for Materials Testing, Materials Science and Strength of Materials (IMWF), University of Stuttgart, Pfaffenwaldring 32, 70569 Stuttgart, Germany

M. Thielen

Plant Biomechanics Group, Botanic Garden, Faculty of Biology, University of Freiburg, Schänzlestraße 1, D-79104 Freiburg, Germany

J. Knippers et al. (eds.), Biomimetic Research for Architecture and Building Construction, Biologically-Inspired Systems 9, DOI 10.1007/978-3-319-46374-2_14

Abstract

The development of lightweight structures exhibiting a high energy dissipation capacity and a locally adapted puncture resistance is of increasing interest in building construction. As discussed in Chap. 7, inspiration can be found in biology, as numerous examples exist that have evolved one or even several of these properties. Major challenges in this interdisciplinary approach, i.e. the transfer of biological principles to building constructional elements, are scaling (different dimensions) and (at least for the botanic examples) the fact that different material classes constitute the structural basis for the functions of interest. Therefore, a mathematical description of the mechanical properties and the scalability is required that is applicable for both biological and technical materials. A basic requisite for the establishment of mathematical descriptions are well-defined test setups rendering a reliable data basis. In the following, two biological role models from the animal and plant kingdoms are presented, namely, sea urchin spines and coconut endocarp, and two experimental setups for quasi-static and dynamic testing of biological and bio-inspired technical materials are discussed.

8.1 Introduction

Intuitively, problems are bound to arise in the transfer of the principles and characteristics of natural materials, which come in millimetre or centimetre sizes, to architectural objects, which may span many metres. However, the analysis of this scaling problem is far from being trivial and is of particular importance in the realm of brittle materials, to which at least the matrix of common building materials such as cement and concrete belongs. A theoretical and experimental evaluation requires proper data sets. In the following, we describe our efforts to develop the methods by which to obtain such data.

In 1921, Griffith reported that the experimentally determined strength of homogeneous, isotropic and brittle solids is several times lower than can be expected from calculations based on their intrinsic properties such as elastic moduli and surface energies (Griffith 1921). Weibull characterised this phenomenon statistically, stating that the probability of failure depends on two factors: a given distribution of stresses (e.g. according to the test method) and, in particular, the volume of the tested specimen. Weibull was the first who took into account the volume of the tested specimen as a reason for the large scatter of experimentally obtained ultimate strength data (Weibull 1939; Bažant 2000).

Weibull's theory is based on the weakest link hypothesis, which assumes that a specimen fails at its weakest point (e.g. an internal flaw or imperfection). In a homogeneous, isotropic and brittle material, in which the failure events are independent of each other, the size of the flaws controlling the strength follows a statistical distribution function for a given volume. If the size of flaws in a volume is a matter of probability, then it is tantamount that the stress needed to break the material of a given volume is statistically distributed. The probability of failure P_{i,V_0} for a specimen i within a given volume P_0 is then, in its simplest form, defined by the two-parameter Weibull formula:

$$P_{i,V_0} = 1 - \mathrm{e}^{-\left(\frac{\sigma i}{\sigma 0}\right)^m} \quad [1]$$

where σ_i is the critical stress at failure for specimen i, σ_0 is the characteristic strength and m the Weibull modulus. The Weibull modulus m is therefore a measure of the reliability of the material: the lower the Weibull modulus, the higher the scatter of critical stresses in a material and the lower the material's reliability. For this reason, technical ceramics are desired to have high Weibull moduli (m = 10 – 20) (Danzer 2014). The characteristic strength is the critical stress at which 63.2 % of the tested specimens with volume V_0 fail. Unlike the Weibull modulus m, the characteristic strength σ_0 is not a material constant as it depends on the volume of the investigated specimen and, therefore, the corresponding material constant is $\sigma_0 {V_0}^{1/m}$. The Weibull modulus and characteristic strength can be determined experimentally by using the empirical distribution function F for P_{V_0}. By fitting a regression line to $ln\ (\ln(1/(1-F_i)))$ versus $ln\ (\sigma_i)$, the Weibull modulus m can be identified as the slope and $\sigma_0 = \exp\left(-\frac{c}{m}\right)$ with c being the intercept of the regression line (Fig. 1). Materials to which this method can be applied are said to show 'Weibull behaviour' (Weibull 1939, 1951; Danzer et al. 2007; Danzer 2014).

Weibull defined the characteristic strength as depending on the respective volume of the specimen. This is because it is more likely to find a critical flaw in a large specimen than in a small one. Thus, a large specimen will statistically fail at lower stresses (i.e. at lower σ_0) than small ones. This effect is called the 'size effect' and is expressed for specimens of the same material having the same probability of failure by:

$$\left(\frac{\sigma_1}{\sigma_1}\right) = \left(\frac{V_2}{V_1}\right)^{1/m} \quad [2]$$

where σ_1 is the strength at failure of the object with volume V_1, σ_2 is the strength at failure of the object with volume V_2 ($F_{1,V_1} = F_{2,V_2}$), and m is the Weibull modulus of the material (Danzer et al. 2007).

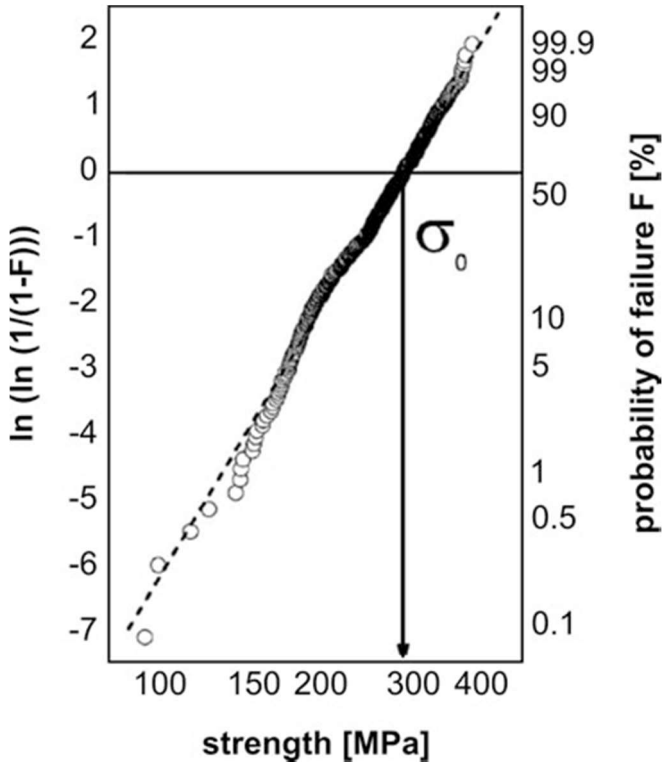

Figure 8-1: Determination of characteristic strength σ_0 and Weibull modulus m of a set of 600 tested varistor ceramics. (σ_0 = 284 MPa; m = 5:8). The regression line represents the related Weibull distribution. The distribution fits the data very well and the material is said to show 'Weibull behaviour' (Adapted from Danzer 2014, p. 3437, Copyright (2016), with permission from Elsevier)

For brittle components (e.g. ceramics), the procedure of defining the Weibull modulus as a material constant is well established (e.g. Lawn 1993). Since samples at their final volume often cannot be tested because of costs and testing procedures, Eq. (2) can be applied for scaling up to the size used under realistic operational conditions of the respective material. This automatically leads to a strong decrease in characteristic strength.

Extending this theory to biological samples and role models (e.g. sea urchin spines and coconut shells) is fairly difficult. As biological samples rarely constitute homogeneous or isotropic materials, verification of Weibull's theory is not easy. Weibull himself proposed empirical tests for whether his distribution function could be applied to mechanical properties of other materials than the standard homogeneous, isotropic and brittle solids, as demanded as preconditions for the theory of the weakest link. Therefore, an application of the

Weibull approach to biological samples with their specific material properties seems to be justified. For some biological materials, 'Weibull behaviour' has previously been proposed, e.g. for the determination of failure strength of sea urchin spines (Presser et al. 2009), abalone shells (Menig et al. 2000), pea seeds (Łysiak 2007), teeth (Chan et al. 2009) or bone (Wagermaier et al. 2015). Many other distributions in nature have recently been identified as being Weibull-distributed (Krumbholz et al. 2014).

For the bones of various animals, Taylor (2000) could prove a fatigue strength behaviour according to Eq. (1). However, interestingly, bones from larger animals failed at similar stresses compared with bones of smaller animals. This seems to contradict the scaling effect (Eq. 2) and Taylor assumed that an improvement in the bone structure counteracted it. Detecting, analysing and understanding such structural features influencing the scaling effect would be of great interest for the development of building construction involving scaling problems and would also help us to comprehend the specific failure behaviour of the biological role models used as concept generators for biomimetic materials in greater detail (reverse biomimetics).

8.2 Sea Urchin Spines – Biological Role Model from the Animal Kingdom

A more detailed description of the spines of *Heterocentrotus mammilatus* (HM) and *Phyllacanthus imperialis* (PI) is given in Chap. 7 (*of the book where this chapter was published, annotation of the author*) "Plants and animals as source of inspiration for energy dissipation in load bearing systems and facades" and elsewhere (Grossmann and Nebelsick 2013; Presser et al. 2009). However, the most relevant properties for scaling purposes will be briefly described here: Sea urchin spines

- are lightweight constructions because of their highly porous microstructure.
- have a hierarchical structure (Seto et al. 2012).
- are composed of a highly sophisticated composite material comprising calcite (>99 wt.%) and organic macromolecules (<1 wt.%, e.g. Seto et al. 2012; Su et al. 2000) that overcome the brittleness of calcite and make it a good building material for undertaking the tasks of such a spine (Moureaux et al. 2010; Presser et al. 2009).
- of PI and especially of HM show a 'graceful failure' behaviour (Presser et al. 2009), which is a quasi-ductile partial failure under uniaxial compression without losing the capacity to withstand the load.

- have a remarkable capability to absorb energy (cp. 14-2c, *of the book where this chapter was published, annotation of the author*).

All these characteristics make the sea urchin spine an object of great scientific interest and of even more interest for biomimetics. In order to scale these properties, the exact figures of merit of the sea urchin spines need to be measured.

Presser et al. (2009) determined the Weibull modulus m by uniaxial compression tests for HM and PI. Su et al. (2000) determined m with 4-point bending tests for Heterocentrotus trigonarius (HT), which belongs to the same genus as HM.

PI exhibits the highest Weibull modulus (m 6.0), whereas HM and HT show a significantly lower reliability with m 3.4 and m 3.2, respectively. Presser et al. (2009) attributed the higher reliability of PI to its regular structure (Fig. 2a), compared with the fairly heterogeneous structure of HM. PI is characterised by dense dome-shaped growth layers, which induce crack deflection (Presser et al. 2009). Although the strength in PI is more reliable, considerable variations exist in the spine structure depending on spine size (Fig. 2a). The highly porous medulla has, in all three spines of Fig. 2a, a comparable size (as indicated by the black bar in the boxes I-III, length 1.5 mm), so that the highest proportion of very porous and low-strength material occurs in the smallest spine, presumably resulting in lower strength. In addition to the above-mentioned heterogeneities in the structure leading to a lower reliability, the determination of m itself is challenging with regard to all these biological samples. A good estimate of the critical stress (σ_c, MPa) can only be found with precise geometric information of the spine. The spines of HM and PI are not perfectly cylindrical (Fig. 2c, d), as is assumed for the quantitative assessment of uniaxial compression experiments, and the spines of HT do not have two perfectly parallel surfaces as assumed by Su et al. (2000) for the 4-point bending tests.

Hence, the geometry of the spines and the heterogeneity of their structure challenge the determination of the Weibull modulus with uniaxial compression or 4- point bending tests. A method is thus needed that does not depend on the geometry of the spine and that has a high spatial resolution for an easier determination of the Weibull modulus and for easier scaling.

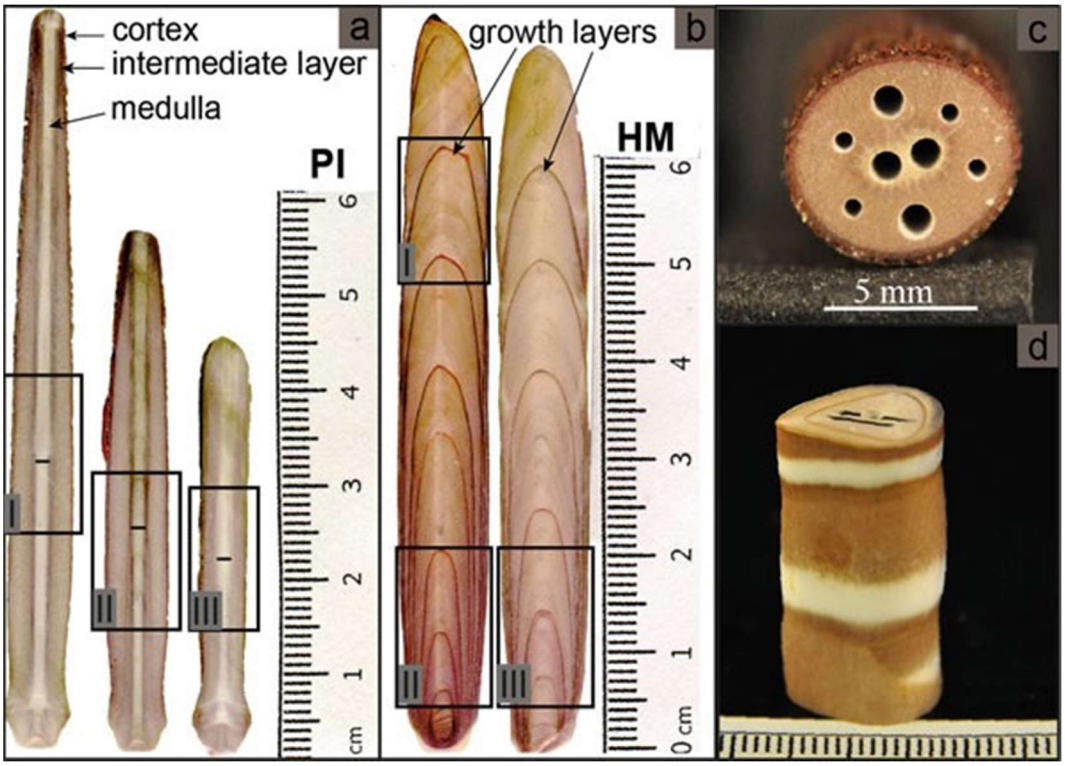

Figure 8-2: Photographs of longitudinal spine sections of (a) PI (*Phyllacanthus imperialis*) and (b) HM (*Heterocentrotus mammilatus*). Black boxes represent sample dimensions for uniaxial compression tests. (c) Detailed view of a spine segment of PI after 8 longitudinal indentation tests (5–10 mm deep). Although the spine is locally damaged, the whole spine is still intact highlighting its capacity to absorb energy. (d) Detailed view of a spine segment of HM typically used in the indentation tests

8.3 Coconut Endocarp – Biological Role Model from the Plant Kingdom

The coconut (*Cocos nucifera*) is a tropical palm that grows in coastal regions and riverbanks and can reach heights of up to 30 m. The ripe fruits, which have the ability to float, remain able to germinate even after several months in seawater and, therefore, the palm is widely distributed in the tropics. The fruits reaching weights of 3.7 kg have to withstand severe impacts of up to 1 kJ when they drop from the crown of the palm onto the ground. To assure the germination of the embryo inside, they have to absorb the impact energy and remain closed to protect the embryo from fungal and bacterial infection. All of these properties are ensured by the triple- layered fruit wall of the drupe consisting of a leathery exocarp, a fibrous mesocarp and a tough endocarp (Chan and Elevitch 2006; Franke et al. 2012; Bauer et al. 2015) (Fig. 3).

The tough endocarp is currently under investigation. Its shape varies from elongated and egg-shaped to almost spherical (Chan and Elevitch 2006). The tricarpelary structure of the ovary is still visible in the mature fruit, as three longitudinal ridges exist representing the fusion marks of the three carpels. Furthermore, three micropyles or 'germinating eyes' are present in the endocarp. These are regions in which the endocarp is thinner and the tissue is much softer, allowing the embryo to 'escape' the endocarp during sprouting (Winton 1901). The endocarp consists predominantly of red to brownish-coloured, isodiametric or strongly elongated stone cells (Fig. 4a), comprising several layers of secondary cell walls (Fig. 4d, e). Dark channels can be observed that serve as a connection between the still young and living cells and can be interpreted as lignified plas- modesmata (Fig. 4e). The elongated cells are mostly oriented with their long axis parallel to the outer surface of the endocarp (Fig. 4b, c). The vascular bundles mainly consist of spiral and pitted tracheids or vessels (Fig. 4f, g). In close vicinity to the vascular bundles, elongated stone cells are found arranged with their longitudinal axis parallel to the bundles, an arrangement that we interpret as ensuring a smooth structural and mechanical transition between the stone cells and vascular bundles in the endocarp (Fig. 4c, f) (Winton 1901).

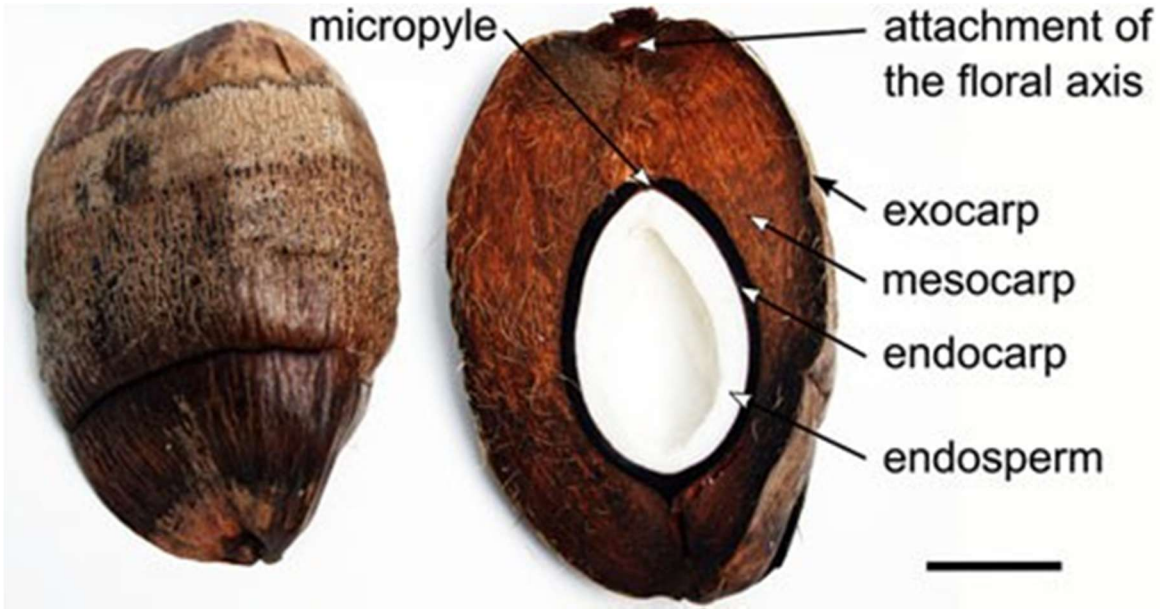

Figure 8-3: Cut open ripe fruit of the coconut palm (*Cocos nucifera*). Left. Exterior view. Right. Interior view: The pericarp consisting of exocarp, mesocarp and endocarp lies over the endosperm, in which the embryo is embedded. The embryo is located under one of the three micropyles at the side at which the fruit is attached to the palm via the floral axis. Not visible is the testa or seed wall surrounding the endosperm. Scale bar: 5 cm

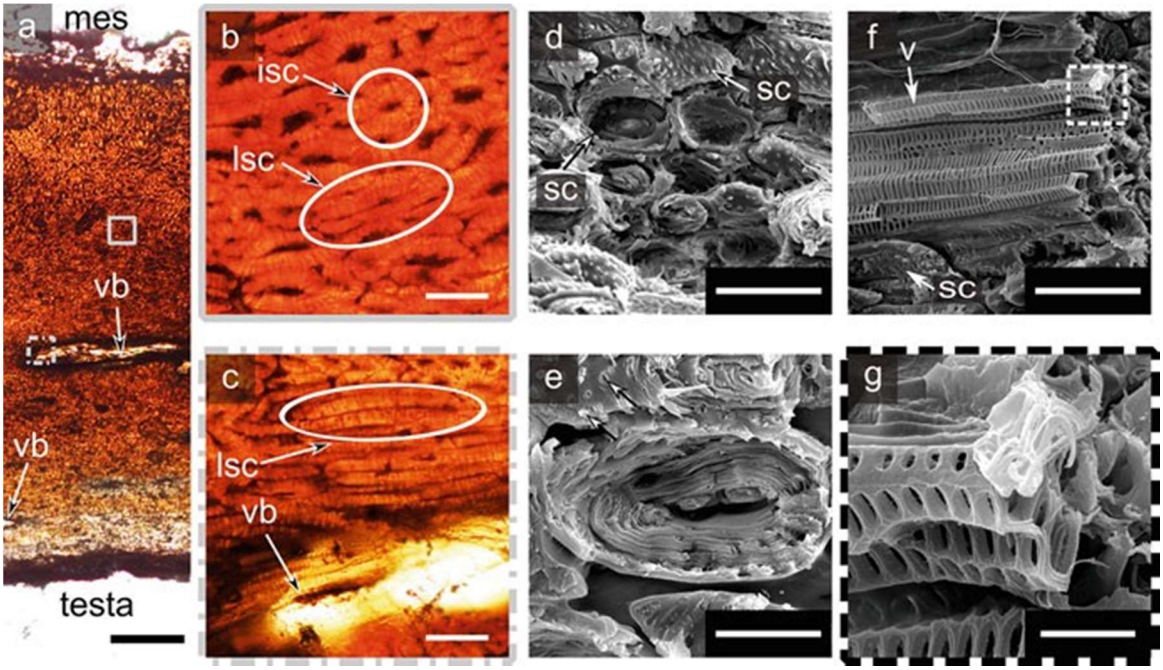

Figure 8-4: (a–c) Light micrographs of a polished cross section and (d–g) SEM micrographs of a fracture surface through the coconut endocarp. (a) The structure mainly consists of densely packed, thick walled stone cells and embedded vascular bundles (vb). The diameter of the stone cells becomes gradually smaller in the direction from the outer side of the endocarp facing the mesocarp (mes) towards the inner side adjacent to the testa. (b) Detailed view of stone cells, which can be either (nearly) isodiametric (isc) or elongated (lsc). (c) Detailed view of a vascular bundle surrounded by longitudinally elongated stone cells. (d) Image of the fracture surface showing individual stone cells (sc). Whereas some cells are still intact, others are fractured, revealing the layered inner structure of the cell walls. (e) Detailed view of a fractured stone cell showing the multi-layered cell wall. The roundish structures (arrows) within the cell walls are plasmodesmata. (f) Pulled out vascular bundle with several rigid tracheids/vessels (v) surrounded by densely packed aligned stone cells (sc). (g) Detailed view of some tracheids/vessels from (c). The rigidity of the scalariform tracheids/vessels is caused by the ladder-like design and lignin deposition in the cell walls. Scale bars: a: 500 µm, b, c, d, f : 50 µm, e: 20 µm, g: 9 µm

The endocarp represents a hierarchically structured material comprising various types of densely packed, typically highly lignified cells in an inhomogeneous agglomeration, resulting in its anisotropic mechanical behaviour. Since botanical materials are rarely purely brittle, we consider the endocarp as a “quasi-brittle” material. This term was introduced by Bažant (2004) for materials such as concrete, bone and biological shells. In the fracture process zone of quasi-brittle materials, microcracks occur that lead to a softening of the material (in brittle materials this zone is negligible). The coconut endocarp was chosen as the botanical role model for quasi-brittle materials.

Once the mechanical tests are well established, comparative studies with coconut dwarf varieties are planned. These varieties have smaller fruits with thinner fruit walls, features that will enable us to test smaller sample sizes of the endocarp and therewith to contribute to the question of the size dependency of fracture behaviour.

8.4 Mechanical Tests

To assure reliable results within this project, two different test setups have been developed. Since the behaviour of materials differs in static and dynamic loading situations, both situations have been taken into account. For the quasi-static loading situation (penetration tests), a constant feed motion has been applied to the samples, whereas in the dynamic situation (impact tests), the sudden impact is caused by an impact pendulum. With the mechanical tests, we aim to identify the Weibull behaviour of the biological materials. Combined with detailed information about the inner structure of the materials, we hope to identify structural parameters (such as cell arrangement or porosity gradients) which have an impact on $\sigma_0 V_0 V_0^{\frac{1}{m}}$.

8.4.1 Penetration Tests on Sea Urchin Spines

The method of choice is known to metallurgists as the ‘impression test’ (Yang and Li 2013). This test is used, for example, to characterise highly porous ductile metallic foams (e.g. Olurin et al. 2000; Kumar et al. 2003). A cylindrical indenter penetrates with a constant velocity several millimetres into the sample. Various geometries of the indenter tip have been reported in the literature, such as a flat-ended cylindrical indenter tip (FEI) or a spherical-ended indenter tip (SEI) (Olurin et al. 2000; Kumar et al. 2003) (Fig. 5a). Based on the first measurements by Presser et al. (2009), this method has been transferred to brittle porous materials and is called the ‘penetration test’ to avoid any possibility of confusion with the ‘impression test’.

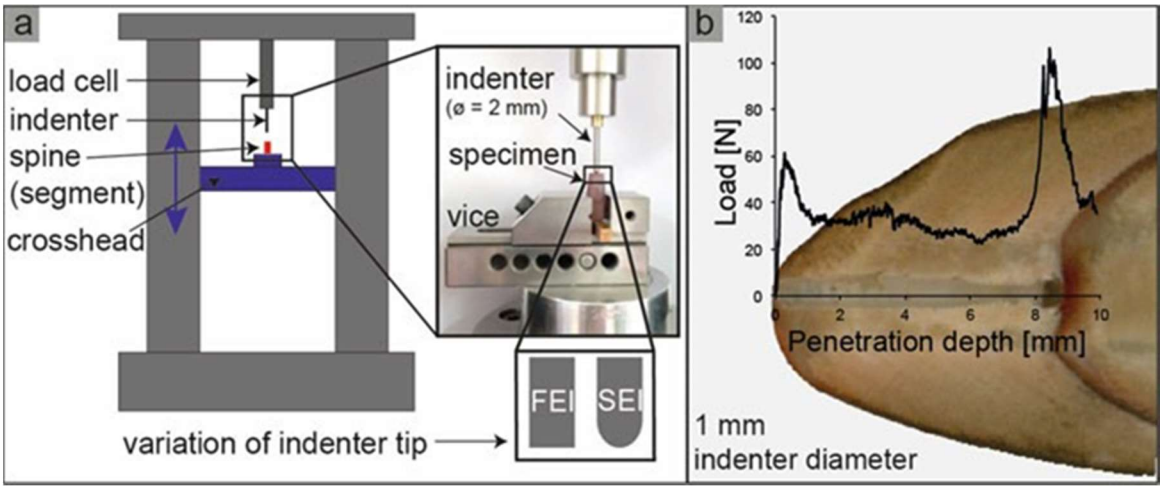

Figure 8-5: (a) Representation of the universal testing machine Instron 4502. The first magnification is a photograph of a fixed spine on the crosshead and the second magnification sketches the shape of a flat-ended and a spherical-ended indenter tip, FEI and SEI, respectively. (b) Correlation of the load penetration curve of HM with its internal structure. The spine was cut longitudinally afterwards. The force is highest when penetrating through the dense growth layers

Hereby, we eliminate some difficulties of the uniaxial compression tests (Chap. 7, *of the book where this chapter was published, annotation of the author*) and provide:

- Simple and low cost sample preparation: a highly precise geometric sample is not required.
- High spatial resolution, which is of special interest for the growth layers of HM and characterisation of the individual intrinsic material properties of the substructures medulla, intermediate layer and cortex.
- The specimens are not destroyed entirely after measurements (Fig. 2c, d), which is advantageous for further investigations.
- Multiple measurements can be made on a single specimen (Fig. 2c).
- Nevertheless, the overall principles of indentation are still similar to uniaxial compression tests (Kumar et al. 2003; Yu et al. 1985; Olurin et al. 2000; Andrews et al. 2001).

For our measurements, cylindrical tungsten carbide indenters (d = 0.6, 1, 2 mm) were used with flat-ended indenter tips and spherical-ended indenter tips (Fig. 5a). Sea urchin spines were cut into segments (Fig. 2c, d) and indented from the top of the spine (crystallographic

c-axis). The indentations were performed with an Instron 4502 universal testing machine (Instron Deutschland GmbH, Pfungstadt, Germany) with a constant cross head speed of 0.5 mm/min. The indentation depth varied from 5 to 20 mm and was mostly chosen to be 10 mm.

8.4.1.1 Spatial Resolution of the Penetration Test

Figure 5b highlights the spatial resolution of this method by showing the load/penetration depth curve of an SEI .ø 1 mm/ in a HM spine section compared with its interior structure (the spine was cut longitudinally afterwards). The force required to penetrate through the outer growth cap into the spine is about 60 N, drops after penetration below 40 N and increases to more than 100 N just shortly before penetrating the next growth cap after 8 mm. This initial load increase might in part be attributable to the accumulation of debris (crushed calcite) in front of the indenter (Presser et al. 2009); this requires further investigation.

In a later stage of this work, the results of the penetration test will be compared with uniaxial compression tests of sea urchin spines. Since markedly different volumes will be used in the two tests, the size effect in sea urchin spines can be evaluated. Of interest will be to determine whether this follows the predictions of Eq. (2) or whether the sea urchin spines manage to overcome the size effect as observed in the bones of animals (Taylor 2000).

8.4.1.2 Influence of Indenter Geometry

Figure 6a shows the influence of the shape of the indenter tip on the measurements. Representative measurements for FEI (d = 0.6 mm, solid grey line) and SEI (d = 0.6 mm, black dotted line) are given. These measurements were conducted in the intermediate layer of the same spine segment of PI (Fig. 2c). For FEI, the load increases sharply right after the touchdown of the indenter on the spine, whereas for SEI, the load increases gradually. This is attributable to the shape of the SEI tip, whereby the cross sectional area increases in the first 0.3 mm of penetration (Fig. 6a on the top left: shape of SEI tip). The load/penetration depth curves of the FEI and SEI intersect after 0.3 mm of penetration, exactly at the point at which the cross sectional areas of these indenters are identical (indicated by the black line in Fig. 6a). Subsequently, similar curves highlight the independence of the indentation response and indenter geometry. These observations agree with Kumar et al. (2003) who have found the same results for the impression of metallic foams. Because calculations with

the FEI are simpler and because the deformation zone is less complicated (Mouginot and Maugis 1985), future measurements will be conducted with an FEI.

The effect of the indenter diameter on penetration stress (strength) is demonstrated in Fig. 6b. Indenter diameters of 0.6, 1 and 2 mm) were used for the intermediate layer (blue colours) and medulla (red colours) of PI. The shaded background colours highlight the range of stresses obtained in the 31 experiments. For clarity, only six stress/penetration depth curves are included in Fig. 6b.

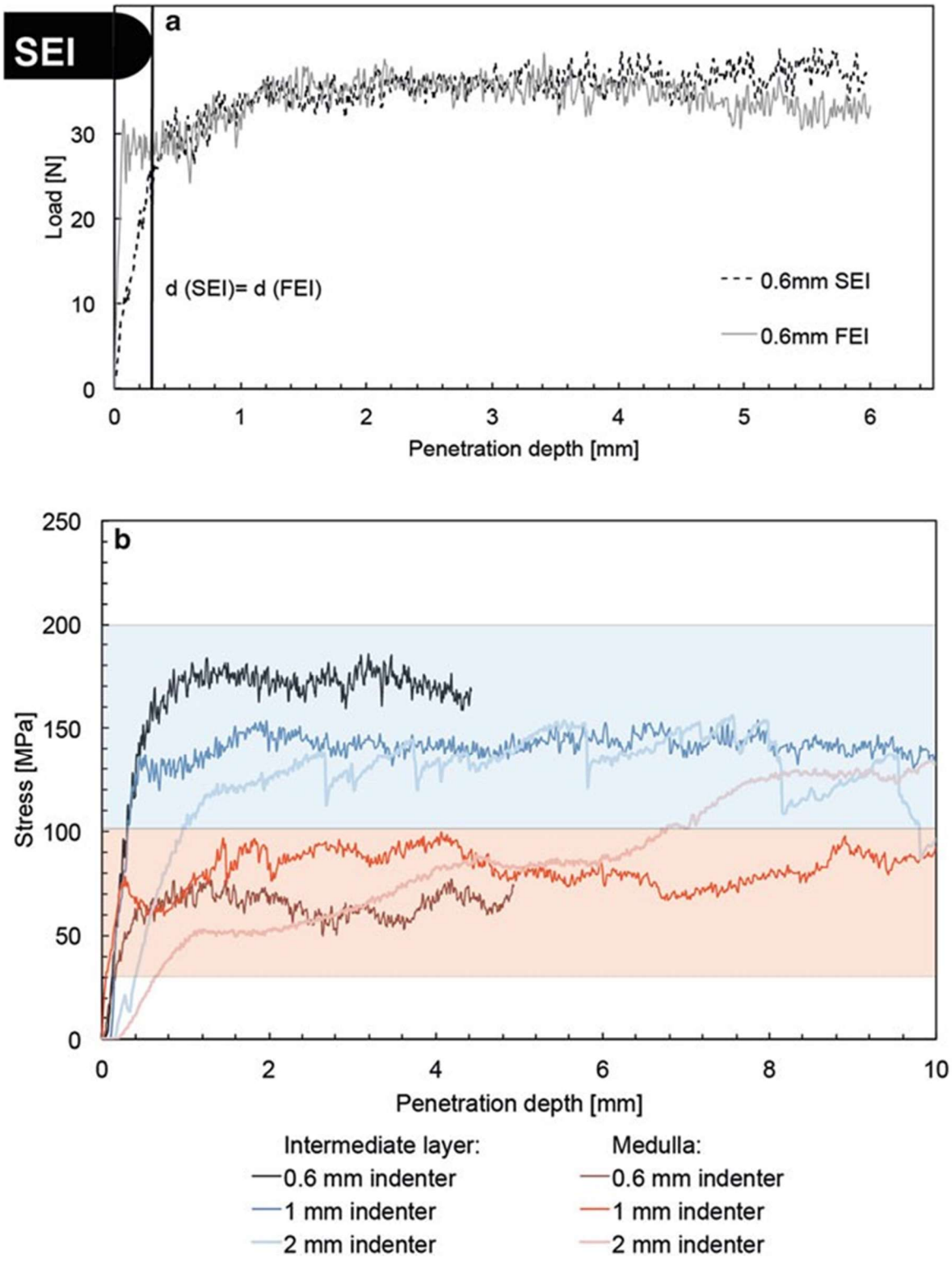

Figure 8-6: (a) Load/penetration depth curve for SEI and FEI of PI. (b) Stress/penetration depth curves for various indenter diameters conducted on 31 PI spine segments; for clarity, only six representative measurements are shown

The strength of the intermediate layer ranges between 100–200 MPa and is generally higher than the strength of the highly porous medulla with 30–100 MPa, concentrating around 40–

80 MPa. The scatter in both structural units of the PI spine is attributable to the heterogeneity of biological materials. Although the statistic is not exhaustive, the 31 measurements suggest that the strength data obtained with various indenter sizes do not vary systematically with indenter sizes.

8.4.2 Impact Pendulum Tests with Coconut Endocarp

In order to determine the mechanical parameters in a dynamic loading situation, a test setup with an instrumented impact pendulum (B5113.303, Zwick GmbH & Co. KG, Ulm, Germany) was developed. The setup is based on the norm for instrumented Charpy impact tests (DIN EN ISO 179-2) of unnotched and straight polymer samples. Our setup differs from that norm because the curvature of the coconut endocarp makes it impossible to obtain the required cuboid and straight sample geometry, as our samples were unnotched but arch-shaped (Fig. 7a). The height of the samples was approximately 10 mm; the curvature and sample width, however, varied depending on the geometric and anatomical parameters of the individual fruits (Fig. 7c). We tested two sample groups differing in their respective orientation within the endocarp: termed equatorial and meridional. The end of the coconut with the micropyles was defined as the north pole, the opposite end as the south pole. The equator was set centrally between the north pole and south pole, with the meridians running through the two poles (Fig. 7b).

The described tests were performed with an instrumented pendulum hammer of 7.5 J work capacity (BRA5113.3145, Zwick GmbH & Co. KG, Ulm, Germany). The span between the abutments was set to 50 mm and was determined to assure that the pendulum hammer did not become immobilised during the test, together with the broken sample fragments between the base of the pendulum. However, for this adapted setup, the exact span of the abutments was of minor interest, as the inner ends of the arch-shaped samples constituted the load-bearing points. The inner sample length is essential for evaluating the comparability of the biological samples, which inevitably differ (slightly) as to their size and shape (Fig. 7c). The samples were centred, so that the force transducer hit the sample in its vertex. This was also the point at which the width and height of the samples was measured (Fig. 7c).

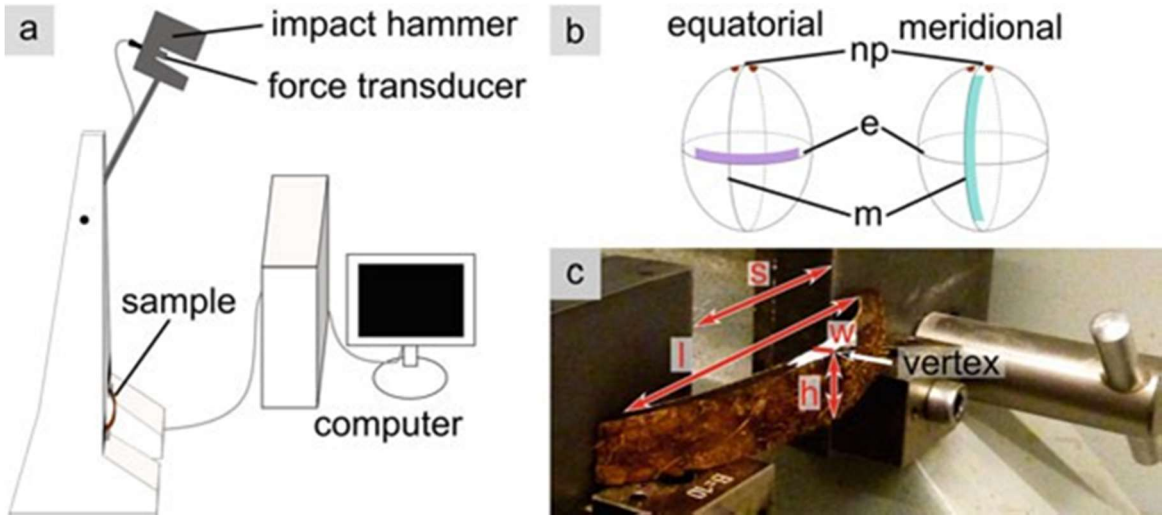

Figure 8-7: Instrumented impact pendulum tests. (a) Sketch of the test setup. (b) Orientation of the test specimen as cut from the coconut endocarp. Abbreviations: np north pole, e equator, m meridian. (c) Detailed view of the mounted sample with geometric sample parameters. The sample geometry is arch-shaped because of the fruit morphology. The impacting hammer hits the sample at the vertex. Abbreviations: s span between abutments, l inner length distance between the inner edges of contact areas of the sample with the abutments, w specimen width at sample centre, h specimen height at sample centre

The tests were performed with 41 equatorial and 58 meridional samples. The equatorial samples had a smaller radius of curvature (median: 43.69 mm) than the meridional samples (median: 63.48 mm), because of the ovoid shape of the endocarp. Moreover, the radius of curvature of the meridional samples had a larger scatter. The radius of curvature showed no significant influence on the impact resistance (rs 0.098). For all other parameters, no significant differences between the equatorial and meridional samples were found (Table 1) and no significant relationship could be observed between the sample dimensions and the impact resistance.

The impact resistance of the equatorial samples (median = 4.46 kJ/m2) was significantly higher than the impact resistance of meridional samples (median = 2.36 kJ/m2) (Fig. 8). This reveals the anisotropy of the biological material, reflected by structural differences within the endocarp, such as the different course of the vascular bundles or the variable cell orientation and cell distribution. A detailed analysis of the structural variations at various hierarchical levels is of special interest not only for a transfer to biomimetic products, but also for characterising quasi-brittle biological materials and is currently being performed.

Table 8.1: Dimensions of the 99 tested coconut endocarp samples

Sample orientation	n	Height [mm]		Radius of curvature [mm]		Width [mm]		Inner length [mm]	
		Median	IQR	Median	IQR	Median	IQR	Median	IQR
Equatorial	41	10.22	0.76	43.69	3.02	3.64	0.60	72.18	17.18
Meridional	58	10.09	0.20	63.48	20.78	3.82	0.48	75.08	14.05

n number of samples, IQR interquartile range

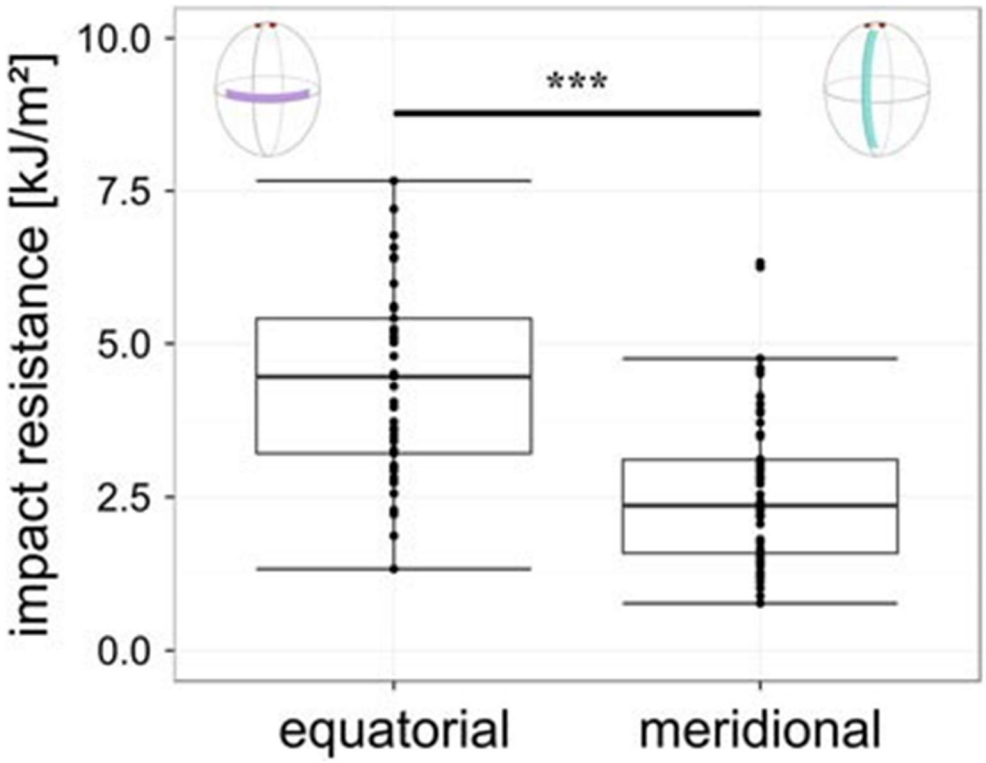

Figure 8-8: Comparison of the impact resistance (absorbed energy per crossectional area) of equatorial (41 specimens) and meridional samples (58 specimens). The equatorial samples had a significantly higher impact resistance (median 4.46 kJ/m2) than the meridional samples (median = 2.36 kJ/m2) (Mann-Whitney-U test; $W = 434$, $p < 0.001$)

8.5 Simulation: Support for Measurement and Scaling Challenges

The description and analysis of the material properties of biological materials is a great challenge. Natural materials show non-uniform directed properties because they often consist of an aggregation of various cell types (such as stone cells and vascular bundles within the coconut endocarp) or have other microstructures, for example, pores of various sizes

(such as in the sea urchin spines), which result in inhomogeneous properties. Finite Element (FE) simulations of the materials and of the experiments might support the measurements and reveal the influence of specimen geometry and microstructure on the results of the experiments.

The failure behaviour during the impact of the coconut endocarp in the revised Charpy impact tests is highly complex, being the result of the inhomogeneous and anisotropic structure of the material and the arch shape of the sample. To generate comparable results and to analyse the influence of the shape of the coconut endocarp (and artefacts connected with it), we have used flat and arch-shaped PVC samples to determine the influence of the geometry of the probe. When the influence is known, a comparison of the properties of the natural arch-shaped samples with samples of other materials tested by Charpy impact tests can be performed. Variations not only of the shape, but also of the material itself can be easily taken into account in the simulation and can help to provide a better understanding of the influence of the geometries.

Simulations can only be as realistic as the input data and boundary conditions. Important input parameters in the case of the PVC samples are the density, elastic modulus and plastic behaviour. All these data can be found in the data sheet provided by the producer, except for the plastic material behaviour. For a first simulation (Fig. 9), literature values of the plastic behaviour of common PVC materials are used, but tensile tests will be performed in the near future to obtain the required information directly from the real tested specimens. The explicit linear elastic/plastic simulation with the FE-software Abaqus includes 5747 elements of type C3D8R, whereas the hammer and the abutment are modelled as 3D analytic rigid shells.

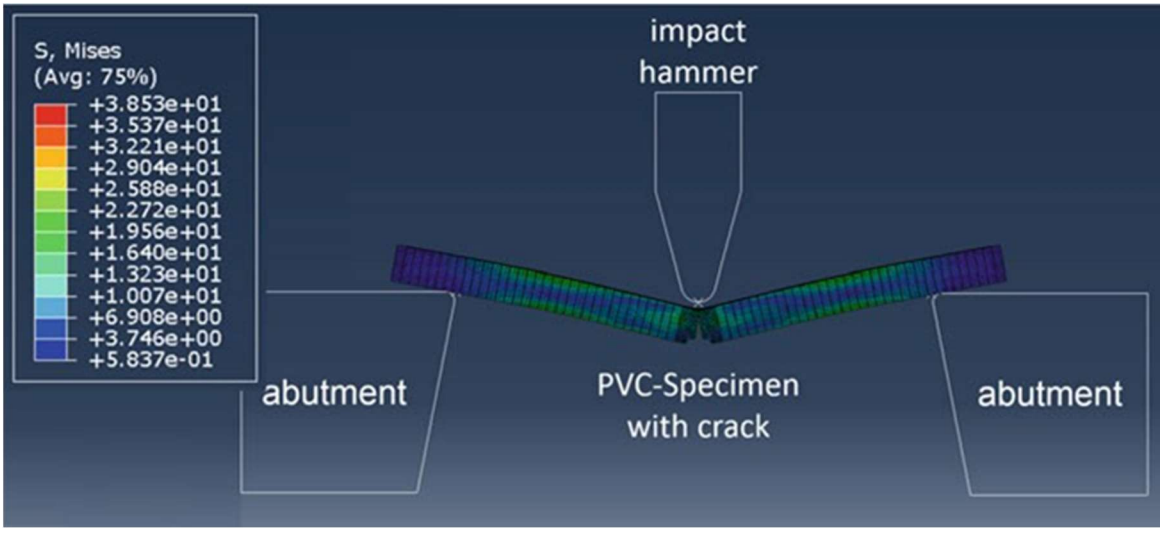

Figure 8-9: Von Mises stress distribution in the simulation of a Charpy impact test of a flat 7 cm long PVC specimen

The simulation includes so-called “cohesive surfaces” to simulate the crack opening behaviour of the sample. Defining these cohesive surface properties is one of the greatest challenges in the modelling of material behaviour. Only with inverse methods will it be possible to find suitable material parameters requiring additional simulations that have to be compared with the experiments. Initial results show good agreement with the experimental data.

The simulation with flat PVC specimen is the first step; the second step is the analysis of arch-shaped PVC samples differing only in their shape from the flat ones in the Charpy impact tests. Thus, reliable information about shape is necessary (the shape dependency is discussed in more detail at the end of this paragraph).

The third step includes the natural material, which shows not only an arch-shaped form, but also inhomogeneous material properties (compare Sect. 3). Therefore, structural information, such as cell forms and dimensions, plus the number and dimensions of embedded vascular bundles need to be included in the simulation. Moreover, the cohesive surface properties will be of special interest here and need to be determined by inverse methods. The results of each experiment will differ in detail, because the tests are performed on a natural material with structural and mechanical variations that are, for example, attributable to differentially distributed vascular bundles. Hence, this step needs to include information about the geometric artefacts found in the first steps of simulation and the relevant structural information in order to estimate the quality of the results obtained with the natural

material. A comparison with artificial materials such as PVC specimens is needed and will help to provide an improved interpretation of the features of the natural material.

As already mentioned the shape needs to be defined exactly. This can be obtained by scanning or exact measuring of the samples or by computer tomography (CT). Revealing the exact shape from the CT-images through a defined process was previously carried out in the group of the IMWF. One example is shown in Fig. 10 in which a sample of a PI sea urchin spine was analysed in a CT and converted into a 3D representation of the surface, which was then meshed and used in FE simulations. In this case, the resolution of the scan was high enough to reveal the macrostructure and the outer surface but not the microstructure such as the porous stereom.

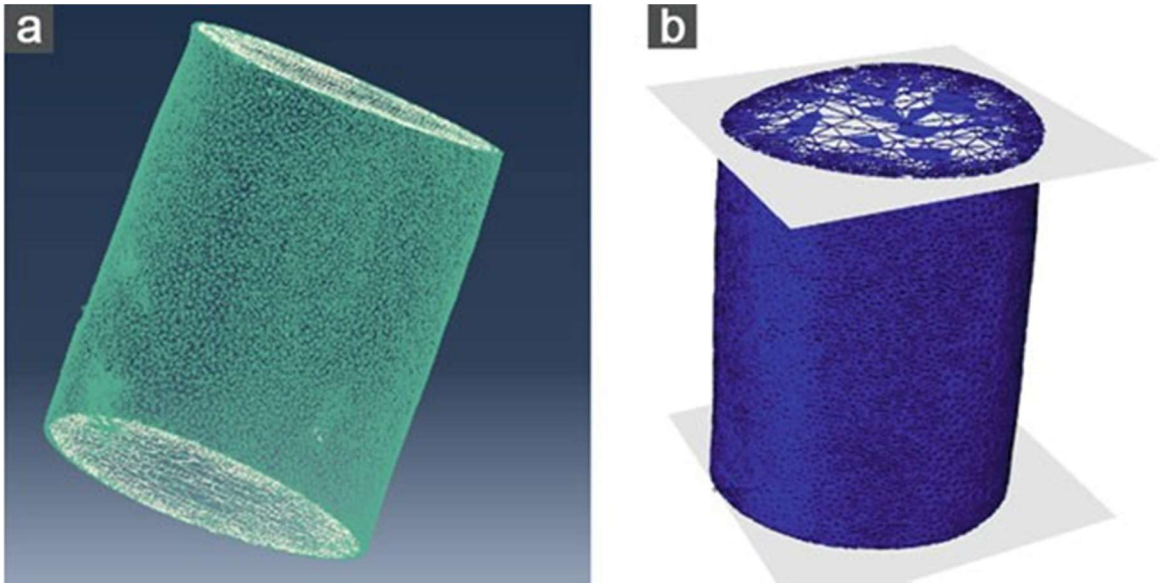

Figure 8-10: Simulations of a PI sea urchin spine test specimen. (a) Mesh reconstructed from a CT scan and (b) screenshot of the FE simulation of the compression test with added pressure plates and filled with a bulk material with isotropic elastic properties as a first approximation

8.6 Discussion

The challenge of scaling up natural constructions to sizes relevant for building construction is complicated for several reasons: natural biological materials show complex mechanical behaviour because of their complex hierarchical internal structure. This often creates a failure mode, which is neither ideally brittle nor ductile making it difficult to predict an upscaling based on classic reliability evaluation treatments such as Weibull algorithms.

In order to evaluate such theories, the main obstacle is the uniqueness of individual natural samples. A first step therefore involves the development of methods suitable for these unique materials in order to build up a reliable data base. In our studies, promising model candidates are spines from large sea urchins, because they have an internal structure that can be characterised by quantitative parameters such as local densities, pore size and shape, while still being made of a single material (calcium carbonate) with little additions. This also makes them attractive for simulation treatment, which should be of great help in the evaluation of properties.

An unusual experimental treatment, namely the penetration of the quasi-brittle highly porous stereom of sea urchins, was chosen to yield quantitative strength and energy dissipation values. We have shown that the treatment represents a local probing method that allows structural evaluation before tests by computer tomography and/or by sectioning the partially destroyed samples after testing and that gives easily understood numbers for materials engineering.

Another, but structurally much more complex candidate is the tough coconut endocarp. Here, we have also tried to adapt a conventional material testing procedure, namely the impact pendulum (Charpy) test, to evaluate dynamic behaviour in terms of energy consumption. Again, we have the chance to investigate the structures both before and after treatment. The non-ideality of samples cut from fruits is still a challenge but, with the aid of computer simulations, we are confident that we can obtain values suitable for use in a scaling up evaluation. If this methodological approach can be evaluated for coconut endocarp, it will be transferred to even more challenging botanical materials such as highly energy dissipating tree barks, which are another role model for bio-inspired construction materials (Chap. 7, *of the book where this chapter was published, annotation of the author*).

8.7 Acknowledgements

This work has been funded by the German Research Foundation (DFG) as part of the Transregional Collaborative Research Centre (SFB/Transregio) 141 ‘Biological Design and Integrative Structures’/project B01 ‘Scaling of Properties of Highly Porous Biological and Biomimetic Constructions’. The Plant Biomechanics Group Freiburg also thanks E. Heizmann and UNIVEG Freiburg, Germany, for providing the coconuts.

8.8 References

[1] Andrews EW, Gioux G, Onck P, Gibson LJ (2001) Size effects in ductile cellular solids. Part II: experimental results. Int J Mech Sci 43(3):701–713

[2] Bauer G, Schmier S, Thielen M, Speck T (2015) Energy dissipation in plants – from puncture resistant seed coats to impact resistant tree barks. In: Yamamoto H, Morita M, Gril J (eds) Proceedings of the 8th plant biomechanics conference, Nagoya, Japan, pp 190–195

[3] Bažant ZP (2000) Size effect. Int J Solids Struct 37(1):69–80

[4] Bažant ZP (2004) Scaling theory for quasibrittle structural failure. Proc Natl Acad Sci U S A 101(37):13400–13407

[5] Chan E, Elevitch CR (2006) Cocos nucifera (coconut). Species Profiles for Pacific Island Agroforestry 2:1–27

[6] Chan YL, Ngan AHW, King NM (2009) Use of focused ion beam milling for investigating the mechanical properties of biological tissues: a study of human primary molars. J Mech Behav Biomed 2(4):375–383

[7] Danzer R (2014) On the relationship between ceramic strength and the requirements for mechani- cal design. J Eur Ceram Soc 34(15):3435–3460

[8] Danzer R, Supancic P, Pascual J, Lube T (2007) Fracture statistics of ceramics–Weibull statistics and deviations from Weibull statistics. Eng Fract Mech 74(18):2919–2932

[9] Franke E, Lieberei R, Reisdorff C (2012) Nutzpflanzen. Georg Thieme Verlag, Stuttgart

[10] Griffith AA (1921) The phenomena of rupture and flow in solids. Phil Trans R Soc A 221:163–198 Grossmann JN, Nebelsick JH (2013) Comparative morphological and structural analysis of selected cidaroid and camarodont sea urchin spines. Zoomorphology 132(3):301–315

[11] Krumbholz M, Hieronymus CF, Burchardt S, Troll VR, Tanner DC, Friese N (2014) Weibull-distributed dyke thickness reflects probabilistic character of host-rock strength. Nat Commun 5:3272

[12] Kumar PS, Ramachandra S, Ramamurty U (2003) Effect of displacement-rate on the indentation behavior of an aluminum foam. Mater Sci Eng A 347(1):330–337

[13] Lawn B (1993) Fracture of brittle solids. Cambridge University Press, Cambridge Łysiak G (2007) Fracture toughness of pea: Weibull analysis. J Food Eng 83(3):436–443

[14] Menig R, Meyers MH, Meyers MA, Vecchio KS (2000) Quasi-static and dynamic mechanical response of Haliotis rufescens (abalone) shells. Acta Mater 48(9):2383–2398

[15] Mouginot R, Maugis D (1985) Fracture indentation beneath flat and spherical punches. J Mater Sci 20(12):4354–4376

[16] Moureaux C, Pérez-Huerta A, Compère P, Zhu W, Leloup T, Cusack M, Dubois P (2010) Structure, composition and mechanical relations to function in sea urchin spine. J Struct Biol 170(1):41– 49

[17] Olurin OB, Fleck NA, Ashby MF (2000) Indentation resistance of an aluminium foam. Scr Mater 43(11):983–989

[18] Presser V, Schultheiß S, Berthold C, Nickel KG (2009) Sea urchin spines as a model-system for permeable, lightweight ceramics with graceful failure behavior. Part I. Mechanical behavior of sea urchin spines under compression. J Bionic Eng 6(3):203–213

[19] Seto J, Ma Y, Davis SA, Meldrum F, Gourrier A, Kim YY, Schilde U, Sztucki M, Burghammer M, Maltsev S, Jäger C, Cölfen H (2012) Structure-property relationships of a biological mesocrystal in the adult sea urchin spine. Proc Natl Acad Sci U S A 109(10):3699–3704

[20] Su X, Kamat S, Heuer AH (2000) The structure of sea urchin spines, large biogenic single crystals of calcite. J Mater Sci 35(22):5545–5551

[21] Taylor D (2000) Scaling effects in the fatigue strength of bones from different animals. J Theor Biol 206(2):299–306

[22] Wagermaier W, Klaushofer K, Fratzl P (2015) Fragility of bone material controlled by internal interfaces. Calcif Tissue Int 97(3):201–212

[23] Weibull W (1939) A statistical theory of the strength of materials. Generalstabens litografiska anstalts förlag, Stockholm

[24] Weibull W (1951) A statistical distribution function of wide applicability. J Appl Mech 18:293–297 Winton AL (1901) Anatomy of the fruit of Cocos nucifera. Am J Sci 70:265–280

[25] Yang F, Li JC (2013) Impression test—a review. Mat Sci Eng R 74(8):233–253

[26] Yu HY, Imam MA, Rath BB (1985) Study of the deformation behaviour of homogeneous materials by impression tests. J Mater Sci 20(2):636–642

9 Kokosnuss: Simulation Kerbschlagbiegeversuch

Die Simulation des Kerbschlagbiegeversuches wird in der Veröffentlichung oben nur kurz angerissen. Um eine ganzheitliche Darstellung zu ermöglichen, folgen nun die unveröffentlichten Details zu der Simulation der PVC-Proben.

Der Anteil meiner Arbeit beträgt 100%.

Wie in der Einleitung beim Abschnitt 1.3.4 Kokosnuss erwähnt, hat auch die Form der Schale einen Einfluss auf die Materialeigenschaften. Um die Zähigkeitseigenschaften gekrümmter Proben, die aus den Kokosnussschalen gesägt werden können, auf die Eigenschaften von geraden Proben schließen zu können, werden Simulationen des Kerbschlagbiegeversuches verwendet. Dort werden Modelle der PVC-Proben mit geraden und gekrümmten Formen hergestellt und im simulierten Kerbschlagbiegeversuch analysiert. Diese Ergebnisse haben die Partner der Plant Biomechanics Group Freiburg bekommen, um die Schädigungsparameter mit ihren gewonnenen Daten (Experimente mit Kokosnussschalen) vergleichen zu können. Um die für die FEM-Simulationen notwendigen Inputparameter für die FEM-Simulationen zu bekommen, werden Zugproben des PVC-Materials durchgeführt.

Zur Bestimmung mechanischer Eigenschaften des biologischen Vorbildes, der Kokosnuss, werden Kerbschlagbiegeversuche durchgeführt. Der Kerbschlagbiegeversuch dient z. B. bei Metallen und Kunststoffen zur Ermittlung der Zähigkeitseigenschaften, unter anderem zur Bestimmung der Kerbschlagzähigkeit der untersuchten Materialien [44]. Die Kerbschlagzähigkeit wird aus der Schlagarbeit im Verhältnis zum Probenkörperquerschnitt berechnet. Die Schlagzähigkeit beschreibt die Eigenschaft eines Materials, eine (Schlag-) Energie abzufangen ohne zu brechen. Sie ist abhängig von der Probenform und der Temperatur. Bei dem hier betrachteten Versuch liegt die Probe an zwei Enden auf.

Für die Kerbschlagbiegeversuche der Kokosnussschale werden Proben aus der harten Schale in horizontaler und vertikaler Richtung geschnitten. Da diese dann eine Krümmung aufweisen (die Schale der Kokosnuss ist gekrümmt) wird zuerst der Einfluss der Krümmung auf den Kerbschlagbiegeversuche in einem Vorversuch bestimmt, welcher im Folgenden beschrieben wird.

In diesem Vorversuch sollen die Spannungs-Dehnungskurven für zwei verschiedene Kunststoffe bestimmt werden. Einerseits werden Kunststoffproben aus PVC-U (Trovidur© EC, Röchling Engineering Plastics SE & Co. KG, Haren Deutschland), aus flachen Platten

nach Din Norm (Vgl. Abbildung 9-3) geschnitten. Die Abkürzung der Proben lautet „flach“ und diese sind in Abbildung 9-1 in der Zugprüfmaschine eingespannt gezeigt. Andererseits werden Kunststoffproben aus Abwasserrohren (orange, PVC-U) längs aus den Rohren geschnitten, um eine gewölbte Form zu erhalten (Vgl. Abbildung 9-2). Die Abkürzung dieser Proben lautet „quergewölbt“. Gemessen wird an einer Zugprüfmaschine des Typs Z005 von Zwick/Roell (Zwick GmbH & Co. KG, D-89079 Ulm) mit einer Maximalkraft von 10 kN.

Abbildung 9-1: Flache Proben in der Zugprüfmaschine

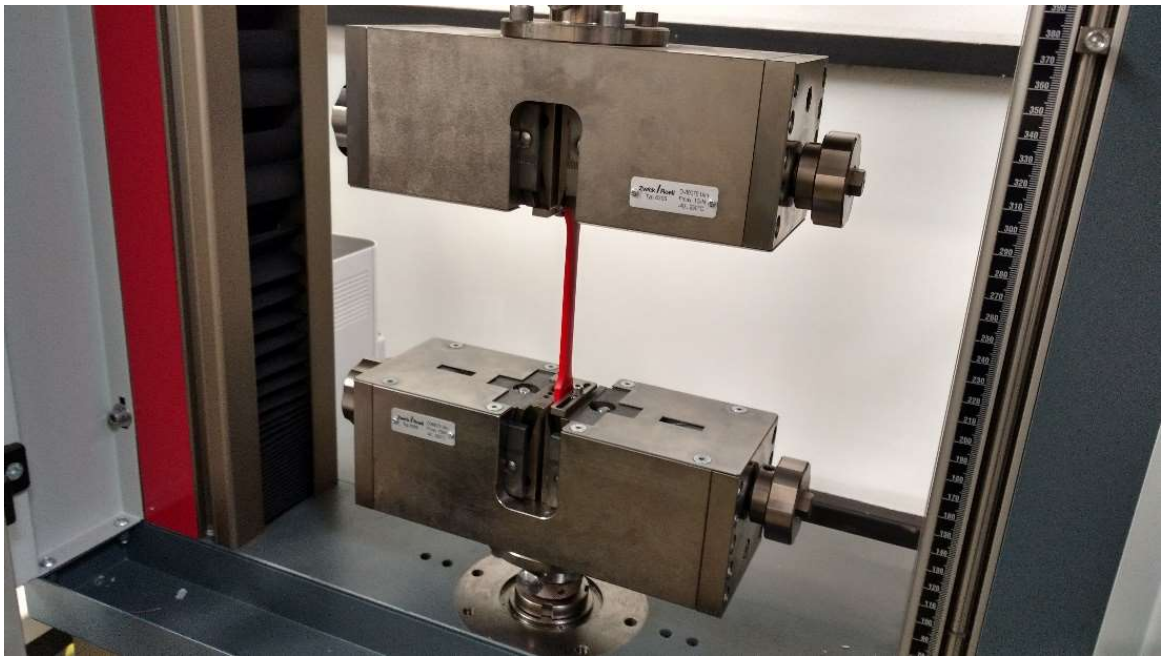

Abbildung 9-2: Quergewölbte Proben in der Zugprüfmaschine

Zur Auswertung wird die Software Testexpert II 3.0 (Zwick GmbH & Co. KG, D-89079 Ulm) benutzt. Die Einspannlänge beträgt 125 mm und der Versuch wird mit einer Geschwindigkeit von 20 mm/min durchgeführt.

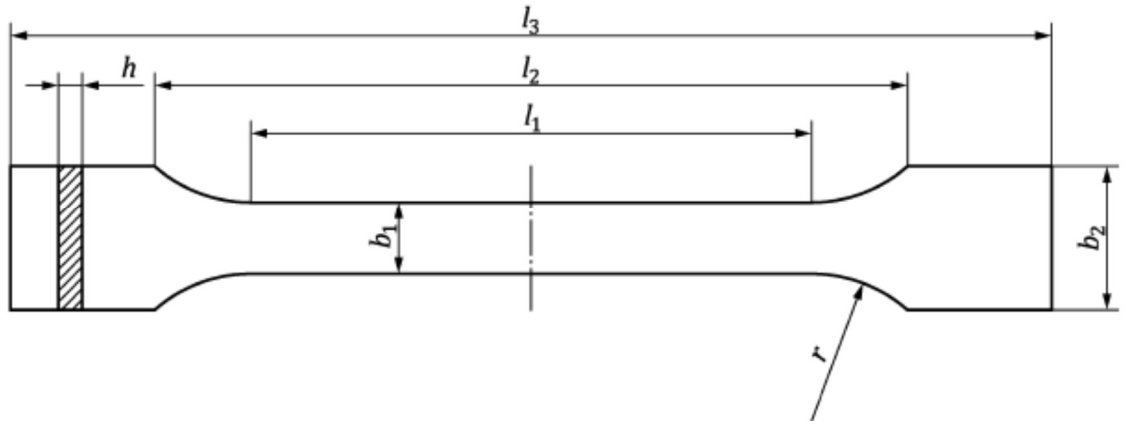

Abbildung 9-3: Normprüfkörper [45], mit folgenden Abmessungen: l2 = 10,9 cm; l1 = 8,3 cm; l3 = 17,9 cm; b1 = 1 cm; b2 = 2 cm; Dicke d = 0,4 cm

Zum Vergleich sind in Tabelle 9.2 einige Literatur-Materialdaten zur Kokosnuss angegeben:

Tabelle 9.2: Literatur-Materialdaten zur Kokosnuss

Kokosnuss (*Coco Nucifera* aus Kammeroon) Quelle: [46]	**Härte**	**Creep Ratio**	**E-Modul**
polare Zone Material aus dem oberen bzw. unteren Bereich der Kokosnuss	1,16*10² MPa	16	3,52*10³ MPa
equitoriale Zone Material aus dem mittleren Bereich der Kokosnuss	0,7*10² MPa	8	1,45*10³ MPa

Auswertung:

Die Kraft-Verlängerungskurven aus dem Zugversuch werden folgendermaßen für die Darstellung im Diagramm aufbereitet (nach [44, p. E25], [45]):

Zuerst wurden die Textdateien mit Origin (9.0.0G, OriginLab Corporation, Northampton, MA, USA) importiert, da dort ein mehrfacher Import von Dateien problemlos möglich ist. Von dort aus wurden die Daten per Copy&Paste in Excel zur weiteren Verarbeitung kopiert.

Die Dehnung wird in absolute Werte umgerechnet (bezogen auf die Einspannlänge von L_0 = 125 mm). Die technische Spannung wird dann aus der Standartkraft bezogen auf den Ausgangsquerschnitt S_0 = 40 mm² (d*b1) bestimmt:

$$\sigma = \frac{F}{S_0} \qquad [1]$$

mit F = gemessen Kraft in N und S_0 Anfangsquerschnitt in mm².

Die technische Dehnung ist definiert durch:

$$\varepsilon = \frac{\Delta L}{L} 100 \qquad [2]$$

mit $\Delta L = L - L_0$ Verlängerung in mm,

L_0 = Anfangsmesslänge in mm (125 mm),

L = momentane Länge in mm.

In Abbildung 9-4 ist der Vergleich von fünf Versuchen mit unterschiedlichen Geschwindigkeiten gezeigt.

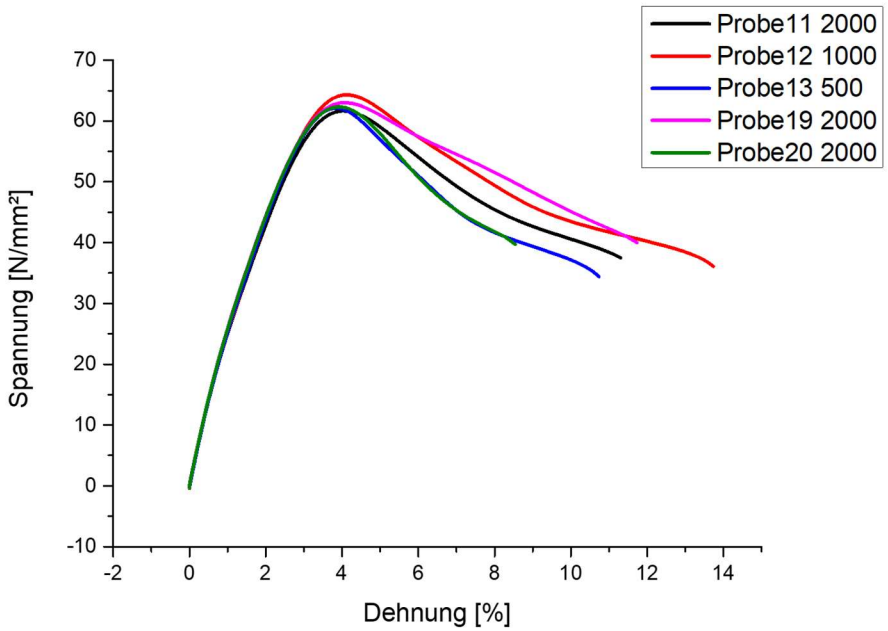

Abbildung 9-4: Vergleich Spannungs-Dehnungskurven der flachen Proben bei unterschiedlich schnellen Geschwindigkeiten 500, 1000 und 2000 mm/min

Diese Spannungs-Dehnungskurven werden bei gleich bleibender Geschwindigkeit gemittelt. Die Zugfestigkeit R_m ist definiert durch das Kraftmaximum bezogen auf den (Ausgangs-)Querschnitt:

$$R_m = \frac{F_{max}}{S_0} \quad [3]$$

Die Streckgrenze wird in dem Fall durch Finden des Maximums in der Spannungs-Dehnungskurve ermittelt. Das ist der Moment, bei dem das Fließen des Materials beginnt bzw. an dem der erste deutliche Kraftabfall auftritt (bis hierhin entsteht nur eine elastische Verformung). Da die Streckgrenze bei PVC nicht deutlich hervortritt, wird die 0,2 %-Dehngrenze als Ersatz ermittelt (siehe Formel 9):

$$R_{p0,2} = \frac{F_{p0,2}}{S_0} \quad [4]$$

Der Wert von $R_{p0,2}$ wird durch einen Schnitt der Kurve mit einer Parallelen zur Hookeschen Geraden bei der Dehnung ε = 0,002 (0,2%) ermittelt. Der Schnittpunkt dieser Parallele mit der Spannungs-Dehnungskurve ist dann die Ersatzstreckgrenze. Der E-Modul (Hookesche Gerade) kann mithilfe des Sekantenmoduls bei 0,05% und 0,25% der Dehnung berechnetet werden:

$$E_t = \frac{\sigma_2 - \sigma_1}{\varepsilon_2 - \varepsilon_1} \quad [5]$$

mit E_t = Zugmodul, in Megapascal (MPa),

σ_1 = die Spannung (in MPa), die bei einem Dehnungswert von ε_1 = 0,0005 (0,05 %) gemessen wird,

σ_2 = die Spannung (in MPa), die bei einem Dehnungswert von ε_2 = 0,0025 (0,25 %) gemessen wird.

Eine Regressionsgerade durch die Punkte bei 0,05 % und 0,25 % wird als Hookesche Gerade angenommen. Der Bereich ab der Ersatzdehngrenze ($R_{p0,2}$) entspricht dann dem plastischen Teil der (technischen) Spannungs-Dehnungskurve. Der so bestimmte plastische Anteil der Dehnung wird zur Berechnung der wahren Spannung und Dehnung und des sogenannten plastic strain, welcher in Abaqus genutzt wird, zur Simulation des plastischen Anteils des Materials, verwendet.

Die wahre Dehnung wird nach folgender Formel berechnet:

$$\varepsilon_{wahr} = \ln(1 + \varepsilon_{techn}) \quad [6]$$

Die wahre Spannung nach wird nach dieser Formel berechnet:

$$\sigma_{wahr} = \sigma_{techn}\,(1 + \varepsilon_{techn}) \qquad [7]$$

Damit können dann die plastischen Materialeigenschaften in Abaqus abgebildet werden.

Die Ergebnisse sind in Tabelle 9.3 aufgelistet:

Tabelle 9.3: Auswertung

Probe/Geschwindigkeit	**Zugfestigkeit R_m [MPa]**	**Ersatzstreck-grenze $R_{p0,2}$ [MPa]**	**E-Modul nach Sekantenmodul [MPa]**
Flache Probe 20 mm/min	52,6	28,6	2928
Flache Probe 2000 mm/min	62,3	31,8	2773
Flache Probe Gemittelt über beide Ge-schwindigkeiten	57,5	30,2	2851
Quergekrümmte Probe 20 mm/min	62,3	31,7	2773
Quergekrümmte Probe 2000 mm/min	66,8	21,8	3011

9.1 Auswertung Kerbschlagbiegeversuch

Die Freiburger Partner führen Kerbschlagbiegeversuche zur Bestimmung der Zähigkeits-eigenschaften von Kokosnussschalen und PVC-Proben durch. Die Probe (ein Ausschnitt der Schale) wird auf die Lager gelegt und dann mit dem Hammer mit einer bestimmten Kraft durchgeschlagen. Zur Bestimmung des Einflusses der Krümmung im Vergleich zu einer geraden Probe werden zwei unterschiedliche Probentypen genutzt, flache und gekrümmte Proben (jeweils gekerbt und nicht gekerbt). Der Vergleich der flachen, gekerbten Proben ist in Abbildung 9.5 zu sehen. Der Einfluss auf die Kraft/Weg Kurve durch die Blöcke, die eine Seitwärtsbewegung der Proben verhindern, ist gering.

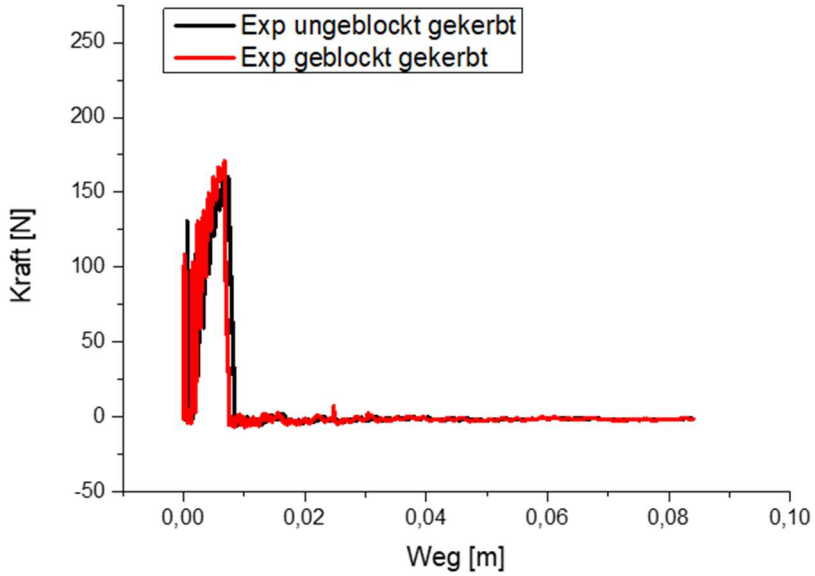

Abbildung 9-5: Vergleich Kraft/Wegkurven der flachen, gekerbten Proben aus PVC mit und ohne Blockierung der Seitwärtsbewegung der Probe

Der Vergleich der flachen, ungekerbten Proben ist in Abbildung 9-6 zu sehen. Der Einfluss durch Blöcke, die eine Seitwärtsbewegung der Proben verhindert ist auch hier gering aber deutlich sichtbarer als bei den gekerbten Proben.

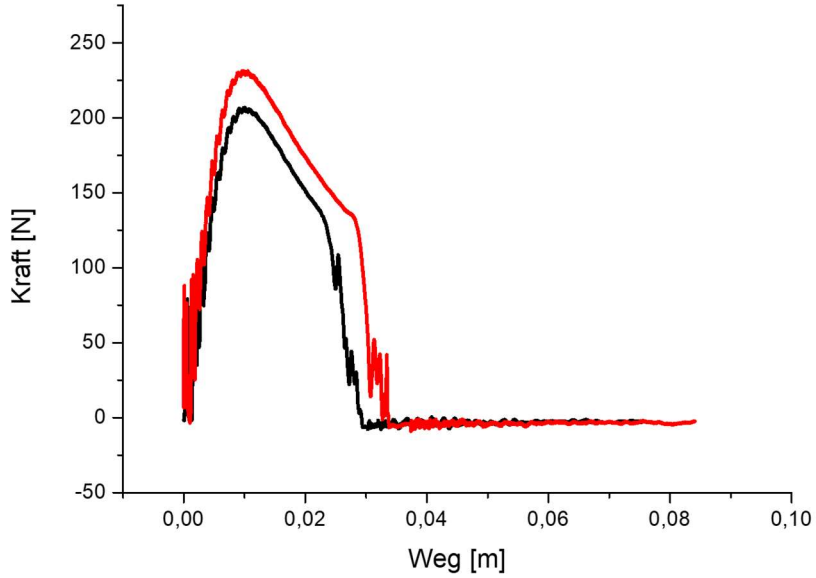

Abbildung 9-6: Vergleich Kraft/Wegkurven der flachen, ungekerbten Proben aus PVC mit (schwarze Linie) und ohne Blockierung (rote Linie)

In Tabelle 9.4 sind die Anzahl der Versuche, das Material und die gemittelten Energien und Zähigkeiten dargestellt.

Tabelle 9.4: Energien und Zähigkeiten

Material	**Anzahl Versuche**	**Energie gemittelt [J]**	**Zähigkeit gemittelt [J/cm²]**
Exp. PVC Flach, gekerbt	5	0,75	2,3055
Exp. PVC Flach, ungekerbt	5	4,02	12,38
Exp. PVC Flach, gekerbt + geblockt	5	0,607	1,866
Exp. PVC Flach, ungekerbt + geblockt	5	4,76	14,65

In Tabelle 9.5 sind wichtige Versuchsdaten aufgelistet:

Tabelle 9.5: Versuchsdaten

Arbeitsvermögen W des Pendels:	Abstand Widerlager	Gewicht Hammer	Geschwindigkeit des Hammers kurz vor dem Aufprall
7,5 J	56,13 mm (frei) 54,56 mm (geblockt)	0,001012 Tonnen	3850 mm/s

9.2 Kerbschlagbiegeversuch-Simulationen

Zur Bestimmung der Materialeigenschaften wie z. B. der Kerbschlagzähigkeit oder der Energieaufnahme werden unter anderem Kerbschlagbiegeversuche durchgeführt. Da die Kokosnussschale gekrümmt ist, sind auch die aus dieser geschnittenen Proben gekrümmt. Um den Einfluss der Krümmung zu bestimmen wurden im Vorversuch flache und gekrümmte PVC-Proben getestet.

Ziel ist die numerische Bestimmung der Kerbschlagbiegearbeit dieser PVC-Materialien.

Die in Kapitel 9 durchgeführten Zugversuche schaffen die Grundlage für die benötigten Materialparameter, die nicht in der Literatur oder in den Herstellerangaben zu finden sind. Darauf aufbauend werden vier Kerbschlagbiegeversuche numerisch abgebildet, um den Einfluss von gekerbten und nicht gekerbten Proben auf die zu erwartende Kraft-Verschiebungs-Kurve der Kerbschlagbiegearbeit untersuchen zu können.

In Tabelle 9.6 sind alle wichtigen Parameter zur Simulation zusammengestellt.

Tabelle 9.6: Materialparameter der flachen PVC-Probe

Materialeigenschaften PVC-Probe flach (Berechnet aus Zugversuchsergebnissen mit Geschwindigkeit von 2000 mm/min [20 mm/min])				
Dichte [47]	E-Modul (Berechnet nach Zugversuch)	E-Modul nach Herstellerangabe [47]	Poisson-Zahl [47]	
$1{,}4 \times 10^{-9}$ Tonne/mm³	27773 [2928] MPa	2700 MPa	0,4	
Interaction Properties:				
Cohesive Behavior (Beschreibt das Bindungsverhalten)	2773 [2928]			
	Damage			
	Initiation	Criterion Maximum nominal stress	Normalrichtung: 62 [52] (Bestimmt aus Zugversuch Zugfestigkeit R_m)	Shear 1 and Shear 2: 7000 (Kein Einfluss in Shear-Richtungen, nur Normalrichtung hat Einfluss)
	Evolution	Type Displacment:	Damage Variable	Total Displacment (Invers bestimmt)
			0	0
			1	0,087
	Stabilization	1000		
Friction	0,5 (zwischen Hammer und Probe) [48]			

Mit einem Wert von 1000 bei *Stabilization* ist eine Verringerung der Ausschläge im Diagramm zu bemerken (nach dem der Hammer die Probe durchgeschlagen hat). Bei Werten von 10 oder deutlich über 1000 sind die Ausschläge deutlich verstärkt. Dieser Wert wurde in Versuchen angenähert und simuliert eine Art viskose Dämpfung, um das System zu stabilisieren.

Das Modell zur numerischen Abbildung des Kerbschlagbiegeversuchs wurde komplett in Abaqus 6.14 aufgebaut (Abbildung 3). Die Widerlager sowie der Hammerkopf (Gewicht = 1,012 kg, Anfangsgeschwindigkeit = 3,85 m/s) wurden als Starrkörper modelliert, da diese im Versuch eine vernachlässigbare Deformation aufweisen. Die Kerbschlagprobe besteht

aus 5724 (ungekerbt, flach) bzw. 5746 (gekerbt, flach) C3D8R-Elementen, wobei die Versagenszone direkt oberhalb der Kerbe (im Fall mit Kerbe, bzw. in der Mitte der Probe ohne Kerbe) mit oberflächenbasierten Kohäsivelementen versehen wurde. Als Kontaktbedingung wurde ein tangentialer Reibungskoeffizient von 0,5 für die allgemeine Reibung zwischen Stahl und PVC für den Kontakt Hammer-Probe sowie Probe-Widerlager gewählt, da Hammer und Widerlager aus Stahl sind. Die Steifigkeit der Kohäsivelemente wurde wie bei dem E-Modul des jeweiligen PVCs definiert, die aus der Spannungs-Dehnungskurve nach dem Sekantenmodul berechnet wurden. Die Schädigung tritt in der flachen PVC Probe bei einer Normalspannung von 62 MPa auf (im Zugversuch mit Materialeigenschaften bestimmt bei 2000 mm/min).

In Abbildung 9-7 ist der Vergleich zwischen Experiment und der Simulation einer gekerbten, nicht geblockten Probe gezeigt.

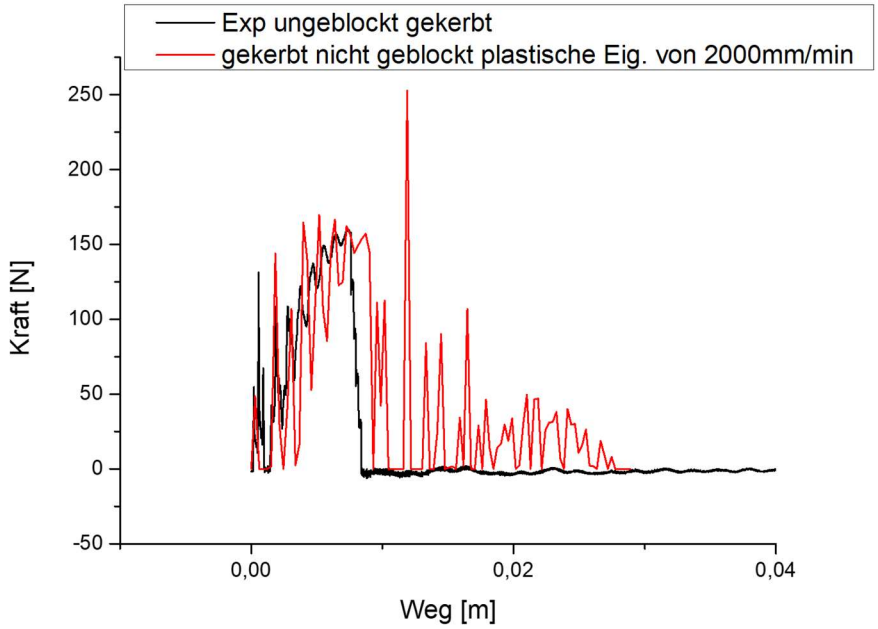

Abbildung 9-7: Vergleich Kraft/Wegkurve der flachen, gekerbten PVC-Proben einmal simulatorisch und einmal experimentell

Die Energie und die Zähigkeit der flachen, gekerbten PVC-Proben sind in Tabelle 9.7 aufgelistet:

Tabelle 9.7: Zähigkeit und Energie flacher, gekerbter PVC-Proben

	Simulation	Experiment geblockt	Experiment nicht geblockt
Energie [J]:	1,34	0,61	0,75
Zähigkeit [J/cm²]:	4,12	1,87	2,31

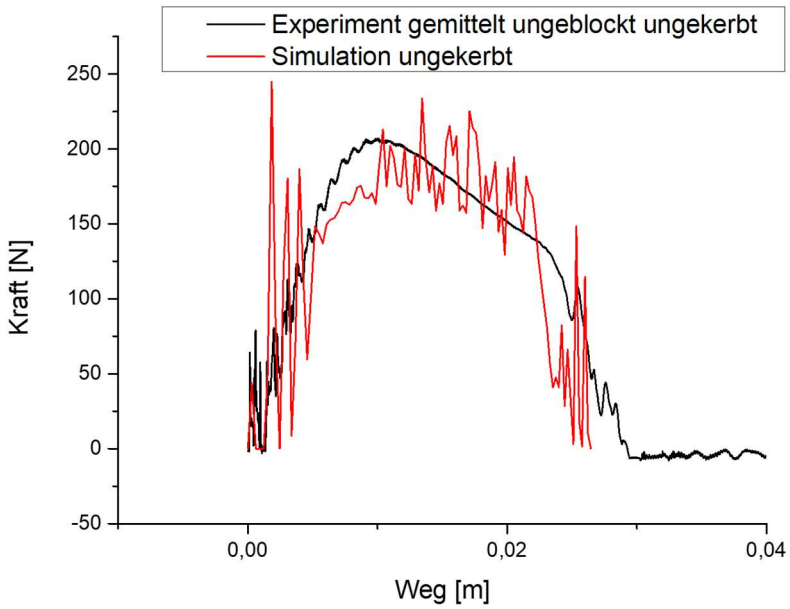

Abbildung 9-8: Vergleich Kraft-Wegkurve der flachen, ungekerbten Proben einmal simulatorisch und einmal experimentell

In Tabelle 9.8 sind die Energien und die Zähigkeiten der flachen, ungekerbten PVC-Proben aufgelistet:

Tabelle 9.8: Zähigkeit und Energie flacher, ungekerbter Proben

	Simulation	Experiment geblockt	Experiment nicht geblockt
Energie [J]:	3,68	4,76	4,02
Zähigkeit [J/cm²]:	11,32	14,65	12,38

Die Diskrepanzen zwischen Simulation und Experiment in Tabelle 9.7 und Tabelle 9.8 und Abbildung 9-7 und Abbildung 9-8 sind auf Nachschwingungen zurückzuführen. Trotzdem

sind die Ergebnisse der Simulation sehr gut mit den Ergebnissen der Experimente vergleichbar. Der Kurvenverlauf der experimentellen Daten wird mit der Simulation gut wiedergegeben.

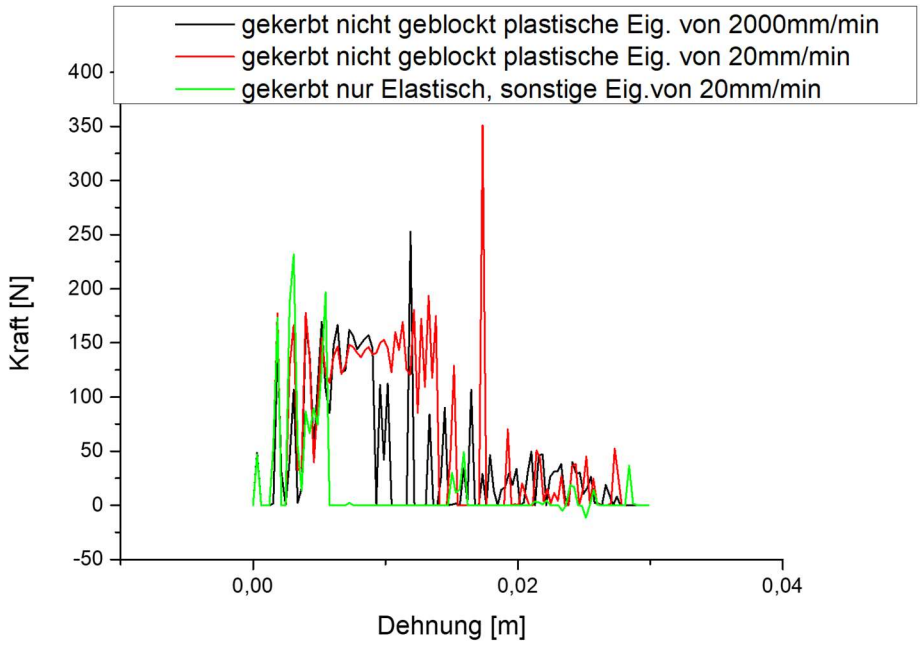

Abbildung 9-9: Vergleich Kraft-Wegkurve der flachen, gekerbten PVC-Proben mit unterschiedlichen Materialeigenschaften (simulatorisch)

Die Unterschiede zwischen den verschiedenen elastischen Materialeigenschaften der flachen, gekerbten PVC-Proben ist in Abbildung 9-9 sehr gut zu erkennen. Der Einfluss der unterschiedlichen Materialeigenschaften ist deutlich zu sehen.

In Abbildung 9-10 ist ein Vergleich zwischen einer quergewölbten Probe mit einer flachen Probe dargestellt. Die Kurvenverläufe unterscheiden sich deutlich voneinander, die Form der Probe hat also einen deutlichen Einfluss auf die Ergebnisse der Kerbschlagbiegeversuche. Die Ergebnisse der Zugversuche (Spannungs-Dehnungskurven) werden zur Bestimmung der plastischen Anteile für die Materialdefinition in Abaqus genutzt. Damit sind alle notwendigen Daten für die Simulation der Kerbschlagbiegeversuche vorhanden.

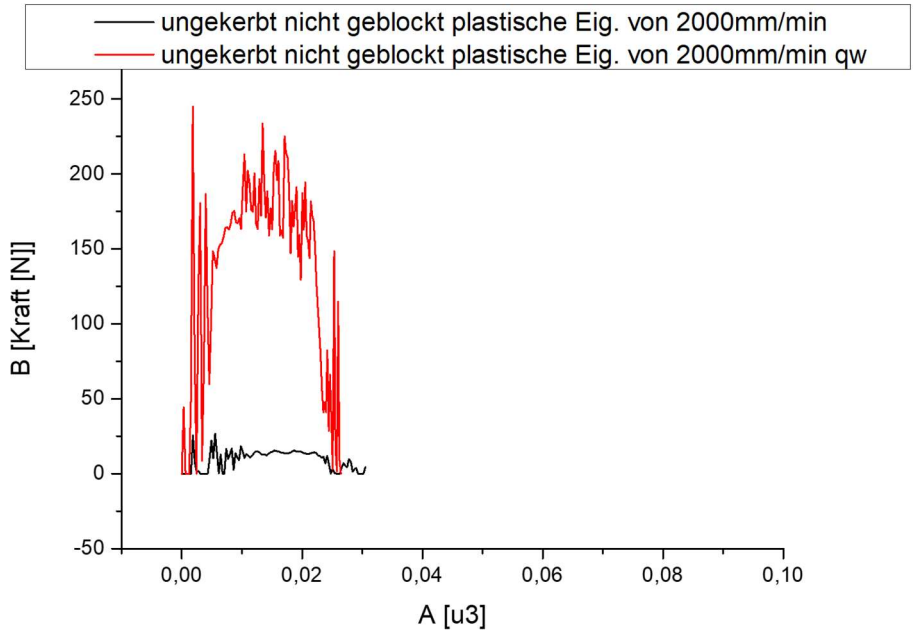

Abbildung 9-10: Kraft-Wegkurven der quergewölbten Probe mit Materialeigenschaften der krummen Zugproben verglichen mit der geraden Probe (mit Materialeigenschaften aus Zugversuchen der flachen Zugproben (simulatorisch)

Diese Daten werden genutzt, um die Simulationsergebnisse der Kerbschlagbiegeversuche zu überprüfen. In Kapitel 9.2 werden für die gekrümmte und nicht gekrümmten Proben mit und ohne Kerben und mit und ohne Blockierung der Probe Simulationen des Kerbschlagbiegeversuchs durchgeführt. Der Vergleich in Abbildung 9-7 und Abbildung 9-8 zeigt eine gute Übereinstimmung der simulatorisch entwickelten Daten mit den experimentell bestimmten. Die Diskrepanzen, die vorhanden sind (Vgl Tabelle 9.7 und Tabelle 9.8), sind auf Nachschwingungen zurückzuführen. Dies wurde auch in anderen Kerbschlagbiegeversuchen festgestellt [49].

10 Seeigelstachel

Wie in Kapitel 8 beschrieben, sind im Transregio 141 auch Seeigelstachel als Vorbilder zur Analyse gekommen.

Die Ergebnisse zum Seeigelstachel sind im folgenden Aufsatz aufgeführt:

IX Schäfer, I., Bräutigam, D., Schmid, P., & Schmauder, S. (2017). Evolution is the better architect : Simulation of cellular solids in sea urchin spines, Conference SMILE 2016, organized by IFP Energies nouvelles (IFPEN), at Rueil-Malmaison, http://www.rs-smile2016.com, *Nicht veröffentlicht / Konferenzbeitrag*

Dieser Aufsatz entstand im Rahmen einer Präsentation für die Konferenz SMILE 2016 (IFPEN, Rueil-Malmaison, from 6 to 8 April 2016) und wurde noch nicht veröffentlicht.

Der Anteil der eigenen Arbeit in der Veröffentlichung umfasst:

- Erstellung des Manuskripts (Der Anteil meiner Arbeit beträgt 100 %)
- FEM-Simulation der Makrostruktur und der Mikrostruktur (direct approach) (Der Anteil meiner Arbeit beträgt 100 %)
- Entwicklung und Übertragung der Methode der Voxelmodelle auf die CT-Bilder (Der Anteil meiner Arbeit beträgt 100 %)
- Anleitung der Studienarbeiten von. D. Bräutigam und P. Schmid mit V. Guski (Der Anteil meiner Arbeit beträgt 50 %)
- Auswahl, und Diskussion der vorgestellten Voxelmodellbeispiele (Der Anteil meiner Arbeit beträgt 100 %)
- Abstrahierte Modelle (parametric modelling) (Der Anteil meiner Arbeit beträgt 100%)

Evolution is the better architect: Simulation of cellular solids in sea urchin spines

I. Schäfer, D. Bräutigam, P. Schmid, S. Schmauder

Conference SMILE 2016, (IFPEN, Rueil-Malmaison, from 6 to 8 April 2016)

all authors form the Institute for Materials Testing, Materials Science and Strength of Materials (IMWF), University of Stuttgart, Stuttgart, Germany

Abstract

The microstructure found inside certain sea urchin spines is analyzed and transferred into Finite-Element-Simulations. Different methods are used to generate the models, directly from computer tomographic images or from scratch as parametric models. The different approaches have their own challenges and the outcomes are usable for different situations. The aim is to extract the principle that is the reason for the high energy dissipation capability and transfer it to architectural applications.

10.1 Introduction

In this work, the microstructures found inside the spine of sea urchins living in the Pacific Ocean are analysed and translated into Finite-Element (FE)-simulations, with the aim to transfer the working principle into architectural applications in the future. The characteristics of sea urchin spines from the species *Heterocentrotus mammilatus* (HM) is described through their lightweight construction (they show a highly porous microstructure), their hierarchical structure and especially of HM's 'graceful failure' behavior (V. Presser, Schultheiß, et al. 2009), a quasi-ductile partial failure under uniaxial compression.

Analysis, creation and simulation of microstructures are an important and ongoing topic in the material science community. One example is the paper of Qin and his coworkers (Qin et al. 2017), they developed the strongest material known until now with a perfectly matching combination of material and microstructure. One of the most important steps in developing a microstructure inspired by biological materials is the analysis of the microstructure of the role model. This is the reason why in the present work about the microstructure of sea urchin spines, the structure is in focus and not the material. Another important aspect is that the simulation will provide insights in structure / material relationships that are beyond the limits of being investigated with classical experiments. E.g. the influence of the different pore sizes or the mesostructure like the caps are not easy to distinguish from the

bulk material / structure properties. The study starts with an analysis of sea urchin spines in a computer tomographic (CT) scanner. These images are the basis for three types of model creation techniques. Because the data from the CT-Scans are enormous, a concept to handle the data efficiently is required. The properties of porous and cellular materials are defined through the very low density and the porous microstructure morphology. Hence the struts which define the pores are having the main influence on the properties of the whole foam. As described in the work of Daxner (Daxner 2010) the standard procedures to analyse foam microstructures is the following:

First, he describes multi-cell models of a finite sample. This are models "which represent a real foam sample in the most accurate manner possible with the available hart- and software. The aim of this approach is to predict the behavior of an actual foam sample under realistic loading conditions, which, in most cases, correspond to uni-axial compression" (Daxner 2010, 51). Our approach here is based on high resolution CT-images to produce and analyse highly detailed models of selected pores of the foam. This is called a direct modeling approach. With that, an understanding of the influences of the parts of the structure like the struts and the size of the pores can be generated. This is the most direct approach to create a model, but this is also the most computational expensive one. However analysis is limited, as only small parts of the structure can be simulated with this method because of the enormous computational costs involved. To overcome these limitations the so called voxel-based models are used here. This approach is also based on CT-images, but reduces the amount of data which needs to be processed significantly.

Secondly, Daxner describes the use of unit cell models, which are periodically repeating structures. With such models, a study over the variations of geometrical parameters can be made. In our method we intended to use the parametrized approach which is comparable with the second method of Daxner et al., where highly idealized structures are considered and analysed. An alternative for this approach would be the use of beam elements as a representation for the struts and also boolean operation based models, but these are not part of this paper and will be discussed shortly at the end of this paper.

Back to the sea urchins: why are their spines so interesting? The spines of *Heterocentrotus mammilatus* show a stereom structure with growth layers, radiating layers and medulla (compare Figure 6, where one growth layer and the microstructure (the stereom) of selected areas is shown). Interestingly, they also show porosity gradients throughout the whole structure. The materials is a biological calcite that is a composite of amorphous calcium

carbonate (ACC), structurally bonded water and water and some organic macromolecules. In a pressure test, a probe of the sea urchin spine behaves more like a ductile material (V. Presser, Schultheiß, et al. 2009; Schmier et al. 2016). The cause of this behavior is maybe found in the microstructure of the sea urchin spine and this work shows different ways to access the microstructure numerically.

10.2 Direct approach

The first modelling approach presented here is a direct approach, directly extracted from the CT images. Basis for that are relative coarse CT-images (scanner: SKYSCAN1072, Institut für Kunststofftechnik (IKT), university of Stuttgart) from a part of the sea urchin spine *Heterocentrotus mammilatus* (HM). The focus was on the outer dimensions and shape, but also on the mesostructure; the caps inside the sea urchin spine. The result is shown in Figure 1, which also shows an untouched CT-Image of the sea urchin spine. One circle in the middle of the spine marks the cap, the white circle represents surface layer. The resolution of the CT-scanner is limited, the microstructure of the stereom is not visible. The 3D-Model of the sea urchin spine is defined by the shape (in blue) or the outer layer, the stereom (in green) inside, which represents the microstructure and the mesostructure, the caps, in red.

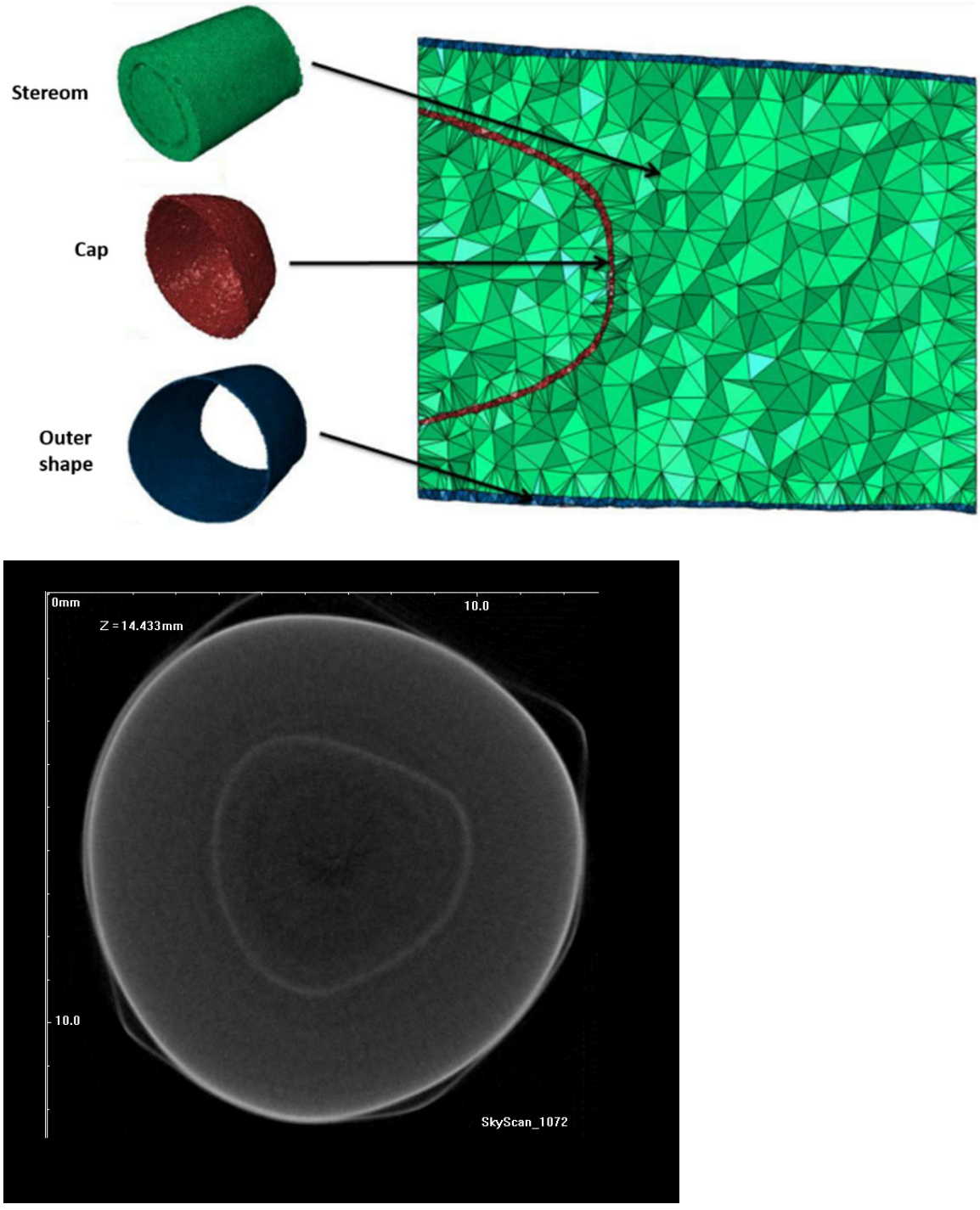

Figure 10-1: First: Three different parts of the model: The stereom (green), the caps (red) and the outer shape. bottom: CT-Image example (untouched)

The procedure to get these parts transferred into the FE- model is as follows:

First the pictures are stacked to create a 3D representation and this stack is then analysed manually and prepared using a picture editing software. The CT-images are cut so that only

the interesting structure is visible and unwanted information like text are removed (compare Figure 1 right) and denoising and other filters are used to optimize the results. The next step involves a segmentation of the pictures based on different grey values. In Figure 2 one result of the grey value analysis is shown on the left with a top view example and right next to it the whole stack. The CT-images show a varying grey value in direction of the z-axis (from bottom to the top of the stack). To overcome this, the stack is split into 7 sub stacks and the grey values were adapted to a local threshold for the 7 sub stacks so that the caps, the stereom and outer shape could be separated correctly. The last step is to combine the three different stacks again with a Matlab (Version R2015b (2015), The Mathworks, Natick, Massachusetts, USA) script that converts the three image stacks into three matrices (through splitting the images into voxels) and combines the three matrices afterwards. To mesh the segmented image stack, the software (or better toolbox) iso2mesh (Fang and Boas 2009) is used. This script crates a 3D-volume mesh which can be used in a FEM-Analysis software (Figure 3).

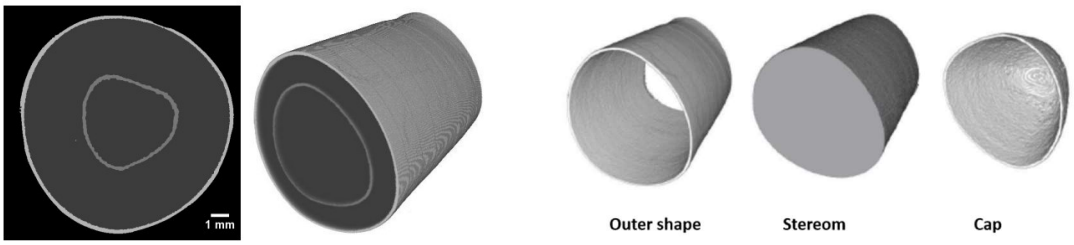

Figure 10-2: Left: Voxelmodels (2 different views, from the top and a side view) as a result of the segmentation procedure. Right: Result of the segmenting procedure based on the three thresholds for the different regions, cap in the middle, the outer shape and the inner part of the sea urchin spine

The direct model with the mesostructure is investigated in an FE-analysis. The example in Figure 3 shows the used boundary conditions of the pressure test and the von-Mises stress distribution on the right. The model is fixed within two rigids (blue), where the one above the model is moving downwards while the lower part is fixed in z-direction to simulate a pressure test. The pure elastic simulation is performed with the (pressure) Young`s modulus (or elastic(E)-modulus) of 8.28 GPa (calculated from experiments done by Presser et al. (V. Presser, Schultheiß, et al. 2009; Volker Presser et al. 2010) and a Poission`s ratio of 0.31 for calcite (KORTH n.d.). The shape of the sample and the shape of the mesostructure

is directly comparable with the cylindrical shape of the original sample. The different regions of the sea urchin spine show different densities and with that the elastic moduli of these regions should show different values.

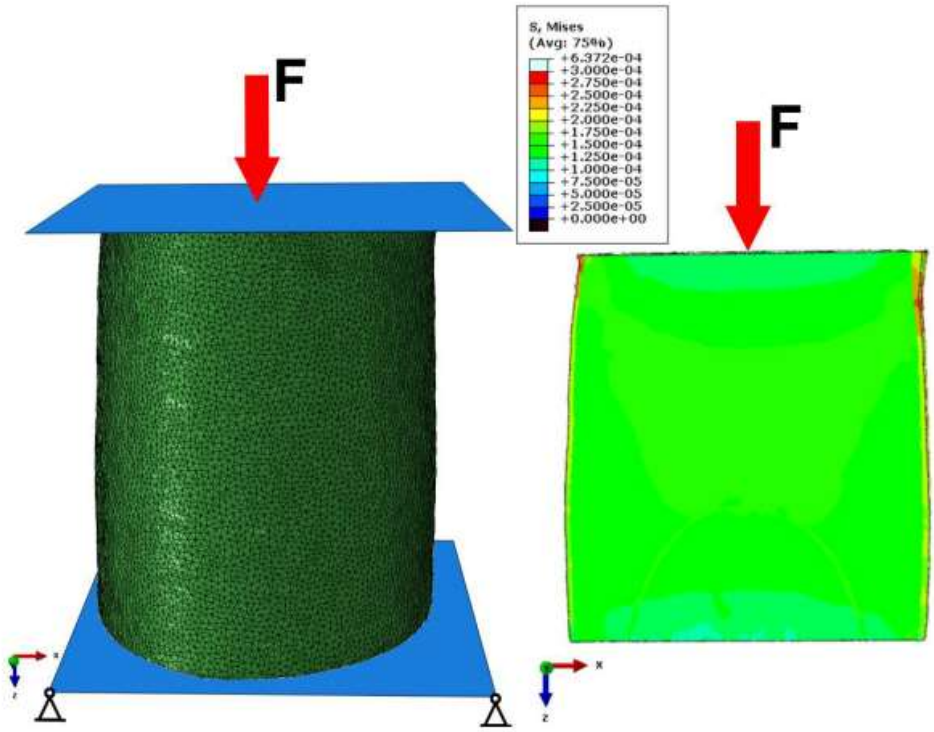

Figure 10-3: Boundary conditions (left) and von-Mises stress distribution as a result of the FEM-simulation

To analyse possible E-moduli for the different regions a parameter study was done (compare Table 1). The aim is to get a combined (calculated) E-modulus of 8.28 GPA for the whole model. The E-modulus for the outer layer is varied in that study from 12 to 20 GPa, the value for the stereom is chosen as 6 GPa and 8 GPa. The results are presented in Figure 4, only variation N7 with values of 14 GPa for the outer layer and 6 GPa for the stereom are showing a significant difference, all other variations are in the region of the experimental curve.

Table 10.1: Values for the E-Modulus in the parameter study

Variation	Outer (Surface) Layer E-Modulus	Cap E-Modulus	Stereom E-Modulus	Resulting E-Modulus	target
Exp.	8.28	8.28	8.28	8.60	100%
N1	12	10	8	8.59	99.9%
N2	12	12	8	8.61	100.1%
N4	12	8	8	8.57	99.7%
N5	20	8	8	9.09	105.7%
N6	8	20	8	8.42	97.9%
N7	14	10	6	6.79	79.0%

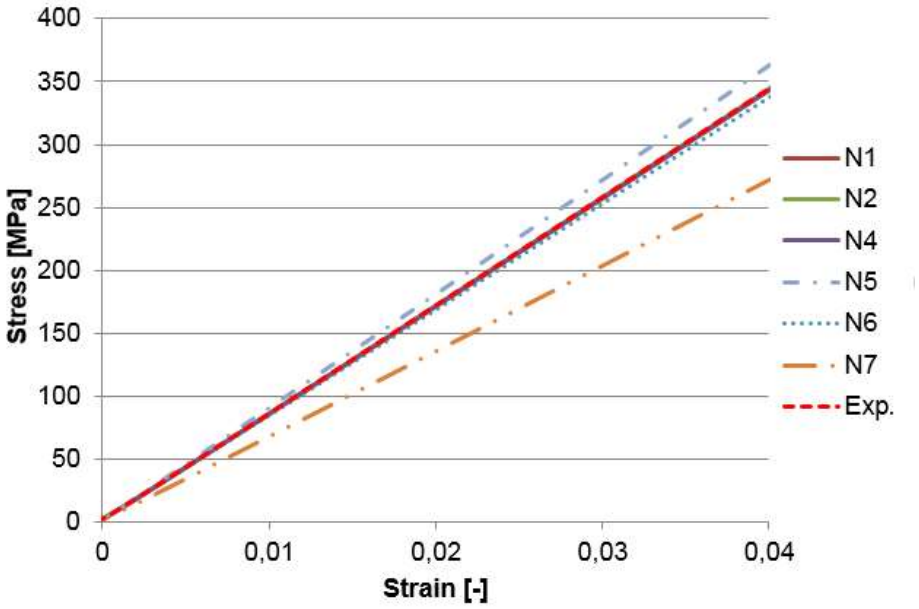

Figure 10-4: Parameter study to reveal the part-E-Modulus of the three regions

As a result the values of 8 GPa for the stereom and a E-modulus between 10 and 12 GPa for the outer layer showed the best agreement with the experimental value in this parameter study. The values for the caps did not have a big influence (see Figure 5): Compared to the stereom and the outer layer the volume of the caps is too small (less than 1% of the whole spine).

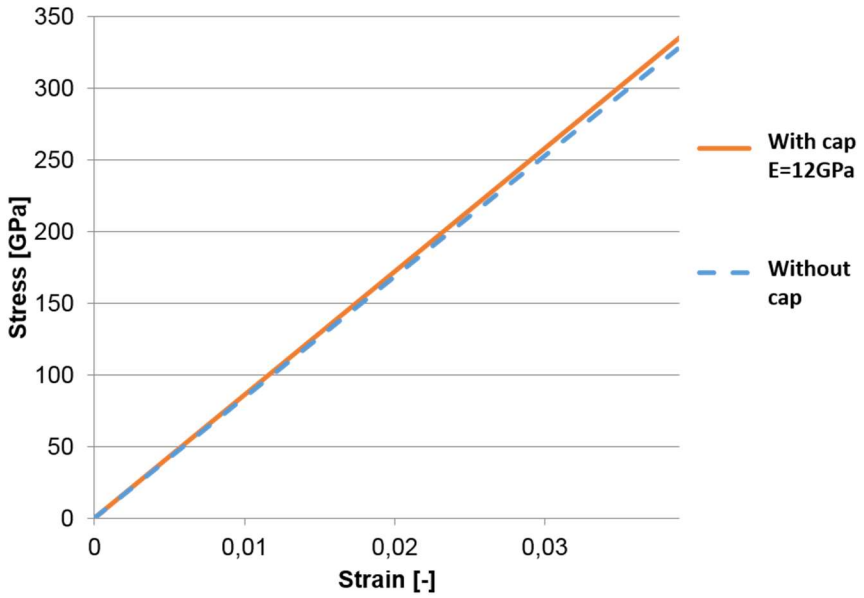

Figure 10-5: Influence of the changed material properties on the stress/strain diagram (only elastic material properties)

10.3 Voxelmodel approach

With a different approach, (voxel-)models with greater attention to detail were analysed. The basis are different CT-images, from a high resolution CT of a sea urchin spine of the same sea urchin spine species Heterocentrotus Mamilatus as above. This enables the creation of models with included microstructure. A voxel model can be calculated more efficiently and thus a much bigger volume can be analysed than with the detailed models shown later. The voxels are cubic elements that have the same size and are used to describe the structure. The use of voxelmodels is on one side efficient, but also some of the information are lost (curvy structures are split into small steps). Here the differences in the microstructure with relation to the density on the elastic properties can be revealed. First, high resolution CT-images are imported into a picture edition software and cut to the right size. The optimal side-length of the analysed cube is around 502.99 mm with the used hardware. Figure 6Figure 3 shows three regions as examples. In that case the part number 7 is obtained from the side part of the spine, 8 is from middle part, the medulla and 9 is from the outer shell.

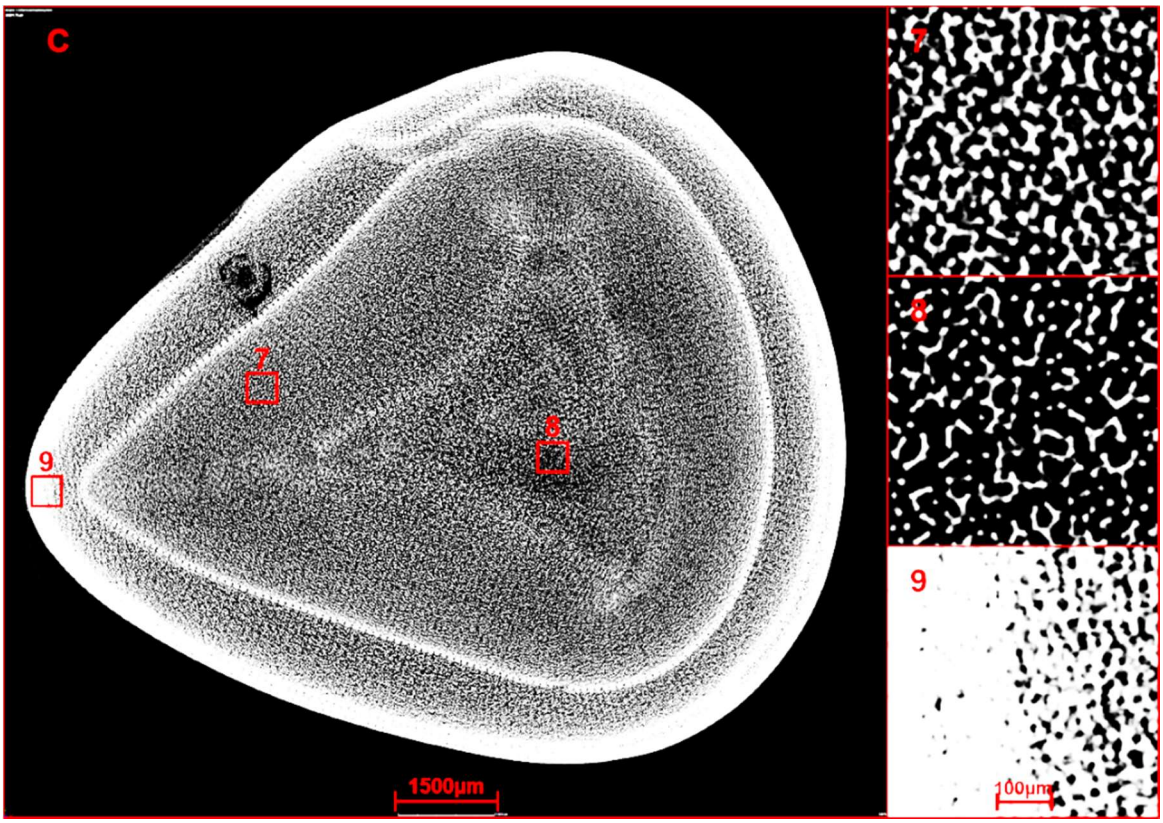

Figure 10-6: One example image of the high resolution CT-scan with marked crops for different areas of the microstructures. FEM-models of these areas are generated. Image Source AG Nickel/ ITV Denkendorf

The next step is then done with the software Dream3D (Version 6.2.327, http://dream3d.bluequartz.net, 30.03.2016). The pipelines (this is the name for the steps used in Dream3D) are first to import the images, than flatten them (convert it into 8bit greyscale images) and next, using a threshold to extract the relevont structures. This is the most important step, because a wrong chosen value can have strong influences on the final result. One good option to define the threshold is to calculate the middle value for the picture brightness (e.g. with a picture editing software). A boolean-operator step then divides the image into two parts, wrong or true, and all voxels with value true are used in the FE-model as elements. The voxel with the values wrong are representing air in that case, but are neglected, because this reduces calculation time while air is not influencing the mechanical simulation in any way. In Figure 7 the different results of two different threshold values are compared. If the threshold is too low or too high, much of the information is lost (Figure 7 B).

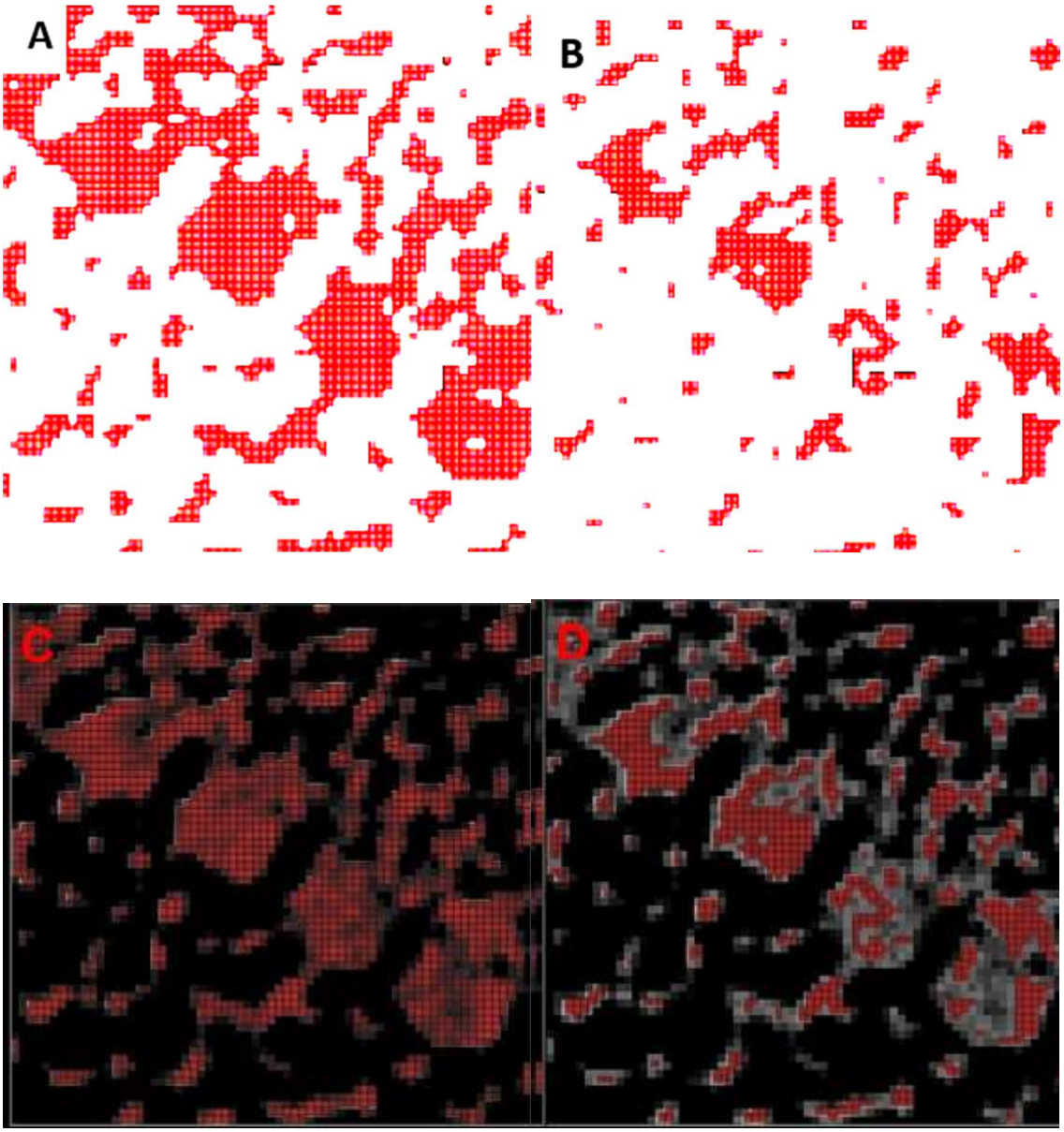

Figure 10-7: Results of different threshold values: A: shows the results of a threshold which remains all the details, C: shows an overlay of the resulting mesh over the original image. B: shows the result of a threshold where a large amount of information is lost, this is clearly visible if compared (the original image and the resulting image are superimposed) with the origi-nal image (compare D)

The next step then uses “segment features” to generate groups of neighbor cells, this helps to create different sets for the use in Abaqus if needed. The next two steps, “find feature size” and “create element array from feature array” were used to convert the information and at last the pipeline “abaqus hexadron write” produces a mesh with c3d8 elements. The final result can be seen in Figure 8 left. The models are then analysed in the FEM-analysis

with elastic material properties of (calcite with a Young`s modulus of 70 GPa and a poisons ratio of 0.31). Boundary conditions are shown in Figure8 right.

Figure 10-8: Left- The final result of the procedure to create a voxelmodel: Green represents the calcium material, white is air, which is deleted before using the mesh in the Finite Element analysis to avoid high amounts of elements.Right: The boundary conditions used in the FEM-simulation: An Analytic Rigid (a not mesh able part in ABAQUS) is used to transfer the force through a Rigid Body Constraint. The bottom part is fixed through the boundary conditions

The models are fixed at the bottom and through an analytical rigid boundary condition the force is introduced into the elastic simulation. The results of these simulations are shown in the next images, were the microstructure from the CT-image is compared with the Von-Misses stress distribution of the model on the right. The material is assumed to be purely elastic (the material is brittle, so no plasticity is assumed and damage is not part of this study). Differences of the microstructures are perfectly visible. Figure 9 shows the result of the crop (compare Figure 6) of the stereom, the Von-Mises stress distribution is relatively even (which fits to the even distributed pores in the analysed part of the stereom).

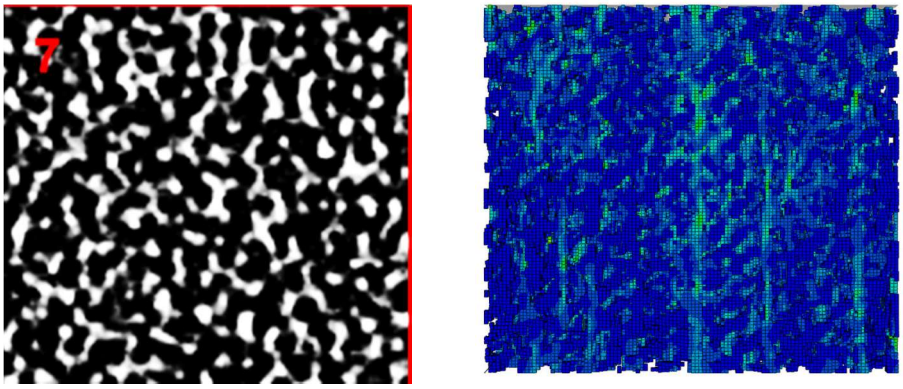

Figure 10-9: A stereom model, the results on the right show an even distributed Von-Misses stress

The next result (Figure 10) is from the outer part of the spine, where one can find much more material, this is clearly visible in the Von-Mises stress distribution which shows a much higher stress on the left side of the model, where the outer layer of the spine is situated.

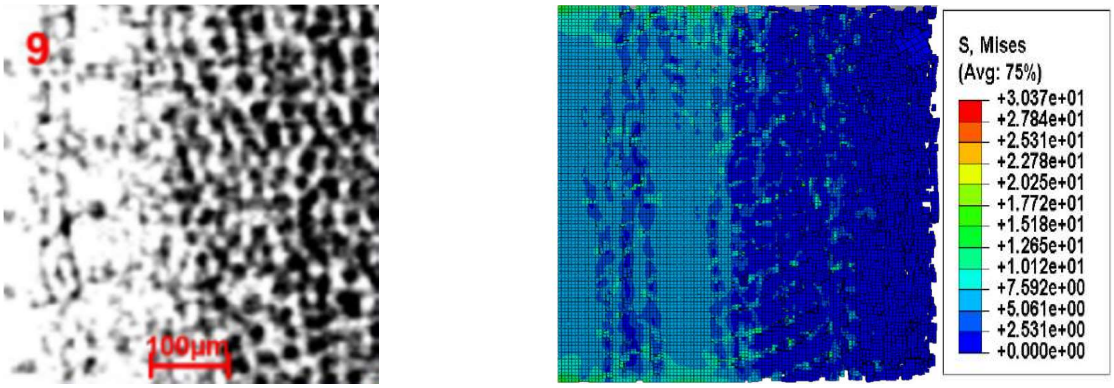

Figure 10-10: The cropped image on the left and the result of the FEM-Simulation on the right. The different microstructure on the outer part is clearly visible. The white part on the left re-presents the thick calcium carbonate structure on the outer shell, in the FEM simulation this part is clearly brighter than the rest of the model and there the highest stress is found

With this approach the analyses of selected parts (with individual microstructures) of the sea urchin spine are possible. Some of the results are compared in Figure 11, where the force-deflection diagram shows the influence of the microstructures of the different models. Values for the forces are between 58 N and 226 N in area 3. The left diagram compares the forces and the porosity values. Interestingly, the values for model 1 and 8 have comparable porosity values, but model 8 shows a significant higher force. Also the areas 2 and 4 show a higher value for the force than area 6 while posessing a higher porosity. For comparison,

the images in Figure 12 (and Figure 6) show the places where the microstructures taken for the models are situated in the sea urchin spine.

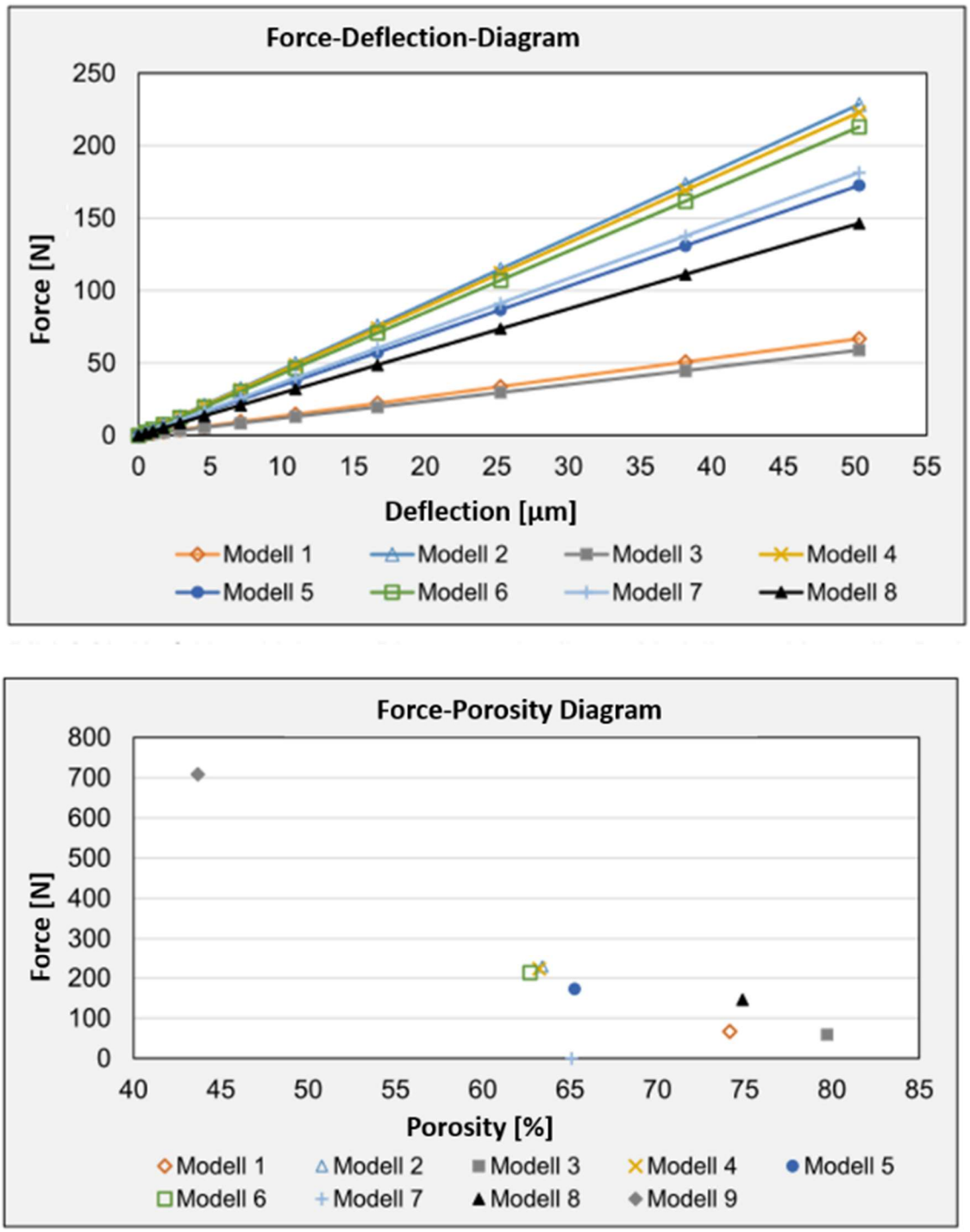

Figure 10-11: Left: The force-deflection diagram for 8 different models. On the right the force-porosity diagram

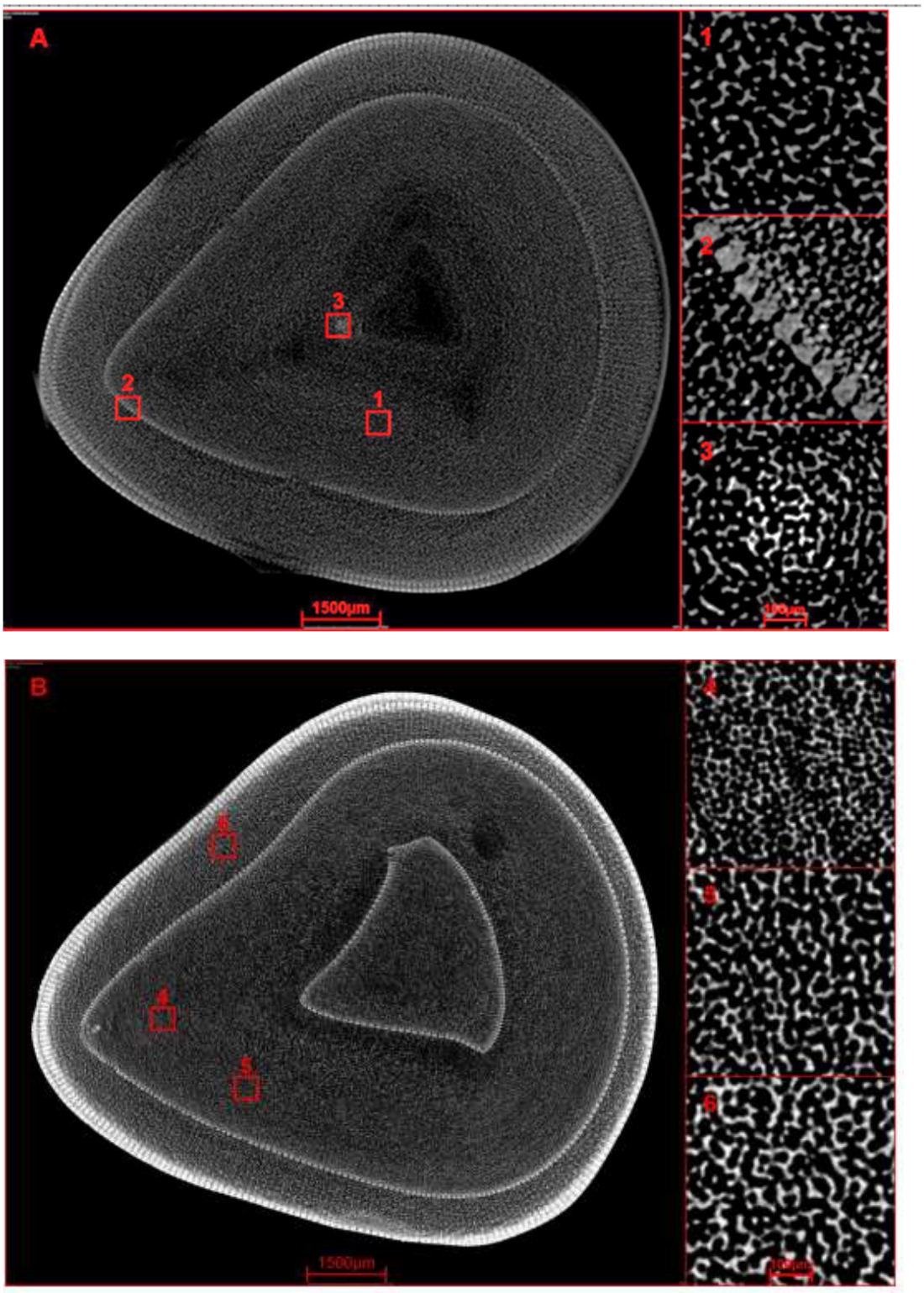

Figure 10-12: The selected areas for the models compared. CT-Image Source AG Nickel/ ITV Denkendorf

The next Figure 13: Model 1 (left) and Model 8 (right) compared. The models represent a comparable porosity, but Model number 1 shows a much higher force in the simulation.

The higher force is based on the different microstructures inside the model. Some possible reasons could be that there exist bigger pores in model 8 resulting in an inhomogeneous material distribution or mean that some thick areas that are reaching from bottom to top and reinforce the material (compare Figure 13 bottom).

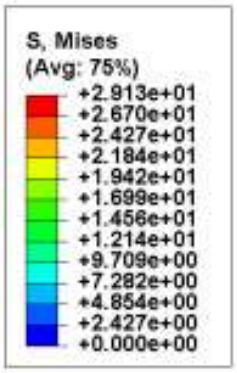
S, Mises
(Avg: 75%)
+2.913e+01
+2.670e+01
+2.427e+01
+2.184e+01
+1.942e+01
+1.699e+01
+1.456e+01
+1.214e+01
+9.709e+00
+7.282e+00
+4.854e+00
+2.427e+00
+0.000e+00

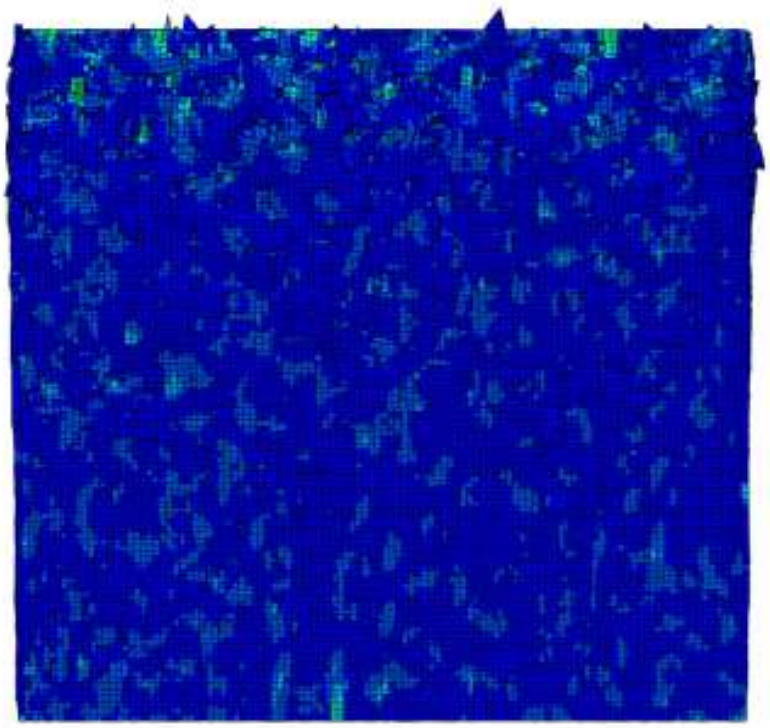

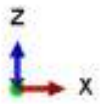
Z
X

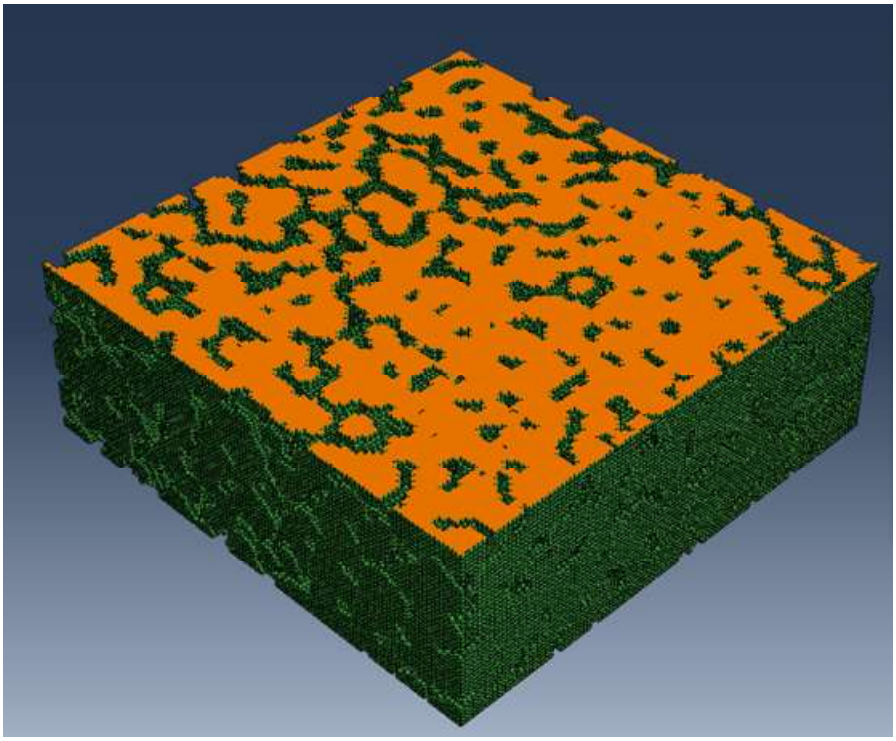

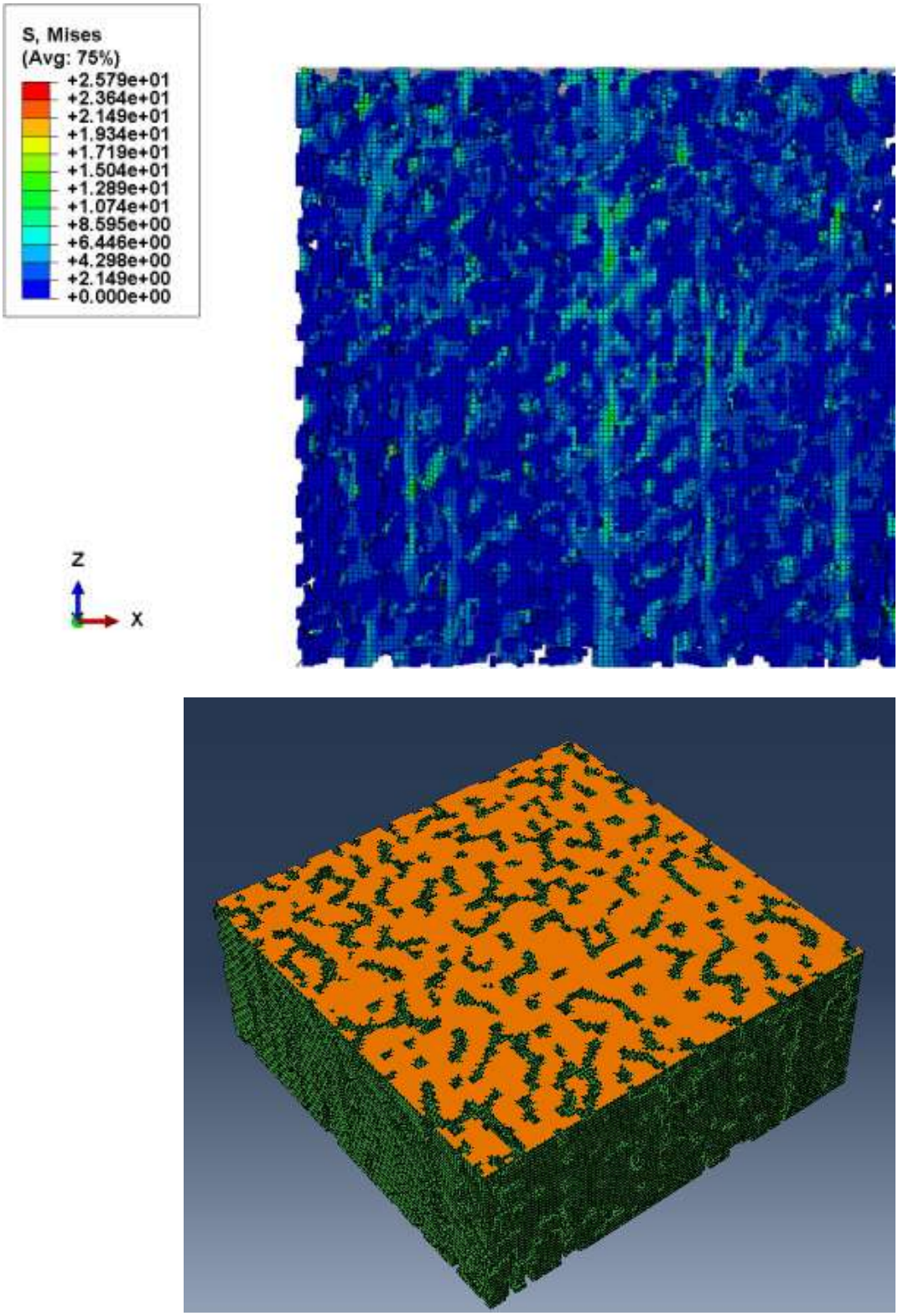

Figure 10-13: Model 1 (first 2 pictures) and Model 8 (last two pictures) compared. The models represent a comparable porosi-ty, but Model number 1 shows a much higher force in the simulation. The images with orange show cuts though the model to show the differences of the microstructure

These results were used in a Weibull analysis and visualized in a Weibull chart (Figure 14). The value for m, one of the important constants in the Weibull analysis, were calculated to be 219. For the calculation the software tool Matlab was used. For the calculations of the Weibull modulus, the stress values from the calculations were adapted to the results from the experiments. For this analysis it was assumed that the structures will break for a strain higher than 2.23% of their original length. This value was calculated from the experiments found in literature (V. Presser, Schultheiß, et al. 2009).

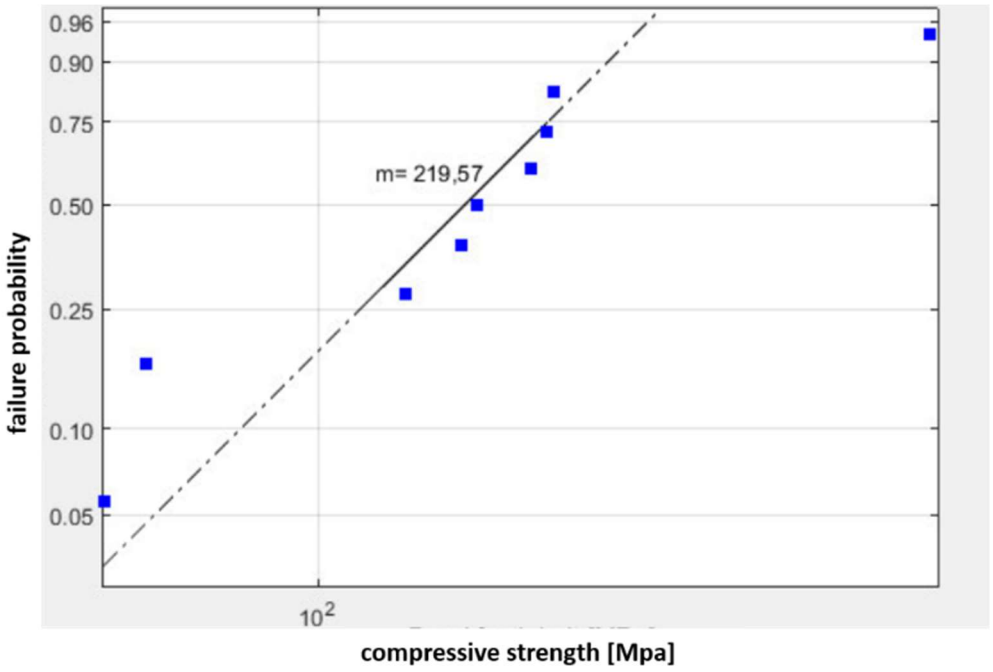

Figure 10-14: Weibull Chart for the analysed models. The values are calculated from the nine voxel models

10.4 High resolution direct modelling approach

The next modelling procedure is again a direct modelling approach, this time with the high resolution CT-images presented before. Now the interest lies in the behavior of the struts and the stress distribution around the pores. For the steps involved it is the same procedure as before. The pictures are prepared with a picture editing software, filter to denoise the images are used, then threshold segmenting and meshing follow as next steps. Because of the high amount of information found in the CT-images, only some pores are used in the model, otherwise the amount of elements would be too high for personal computer. One example is shown in Figure 15, the model is analysed in a pressure simulation and the stresses are shown. The green areas (brighter ones) show a higher stress than the blue areas,

in that example the knots at the top but even more at the bottom show the highest stress. Stress maxima at the struts and the influence of different pores or the structure /ordering of pores and struts combinations are now to be analysed with that procedure.

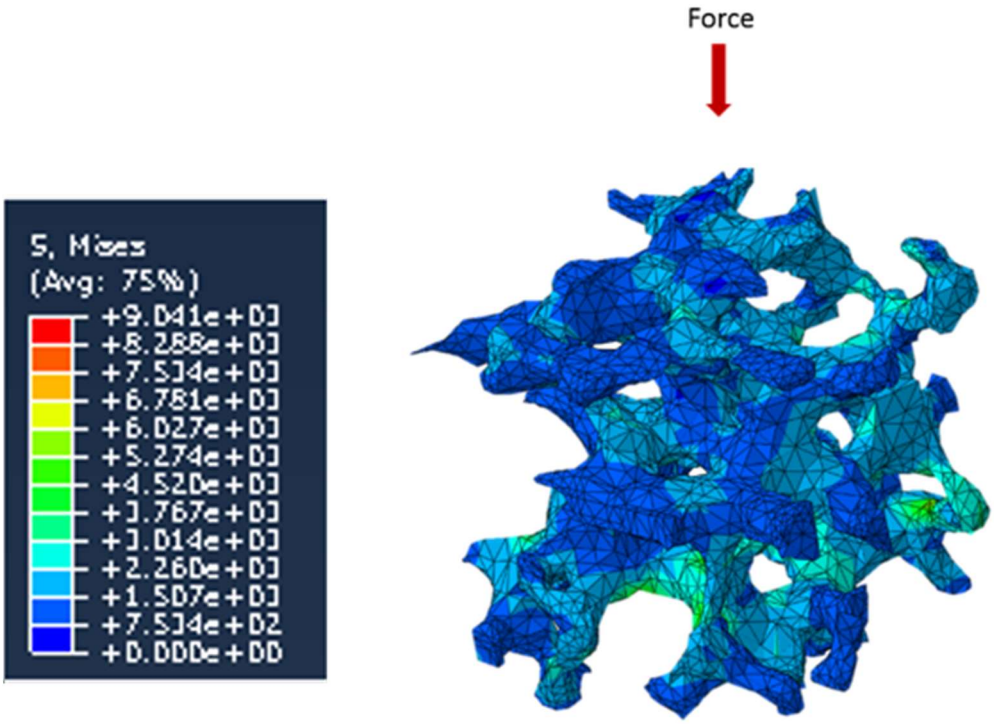

Figure 10-15: The high resolution model with stress distribution. The model is fixed at the bottom

10.5 Artificial structures

Abstraction and simplification of the models for simulations are a key aim otherwise the simulations are getting too complicated and computational expensive as shown with the examples above. With the information from the shown results the next step is producing artificial structures. To be able to generate different structures in a fast manner, a parametric modelling approach is used. The generated structures are then analysed in FE-simulations. The parameters are the pore or strut size, pore number or material, an example for the different structures can be found in Figure 18. In this example the sizes of the pores is varied, (50 µm and 70 µm diameter) this results is a different structure and a different strut size. The small change in the pore size results in big change for the generated structure. A box with a side length of 20 µm in the case of the pore radius of 25 µm (and in the case of pore radius of 35 µm the box possess a side length of 30 µm) is combined through a boolean

operation step with a pore and this step creates an open porous system (compare Figure 16).

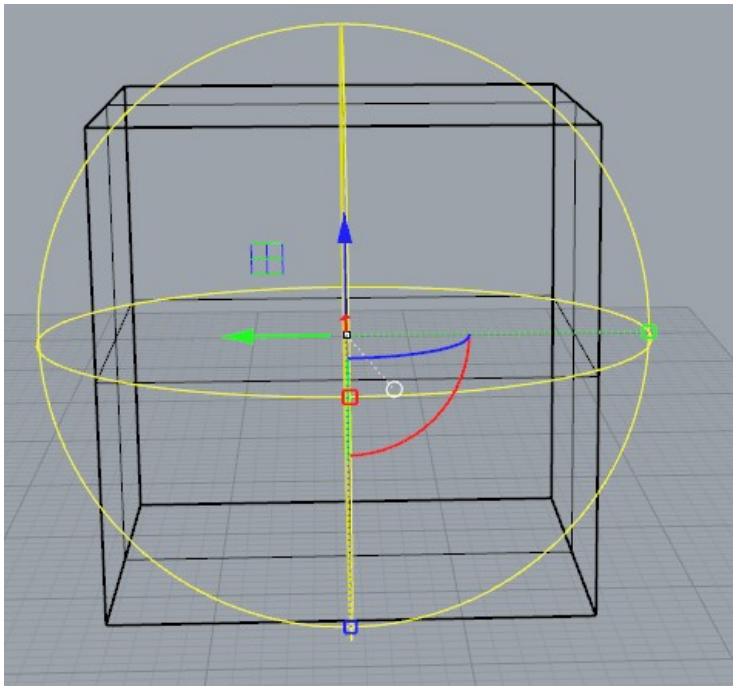

Figure 10-16: The box and the pore (yellow) which are the basis to construct the artificial models

The parametric models are generated with grasshopper (version August-2014, Build 0.9.0076), a plugin for Rhinoceros (Version 5 SR13 64-bit, McNeel Europe, Barcelona, Spain), baked and exported in a SAT file format. They are constructed in a way that all models fill out the same volume. The next steps are then to import it into ABAQUS, import the model as a part and mesh them. The first two structures are generated with relatively big pore sizes between the struts.

The results of the FEM simulation is shown in Figure 17 and Figure 18. For the simulation, a fully elastic material behavior with the material properties for Calcite (Young`s modulus of 72 GPa and a Poisson's ratio of 0.31, (KORTH n.d.)) was chosen. The stress distribution is shown in the figures. The first principal stress is higher in the model with smaller pores.

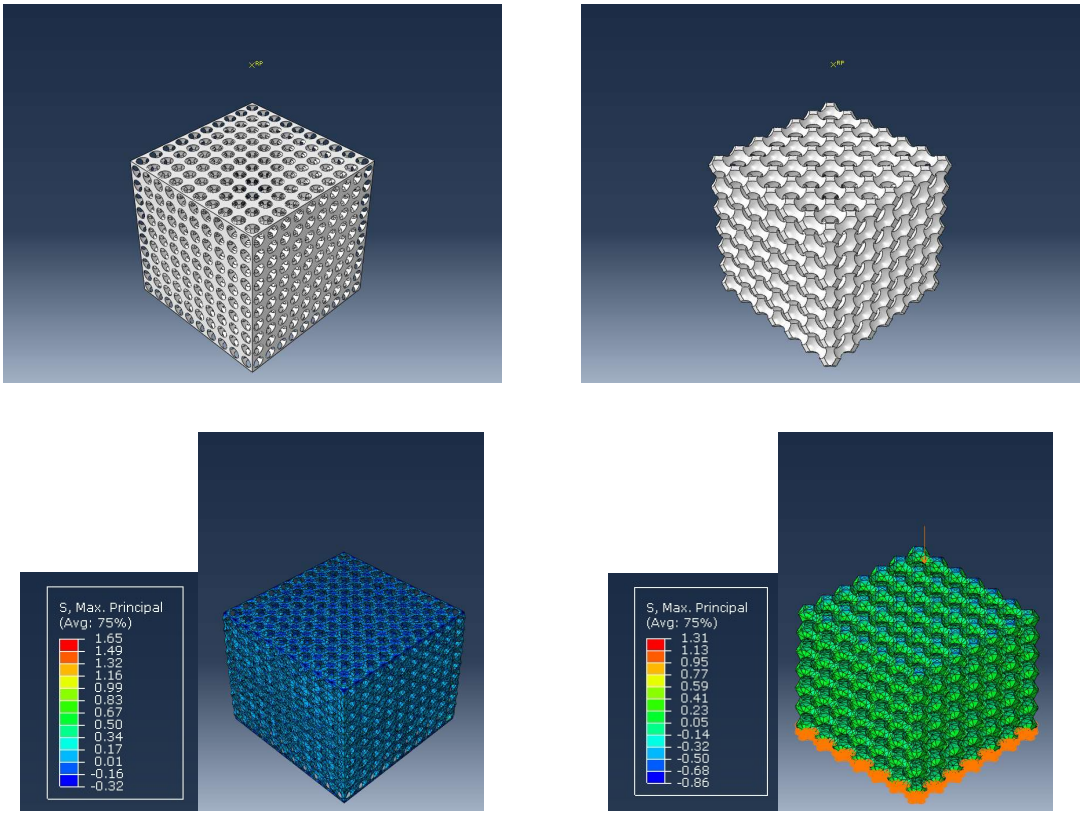

Figure 10-17: Models with different approaches in the modelling: Different radii of the pores. Left: 25 µm, right: 35 µm, first principles stresses are shown

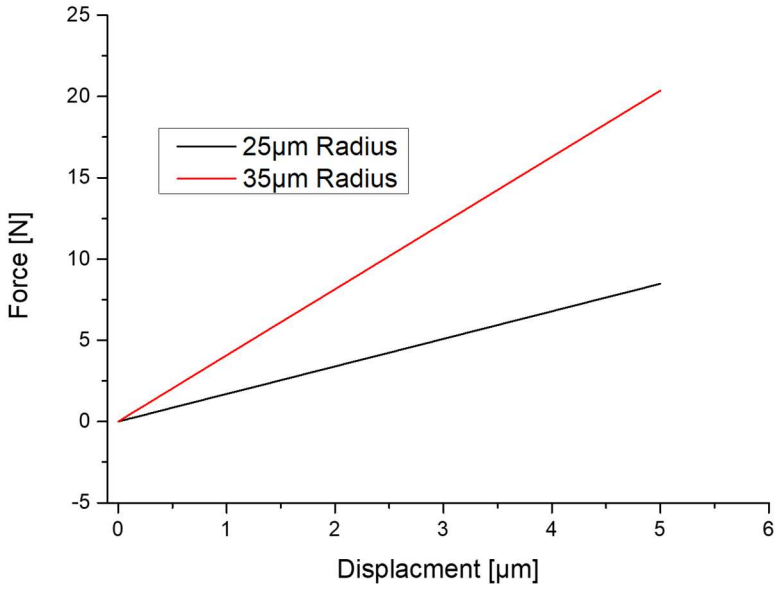

Figure 10-18: Results of the parametrized models analysed in the FEM-simulation. The model with bigger pores shows a higher force-displacment resistance

10.6 Discussion and Outlook

The different approaches to access the microstructure of sea urchin spines have their advantages and disadvantages and are usable for different experimental mechanical test simulations.

The direct approach with low resolution CT-images as a basis are suitable to create models which are on the macro-level, that represent structures in the mm-regime. The direct approach shows good results but needs a careful handling. The grey values differ from image to image (in z-direction, from top to bottom) and need to be distinguished from other parts by hand. The example shown here was able to proof the small influence on the elastic simulation of the caps. To confirm this result, the simulation of a whole sea urchin spine or at least a part of a sea urchin spine with more than on cap should be made. The direct approach presents the possibilities to analyse and transfer the reaction force of the experiments of the whole structure to two mesostructures, the stereom and the outer layer. In this example, the values of 8 GPa for the stereom and a pressure E-modulus between 10 and 12 GPa for the outer layer showed a good agreement with the experimental value. A damage simulation (e.g. a pin indentation simulation) should reveal more information about the influence of the caps in such a case and is planned as next a step in future.

The same is true for the models created from high resolution CT-images. They are helpful to define the struts and regions in a small cut / region of the sea urchin spine microstructure, but should also be analysed in damage simulations.

Also of importance would be to consider in future simulations an anisotropic material behavior for calcite. Calcite is build up from many crystals combined with proteins and this results in an anisotropic material behavior. A good start for such a material model could be the work of Naomi Tsafnat (Tsafnat et al. 2012). Such models will be analysed in future works in damage experiments. The different microstructures should have different results if used in pin indentations. The voxel models are defined through the resolution of the CT scans and of the settings used in Dream3D. The higher the resolution, the higher the number of elements produced with Dream3D. With the presented resolution of the CT-scans one cube with 1.2 mm side length generates a model with more than 19 million elements. The calculation of such big models is time and CPU expensive and thus the area which can be analysed with such a procedure is limited.

The next steps should also include the nanostructure of the sea urchin spine. The struts are showing a brick and mortar structure in the nano scale, which are also found in the nacre of the shells of sea snails and seashells (Ma et al. 2012). If the nanostructure of the sea urchin spine struts could be transferred into concrete materials the flexural strength of it could be in the range of 40 100 times higher than the flexural strength of regular concrete (Picker et al. 2017). If one could combine the nanostructure with the porosity on the micro scale, the development of light and strong concrete would be possible and would show a graceful (step by step) failure behavior.

The high Weibull value of nearly 220, which corresponds to 64 times the value from the actual compression test is much higher than one would expect if compared to ceramics which provide values between 10 and 20. According to literature, Heterocentrotus mammillatus has a Weibull modulus of 3,4 (V. Presser, Kohler, et al. 2009). In the simulation, the Weibull modulus is the straight line gradient, which consists of failure probability and fracture stress due to the purely linear elasticity of the model settings without a definition of the fracture mechanics. The tensions were therefore adjusted according to the original data (to 2.23% of the original length - > then damage starts in the experiments). However, the samples used in the real pressure tests consist of different structures and much bigger volumes. The simulations only covered certain areas of the spine and much smaller volumes. These are possible reasons for the high Weibull values.

The artificial structures produced with a parametric approach were able to produce interesting microstructures with simple methods and fast processing times. In contrary to a boolean approach (creating the pores through subtracting the spheres from a bulk material e.g.), the models are produced much faster and could be meshed after the models were finished and not as in the case of the boolean models, before and after the boolean operation. Compared to beam elements, the parametric models show curved pores and where much more comparable to the original structures than what would be possible with beam elements. Beam elements would introduce areas and corners which would result in highly stressed areas, which would not be comparable to the sea urchin spine stereom which only shows curved corners. With the parametric modelling approach, the analysation of many different microstructures is possible and so the influence of one parameter like the strut thickness or the pore size is easily accessible. In the examples shown here, the structure with bigger pores did show a higher reaction force in the pressure simulation most likely because of the thicker struts. In future, these models will be selected for special parameters, gradients will

be introduced and damage behavior will be simulated, to generate knowledge about the most important features in the behavior of the sea urchin spine microstructure in pressure tests analysed. With these results the development of the microstructures which could withstand higher forces but while staying lightweight would be enabled and should help the world in producing longer lasting and less energy and material demanding building structures.

We thank the Institut für Kunststofftechnik (IKT), University of Stuttgart for the low resolution CT scan and the working group of Prof. K. G. Nickel, University Tübingen for the high resolution CT-images of the sea urchin spine scanned at the ITV Denkendorf.

This work has been funded by the German Research Foundation (DFG) as part of the Transregional Collaborative Research Centre (SFB/Transregio) 141 'Biological Design and Integrative Structures'.

10.7 Literature

[1] Daxner, Thomas. 2010. "Finite Element Modeling of Cellular Materials." In Cellular and Porous Materials in Structures and Processes, eds. Holm Altenbach and Andreas Öchsner. Vienna: Springer Vienna, 47–106. http://dx.doi.org/10.1007/978-3-7091-0297-8_2.

[2] Fang, Qianqian, and David A. Boas. 2009. "Tetrahedral Mesh Generation from Volumetric Binary and Gray-Scale Images." 1142–45. http://dl.acm.org/citation.cfm?id=1699872.1700164 (February 16, 2016).

[3] KORTH. "Material: Calzit (CaCO3) - Korth Kristalle GmbH." http://www.korth.de/index.php/material-detailansicht/items/11.html.

[4] Ma, Yurong et al. 2012. "Structure-Property Relationships of a Biological Mesocrystal in the Adult Sea Urchin Spine." Proceedings of the National Academy of Sciences 109(18): 7126–7126. http://www.pnas.org/cgi/doi/10.1073/pnas.1204261109.

[5] Picker, Andreas et al. 2017. "Mesocrystalline Calcium Silicate Hydrate: A Bioinspired Route toward Elastic Concrete Materials." Science Advances 3(11): e1701216. http://advances.sciencemag.org/lookup/doi/10.1126/sciadv.1701216.

[6] Presser, V., C. Kohler, et al. 2009. "Sea Urchin Spines as a Model-System for Permeable, Light-Weight Ceramics with Graceful Failure Behavior. Part II. Mechanical Behavior of Sea Urchin Spine Inspired Porous Aluminum Oxide Ceramics under Compression." Journal of Bionic Engineering 6(4): 357–64. http://dx.doi.org/10.1016/S1672-6529(08)60143-2.

[7] Presser, V., S. Schultheiß, C. Berthold, and K.G. Nickel. 2009. "Sea Urchin Spines as a Model-System for Permeable, Light-Weight Ceramics with Graceful Failure Behavior. Part I. Mechanical Behavior of Sea Urchin Spines under Compression." Journal of Bionic Engineering 6(3): 203–13. http://linkinghub.elsevier.com/retrieve/pii/S1672652908601250 (May 28, 2013).

[8] Presser, Volker et al. 2010. “Determination of the Elastic Modulus of Highly Porous Samples by Nanoindentation: A Case Study on Sea Urchin Spines.” Journal of Materials Science 45(9): 2408–18. http://link.springer.com/10.1007/s10853-010-4208-y (October 7, 2015).

[9] Qin, Zhao, Gang Seob Jung, Min Jeong Kang, and Markus J Buehler. 2017. “The Mechanics and Design of a Light-weight Three-Dimensional Graphene Assembly.” (JANUARY): 1–8.

[10] Schmier, Stefanie et al. 2016. “Developing the Experimental Basis for an Evaluation of Scaling Properties of Brittle and ‘Quasi-Brittle’ Biological Materials.” In Biomimetic Research for Architecture and Building Construction, Springer, Cham, 277–94. http://link.springer.com/10.1007/978-3-319-46374-2_14 (July 6, 2017).

[11] Tsafnat, Naomi, John D Fitz Gerald, Hai N Le, and Zbigniew H Stachurski. 2012. “Micromechanics of Sea Urchin Spines.” PloS one 7(9): e44140. http://www.pubmedcentral.nih.gov/articlerender.fcgi?artid=3439470&tool=pmcentrez&rendertype=abstract (March 7, 2013).

11 Zusammenfassung und Ausblick

In den letzten Jahren und vor allem den letzten Monaten hat sich unsere Sichtweise auf die Erde und unsere Umwelt verändert. Sie ist nicht mehr nur Ressource und Abfalleimer, sondern wir Menschen haben realisiert, dass wir sie durch unsere Aktivitäten stark beeinflussen und vor allem durch und durch von ihr abhängig sind. Das Massensterben der Arten, Umweltverschmutzung, Überbevölkerung und einhergehende Probleme wie der Klimawandel zeigen, dass wir neuartige Lösungen und Lösungsansätze brauchen. Diese können unter anderem in der Bionik gefunden werden. In dieser Dissertation sind einige Ansätze beschrieben, die kleine aber wirkungsvolle Beiträge zur Reduzierung der Ressourcennutzung und des Energieverbrauches leisten können. Durch die Verbindung von Simulationen mit bionischen Ansätzen sind Lösungen gefunden worden, die rein experimentell schwer oder nicht erreichbar gewesen wären. Dabei ist der Ansatz selbst umweltschonend (wenn man den elektrischen Energieverbrauch für die Simulationen nicht betrachtet oder besser, davon ausgeht, dass dieser mit erneuerbaren Energien erzeugt würde). Natürlich sind echte Experimente wichtig zur Generierung von Inputdaten für die Simulationen, wie im Kapitel 9 vorgestellt, oder zur Validierung der simulatorisch erzeugten Ergebnisse. Doch dass die Simulation eine sinnvolle Ergänzung für bionische Studien ist, ist mit dieser Dissertation gezeigt worden. Im Folgenden werden die einzelnen Kapitel diskutiert und im Hinblick auf die Kombination von Simulation und Bionik analysiert.

Die erste Arbeit, die in Kapitel 2 vorgestellt wird, berichtet über die Fensterpflanze. Die Prinzipien der Pflanze wurden erarbeitet, analysiert und Ideen für bionische Produkte wurden entwickelt. Die Arbeit zeigt den kompletten Vorgang von der Idee bzw. dem biologischen Vorbild, die Ansätze zur Analyse der Prinzipen und der Anwendung der Prinzipien in technischen Lösungen.

In Kapitel 3 und Kapitel 4, in denen es um die Simulation von Perlmutt-inspiriertem Komposit-Material geht, sind die mechanischen Eigenschaften von bioinspiriertem TiO_2/PE-überzogenem Nanokompositen untersucht worden. Das Kompositmaterial ist durch chemische Badabscheidung bei niedrigen Temperaturen und Schicht-für-Schicht Technik hergestellt worden. Der Einfluss unterschiedlicher Dickenverhältnisse der Bestandteile (organische (PE) und anorganische (TiO_2) Phasen) und der Einfluss von Mineralbrücken auf den E-Modul des Nanokomposits wurde mit analytischen und numerischen Methoden untersucht. Das elasto-plastische Spannungs-Dehnungsverhalten der TiO_2- und PE-Phasen der geschichteten Nanokompositen wurde durch inverses Modellieren auf der Grundlage von

FE-Simulationen von Nanoindentationstests der einzelnen Phasen zum Vergleich mit den experimentellen Ergebnissen von Nanoindentationstests ermittelt. Die Simulationen von Eindrucktests mit einem 2D-achsensymmetrischen Modell wurden bis zu einer Eindringtiefe von 120 nm durchgeführt. Es wurde festgestellt, dass aufgrund des strukturellen Aufbaus der Schichtstruktur des Nanokomposits der E-Modul des Verbundwerkstoffs nicht einfach nach der Regel der Mischung seiner Bestandteile erreicht werden kann. Es wird angenommen, dass der hohe Elastizitätsmodul des Nanokomposits durch die Bildung von mineralischen Brücken erreicht wird. Das betrachtete bioinspirierte Material (TiO_2/PE) weist ähnliche Verstärkungen durch mineralische Brücken auf wie die in natürlichem Perlmutt. Nur mit dem Vorhandensein unterschiedlicher Volumenanteile von Mineralbrücken bei jedem Dickenverhältnis der Bestandteile und einem sehr hohen E-Modul dieser Mineralbrücken zeigen die Computersimulationen und analytischen Berechnungen vergleichbare Ergebnisse wie die Ergebnisse des Experiments. Diese Brücken verbinden die harten Schichten wie bei Perlmutt und verstärken das Material. Zusätzlich sind diese Brücken klein genug, um als Kristall betrachtet zu werden. Die Brücken weisen dann andere Materialeigenschaften auf als das amorphe TiO_2; der E-Modul erreicht den Wert von rutilem TiO_2 von ca. 282 GPa. Mit dieser Theorie können die resultierenden E-Moduln des Experiments durch die analytischen und numerischen Modelle reproduziert werden. Durch die Anwendung des hier vorgestellten Ansatzes können die mechanischen Eigenschaften (insbesondere die hohe Festigkeit) von künstlich hergestellten Materialien und die mineral bridges (die Schichtung der einzelnen Bestandteile des Nanokomposits) der Struktur von Perlmutt vorhergesagt werden. Diese Ergebnisse sind ein gutes Beispiel für die Aussagekraft der Simulation, in dem Theorien, ob die Mineralbrücken, die im natürlichen Vorbild existieren, auch im bioinspirierten Material vorhanden sein müssen, im Computer schnell überprüft werden können.

In Kapitel 5, *Simulation der Proteinbindungseigenschaften an Zinkoxid*, wird beschrieben, wie MD-Simulationen eingesetzt wurden, um die Adsorptionskraft und Bindungsaffinität eines an der ZnO(0001)-O Oberfläche adsorbierten Modellpeptids zu modellieren. Parameter wie Kontaktfläche, Maximalkraft, Weg bei maximaler Kraft und maximaler Weg bei Bruch wurden aus der Simulation extrahiert und als Parameter für nachfolgende FEM-Simulationen verwendet. Die Kohäsionsanalyse und das Traktionstrennungsgesetz zeigten eine gute Konsistenz. Obwohl die Kraftkurven der MD-Simulationen durch die FEM-Si-

mulationen angenähert wurden, sowie angenommen wurde, dass das Peptid in verschiedenen Konformationen gebunden war, waren die Ergebnisse robust. Eine realistischere Simulation einer ganzen Peptidschicht verspricht in Zukunft, die Peptid-Peptid-Wechselwirkungen noch präziser quantitativ zu erklären. Auch kompliziertere Strukturen könnten so analysiert werden, wie z. B. eine so genannte Ziegel- und Mörtelstruktur, die in natürlichen Perlmutt- und anderen vielversprechenden Anordnungen im kleineren Maßstab zu finden ist. Dies kann zur Entwicklung von neuartigen Keramiken aus ZnO und Peptiden führen, die widerstandsfähig gegen Risse sind. Auch zeigen sich die Vorteile der Simulation: Die Idee stammt aus der Biologie (Peptide mit guten Bindungseigenschaften für Zinkoxid zu bestimmen) und kann mit der Simulation relativ schnell überprüft und bestätigt werden. Die Proteine könnten nun synthetisch hergestellt werden und in ein Komposit mit Zinkoxid eingebracht werden. Dieses Material könnte dann mit echten Experimenten getestet werden, um es dann zu neuartigen Produkten weiter zu entwickeln.

In Kapitel 7, Pomelo, geht es um den weichen, weißen Anteil der Schale der größten Zitrusfrucht. Es wird angenommen, dass das Zusammenspiel von strukturellen Merkmalen auf verschiedenen Längenskalen solcher Früchte die Ableitung großer Energiemengen während ihres Aufpralls auf eine harte Oberfläche ermöglicht. Hier ist das Ziel, ein numerisches Modell auf verschiedenen hierarchischen Ebenen mittels der Finite-Elemente-Methoden (FEM) zu verwenden, um verschiedene strukturelle Merkmale zu identifizieren, die zur Dämpfungsleistung der Pomelofrucht beitragen. Das betrachtete numerische Modell wurde auf der Grundlage einer homogenen Aluminiumschaumstruktur (AlSi7Mg0.3) erstellt, die von der Pomelofrucht-Schalenstruktur inspiriert ist. Im vorliegenden Ansatz werden Si- oder Fe-reiche intermetallische Partikel auf den Streben des Schaums AlSi7Mg0.3 zusätzlich berücksichtigt, was spezielle Untersuchungen des strukturellen Verhaltens des Schaums unter verschiedenen Belastungsbedingungen ermöglichte. Der Vergleich der Ergebnisse aus Simulationen und experimentellen Druckversuchen zeigte vielversprechende Ergebnisse in Bezug auf das Verformungsverhalten, die die Konstruktion biomimetischer metallischer Schaumstoffe z. B. bei der Auswahl von vergleichbaren Strukturen unterstützen. Das Verständnis der Prinzipien der Kombination von Struktur und Material, die von biologischen Systemen inspiriert sind, kann in Zukunft die Konstruktion neuer leichter, bioinspirierter Materialien mit hoher Schlag- und Durchstoßfestigkeit und einer Kombination aus hochenergetischer Dissipation, hohen Dämpfungseigenschaften und einer signifikanten Erholung nach großen Verformungen ermöglichen.

In Kapitel 8 und 9 ist der Ansatz zur Analyse der Kokosnuss gezeigt. Die Anpassung des traditionell genutzten Kerbschlagbiegeversuchs auf ein natürliches Vorbild, die Kokosnuss wird beschrieben. Die Übertragung der Probenform in die Simulation und die dabei enstehenden Schwierigkeiten wurden im Detail besprochen. Ziel war es, die experimentell bestimmten Ergebnisse eines Kerbschlagbiegeversuches von flachen aber auch von gekrümmten Proben aus PVC simulatorisch nachzubilden. Die dafür notwendigen Materialparameter sind durch Zugversuche ermittelt worden. Die Ergebnisse der Simulation zeigten eine sehr gute Übereinstimmung mit den experimentell bestimmten Kraft-Weg-Kurven. In Zukunft sollten sich diese Simulationen auch auf die Kokosnussschale übertragen lassen.

In Kapitel 10, Seeigelstachel, werden die verschiedenen Ansätze für realistische Modellierung der Mikrostruktur von Seeigelstacheln diskutiert. Die jeweiligen Vor- und Nachteile wie Schnelligkeit oder Genauigkeit, z. B. machen sie für unterschiedliche Analysen verwendbar. Der direkte Ansatz mit niedrigauflösenden CT-Bildern als Grundlage eignet sich, um Modelle zu erstellen, die sich auf der Makroebene befinden und die Strukturen im Millimeter-Bereich repräsentieren. Der direkte Ansatz zeigte genaue und sehr an der Realität orientierten Ergebnisse, erforderte aber eine sorgfältige Handhabung, bezüglich der gewählten Variablen. Die Grauwerte zum Beispiel unterscheiden sich von Bild zu Bild der Scans (in z-Richtung, von oben nach unten) und sind händisch an das jeweilige Bild anzupassen (Neudefinition der Werte für $CaCo_3$). Das hier gezeigte Beispiel konnte den geringen Einfluss der Kappen auf die elastische Simulation nachweisen. Um dieses Ergebnis zu bestätigen, sollte in zukünftigen Arbeiten die Simulation eines ganzen Seeigelstachels oder zumindest eines Teils eines Seeigelstachel mit mehr als einer Kappe durchgeführt werden. Eine Schadensimulation (z. B. eine Pin-Eindrucks-Simulation) sollte in einem solchen Fall mehr Informationen über den Einfluss der Kappen liefern und ist als nächster Schritt in der Zukunft geplant. Das Gleiche gilt für Modelle, die aus hochauflösenden CT-Bildern erstellt wurden. Sie sind hilfreich, um die Stege und Regionen in einem kleinen Schnitt bzw. Bereich der Seeigelstereome zu definieren, sollten aber in Zukunft auch mit Schadenssimulationen analysiert werden. Die Voxelmodelle der Mikrostruktur des Stereoms werden durch die Auflösung der CT-Scans und der in Dream3D verwendeten Einstellungen (siehe Kapitel 10) definiert. Je höher die Auflösung, desto höher ist die Anzahl der mit Dream3D erzeugten Elemente. Mit der dargestellten Auflösung der CT-Scans erzeugt ein Würfel mit 1,2 mm Seitenlänge ein Modell mit mehr als 19 Millionen Elementen. Die Berechnung sol-

cher großen Modelle ist zeit- und rechenintensiv und somit ist der mit einem solchen Verfahren zu analysierende Bereich in Wirklichkeit durch die zur Verfügung stehenden Kapazitäten begrenzt. Die nächsten Schritte sollten auch die Nanostruktur der Seeigelstereome umfassen. Die Stege zeigen eine Ziegel- und Mörtelstruktur im Nanobereich, die auch im Perlmutt der Muscheln von Meeresschnecken und Muscheln zu finden ist [29]. Wenn die Nanostruktur der Seeigelstereome in Betonmaterialien übertragen werden könnte, wäre ihre Biegefestigkeit im Bereich von 40 und damit ca. 100 mal höher als die Biegefestigkeit von Normalbeton [52]. Könnte man die Nanostruktur mit der Porosität im Mikromaßstab kombinieren, wäre die Entwicklung von gleichzeitig leichtem und festem Beton möglich. Wenn es zum Versagen kommen sollte, würde er voraussichtlich auch ein elegantes (schrittweises) Versagensverhalten, wie es beim Seeigelstachel zu beobachten ist, zeigen. Mit einem parametrischen Ansatz konnten mit einfachen Methoden und schnellen Verarbeitungszeiten interessante (künstliche) Mikrostrukturen erzeugt werden, die das Seeigelstereom nachempfinden. Im Gegensatz zu einem booleschen Ansatz (Erzeugen der Poren durch Subtraktion der Kugeln von einem Schüttgut z. B.) werden die Modelle viel schneller berechnet und konnten nach Fertigstellung der Modelle (und nicht wie bei den booleschen Modellen vor und nach dem booleschen Vorgang) vernetzt werden. Im Vergleich zu Stabelementen weisen die parametrischen Modelle gekrümmte Poren auf und sind mit den ursprünglichen Strukturen besser vergleichbar als Strukturen, die mit Stabelementen erzeugt werden. Mit dem parametrischen Modellierungsansatz ist die Analyse vieler verschiedener Mikrostrukturen möglich und damit Untersuchungen zum Einfluss eines Parameters wie der Geometrie der Stege. Dadurch lassen sich aufgrund der Analysen der biologischen Vorbilder optimierte Strukturen generieren, in verschiedenen Variationen schnell und einfach erzeugen und in FEM-Simulationen testen. Damit zeigt sich die Schönheit und Effektivität der Kombination der Bionik und der Simulation ein weiteres Mal.

Die hier gezeigten Vorbilder, bioinspirierten Prinzipien und Simulationen arbeiten alle auf das eine Ziel hin, Ressourcen einzusparen und besser zu nutzen. Dafür ist, wie hier gezeigt, das Verständnis des natürlichen Vorbilds, aber auch des bioinspirierten Materials essentiell. Damit können Materialeigenschaften erklärt (im Falle der mineral bridges des Perlmutts zum Beispiel) aber auch Strukturen auf neue Belastungen optimierter werden. Wenn damit Energie und Material eingespart werden kann und die Produkte danach auch noch genauso leistungsfähig, aber am besten noch besser sind als zuvor, ist ein großer Fortschritt gemacht. Auch wenn das nicht gelingen sollte - ein besseres Verständnis der Natur und der

in der Natur genutzten Möglichkeiten des Materialeinsatzes lohnt die eingesetzte Mühe und Zeit jederzeit.

12 Summary and Outlook

In recent years and especially in the last few months our view of the earth and our environment has changed. It is no longer just a resource and waste bin, but we humans have realised that we influence it strongly through our activities and are above all thoroughly dependent on it. The mass extinction of species, environmental pollution, overpopulation and associated problems such as climate change show that we need new solutions and approaches to solutions, which are not only to be found in biomimetics. This dissertation describes some approaches that can make small but effective contributions to reducing the use of resources and energy. By combining simulations with biomimetic approaches, solutions have been found that would have been difficult or even impossible to achieve purely experimentally. The approach itself is environmentally friendly (if one does not consider the electrical energy consumption for the simulations or better, assumes that it would be generated with renewable energies). Of course, real experiments are still important for generating input data for the simulations, for example as shown in chapter 9, or for validating the results generated by the simulations. But that simulation is a useful supplement for biomimetic studies has been shown within this thesis.

In the following, the individual chapters are summarized and discussed and analysed with regard to the combination of simulation and biomimetics.

The first work in chapter 1 that is presented in this cumulative thesis reports on the window plant. The biological principles of the plant are worked out, analysed in detail and ideas for biomimetic products are developed. The work shows the complete process from the idea or biological model, on the approaches of the analysis of the principles (like heat and light processing) up to the application of the principles in technical solutions.

In chapter 3 and chapter 4, which are dealing with the simulation of nacre-inspired composite material, the mechanical properties of bio-inspired TiO_2/PE-coated nanocomposites are investigated. The composite material has been produced by chemical bath deposition at low temperatures and layer-by-layer technique. The influence of different thickness ratios of the components (organic (PE) and inorganic (TiO_2) phases) and the influence of mineral bridges on the E-modulus of the nanocomposite has been investigated by analytical and numerical methods. The elasto-plastic stress-strain behavior of the TiO_2 and PE phases of the layered nanocomposites was determined by inverse modeling based on FE simulations of nanoindentation tests of the individual phases for comparison with the experimental results of nanoindentation tests. The simulations of indentation tests with a 2D axisymmetric

model were performed up to a penetration depth of 120 nm. It is found that due to the structural composition of the layer structure of the nanocomposite, the E-modulus of the composite material cannot be achieved simply by following the rule of mixing its constituents. It is assumed that the high modulus of elasticity of the nanocomposite is achieved by the formation of mineral bridges. The considered bio-inspired material (TiO_2/PE) shows similar reinforcements by mineral bridges as those in natural mother-of-pearl. Only with the presence of different volume fractions of mineral bridges at each thickness ratio of the constituents and a very high modulus of elasticity of these mineral bridges, the computer simulations and analytical calculations show comparable results as the results of the experiment. These bridges connect the hard layers like in the mother of pearl and strengthen the material. In addition, these bridges are small enough to be considered as crystals. The bridges then exhibit more attractive material properties than the amorphous TiO_2; the modulus of elasticity reaches the value of rutile TiO_2 of about 282 GPa. With this theory, the resulting E-moduli of the experiment can be reproduced by the analytical and numerical models. By applying the approach presented here, the mechanical properties (high strength) of man-made materials and the mineral bridges (the layering of the individual components of the nanocomposite) of the structure of nacre can be predicted. These results are a good example of the strengths of the simulation, in which theories as to whether the mineral bridges that exist in the natural model must also be present in the bio-inspired material can be quickly checked.

In chapter 5, simulation of protein binding properties to zinc oxide, we describe how MD simulations were used to model the adsorption power and binding efficiency of a model peptide adsorbed on the ZnO(0001)-O surface. Parameters such as contact area, maximum force, displacement at maximum force and maximum displacement at break were extracted from the simulation and used as parameters for subsequent FEM simulations. Cohesion analysis and the traction separation law showed good consistency. Although the force curves of the MD simulations were approximated by the FEM simulations and it was assumed that the peptide was bound in different conformations, the results were robust. A more realistic simulation of an entire peptide layer promises to explain the peptide-peptide interactions quantitatively with even greater precision in the future. Even more complicated structures could be analyzed in this way, such as a so-called brick and mortar structure, which is found in natural mother-of-pearl and other promising arrangements on a smaller scale. This may lead to the development of novel ceramics made of ZnO and peptides that

are resistant to cracking. The advantages of simulation also become apparent: The idea comes from biology (to search for peptides with good binding properties for zinc oxide) and can be tested and confirmed relatively quickly with simulation. The proteins could now be produced synthetically and incorporated into a composite with zinc oxide. This material could then be tested in real experiments and lead to novel products.

Chapter 7, Pomelo, deals with the soft, white part of the skin of the largest citrus fruit. It is believed that the interplay of structural features on different length scales of such fruits allows the dissipation of large amounts of energy during their impact on a hard surface. Here, the aim is to use a numerical model at different hierarchical levels using finite element methods (FEM) to identify different structural features that contribute to the damping performance of the pomelo fruit. The numerical model under consideration was created on the basis of a homogeneous aluminium foam structure (AlSi7Mg0.3) inspired by the pomelo fruit shell structure. In the present approach, Si or Fe rich intermetallic particles on the struts of the foam Al-Si7Mg0.3 are additionally considered, which allowed more specialized investigations of the structural behaviour of the foam under different loading conditions. The comparison of the results from simulation and experimental compression tests showed promising results regarding the deformation behaviour, which support the design of biomimetic metallic foams e.g. in the selection of comparable structures. Understanding the principles of combining structure and material inspired by biological systems may in the future enable the design of new lightweight, bio-inspired materials with high impact and puncture resistance and a combination of high energy dissipation, high damping properties and significant recovery from large deformations.

In chapters 8 and 9, the approach to the coconut analysis is shown. The adaptation of the traditionally used notched bar impact test to a natural model, the coconut, is described. The transfer of the difficulties of the sample shape into the simulation is discussed in detail. The aim was to simulate the experimentally determined results of an impact test on flat and curved PVC samples. The necessary material parameters were determined by tensile tests. The results of the simulation show very good agreement with the experimentally determined force-displacement curves. In the future it should be possible to transfer these simulations to the coconut shell.

In chapter 10, sea urchin spines, the different approaches for realistic modelling of the microstructure of sea urchin spines are discussed. The respective advantages and disadvantages, such as speed or accuracy, e.g. make them applicable for different analyses. The

direct approach with low-resolution CT images as a basis is suitable to create models that are on the macro level and represent the structures in the millimeter regime. The direct approach shows accurate and very realistic results, but requires careful handling of the selected variables. The grey values, for example, differ from image to image of the scans (in z-direction, from top to bottom) and have to be adjusted manually to the respective image (redefinition of the values for $CaCo_3$). The example shown here could prove the limited influence of the caps on the elastic simulation. To confirm this result, future work should include the simulation of a whole urchin spine or at least a part of an urchin spine with more than one cap. A damage simulation (e.g. a pin impression simulation) should provide more information about the influence of the caps in such a case and is planned as a next step in the future. The same applies to models created from high-resolution CT images. They are helpful to define the struts and regions in a small section/area of sea urchin stereoms, but should also be analysed with damage simulations in the future. The voxel models of the microstructure of the stereom are defined by the resolution of the CT scans and the settings used in Dream3D (see chapter 10). The higher the resolution, the higher the number of elements generated with Dream3D. With the resolution of the CT scans shown, a cube with 1.2 mm side length produces a model with more than 19 million elements. The calculation of such large models is time-consuming and computationally intensive and, therefore, the area to be analysed with such a procedure is in reality limited by the available capacities.

The next steps should also include the nanostructure of sea urchin stereomes. The struts show a brick and mortar structure on the nanoscale, which is also found in the mother-of-pearl of the shells of marine gastropods and bivalves [29]. If the nanostructure of the sea urchin stereoms could be transferred into concrete materials, their bending strength would be in the range of 40 and thus about 100 times higher than the bending strength of normal concrete [52]. If the nanostructure could be combined with the porosity on the micro-scale, the development of simultaneously light and strong concrete would be possible and would show an elegant (stepwise) failure behavior. The artificial structures created with a parametric approach (which mimic the sea urchin stereom) were able to create interesting microstructures with simple methods and fast processing times. In contrast to a Boolean approach (creating pores by subtracting the spheres from a bulk material, for example), the models are produced much faster and could be cross-linked after the models are finished (instead before and after the Boolean process). The parametric models have curved pores

and are much more comparable with the original structures than what would be possible with rod elements. With the parametric modelling approach the analysis of many different microstructures is possible and thus investigations on the influence of a parameter like the strut. Based on the experience and analysis of the biological models, optimized structures can be generated, quickly and easily generated in different variations and tested in FEM simulations. This shows once again the beauty and effectiveness of the combination of bi-omimetic and simulation.

The models, bio-inspired principles and simulations shown here all work towards the one goal of saving resources and making better use of them. To achieve this, as shown here, an understanding of the natural model, but also of the bio-inspired material, is essential. This can explain material properties (in the case of the mineral bridges of mother-of-pearl, for example) but also enable structures to be optimised for new loads. If some energy and material can be saved, and the products are just as efficient, but preferably even better than before, a big step forward has been made. Even if this should not succeed, a better understanding of nature and the possibilities of material applications used in nature is always worth the effort and time invested.

13 Ausstellung im Rosensteinmuseum

Der Anteil der eigenen Arbeit in dem Aufsatz unten umfasst (jeweils 100 %):

- Erstellung des Manuskripts und der Bilder
- Planung, Einkauf und Zusammenbau der Computer Hardware
- Planung des Präsentationstisches, Einbau der Hardware
- Anpassung und Programmierung der Software
- Erstellung der Videos mit eigenen Daten und Daten der Partner des Projekts

Im Rahmen des transregionalen Sonderforschungsbereiches „Biological Design and Integrative Structures“ TRR141 wurde auch eine Sonderausstellung zur Baubionik durchgeführt. Diese Sonderausstellung fand vom 19.10.2017 bis 6.5.2018 im Schloss Rosenstein statt, das zum Naturkundemuseum Stuttgart gehört.

Abbildung 13-1: Flyer des Naturkundemuseums [53]

In drei Räumen des Museums finden wechselnd Sonderausstellungen statt, die nachfolgend beschriebene interaktive Station befand sich im sogenannten Frühstückszimmer des Schlosses. Dort werden verschiedenste natürliche Materialien vorgestellt, die auf ihre Eigenschaften hinsichtlich Dämpfung, Energiedissipation (graceful failur behaviour), Leichtbau und Widerstandsfähigkeit gegen Einfrieren untersucht werden.

13.1 Interaktive Station

Die interaktive Station ist als Bindeglied zwischen der natürlichen und der künstlichen Welt gedacht. Sie besteht aus einem Podest, auf dem sich eine Ablagefläche befindet, in dem ein NearFieldCommunication(NFC)-Lesegerät eingebaut und mit einem Bildschirm versehen ist. Auf diesem werden Videos abgespielt, die durch NFC-Chips gestartet werden. Die Besucher können das Objekt anfassen, berühren und genau anschauen/untersuchen und wenn sie mehr wissen wollen, können sie die Objekte auf das Lesegerät legen und damit einen Film auf dem Bildschirm starten, der weitere Erklärungen liefert.

NFC steht für Near Field Communication und ist eine Funktechnik (basierend auf der 13,56 MHz Frequenz) die mit passiven Sendern (NFC-Chips) funktioniert, die mit einer aktiven Empfangsstation auf sehr kurze Distanzen kommunizieren können. Die Antenne der Chips wird durch Induktion angeregt und eine UID (Unique Identifier, eine eindeutige Kennung) wird zum Empfänger gesendet. Damit lassen sich die NFC-Chips eindeutig identifizieren. Diese Chips sind in Objekte integriert, die für bestimmte untersuchte Strukturen stehen. In Tabelle 13.2 und folgenden Abbildung (Abbildung 13-2) sind alle Objekte aufgelistet bzw. gezeigt.

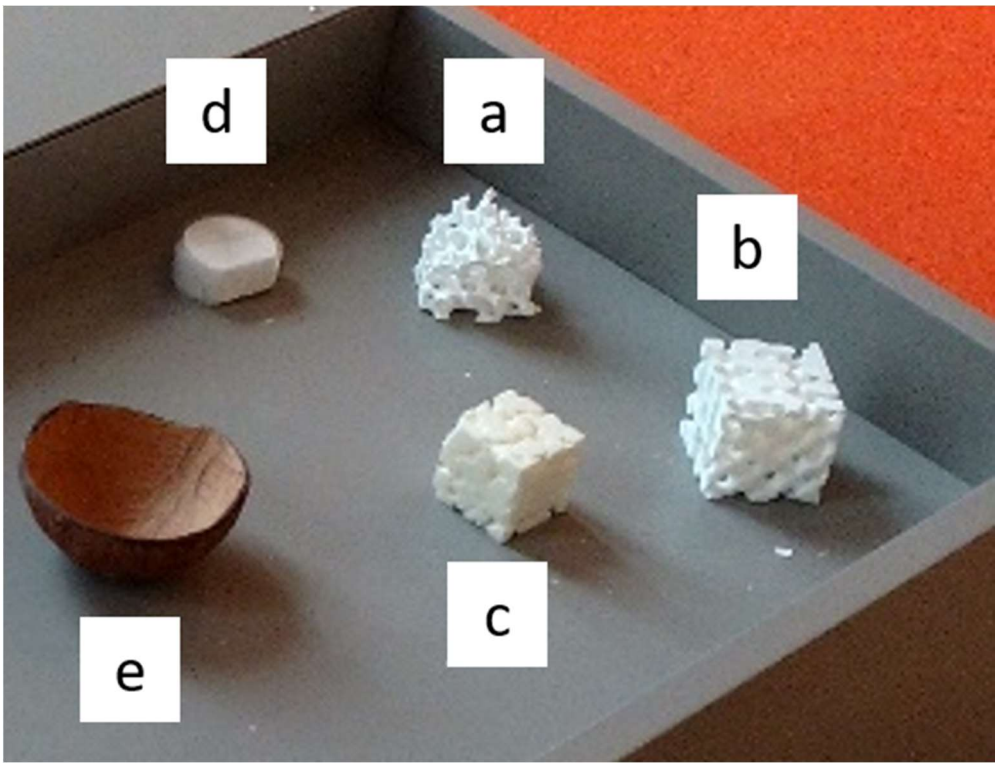

Abbildung 13-2: Ein Auswahl der Objekte, die mit NFC-Chips ausgestattet sind. Zuordnung siehe Tabelle 13.2: Objekte

Die drei 3D-gedruckten Strukturen (Abbildung 13-2 a, b und c) sind poröse Würfel mit einer Kantenlänge von 5 cm (abstrahierte Struktur) bzw. 6 cm und sind direkt aus der Mikrostruktur des Seeigelstachels umgesetzt worden. Der Würfel mit der abstrahierten Struktur aus dem Stereom des Seeigels *Heterocentrotus mamillatus* (Abbildung 13-2 b) wurde durch eine Reduzierung der Informationen, d. h. die Struktur wird durch Voxel repräsentiert (geringere Auflösung, vollständige Beschreibung in Kapitel 10), umgesetzt. Das Kokosnussobjekt ist eine natürliche, halbierte Kokosnussschale (das Endokarp). Die Mammutbaumrinde ist genau wie die Keramik (Abbildung 13-2 d) in Epoxidharz eingelegt, da ansonsten die Gefahr besteht, dass die Objekte durch das häufige Anfassen zerstört werden. Die Keramik wurde wie in [20] beschrieben hergestellt, die Mammutbaumrinde wurde passend zugesägt, so dass die Borke und auch ein Teil des Holzes sichtbar sind. Die NFC-Chips (Typ: COIN, NTAG 203, Ø 30 mm oder als Folie, Typ Label, NTAG 213, Ø 25mm) wurden in eingeschliffene Vertiefungen eingeklebt oder, wie im Fall der Folien-Chips, aufgeklebt.

Tabelle 13.2: Objekte

Objekt	Was zeigt es	Quelle	Bezeichnung in Abbildung 13-2
Mammutrinde in Epoxid-Harz	Ein Stück der Borke	Partner	Nicht vorhanden
Kokosnuss	Kokosnussendokarp, halbiert	Selbst hergestellt	**e**
Seeigelstachelstruktur 3D-gedruckt PHIL	Ein stark vergrößerter Ausschnitt der Mikrostruktur des Stachels der Seeigelart *Phyllacanthus imperialis*	Partner	**a**
Seeigelstachelstruktur 3D-gedruckt MAM	Ein stark vergrößerter Ausschnitt der Mikrostruktur des Stachels der Seeigelart *Heterocentrotus mamillatus*	Partner	**c**
Keramik	Eine poröse Keramik in Harz eingelegt	Partner	**d**
Abstrahierte Seeigelstruktur gedruckt	Ein stark vergrößerter Ausschnitt der Mikrostruktur des Stachels der Seeigelart *Heterocentrotus mamillatus* abstrahiert als Voxelmodel	Selbst designt und 3D gedruckt bei Fa. Rioprinto UG (Wernau, Deutschland rioprinto.de)	**b**

Die Verknüpfung der gelesenen UID mit dem Video erfolgt hardwareseitig durch ein Microprozessor-System (Einplatinencomputer). Das MRFC522 NFC-Reader (bzw. RFID(Radio-Frequency Identification)-) Modul (vgl. Abbildung 13-3 und folgende) enthält den Chip MFRC522 von NXP Semiconductors, NL [54], der über den SPI-Bus (vgl. Tabelle 13.3) mit einem Raspberry Pi 3 (Raspberrry Pi Foundation, UK) kommuniziert. Die Verkabelung erfolgte dabei nach Tabelle 13.2 mit Steckbrücken-Kabeln (zum Abgleich sind die Fotos der Steckverbindungen in Abbildung 13-3 und Abbildung 13-4 zu finden) am GPIO(General Purpose Input Output)-Interface des Raspberry Pi.

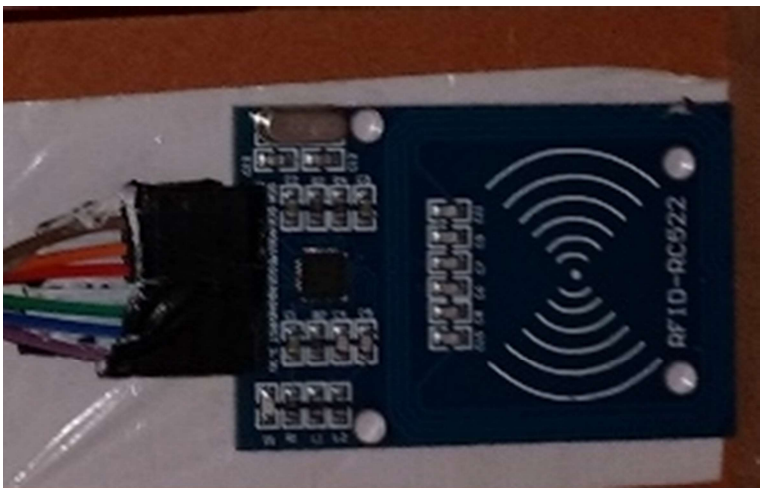

Abbildung 13-3: NFC-Reader

Abbildung 13-4: NFC-Reader und die Steckverbindungen am Raspberry Pi aus zwei unterschiedlichen Blickrichtungen

Der Raspberry Pi ist über HDMI einem Bildschirm (Model 3202L, Elo Touch Solutions, CA, USA) verbunden. Als Software läuft ein Raspbian Jessie, Stand (2017-01-11-raspbian-jessie, Raspberrry Pi Foundation, UK) mit den Python-Bibliotheken MRFC522 [55] und SPI-Py von Louis Thiery & Connor Wolf [56] und der Software *Pi presents* [57] und orientiert sich an einem Pythonscript (rfidmp3player.py) von Roaldh (2015). Name des Scripts: `NFC-MuseumPi.py`.

Tabelle 13.3: Raspberry GPIOs

RFID-RC522 Pin	Raspberry Pi Pin	Raspberry Pi Pin Bezeichnung
SDA/NSS	24	GPIO8
SCK	23	GPIO11
MOSI	19	GPIO10
MISO	21	GPIO9
IRQ	None	None
GND	20	GND
RST	22	GPIO25
3.3V/VCC	17	3V3

Nach der Verkabelung des Moduls, Installation des Raspbian Image auf einer Micro-SDKarte (mindestens 8gb), Anschluss von HDMI-Kabel (und einem Bildschirm), USB-Stromversorgung, Netzwerk und einer Tastatur/Maus (alternativ Kommunikation via SSH) wird die benötigte Software via command line interface (cli) installiert (Befehle in CODE-Formatierung):

Python Installation:

```
sudo apt-get install python-dev
```

SPI-Python und MFRC522-python Bibliothek installieren:

```
git clone https://github.com/lthiery/SPI-Py.git
cd SPI-Py
sudo python setup.py install
git clone https://github.com/mxgxw/MFRC522-python.git && cd MFRC522-python
```

SPI aktivieren:

```
sudo raspi-config
```

und dort dann SPI aktivieren.

Alle Dateien müssen nun aus den Ordnern SPI-Py und MRFC533-python in einen neuen Ordner „NFC“ kopiert, oder Pfade zu den oben genannten Ordnern müssen in den jeweiligen Skripten angepasst werden.

In dem Order NFC folgende Datei erstellen:

NFC-MuseumPi.py

Inhalt:

```
#!/usr/bin/python
import MFRC522
import signal
import ConfigParser
import os

# Read  config file
Config = ConfigParser.ConfigParser()
Config.read("/home/pi/NFC/rfidconfig.txt")

# From https://wiki.python.org/moin/ConfigParserExamples
def ConfigSectionMap(section):
  dict1 = {}
  options = Config.options(section)
  for option in options:
 try:
       dict1[option] = Config.get(section, option)
       if dict1[option] == -1:
            DebugPrint("skip: %s" % option)
 except:
       print("exception on %s!" % option)
       dict1[option] = None
  return dict1

# Open movie wit omxplayer (movieXX.py)
def TagToomxplayer (strTag):
  try:
 # Read tag attributes from config
 strActionType = ConfigSectionMap(strTag)['actiontype']
 strFileUrlFunction = ConfigSectionMap(strTag)['fileurlfunction']
 strDescription = ConfigSectionMap(strTag)['description']

       if strActionType == "OS":
   strAction = ""
   # Execute on OS, be careful, running as ROOT
```

```
    print ("Function")
    os.system (strFileUrlFunction)

  else:
    strAction = ""

  # Write to cfile
  with open(cfile, "w") as myfile:
    myfile.write(strAction+"\n")

   except:
  pass

continue_reading = True
MIFAREReader = MFRC522.MFRC522()

# --
#cfile = "/tmp/mplayer-control"

def end_read(signal, frame):
  global continue_reading
  continue_reading = False
  print "Ctrl+C captured, ending read."
  MIFAREReader.GPIO_CLEEN()

signal.signal(signal.SIGINT, end_read)

# Never stop reading
while continue_reading:
  (status,TagType)      =      MIFAREReader.MFRC522_Request(MIFARE-
Reader.PICC_REQIDL)
  if status == MIFAREReader.MI_OK:
    print "Card detected"
  (status,backData) = MIFAREReader.MFRC522_Anticoll()
  if status == MIFAREReader.MI_OK:
    strbackData          =          str(backData[0])+","+str(back-
Data[1])+","+str(backData[2])+","+str(backData[3])+","+str(back-
Data[4])

    print "Card read UID: " + strbackData

    # Do something (based on card and config file)
    TagToomxplayer(strbackData)
```

In dem Order NFC sollten jetzt zusätzlich die Dateien key1.py bis keyXX.py erstellt werden (für pipresent):

Beispiel: „key1.py “

Diese Dateien dann mit folgenden Inhalt füllen und logisch anpassen (key1.py hat die „1“ als Eintrag bei Befehl: *pyautogui.press* …, key 2.py die „2“ etc.:

```
import pyautogui
pyautogui.press('1')
```

Für jedes Video, das über einen NFC-Chip gestartet werden soll, wird solch eine keyxx.py Datei benötigt (also key1-Film1 etc).

Die Zuordnung von den UIDs zu den passenden Skripten (key1.py etc) wird in der rfidconfig.txt festgelegt.

Beispiel:

```
[136,4,76,0,192]   # UID des Chips
Description: sisvoxel    # Name
FileUrlFunction: python /home/pi/NFC/key1.py     # Funktion die ausgeführt wird, in dem fall wird das Skript aufgerufen.
ActionType: OS     # wichtig, damit das Skript mit Adminrechten ausgeführt wird.
TagType: Tag_1VoxelCaCO3 # Name des Tags (optional)
```

Das automatische Starten des Scriptes NFC-MuesumPi.py beim Booten Computers wird wie folgt konfiguriert:

```
sudo nano /etc/rc.local
```

Dann vor dem “Exit 0” Ausdruck hineinschreiben:

```
# Start Python RFID-reader-mplayer-control script
/home/pi/NFC/NFC-MuseumPi.py &
```

Neue Chips einlesen:

Neue Chips werden durch ihre UID erkannt. Der UID muss erst eingelesen werden. Das Skript Read.py ist im Ordner MREFC522 zu finden und kann zum Auslesen der Chips genutzt werden.

Dafür muss das Skript NFC-MusemPi.py deaktiviert werden, da ansonsten das Auslesen der Chips nicht korrekt funktioniert (Falsche UID!).

Dafür Autostart von NFC-MusemPi.py deaktivieren:

```
sudo nano /etc/rc.local
```

mit "#" den Autostart deaktivieren:

```
# Start Python RFID-reader-mplayer-control script
#/home/pi/NFC/NFC-MuseumPi.py &
```

Dann Raspberry Pi Neustarten und im Ordner NFC die Read.py ausführen:

```
cd NFC
python Read.py
```

Nun können die Chips eingelesen werden und deren UID notiert werden. Danach in die rfidconfig.txt eintragen und mit den keyXX.py Dateien verknüpfen.

Die zugehörigen Videos/Audios werden mit der folgenden Konfiguration von *Pi presents* eingerichtet. (Danach sollte der Autostart wieder eingerichtet werden und ein Neustart des Computers steht an.)

Pi-presents:

Pi presents wurde von Ken Thompson entwickelt [57]. Es ist für die Nutzung in Museen oder Ausstellungen optimiert, damit Musik, Videos und Bilder abgespielt werden können. Es nutzt auch die GPIO-Interfaces des Raspberry Pis und kann somit auch auf Tastendruck, Bewegungsmeldern und anderen Sensoren reagieren oder Lichteffekte etc. über die GPIO Leiste steuern.

In dem hier vorgestellten Fall wird ein Standbild durch die Software *Pi presents* abgespielt. Sobald eines der Objekte mit dem NFC Chip auf die markierte Stelle gelegt wird, läuft das hinterlegte Videos ab. Dabei wird die Fähigkeit der Software ausgenutzt, auf Tastatureingaben zu reagieren (es wird eine sogenannte „*Radiobuttonshow*" genutzt. Für weitere Erklärungen zu den jeweiligen Einstellungsmöglichkeiten der Software *Pi-presents* wird auf die Seite www.pipresents.wordpress.com verwiesen). Die UIDs der NFC-Chips sind durch die Datei *rfidconfig.txt* mit den Skripten *keyXX.py* verknüpft, die durch das Script *NFC-Museumpi.py* aufgerufen werden, wenn der passende NFCChip gelesen wird.

Das Skript *keyxx.py* sendet dann einen Tastenanschlag (z. B. „1“) an die Software *Pi-presents*, diese wiederum hat ein Verknüpfung von Tastaturbefehl „1“ mit einem zum Objekt passenden Video und spielt es ab. Die Videowiedergabe wird unterbrochen, wenn ein weiterer Chip erkannt wird.

Durch einen weiteren Autostarteintrag wird *Pi-presents* beim Starten des Betriebssystems auf dem Raspberry Pi gestartet.

Damit ist die softwareseitige Einrichtung der interaktiven Station abgeschlossen.

Eine sinnvolle Ergänzung des Setups ist das Betriebssystem Read-Only einzurichten. Damit kann auch ein plötzlicher Stromverlust keine Probleme (korrupte SDKarte z. B.) verursachen. Die Befestigung der Hardware ist in Abbildung 13-5 und Abbildung 13-6 gezeigt.

Abbildung 13-5: Befestigung NFC-Lesegerät und Raspberry Pi

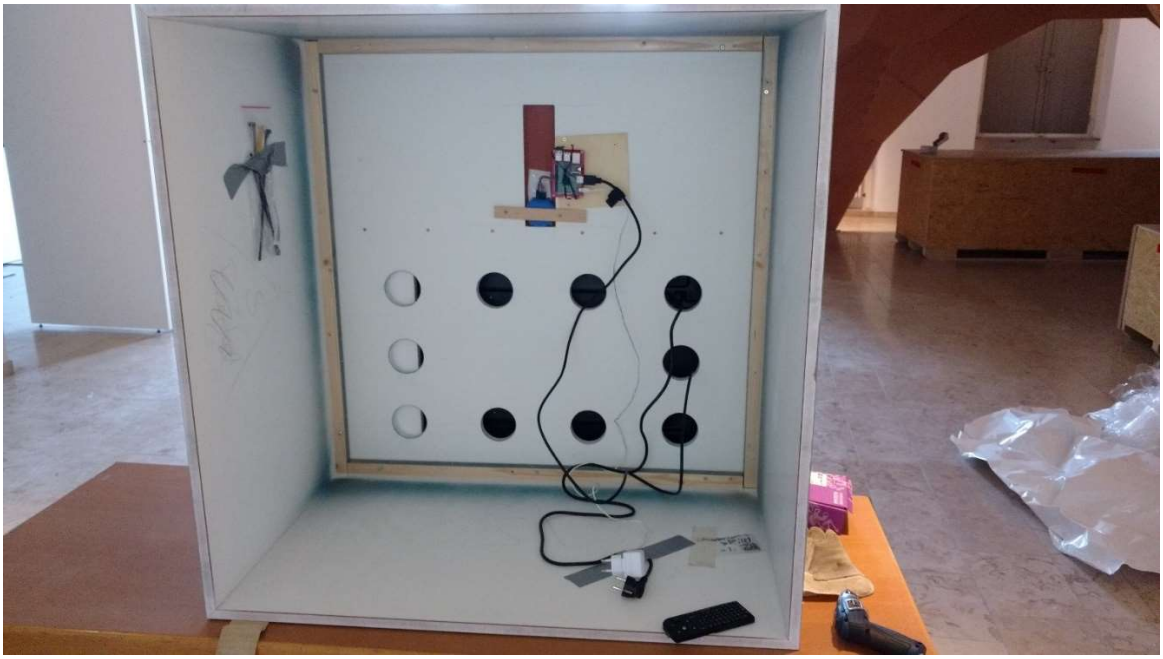

Abbildung 13-6: Fertige Hardware Befestigung an der interaktiven Station

In Abbildung 13-7 ist das Podest von vorne zu sehen. Man erkennt den Bildschirm und die Ablage, in der das NFC-Lesegerät eingebracht ist und die Ablage für die Ausstellungsstücke.

Abbildung 13-7: Podest der interaktiven Station von vorne im Rohbau

Abbildung 13-8: Interaktive Station in Aktion

Die interaktive Station (Abbildung 13-8) wurde gerne ausprobiert, zumindest waren am Ende der Ausstellung einige Abnutzungsspuren an den Objekten vorhanden. Zwei Objekte mussten sogar ersetzt werden, vermutlich weil sie den Besuchern zu gut gefallen haben (sie waren nicht mehr auffindbar). Die Möglichkeit, Objekte zum Anfassen mit den Videos und mit den Informationen und Ergebnissen unserer Forschung zu verbinden, war einzigartig und kam gut beim Publikum an. Die Aufbereitung der Information für eine solche Art der

Präsentation war ganz anders, als wir Wissenschaftler es von Konferenzen oder Meetings gewohnt sind. Für mich war insbesondere das Setup der Software bzw. Skripte und die Planung, Zusammenstellung und Zusammenbau der Hardware mit den Mitarbeitern des Museums und natürlich die Ausstellung als Gesamtheit mit allen Ergebnissen des Transregios TRR141 eine tolle und neue Erfahrung.

14 Übersicht aller Veröffentlichungen

Die folgenden Veröffentlichungen sind alle im Rahmen der Mitarbeit am Institut für Materialprüfung, Werkstoffkunde und Festigkeitslehre (IMWF) entstanden und werden der Vollständigkeitshalber aufgelistet (Nummerierung nach Erscheinen in der vorliegenden Arbeit):

I. Schäfer, I. (2013). Biomimetics in Energy Systems: Light Transmission in the Window Plant *Fenestraria aurantiaca* as Inspiration for New Solutions in the Technical World. Advances in Science and Technology, 84, pp. 51–56.

II. Lasko, G., Schäfer, I., Burghard, Ž., Bill, J., Schmauder, S., Weber, U., & Galler, D. (2013). Derivation of the Stress-Strain Behavior of the constituents of Bio-Inspired Layered TiO_2/PE-Nanocomposites by Inverse Modeling Based on FE-Simulations of Nanoindentation Test. *Molecular & Celullar Biomechanics*, *10*(1), pp. 27–42.

III. Lasko, G., Burghard, Ž., Bill, J., Schäfer, I., Weber, U., & Schmauder, S. (2013). Simulation of Mechanical Properties of Bio-Inspired TiO_2/PE Nanocomposites. *Advanced Engineering Materials*, *15*(10), pp. 908–920.

IV. Schäfer, I., Lasko, G., Do, T. A., Pleiss, J., Weber, U., & Schmauder, S. (2014). Peptide-zinc oxide interaction: Finite element simulation using cohesive zone models based on molecular dynamics simulation. *Computational Materials Science*, *95*, pp. 320–327.

V. Schmauder, S., & Schäfer, I. (Eds.). (2016). *Multiscale materials modeling: approaches to full multiscaling*. Berlin: De Gruyter.

VI. Schäfer, I., Lasko, G., Do, T. A., Pleiss, J., Weber, U., & Schmauder, S. (2016). Peptide-zinc oxide interaction: Finite element simulation using cohesive zone models based on molecular dynamics simulation. In Multiscale Materials Modeling: Approaches to Full Multiscaling, (2016), pp. 303–322.

VII. Schäfer, I., Mlikota, M., Schmauder, S., & Weber, U. (2020). Modelling the damping response of biomimetic foams based on pomelo fruit. Computational Materials Science, 183, pp. 109801.

VIII. Schmier, S., Lauer, C., Schäfer, I., Klang, K., Bauer, G., Thielen, M., Termin, K., Berthold, C., Schmauder, S., Speck, T., Nickel, K. G. (2016). Developing the Experimental Basis for an Evaluation of Scaling Properties of Brittle and 'Quasi-Brittle' Biological Materials. In *Biomimetic Research for Architecture and Building Construction*, pp. 277–294.

Nicht veröffentlicht/Konferenzbeitrag:

IX. Schäfer, I., Bräutigam, D., Schmid, P., & Schmauder, S. (2017). Evolution is the better architect: Simulation of cellular solids in sea urchin spines, Conference SMILE 2016, organized by IFP Energies nouvelles (IFPEN), at Rueil-Malmaison, http://www.rs-smile2016.com/

Nicht in dieser Arbeit behandelt:

X. Schmauder, S., & Schäfer, I. (2016). Materialprüfung an der MPA Stuttgart. In K. Hentschel & J. Webel (Eds.), *Geschichte und Praxis der Materialforschung*. Diepholz: GNT-Verlag, pp. 152–177

XI. (Übersetzung von VIII) Schmier, S., Bauer, G., Buck, G., Klang, K., Lauer, C., Toader, N., Gericke, O., Haase, W., Schäfer, I., Schmauder, S., Sobek, W., Nickel, K., G., Speck, T., (2017). Hohe Belastungen sicher überstehen, in *Baubionik* (J. Knippers, U. Schmid, & T. Speck, eds.) Stuttgart: Stuttgarter Beiträge zur Naturkunde. Band 82, pp. 41–61)

15 Verzeichnisse

15.1 Literaturverzeichnis

Hier werden alle Quellen genannt, die außerhalb der Veröffentlichungen zitiert wurden.

[1] R. H. Francé, *Die Pflanze als Erfinder*. Stuttgart: Kosmos, Gesellschaft der Naturfreunde, 1920.

[2] I. C. Gebeshuber and Ecowin bei Benevento Publishing eine Marke der Red Bull Media House GmbH, *Wo die Maschinen wachsen Wie Lösungen aus dem Dschungel unser Leben verändern werden*. 2016.

[3] J. Knippers, K. G. Nickel, and T. Speck, Biomimetic Research for Architecture and Building Construction, vol. 8. 2016.

[4] S. Littmarck, "COMSOL NEWS 2015," 2015.

[5] M.-D. Weitze and C. Berger, Werkstoffe: Unsichtbar, aber unverzichtbar. 2013.

[6] M. F. Ashby and D. R. H. Jones, *Engineering Materials 1*. 2012.

[7] Werkstoffe 1: Eigenschaften, Mechanismen und Anwendungen: Deutsche Ausgabe herausgegeben von Michael Heinzelmann: Amazon.de: Michael F. Ashby, David R. H. Jones: Bücher." [Online]. Available: http://www.amazon.de/Werkstoffe-Eigenschaften-Mechanismen-Anwendungen-herausgegeben/dp/3827417082. [Accessed: 14-Oct-2015].

[8] P.-Y. Chen, J. McKittrick, and M. A. Meyers, "Biological materials: Functional adaptations and bioinspired designs," *Prog. Mater. Sci.*, vol. 57, no. 8, pp. 1492–1704, Nov. 2012.

[9] I. Schäfer, "Biomimetics in Energy Systems: Light Transmission in the Window Plant *Fenestraria aurantiaca* as Inspiration for New Solutions in the Technical World," *Adv. Sci. Technol.*, vol. 84, pp. 51–56, Jan. 2013.

[10] H. Gao, B. Ji, I. L. Jäger, E. Arzt, and P. Fratzl, "Materials become insensitive to flaws at nanoscale: Lessons from nature," *Proc. Natl. Acad. Sci. U.S.A.*, vol. 100, no. 10, pp. 5597–5600, 2003.

[11] A. P. Jackson, J. F. V. Vincent, and R. M. Turner, "The mechanical design of nacre," *Proc. R. Soc. London. Ser. B, Biol. Sci.*, vol. 234, no. 1277, pp. 415–440, 1988.

[12] I. Jäger and P. Fratzl, "Mineralized collagen fibrils: a mechanical model with a staggered arrangement of mineral particles," *Biophys. J.*, vol. 79, no. October, pp. 1737–1746, 2000.

[13] Biomimetic and Bioinspired Nanomaterials (Nanomaterials for Life Sciences (VCH)). Wiley-VCH, 2010.

[14] F. Barthelat, C.-M. Li, C. Comi, and H. D. Espinosa, "Mechanical properties of nacre constituents and their impact on mechanical performance," *J. Mater. Res.*, vol. 21, no. 08, pp. 1977–1986, Mar. 2011.

[15] D. R. Katti, S. Pradhan, and K. Katti, "Modeling the organic-inorganic interfacial nanoasperities in a model bio-nanocomposite, nacre.," *Rev. Adv. Mater. Sci.*, vol. 6, pp. 162–168, 2004.

[16] F. Song, X. H. Zhang, and Y. L. Bai, "Microstructure and Characteristics in the Organic Matrix Layers of Nacre," *J. Mater. Res.*, vol. 17, no. 07, pp. 1567–1570, Jan. 2011.

[17] T. Schäffer *et al.*, "Does abalone nacre form by heteroepitaxial nucleation or by growth through mineral bridges?," *Chem. Mater.*, vol. 4756, no. 27, pp. 1731–1740, 1997.

[18] A. Bührig-Polaczek *et al.*, "Biomimetic cellular metals—using hierarchical structuring for energy absorption," *Bioinspir. Biomim.*, vol. 11, no. 4, p. 045002, 2016.

[19] M. Thielen, T. Speck, and R. Seidel, "Impact behaviour of freeze-dried and fresh pomelo (Citrus maxima) peel: Influence of the hydration state," *R. Soc. Open Sci.*, vol. 2, no. 6, 2015.

[20] S. Schmier *et al.*, "Developing the Experimental Basis for an Evaluation of Scaling Properties of Brittle and 'Quasi-Brittle' Biological Materials," in *Biomimetic Research for Architecture and Building Construction*, Springer, Cham, 2016, pp. 277–294.

[21] S. Schmier *et al.*, “Baubionik,” 82nd ed., J. Knippers, U. Schmid, and T. Speck, Eds. Stuttgart: Stuttgarter Beiträge zur Naturkunde, 2017, pp. 41–61.

[22] V. Presser *et al.*, “Sea Urchin Spines as a Model-System for Permeable, Light-Weight Ceramics with Graceful Failure Behavior. Part II. Mechanical Behavior of Sea Urchin Spine Inspired Porous Aluminum Oxide Ceramics under Compression,” *J. Bionic Eng.*, vol. 6, no. 4, pp. 357–364, 2009.

[23] J. N. Weber, “The incorporation of magnesium into the skeletal calcites of echinoderms,” *Am. J. Sci.*, vol. 267, no. 5, pp. 537–566, May 1969.

[24] V. Presser, K. Gerlach, A. Vohrer, K. G. Nickel, and W. F. Dreher, “Determination of the elastic modulus of highly porous samples by nanoindentation: a case study on sea urchin spines,” *J. Mater. Sci.*, vol. 45, no. 9, pp. 2408–2418, May 2010.

[25] V. Presser, S. Schultheiß, C. Berthold, and K. G. Nickel, “Sea Urchin Spines as a Model-System for Permeable, Light-Weight Ceramics with Graceful Failure Behavior. Part I. Mechanical Behavior of Sea Urchin Spines under Compression,” *J. Bionic Eng.*, vol. 6, no. 3, pp. 203–213, Sep. 2009.

[26] J. Seto *et al.*, “Correction for Seto et al., Structure-property relationships of a biological mesocrystal in the adult sea urchin spine,” *Proc. Natl. Acad. Sci.*, vol. 109, no. 18, pp. 7126–7126, May 2012.

[27] H. Cölfen and M. Antonietti, “Mesokristalle: anorganische Überstrukturen durch hochparallele Kristallisation und kontrollierte Ausrichtung,” *Angew. Chemie*, vol. 117, no. 35, pp. 5714–5730, 2005.

[28] a B. Smith, “Stereom microstructure of the echinoid test,” *Special Papers in Palaeontology*, vol. 25. pp. 1–81, 1980.

[29] Y. Ma *et al.*, “Structure-property relationships of a biological mesocrystal in the adult sea urchin spine,” *Proc. Natl. Acad. Sci.*, vol. 109, no. 18, pp. 7126–7126, 2012.

[30] S. Schmauder and I. Schäfer, “Multiscale materials modeling,” *Materials Today*, vol. 19, no. 3. pp. 130–131, 2016.

[31] D. Molnar *et al.*, “Multiscale simulations on the coarsening of Cu-rich precipitates in α-Fe using kinetic Monte Carlo, molecular dynamics and phase-field simulations,” *Acta Mater.*, vol. 60, no. 20, pp. 6961–6971, Dec. 2012.

[32] A. Siddiq and S. Schmauder, “Interface fracture analyses of a bicrystal niobium/alumina specimen using a cohesive modelling approach,” *Model. Simul. Mater. Sci. Eng.*, vol. 14, no. 6, pp. 1015–1030, Sep. 2006.

[33] M. Karplus and G. Petsko, “Molecular dynamics simulations in biology,” *Nature*, vol. 347, pp. 631–639, 1990.

[34] M. Karplus and J. A. McCammon, “Molecular dynamics simulations of biomolecules.,” *Nat. Struct. Biol.*, vol. 9, no. 9, pp. 646–52, Sep. 2002.

[35] M. C. Zwier and L. T. Chong, “Reaching biological timescales with all-atom molecular dynamics simulations.,” *Curr. Opin. Pharmacol.*, vol. 10, no. 6, pp. 745–752, Dec. 2010.

[36] B. Ji and H. Gao, “Mechanical properties of nanostructure of biological materials,” *J. Mech. Phys. Solids*, vol. 52, no. 9, pp. 1963–1990, Sep. 2004.

[37] D. Sikdar, S. M. Pradhan, D. R. Katti, K. S. Katti, and B. Mohanty, “Altered phase model for polymer clay nanocomposites.,” *Langmuir*, vol. 24, no. 10, pp. 5599–5607, May 2008.

[38] V. S. Deshpande and N. A. Fleck, “Isotropic constitutive models for metallic foams,” *J. Mech. Phys. Solids*, vol. 48, no. 6, pp. 1253–1283, 2000.

[39] T. Daxner, “Finite Element Modeling of Cellular Materials,” in *Cellular and Porous Materials in Structures and Processes*, H. Altenbach and A. Öchsner, Eds. Vienna: Springer Vienna, 2010, pp. 47–106.

[40] G. Lasko *et al.*, “Derivation of the Stress-Strain Behavior of the constituents of Bio-Inspired Layered TiO_2/PE-Nanocomposites by Inverse Modeling Based on FE-Simulations of Nanoindentation Test,” *Mol. Celullar Biomech.*, vol. 10, no. 1, pp. 27–42, 2013.

[41] G. Lasko, Ž. Burghard, J. Bill, I. Schäfer, U. Weber, and S. Schmauder, “Simulation of Mechanical Properties of Bio-Inspired TiO_2/PE Nanocomposites,” *Adv. Eng. Mater.*, vol. 15, no. 10, pp. 908–920, Apr. 2013.

[42] I. Schäfer, G. Lasko, T. A. Do, J. Pleiss, U. Weber, and S. Schmauder, “Peptide-zinc oxide interaction: Finite element simulation using cohesive zone models based on molecular dynamics simulation,” *Comput. Mater. Sci.*, vol. 95, 2014.

[43] I. Schäfer, G. Lasko, T. A. Do, J. Pleiss, U. Weber, and S. Schmauder, Peptide-zinc oxide interaction: Finite element simulation using cohesive zone models based on molecular dynamics simulation. 2016.

[44] K.-H. Grote and J. (Jörg) Feldhusen, *Dubbel : Taschenbuch für den Maschinenbau*. Springer, 2011.

[45] Normenausschus Kunststoffe, “DIN EN ISO 527-1,” 2014.

[46] E. Njeugna, M. B. K. Ganou, D. Ndapeu, J. N. T. Foba, N. R. T. Sikame, and P. W. M. Huisken, “An Instrumented Macro-Indentation Method for Determining the Mechanical Properties of Coconut Shell (Coco Nucifera of Cameroon),” *Mech. Mater. Sci. Eng.*, no. July, 2016.

[47] Röchling, “Technisches Datenblatt Trovidur PVC,” 2014.

[48] B. Schröder, *Kunststoffe für Ingenieure*, vol. 1. Wiesbaden: Springer Fachmedien Wiesbaden, 2014.

[49] J. Wiedmaier, U. Weber, and S. Schmauder, “Simulation of the Mechanical Behavior of Nanodispersed Elastomer Particle-Modified Polyamide 6,” *Adv. Mater. Res.*, vol. 746, pp. 250–255, Aug. 2013.

[50] I. Schäfer, D. Bräutigam, P. Schmid, and S. Schmauder, “Evolution is the better architect : Simulation of cellular solids in sea urchin spines,” in *Energy - Sustainable Advanced Materials; E-SAM*, T. N. Lambert and M. E. Alston, Eds. NYC, USA: Springer Nature, Materials Science and Engineering, 2017.

[51] N. Tsafnat, J. D. Fitz Gerald, H. N. Le, and Z. H. Stachurski, “Micromechanics of Sea Urchin spines.,” *PLoS One*, vol. 7, no. 9, p. e44140, Jan. 2012.

[52] A. Picker *et al.*, “Mesocrystalline calcium silicate hydrate: A bioinspired route toward elastic concrete materials,” *Sci. Adv.*, vol. 3, no. 11, p. e1701216, 2017.

[53] “hp_baubionik_folder_titel_s1_neu-kl.” [Online]. Available: http://www.naturkundemuseum-bw.de/sites/default/files/imagecache/allgemein_inhalt/sonderausstellung/hp_baubionik_folder_titel_s1_neu-kl.jpg. [Accessed: 22-Feb-2018].

[54] NXP, “MFRC522 Chip,” *product data sheet*, 2016. [Online]. Available: https://www.nxp.com/docs/en/data-sheet/MFRC522.pdf.

[55] mxgxw, “MFRC522-python,” *www.github.com*, 2013. [Online]. Available: https://github.com/mxgxw/MFRC522-python. [Accessed: 23-Oct-2017].

[56] Lthiery, “SPI-Py,” *www.github.com*, 2013. [Online]. Available: https://github.com/lthiery/SPI-Py. [Accessed: 23-Oct-2017].

[57] KenT2, “pipresents-next,” *www.github.com*, 2013. [Online]. Available: https://github.com/KenT2/pipresents-next. [Accessed: 10-Aug-2017].

[58] Roaldh, “Raspberry Pi based RFID Music Robot,” *http://www.instructables.com*, 2015. [Online]. Available: http://www.instructables.com/id/Raspberry-Pi-based-RFID-Music-Robot/. [Accessed: 10-Aug-2017].

15.2 Abbildungsverzeichniss

15.3 Tabellenverzeichnis

Eidesstattliche Erklärung

Eidesstattliche Erklärung zu meiner Dissertation mit dem Titel:

„Numerische Simulationen von bioinspirierten und natürlichen Materialien“

Hiermit erkläre ich, dass ich die beigefügte Dissertation selbstständig verfasst und keine anderen als die angegebenen Hilfsmittel genutzt habe. Alle wörtlich oder inhaltlich übernommenen Stellen habe ich als solche gekennzeichnet.

Ich versichere außerdem, dass ich die beigefügte Dissertation nur in diesem und keinem anderen Promotionsverfahren eingereicht habe und dass diesem Promotionsverfahren keine endgültig gescheiterten Promotionsverfahren vorausgegangen sind.

Radolfzell, den 06.07.2020 Immanuel Schäfer

i.schaefer@mailbox.org